UNIVERSITÄT ZU LÜBECK
INSTITUT FÜR BIOMEDIZINISCHE OPTIK

From the Institute of Biomedical Optics
of the University of Lübeck
Director: Prof. Dr. rer. nat. Robert Huber

Functional imaging with MHz-OCT

Dissertation
for the Fulfillment of
Requirements
for the Doctoral Degree
of the University of Lübeck

from the Department of Natural Sciences

submitted by
Sazgar Burhan
from Lübeck, Germany

Lübeck 2025

First referee: Prof. Dr. rer. nat. Robert Huber
Second referee: Prof. Dr. rer. nat. habil. Heinz Handels
Date of oral examination: 08.06.2026
Approved for printing: 10.06.2026

Diese Arbeit widme ich meinen Eltern,
die Berge hinter sich ließen,
damit ich zwischen fremden Türmen wachsen konnte.

Contents

List of figures

List of tables

Summary

Functional imaging enables the visualization of tissue structure alongside a map of its dynamic activity. This could include movements at the cellular level, mechanical changes, or metabolically induced activity patterns. Such information complements conventional imaging and can be particularly important where morphological differences alone do not allow for reliable diagnostic conclusions. In many clinical situations, this kind of functional additional information is crucial, for example, when assessing tissue function and integrity or localizing tumor tissue during surgery. The goal of current developments is therefore to provide imaging methods that can capture these functional signals quickly, non-invasively, and without the use of exogenous contrast agents, ideally in real-time and with a high resolution.

Optical coherence tomography (OCT) is a non-invasive optical imaging technique that provides high-resolution cross-sectional images of biological tissue. In recent years, OCT has advanced considerably beyond its initial role as a purely structural imaging method. Notably, progress in achieving A-scan rates in the megahertz range has created new opportunities. With these so-called MHz-OCT systems, large data sets can be collected quickly and with high phase stability, which is essential for accurately visualizing the functional properties of tissue. In this work, two complementary functional approaches based on MHz-OCT were examined and further developed with a focus on their potential applications in biomedical imaging.

In the first part of the work, the suitability of MHz-OCT for optical coherence elastography (OCE) to distinguish between healthy and tumorous brain tissue was evaluated. Two strategies were implemented for this purpose. One was a phase-sensitive method for the precise measurement of microscopic tissue displacements, and the other was an alternative contrast approach based on a Fourier analysis of the complex OCT signal. The approaches were experimentally validated using phantoms, *ex vivo* porcine brain tissue, and *ex vivo* human brain tumor tissue. The resulting elasticity maps were correlated with histological reference data and clearly showed differences in mechanical tissue stiffness. Additionally, analyses of stability and reproducibility were conducted to confirm the reliability and robustness of the method.

In the second part of this work, dynamic MHz-OCT (dOCT) was used to study speckle-based intensity fluctuations in *ex vivo* kidney tissue. The aim was to determine whether these signals could provide an additional imaging contrast that may be valuable in the context of kidney transplantation. To enable large-area imaging, a self-built,

high-precision, motorized three-axis linear robot was realized and comprehensively characterized in terms of its positioning accuracy. Furthermore, various temporal sampling strategies were investigated, with particular emphasis on non-equidistant sampling schemes aimed at reducing the number of repetitive frames while maintaining high dynamic contrast quality. Principal component analysis was used as part of the evaluation.

The methods developed and analyzed in this dissertation demonstrate the strong potential of MHz-OCT for functional tissue analysis. Both OCE and dOCT offer a significantly deeper understanding of tissue composition and activity without relying on external contrast agents, tissue markers, or time-consuming histological processing. The concept shown in this work illustrates how dynamic MHz-OCT could support fast and objective tissue analysis in clinical practice. Additionally, the elastographic brain tissue measurements indicate that MHz-OCT may provide meaningful support in situations where existing intraoperative imaging techniques are insufficient.

Zusammenfassung

Funktionelle Bildgebung ermöglicht die Visualisierung der Gewebestruktur und zugleich ihrer dynamischen Aktivität. Dazu zählen etwa Bewegungen auf zellulärer Ebene, mechanische Veränderungen oder metabolisch bedingte Aktivitätsmuster. Solche Informationen ergänzen die klassische Bildgebung und können insbesondere dort von Bedeutung sein, wo morphologische Unterschiede allein keine verlässliche diagnostische Aussage erlauben. In vielen klinischen Situationen ist eine solche funktionelle Zusatzinformation entscheidend, etwa bei der Beurteilung der Funktionsfähigkeit bzw. Integrität des Gewebes oder bei der intraoperativen Abgrenzung von Tumorgewebe. Ziel aktueller Forschung ist es daher, Verfahren zu entwickeln, die solche funktionellen Signale schnell, nicht-invasiv und ohne Zugabe von exogenen Kontrastmitteln erfassen, möglichst in Echtzeit und mit hoher Auflösung.

Die optische Kohärenztomographie (OCT) ist eine nicht-invasive optische Bildgebungstechnik, die hochauflösende Querschnittsbilder von biologischem Gewebe liefert. In den letzten Jahren hat sich OCT deutlich über ihre ursprüngliche Rolle als rein strukturelles Bildgebungsverfahren hinausentwickelt. Insbesondere der technische Fortschritt hin zu A-Scan-Raten im Megahertz-Bereich hat neue Möglichkeiten eröffnet. Mit diesen sogenannten MHz-OCT-Systemen lassen sich große Datenmengen in sehr kurzer Zeit und mit hoher Phasenstabilität erfassen, was eine wichtige Voraussetzung ist, um auch funktionelle Eigenschaften des Gewebes zuverlässig abzubilden. In dieser Arbeit wurden daher zwei komplementäre funktionelle Ansätze auf Basis von MHz-OCT erforscht und gezielt weiterentwickelt, wobei der Schwerpunkt auf ihren potenziellen Anwendungen in der biomedizinischen Bildgebung lag.

Im ersten Teil der Arbeit wurde die Eignung von MHz-OCT für die optische Kohärenzelastographie (OCE) zur Unterscheidung von gesundem und tumorösem Hirngewebe evaluiert. Dafür wurden zwei Auswertestrategien umgesetzt. Eine phasensensitive Methode zur präzisen Messung mikroskopischer Gewebsverschiebungen sowie eine alternative Kontrastform auf Basis einer Fourier-Analyse des komplexwertigen OCT-Signals. Die Ansätze wurden experimentell an Phantomen, *ex vivo* Schweinegehirnen und *ex vivo* humanem Hirntumorgewebe validiert. Die resultierenden Elastizitätskarten korrelierten mit histologischen Referenzdaten, wobei insbesondere Unterschiede in der mechanischen Gewebesteifigkeit klar dargestellt werden konnten. Zusätzlich wurden Stabilitäts- und Reproduzierbarkeitsanalysen durchgeführt, um die Aussagekraft und Robustheit des Verfahrens zu belegen.

Im zweiten Teil der Arbeit wurde dynamische MHz-OCT (dOCT) eingesetzt, um specklebasierte Intensitätsschwankungen in *ex vivo* Nierengewebe zu untersuchen. Ziel war es festzustellen, ob diese Signale einen zusätzlichen Bildgebungskontrast liefern können, der im Kontext von Nierentransplantationen von Nutzen sein könnte. Um großflächiges Scannen zu ermöglichen, wurde ein eigen entwickelter hochpräziser, motorisierter Drei-Achsen-Linearroboter realisiert und hinsichtlich seiner Positioniergenauigkeit umfassend charakterisiert. Darüber hinaus wurden verschiedene zeitliche Abtaststrategien untersucht, wobei insbesondere nicht-äquidistante Sampling-Schemata zur Reduktion der repetitiven Bildanzahl bei gleichbleibender hoher dynamischer Kontrastqualität evaluiert wurden. Dabei kam unter anderem eine Hauptkomponentenanalyse zum Einsatz.

Die in dieser Dissertation entwickelten und getesteten Methoden zeigen das hohe Potenzial von MHz-OCT für die funktionelle Gewebeanalyse. Sowohl OCE als auch dOCT ermöglichen einen deutlich tieferen Einblick in die Gewebezusammensetzung und -aktivität, ohne auf externe Kontrastmittel, Gewebemarker oder zeitaufwändige histologische Aufbereitung angewiesen zu sein. Das in dieser Arbeit demonstrierte Konzept zeigt, wie die dynamische MHz-OCT zur schnellen und objektiven Gewebeanalyse im klinischen Alltag beitragen könnte. Gleichzeitig verdeutlichen die Ergebnisse der elastographischen Hirngewebemessungen, dass MHz-OCT auch dort eine wertvolle Ergänzung sein kann, wo bisherige intraoperative Bildgebungsverfahren an ihre Grenzen stoßen.

Abbreviations

5-ALA	5-aminolevulinic acid
AI	Artificial intelligence
ASE	Amplified spontaneous emission
BOA	Booster optical amplifier
CNR	Contrast-to-noise ratio
CT	Computed tomography
DC	Direct current
dOCT	Dynamic optical coherence tomography
ECD	Expanded criteria donor
FDML	Fourier domain mode locking
FFT	Fast Fourier transform
FOV	Field of view
FSR	Free spectral range
FWHM	Full width at half maximum
GUI	Graphical user interface
H&E	Hematoxylin & eosin
HMP	Hypothermic machine perfusion
HTD	High-torque drive
iMRI	Intraoperative magnetic resonance imaging
InGaAs	Indium gallium arsenide
MRI	Magnetic resonance imaging
NA	Numerical aperture
OCE	Optical coherence elastography
OCT	Optical coherence tomography
PCA	Principal component analysis
PSF	Point spread function
PVA	Polyvinyl alcohol
RIN	Relative intensity noise
SNR	Signal-to-noise ratio
SOA	Semiconductor optical amplifier
VISA	Virtual Instrument Software Architecture
WHO	World Health Organization

1 Introduction

Functional imaging has become essential in many medical fields, as it reveals dynamic biological processes that are difficult to observe with structural imaging alone. Therefore, a key aim of current biomedical imaging research is to visualize tissue behavior, not just its appearance. Whether assessing organ health or detecting subtle pathological changes, these insights support more informed clinical decisions and enhance the understanding of tissue function across various fields.

The vision for functional imaging is clear. It should combine high precision with seamless integration into clinical practice. Ideally, such a system would be compact, non-invasive, and operate without the use of contrast agents or ionizing radiation. It would offer the speed and flexibility required for direct use at the point of care, including in the confined environment of an operating room. Such a tool could provide simultaneous access to structural and functional information, enabling clinicians to make informed decisions during procedures, adapt treatments immediately, and overcome the limitations of relying solely on preoperative imaging.

In recent years, advances in optical imaging have brought this idea closer to reality. One of the most significant developments in this field has been optical coherence tomography (OCT), first introduced in the early 1990s [1]. Originally developed for retina imaging, its ability to produce micrometer-scale cross-sectional images in real-time soon led to its adoption in other clinical research fields [2]. Over the past two decades, OCT has seen substantial technological progress. The axial resolution has improved by more than a factor of ten, imaging speeds have increased by over half a million times, and image contrast has been significantly enhanced [3]. These technical advances have paved the way for various functional OCT techniques [4-6].

Within six months after the first demonstration of OCT, polarization-sensitive OCT was introduced [7], enabling discrimination of birefringent structures such as muscle, nerve fibers, and collagen-rich tissues [8]. Following its success, early Doppler OCT implementations emerged around 1997 [9], and the first phase-resolved Doppler OCT was introduced by Yonghua Zhao et al. in 2000 [10]. They detected subtle phase differences between consecutive A-scans caused by the motion of particles, particularly red blood cells. Since

then, this approach has remained the most widely adopted functional-OCT modality, offering a noninvasive evaluation of depth-resolved blood flow velocities *in vivo* [9-15]. Beyond flow-based measurements, several techniques have been developed to extract vascular information by analyzing different components of the OCT signal. Some techniques use the full complex signal to enhance sensitivity to dynamic changes [16-18]. Others extract contrast by analyzing only intensity fluctuations over time, as in speckle variance OCT [19-22]. For example, Figure 1.1 shows depth-resolved OCT angiograms of the human retina, which were acquired using the SPECTRALIS system (Heidelberg Engineering GmbH, Germany). Each of these techniques offers distinct advantages and limitations, and the choice of method depends on the specific application scenario, such as the need for speed, sensitivity, or robustness to motion artifacts.

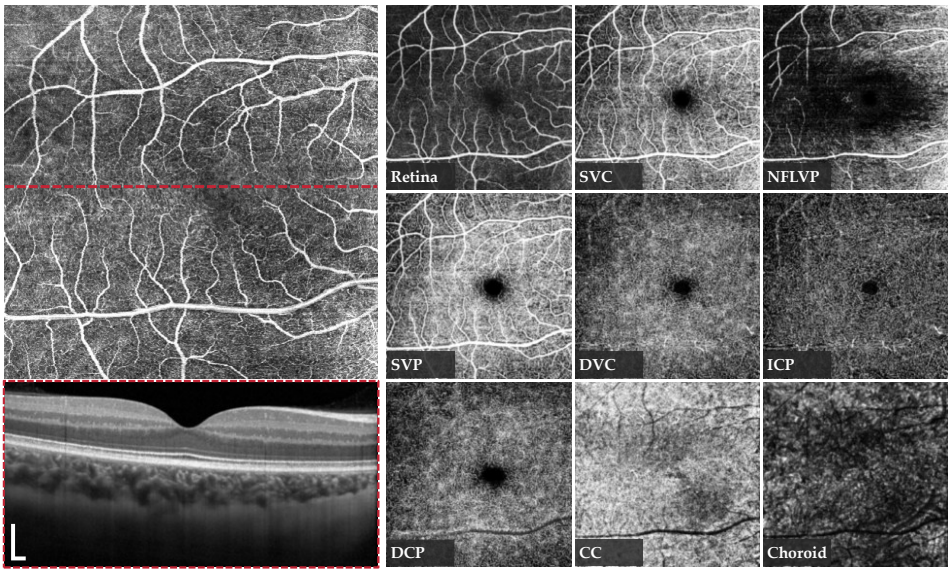

Figure 1.1 Depth-resolved OCT angiography of the human retina. The left panel shows a full *en face* OCT angiogram of the retina, combining signals from all vascular layers. The lower-left image displays the corresponding structural B-scan. The right panel presents depth-resolved *en face* OCT angiograms from the retinal and choroidal layers, including the superficial vascular complex (SVC), nerve fiber layer vascular plexus (NFLVP), superficial vascular plexus (SVP), deep vascular complex (DVC), intermediate capillary plexus (ICP), deep capillary plexus (DCP), choriocapillaris (CC), and choroid. Each layer highlights distinct vascular patterns corresponding to its anatomical depth. The scale bar represents 200 μm.

This thesis investigates two complementary functional OCT modalities: dynamic OCT (dOCT) and optical coherence elastography (OCE). Dynamic OCT analyzes rapid speckle fluctuations to reveal microscopic cellular motions, offering insights into cell viability and metabolic activity. Conversely, OCE applies controlled mechanical excitation and tracks the resulting phase shifts to quantify tissue stiffness and mechanical heterogeneity. These methods are evaluated in two different biomedical contexts using MHz-OCT systems.

1.1 State of the art in functional MHz-OCT imaging

By overcoming the speed limitations of conventional kHz-range setups, MHz-OCT systems have brought substantial progress to OCT imaging. This advancement is driven by the development of the Fourier domain mode locking (FDML) laser, which enables the acquisition of several million A-scans per second while maintaining high phase stability and long coherence length [23, 24]. These capabilities facilitate rapid capture of densely sampled volumetric data, significantly reducing motion artifacts and improving temporal resolution. As a result, MHz-OCT provides the speed and precision necessary to image fast biological processes in real-time.

In ophthalmology, functional MHz-OCT has enabled wide-field retinal imaging, allowing noninvasive visualization of retinal microvasculature *in vivo*. Blatter et al. presented OCT angiography over a wide ~48° field of view (FOV), acquired in just a few seconds in a single recording without needing image stitching [21]. Further work by Azimipour et al. combined adaptive optics with a 1.6 MHz-OCT system to study functional responses of individual photoreceptors in the human retina [25]. By analyzing repeated 3D scans over time, they observed small changes in the shape and length of the photoreceptor segments in response to light stimulations. These changes were proportional to the stimulus's intensity and affected surrounding layers, such as the retinal pigment epithelium. Additional studies have shown that OCT angiography at a 1.6 MHz A-scan rate produces significantly higher contrast images of the human choriocapillaris and choroid than a conventional 100 kHz system [26]. In healthy subjects, an average contrast improvement of 23 % was observed. This enhancement is attributed to reduced motion artifacts and improved sensitivity to blood flow, underscoring its advantages in vascular imaging.

Beyond retinal imaging, functional MHz-OCT has also been used in dermatology and for imaging cardiovascular development in live mouse embryos. Ruikang Wang's group demonstrated high-speed optical microangiography using a 1.6 MHz-OCT system to visualize microcirculation in human skin. By employing an intensity-based inter-frame subtraction algorithm, they were able to extract blood flow information without requiring motion correction [27]. In a separate study, Irina Larina's research group employed MHz-OCT for four-dimensional imaging of cardiovascular dynamics in live mouse embryos, enabling time-resolved visualization of heart wall motion and spatially resolved blood flow at a volume rate of approximately 43 Hz [28].

The potential of MHz-OCT for biomechanical imaging has also been explored. In one approach, shear-wave imaging OCE was performed using MHz-OCT combined with a focused air-pulse to generate elastic waves, reducing acquisition time to the millisecond

range. The method was validated in tissue-mimicking phantoms and *ex vivo* porcine cornea under varying intraocular pressures [29]. A separate study used MHz-OCT to map mechanical wave propagation in the cornea with nanometer-scale strain sensitivity. Analyzing phase differences between adjacent B-scans enabled real-time, non-contact imaging of tissue biomechanics using a pulsed UV laser for excitation [30].

1.2 Motivation and objectives

Despite high-speed acquisition and phase stability advantages, only a handful of studies have demonstrated the feasibility of functional imaging with MHz-OCT, leaving its potential in this area largely underexplored. This thesis aims to address this gap by evaluating the capabilities of functional MHz-OCT in two distinct biomedical contexts.

One promising application area is neurosurgery, where the intraoperative differentiation between healthy and pathological tissue remains a major clinical challenge [31-33]. Complete resection of brain tumors, such as glioblastomas and metastases, significantly improves patient outcomes [34-37], yet surgeons often rely on imperfect imaging systems or subjective haptic feedback to detect tumor margins. Existing intraoperative techniques either disrupt surgical workflow [38-40], depend on preoperative images prone to brain shift [31, 41-43], or lack sufficient precision [44, 45]. Since tumor tissue often differs mechanically from healthy brain tissue, elasticity-based contrast offers a compelling alternative [46-48]. However, the application of OCE in brain tumor imaging has barely been explored. The complex viscoelastic nature of brain tissue, together with limitations on mechanical loading, requires highly sensitive and robust measurement strategies.

A second focus of this thesis is the use of dOCT to evaluate renal tissue function. While dOCT techniques have shown the ability to reveal sub-resolution cellular activity through speckle fluctuations [49-51], their implementation with MHz-OCT systems has not yet been explored. This is particularly relevant in kidney transplantation, where the growing mismatch between donor organ availability and patient demand has led to increased reliance on marginal or expanded criteria donor kidneys [52, 53]. Currently available imaging techniques, such as Doppler ultrasound or computed tomography angiography, are limited to pre-retrieval assessment. Once the kidney is explanted, there is no established method for reliably evaluating its viability in real-time [53]. In clinical practice, organ viability is usually assessed through visual inspection or invasive biopsy. However, these methods are inherently subjective, have restricted coverage, and may lead to misinterpretation or tissue damage. This highlights the clinical need for a non-invasive imaging ap-

proach that can provide a rapid and quantitative assessment of organ viability immediately after retrieval. Dynamic OCT offers significant potential by visualizing dynamic intracellular activity without the need for contrast agents or labeling.

Therefore, the goal of this thesis is to explore the use of MHz-OCT for functional imaging, addressed through the following objectives:

1. **To develop and evaluate MHz-OCE methods** for brain tissue assessment. It involves the implementation of a phase-sensitive displacement-based pipeline and a complementary Fourier-based approach using the complex OCT signal to generate elasticity-related contrast for distinguishing between healthy and tumor brain tissue.
2. **To investigate the feasibility of MHz-dOCT** for assessing renal tissue viability by capturing speckle-based contrast related to functional dynamics. This includes enabling fast, large-area imaging by developing a motorized high-precision three-axis linear robot with dedicated control software and evaluating optimized scanning protocols.
3. **To validate the proposed methods** through phantom experiments and *ex vivo* tissue measurements. Comparative analysis with histological references assesses the accuracy and biomedical relevance of both functional imaging approaches.

1.3 Thesis structure

This thesis is structured into five main chapters. Chapter 2 provides the theoretical foundations of OCT, beginning with basic wave optics and the principles of coherence and interference. It then introduces the fundamental concepts of OCT, including time-domain and Fourier-domain modalities, followed by an in-depth discussion of MHz-OCT systems, FDML lasers, speckle behavior, and phase-sensitive signal analysis.

Chapter 3 focuses on developing and evaluating OCE techniques for the biomechanical assessment of brain tissue. It outlines clinical motivation, experimental setup, signal processing pipeline, and validation strategies, including the implementation of a phase-sensitive unwrapping algorithm and a Fourier-based contrast method. The performance of these methods is assessed using phantoms and *ex vivo* brain samples, with additional comparison to histological results.

Chapter 4 discusses the implementation of dOCT for the functional analysis of kidney tissue. It starts with the clinical background and motivation, emphasizing the difficulties in evaluating tissue viability and how dOCT can offer valuable additional functional information. The chapter then describes the experimental setup, including the MHz-dOCT system, data acquisition workflow, and computation of functional contrast, along with

sample preparation and histological validation. Large-area imaging using a three-axis linear robot is presented, followed by strategies for non-equidistant temporal scanning to reduce acquisition time while preserving functional information. Lastly, the chapter assesses the effectiveness of these techniques in terms of spatial resolution, visualization of renal anatomy, functional contrast, and potential for clinical application.

Chapter 5 concludes the thesis with a summary of the findings and a discussion of future directions. It reflects on the potential clinical translation of both OCE and dOCT techniques and outlines future research steps.

2 Fundamentals

The following chapter provides an overview of the fundamental principles and mechanisms of OCT, beginning with key concepts in interference and coherence. It then examines various OCT techniques, including MHz-OCT, and addresses factors that impact image quality, such as resolution, noise, and sensitivity.

2.1 Optical wave theory

2.1.1 Coherence

Coherence is a fundamental concept in wave physics that describes the ability of two or more waves to interfere with each other. It reflects how much their phases remain correlated at different points in space and time. Considering a narrowband laser source emitting a single wavelength centered at λ_0 with corresponding frequency f. Its propagation in the x-direction can then be represented in complex form as a time-dependent electric field:

$$E = E_0 \exp\big(i(kx - \omega t + \Phi)\big), \tag{2.1}$$

where E_0 is the amplitude, $k = 2\pi/\lambda_0$ the wave number, $\omega = 2\pi f$ the angular frequency, Φ the phase, and t the time variable. The total amplitude after the superposition of multiple light wave fields is given by the superposition principle:

$$E_{total} = \sum_{n=1}^{N} E_n, \tag{2.2}$$

with N representing the number of contributing light waves. The degree of coherence between two different waves at two space-time points (x_1, t_1) and (x_2, t_2) is described by the coherence function [54]:

$$\Gamma(x_1, t_1; x_2, t_2) = \langle E_1^*(x_1, t_1) E_2(x_2, t_2) \rangle_t \tag{2.3}$$

The angle bracket $\langle \cdots \rangle_t$ represents the average over time. This function assesses the statistical correlation between wave fields at specified locations and times. To compare coherence between different wave fields, we define its degree by using the normalized coherence coefficient:

$$\gamma(x_1, t_1; x_2, t_2) = \frac{\Gamma(x_1, t_1; x_2, t_2)}{\sqrt{\Gamma(x_1, t_1; x_1, t_1)\Gamma(x_2, t_2; x_2, t_2)}}, \tag{2.4}$$

where γ represents how well the wave fields at different points are correlated, while 1 indicates perfect coherence and 0 indicates complete incoherence [6]. Coherence can be classified into spatial coherence and temporal coherence. Spatial coherence describes the ability of a wave to interfere constructively at different points in space. Temporal coherence measures how well a wave maintains a stable phase relationship over time at a single location. For purely temporal coherence, we consider the case where measurements are taken at the same spatial position x but at different times, separated by a time delay Δt. The normalized coherence function in this case is given by [54]:

$$\gamma(\Delta t) = \frac{\Gamma(\Delta t)}{\Gamma(0)} = \frac{\langle E_1^*(x,t)E_2(x,t+\Delta t)\rangle_t}{\langle E_1^*(x,t)E_2(x,t)\rangle_t}. \tag{2.5}$$

The degree of temporal coherence can be assessed by measuring the fringe visibility, or contrast of the interference pattern (see Chapter 2.1.2), in a Michelson interferometer.

The coherence length l_c defines the resolution and depth range over which coherent interference can be observed. It is directly related to both the central wavelength λ_0 and the spectral bandwidth $\Delta\lambda$ of the light source, as shown in the following equation [55]:

$$l_c = \alpha \frac{\lambda_0^2}{\Delta\lambda_{Source}}. \tag{2.6}$$

$\Delta\lambda_{Source}$ represents the full spectral bandwidth of the light source, with the parameter α ranging from 0.6 to 1, depending on the spectral shape. This relationship indicates that the coherence length increases with a longer central wavelength and decreases with a broader spectral bandwidth.

2.1.2 Interference

Interference occurs when electromagnetic waves overlap, leading to variations in intensity depending on their relative phase. When the waves are in phase, constructive interference occurs, resulting in an increased intensity. Conversely, destructive interference reduces the intensity when the waves are out of phase. A constant phase relationship must be maintained to produce a stable and observable interference pattern.

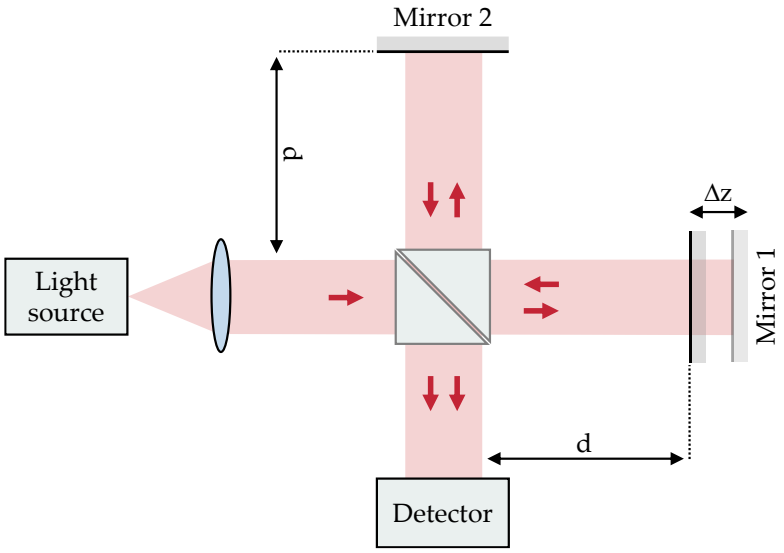

Figure 2.1 Schematic drawing of a Michelson interferometer. Collimated coherent laser light is directed toward a beam splitter, which divides the beam into two arms. A mirror reflects each beam, with one positioned at a fixed distance d and the other at an adjustable distance. The two beams recombine at the beam splitter, where they interfere and are subsequently detected. The resulting interference pattern depends on the optical path length difference Δz between the two arms.

This principle is shown in Figure 2.1, where the interaction of two light waves within a Michelson interferometer is examined to gain a deeper understanding of the interference phenomenon. When light enters the interferometer, a beamsplitter divides it into two paths: the reference and sample arm. The electric fields E of both arms can then be described as:

$$E_R = E_{R_0} \exp\big(i(kx - \omega t + \Phi_R)\big), \tag{2.7}$$

$$E_S = E_{S_0} \exp\big(i(kx - \omega t + \Phi_S)\big). \tag{2.8}$$

The amplitudes of the reference and sample optical fields are denoted by E_{R_0} and E_{S_0}, with Φ_R and Φ_S representing their respective phase shifts. During recombination at the beamsplitter, interference occurs, and the total optical field $E_{total}(x,t)$ is given by the superposition:

$$E_{total} = E_R + E_S. \tag{2.9}$$

If the phase difference $\Delta\phi = (\phi_R - \phi_S)$ is zero or a multiple of 2π, the fields are in phase and interfere constructively. Conversely, if $\Delta\phi$ is an odd multiple of π, the fields are out of phase and interfere destructively. The recombined light is then detected by a photodetector, which measures its intensity and converts this into an electrical signal for further

analysis. Since the intensity of the light is proportional to the square of the amplitude of the electric field, the detected intensity at the photodiode $I_D(x,t)$ is given by:

$$I_D \propto |E_{total}|^2. \tag{2.10}$$

In the case of multiple time-harmonic fields with the same frequency, the total intensity is provided by the coherent sum of the individual fields:

$$I_D = \left|\sum_i E_i\right|^2, \tag{2.11}$$

where $E_i(x,k,t)$ represents the individual electric field components and i is the index of each field. However, if the fields are not coherent, the interference terms vanish. In this case, the intensity is given by the incoherent sum:

$$I_D = \sum_i |E_i|^2. \tag{2.12}$$

This means that the cross terms average out to zero over time due to random phase fluctuations. When the fields are coherent, by substituting equation 2.9, the following expression for the intensity is obtained:

$$I_D \propto |E_R + E_S|^2 = |E_R|^2 + |E_S|^2 + 2Re\{E_R^* E_S\}. \tag{2.13}$$

The individual intensities of both beams are represented by the first two terms $I_R \propto |E_R|^2$ and $I_S \propto |E_S|^2$. The term $2Re\{E_R^* E_S\}$, corresponds to the interference term, which reflects the interaction between the two beams and encodes the phase-related effects of their superposition. Here, the asterisk indicates the complex conjugate of E_R. Consequently, the detected intensity can be written as:

$$I_D = I_R + I_S + 2\sqrt{I_R I_S}\, cos(kn\tau + \Delta\phi) \tag{2.14}$$

with n being the refractive index of the sample, $\Delta\phi = (\phi_S - \phi_R)$ the phase term, and τ the optical path length difference between the reference and sample arm. Since the light passes through both arms twice, the total optical path length difference for the round-trip is $2\tau = (\tau_R - \tau_S)$.

To obtain strong and detectable interference fringes, the reference arm intensity is typically much higher than the reflected signal from the sample. The fringe intensity varies between two limits $I_{max}$and I_{min} and can be written as [6]:

$$I_{max} = I_R + I_S + 2\sqrt{I_R I_S}|\gamma|, \tag{2.15}$$

$$I_{min} = I_R + I_S - 2\sqrt{I_R I_S}|\gamma|. \tag{2.16}$$

with γ being the coherence function (see Equation 2.4). Its ratio defines the visibility of the fringe V:

$$V = \frac{I_{max} - I_{min}}{I_{max} + I_{min}} = \frac{2\sqrt{I_R I_S}|\gamma|}{I_R + I_S}. \tag{2.17}$$

It describes the dependence of fringe visibility on the intensity ratio between the sample and reference arms, as well as the coherence properties of the light source.

For interference to occur, the condition $2\tau < \Delta l_c$ must be fulfilled, which ensures that the optical path length difference remains within the coherence length of the light source. Interference is most effective when the path lengths in both arms are matched. If it surpasses the coherence length, the interference signal diminishes rapidly. As a result, reflections from other depths that exceed the coherence length do not contribute to the detected signal.

2.2 Optical coherence tomography

Tomography originates from the Greek words *tomos* (slice or section) and *graphein* (to write). It refers to a group of imaging techniques that produce multidimensional anatomical views of a sample, utilizing different physical principles such as penetrating waves or magnetic fields. Historically, the term tomography is primarily associated with X-ray imaging, particularly computed tomography (CT), which produces cross-sectional images that reveal the attenuation properties of the X-rays. Later, magnetic resonance imaging (MRI) was added, which uses magnetic fields and radio waves to visualize soft tissue.

However, while CT and MRI are effective for imaging deeper tissues, they typically do not provide the fine details required for microscopic examination. Optical coherence tomography (OCT) acts as a type of optical biopsy, enabling the visualization of tissue pathology in real-time without the need for tissue removal or the extensive processing typically required with traditional biopsy procedures. It bridges the gap between confocal microscopy and ultrasound regarding resolution, with an axial resolution of approximately 10 μm and a lateral resolution of 20 μm [2]. Its compact design, real-time imaging capability, and affordability make OCT a viable option for clinical use. Unlike ultrasound, which relies on acoustic waves, OCT utilizes a coherent light source in the near-infrared range. The depth information is obtained through interferometry, producing an interference pattern that encodes depth-related information, resulting in an imaging depth ranging from around 1 to 3 mm in scattering tissue.

An A-scan (amplitude scan) represents a depth-resolved reflectivity profile at a single position. By acquiring multiple A-scans while scanning laterally across the sample, a B-scan (brightness scan) is generated, forming a two-dimensional cross-sectional image. The terms "amplitude scan" and "brightness scan" originate from ultrasound imaging, where the signal amplitude reflects the strength of the reflected sound waves, and variations in brightness represent the structural reflectivity. Extending this further, a C-scan is obtained by combining multiple B-scans, which enables three-dimensional volumetric visualization. Additionally, *en face* projections integrate intensity information along the depth axis, producing a top-down view of the sample.

2.2.1 Time-domain OCT (TD-OCT)

Over the past few decades, significant advances have led to the development of various OCT techniques. Time-domain OCT (TD-OCT) is the earliest form of OCT and uses a Michelson interferometer, where the interferometric light intensity is measured over time. A schematic of this setup is shown in Figure 2.2.

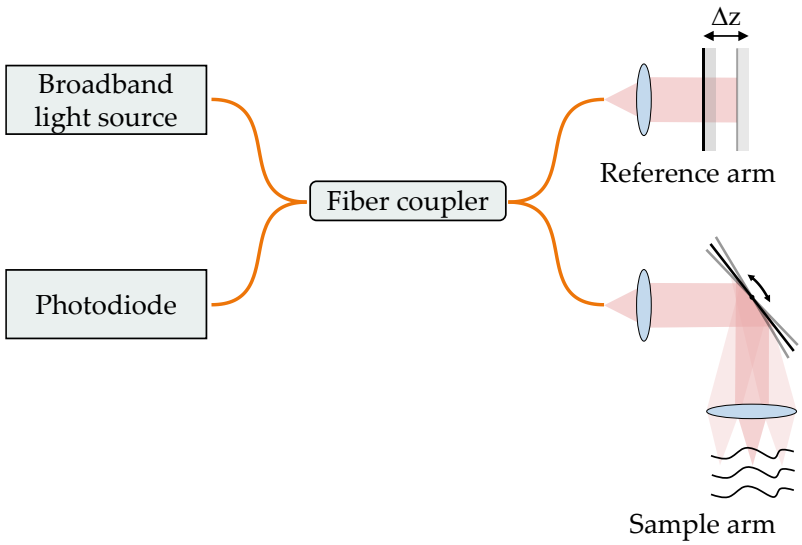

Figure 2.2 Schematic drawing of a time-domain OCT system. Light from a broadband source is guided into a fiber coupler, which splits it into a reference and a sample arm. In the reference arm, light is reflected by an adjustable mirror. The signals from both arms are recombined at the coupler. A photodiode measures the interference signal.

It employs a broadband light source with a well-defined and short coherence length, typically in the micrometer range. This short coherence length enables high axial resolution by ensuring interference occurs only within a well-defined depth range. The signals from both arms are recombined at the coupler, where they interfere, and a photodetector then detects the resulting interference signal. The reference arm has a movable mirror that

adjusts the optical path length to generate strong interference signals. This enables the system to match the reference arm's path length with reflections from different depths within the sample sequentially. A single A-scan is obtained by mechanically scanning the reference mirror across an axial imaging range of 2 to 3 mm.

In the case of a broadband light source, each wavelength component can be viewed as an independent light source, and interference happens only within the spectrum of each wavelength. As seen in Equations 2.7 and 2.8, the electric fields for the reference and sample arms in a general interferometric setup are expressed as plane waves with spatial and temporal dependence. However, for TD-OCT, the interference effects are mainly determined by the optical path lengths in both arms of the interferometer. Therefore, the electric fields for the reference and sample arm are given by the following expressions, with S_0 being the amplitude of the light source and R being the reflectivity of the reference and sample arm:

$$E_R = S_0\sqrt{R_R}\exp(-ik\tau_R), \tag{2.18}$$

$$E_S = S_0\sqrt{R_S}\exp(-ik\tau_S). \tag{2.19}$$

For simplicity, the phase terms are ignored in these equations. The resulting detected intensity for a Gaussian-shaped light source spectrum can then be described as a function of the reference arm path length τ_R [56, 57]:

$$\begin{aligned} I_{TD-OCT}(\tau_R) = {} & S_0\left\{R_R + \sum_{n=1}^{N} R_{Sn}\right\} \\ & + S_0\left\{2\sum_{n=1}^{N}\sqrt{R_R R_{Sn}}e^{-(\tau_R-\tau_{Sn})^2\Delta k^2}\cos\big(2k_0(\tau_R-\tau_{Sn})\big)\right\} \\ & + S_0\left\{2\sum_{n\neq m=1}^{N}\sqrt{R_{Sn}R_{Sm}}e^{-(\tau_{Sn}-\tau_{Sm})^2\Delta k^2}\cos\big(2k_0(\tau_{Sn}-\tau_{Sm})\big)\right\}. \end{aligned} \tag{2.20}$$

Here, R_{Sn} represents the reflectivity of the n-th reflector with the corresponding sample arm path length τ_{Sn}. The sum is taken over all reflectors N. The first two terms describe a constant signal level that is not dependent on the path length difference and is usually called a direct current (DC) offset. The third term is the interference component of the OCT signal. It is called the cross-correlation term as it describes the interaction between the reference and sample arm signals. The fourth term represents the autocorrelation signal, which arises from the interference between reflections from different sample reflectors. It is independent of τ_R and contributes to an additional signal offset. A specific depth range

can be scanned when the reference arm is moved. The resulting interference signal, containing information from all depths, is demodulated by extracting its envelope to obtain a depth-resolved reflection profile.

A key advantage of TD-OCT is its ability to synchronize the focus position with the mirror movement, which enables high transverse resolution over the entire imaging depth. However, this necessitates fast and precise control. Due to the refractive index n, the optical path length is given by $n \cdot d$, where d represents the depth of focus within the sample. At the same time, the actual focus shifts by d/n. Therefore, to maintain synchronization and compensate for the shift, the reference mirror must be precisely adjusted at a velocity n^2 times greater than the focus. However, its speed is constrained by the mechanical scanning, limiting the maximum sampling rate to a few kilohertz [58].

These speed limitations posed considerable challenges in clinical settings, where patient movements or external influences create motion artifacts. Such artifacts often degraded image quality and, in some cases, made reliable interpretation nearly impossible. In addition, functional imaging methods that relied on phase information or subtle signal variations were challenging to implement effectively. As a result, future improvements in OCT systems have aimed to overcome this limitation and achieve faster scanning speeds.

2.2.2 Fourier-domain OCT (FD-OCT)

A breakthrough in the speed of OCT systems was achieved with the introduction of Fourier-domain OCT (FD-OCT), a principle first demonstrated by Fercher et al. in 1995 [59]. In FD-OCT, the spectral composition of the interference signal encodes the depth-dependent reflectivity profile of the sample. By capturing the entire interference spectrum in a single measurement, an entire depth scan can be obtained without mechanically moving the reference mirror. This principle not only enables a substantial increase in imaging speed but also lays the foundation for early developments in phase-based functional imaging methods [10, 12, 60]. Building on this principle, two primary variants have emerged: spectral-domain OCT (SD-OCT) and swept-source OCT (SS-OCT).

In both approaches, the overall interference signal results from the sum of the interference patterns produced by each wavelength [56, 57]:

$$
\begin{aligned}
I_{FD-OCT}(k) = S(k)&\left\{R_R + \sum_{n=1}^{N} R_{Sn}\right\} \\
&+ S(k)\left\{2\sum_{n=1}^{N}\sqrt{R_R R_{Sn}}\,cos\big(2k(\tau_R - \tau_{Sn})\big)\right\} \\
&+ S(k)\left\{2\sum_{n\neq m=1}^{N}\sqrt{R_{Sn}R_{Sm}}\,cos\big(2k(\tau_{Sn} - \tau_{Sm})\big)\right\}.
\end{aligned}
\tag{2.21}
$$

$S(k)$ denotes the spectral density of the light source to the wavenumber k. In this case, the autocorrelation term is not just a constant signal offset and can interfere with the A-scan. However, its effect is minimal due to the typically higher modulation frequency between the interferometer arms. This frequency difference arises because the optical path length differences within the sample are much smaller than those between the two arms. Additionally, the autocorrelation signal is comparatively weak because the reference arm typically exhibits much greater reflectivity than the sample. Consequently, the interference between the autocorrelation signal and the sample's interference information is minimal. Balanced detection further minimizes the effects of the autocorrelation signal and reflectivity offsets by canceling common-mode noise [57].

The depth-resolved reflectivity profile, or A-scan, can be obtained by applying a fast Fourier transform (FFT) to Equation 2.21:

$$
\begin{aligned}
I_{FD-OCT}(\tau) = \ &\mathcal{F}^{-1}\{I_{FD-OCT}(k)\} \\
= \ &\mathcal{F}^{-1}\{\mathrm{S(k)}\} \cdot \left\{R_R + \sum_{n=1}^{N} R_{Sn}\right\} \\
&+ \mathcal{F}^{-1}\{\mathrm{S(k)}\} \otimes \left\{\sum_{n=1}^{N}\sqrt{R_R R_{Sn}}\,\delta\big(z \pm 2(\tau_R - \tau_{Sn})\big)\right\} \\
&+ \mathcal{F}^{-1}\{\mathrm{S(k)}\} \otimes \left\{\sum_{n\neq m=1}^{N}\sqrt{R_{Sn}R_{Sm}}\,\delta\big(z \pm 2(\tau_R - \tau_{Sn})\big)\right\}.
\end{aligned}
\tag{2.22}
$$

with the operator $\otimes$ indicating convolution. Here, $\mathcal{F}^{-1}\{\mathrm{S(k)}\}$ represents the inverse FFT the light source spectrum. According to the Wiener-Khinchin theorem, this is equivalent to the autocorrelation or temporal coherence function of the light source $\Gamma(\tau)$ [61]. Note that only the Fourier amplitude is shown, while the phase information is omitted for simplicity. The reflectors are represented as delta functions δ at depths corresponding to an optical path difference of $2\tau = (\tau_R - \tau_S)$ with the FFT:

$$
\frac{1}{2}[\delta(z + z_0) + \delta(z - z_0)] \overset{\mathcal{F}}{\leftrightarrow} \cos(kz_0). \tag{2.23}
$$

The equation shows that since $I_{FD-OCT}(k)$ is a real-valued function, its FFT leads to a mirror term, creating an ambiguity between positive and negative frequencies. This ambiguity affects the interpretation of the depth information. Therefore, the measured spectrum alone cannot indicate whether the optical path difference between the sample and reference arms is positive or negative [5].

2.2.2.1 Spectral-domain OCT (SD-OCT)

A broadband light source with a non-balanced Michelson interferometer is employed in SD-OCT systems, as shown in Figure 2.3. The primary advantage of the non-balanced Michelson interferometer lies in its simplicity, as it requires only a fiber coupler and polarization controllers for basic functionality. To ensure stable operation and prevent undesired back reflections into the light source, an optical isolator must also be included if it is not already incorporated within the laser source. A superluminescent diode (SLD) is commonly used as a light source due to its cost-effectiveness and large bandwidth [5].

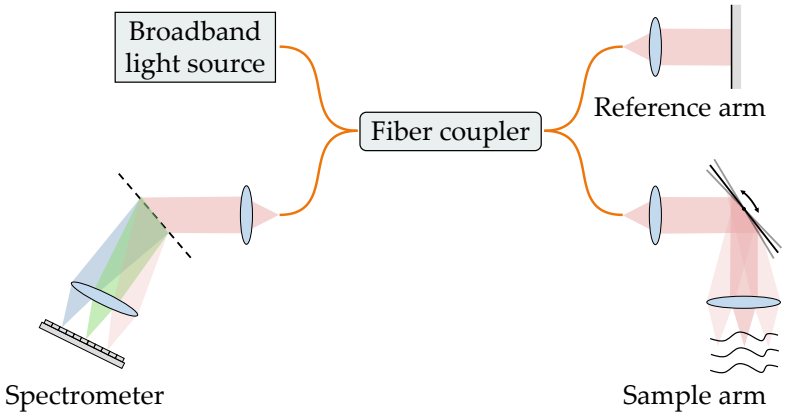

Figure 2.3 Schematic drawing of a spectral-domain OCT system. Light from a broadband source is guided into a fiber coupler, which splits it into a fixed reference and a sample arm. The reflected signals from both arms are recombined at the coupler and directed to a spectrometer. A diffraction grating and focusing lens disperse and focus the light onto a line scan camera, which records the spectrally resolved interference pattern. This allows depth information to be retrieved without mechanical scanning.

Unlike TD-OCT, the reference arm features a fixed reference mirror. In addition, instead of using a photodetector, the interferometric signal is captured by a line detector, typically within a spectrometer. The spectrometer disperses the collected light into its constituent wavelengths using a diffraction grating and then focuses it onto a high-speed line sensor. The most used cameras are 1D CCD (charge-coupled device) or CMOS (complementary metal-oxide-semiconductor) sensors. Each time the line camera is read out, an A-scan is obtained. SD-OCT systems achieved a substantial increase in imaging speed over TD-OCT, with experimental SD-OCT setups reaching A-scan rates of up to 1 MHz

[62]. The first retinal SD-OCT images demonstrating these advancements were published by Wojtkowski et al. in 2002 [63], and the technology was commercially introduced in 2006 [64].

The choice between SD- or SS-OCT primarily depends on the operating wavelength. Silicon-based line sensors are widely used and are sensitive only to wavelengths below 1 µm. As a result, SD-OCT systems operate with shorter wavelengths to meet the sensor's requirements. Although InGaAs (indium gallium arsenide) line sensors can detect longer wavelengths, their high price limits their widespread use [4, 7].

2.2.2.2 Swept-source OCT (SS-OCT)

Swept-source OCT systems employ a light source that is tunable over a wide wavelength range but has a narrow instantaneous bandwidth. A balanced photodetector, commonly an InGaAs detector, captures the output signal. The basic setup of such a system is shown in Figure 2.4. The detector converts the intensity of the interferometric signal into an electrical current. They can operate at speeds up to 2.5 GHz and are well-suited for wavelengths between 1 and 1.7 µm. By sweeping the wavelength over time, depth-resolved interference signals are generated. As a result, SS-OCT systems do not require the mechanical movement of the reference mirror, nor do they rely on the typically slower spectrometers. This eliminates key limitations, significantly improving the imaging speed of SS-OCT compared to its predecessors.

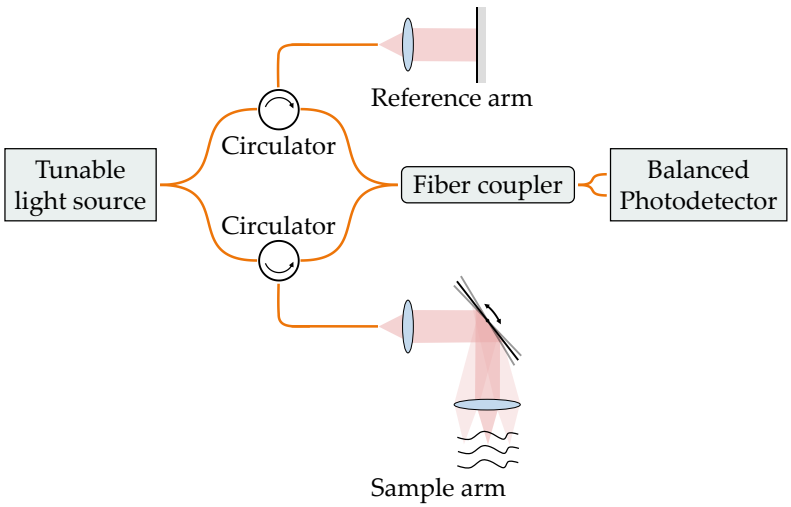

Figure 2.4 Schematic drawing of a swept-source OCT system. Light from a tunable laser source enters a fiber coupler, which splits it into a reference and a sample arm. The backscattered signals from both arms are recombined at the coupler and measured by a balanced photodetector. Sweeping the wavelength over time produces depth-resolved interference signals without requiring a spectrometer.

Swept-source lasers enable imaging speeds of several million A-scans per second [65]. Throughout the imaging process, various wave trains, known as sweeps, are sequentially sent into each arm of the interferometer. A sweep refers to the optical signal generated over the entire tuning range or sweep range $\Delta\lambda$. Ideally, each sweep has a continuous frequency increase, with the amplitude remaining constant across the tuning range. The wavelength can evolve in two directions. A transition from short to long wavelengths is termed a "forward sweep," while a movement from long to short is known as a "backward sweep". They can function in two modes: unidirectional, where the sweep moves in a single direction, and bidirectional, where the laser alternates between sweeping forward and backward [66].

Either a balanced Michelson or Mach-Zehnder interferometer is used to detect the interferometric signal. The Mach-Zehnder interferometer maximizes the use of the backscattered light from the sample by replacing the 50:50 coupler with a circulator, which recouples most of the backscattered light and enhances the system's sensitivity. However, a potential drawback is that circulators are well-suited for 1310 nm wavelengths but become less efficient, more expensive, and generate ripples and dispersion at 1050 nm [67].

2.2.3 Imaging characteristics

2.2.3.1 Axial resolution

In traditional optical microscopy, both lateral and axial resolution are constrained by diffraction. Abbe's law describes the lateral resolution and depends on the wavelength of the light source and the numerical aperture (NA) of the objective lens. These parameters also influence the axial resolution. A higher NA enhances lateral resolution but decreases the depth of field, which in turn limits axial resolution.

In contrast, the NA of the objective does not determine the axial resolution in OCT. Instead, it is primarily determined by the coherence properties of the light source. As outlined in Equation 2.22, the axial point spread function (PSF) in OCT is directly related to the coherence function $\Gamma(\tau)$ [67]. This means that the coherence properties of the light source determine the axial resolution in OCT. For a Gaussian-shaped spectrum, the coherence length l_c (see Equation 2.6) and accordingly axial resolution Δz is given by [55, 56, 68]:

$$\Delta z_{Gaussian} = l_{c,Gaussian} = \frac{2\ln(2)}{\pi}\frac{{\lambda_0}^2}{n\cdot\Delta\lambda_{FWHM}} = 0.44\frac{{\lambda_0}^2}{n\cdot\Delta\lambda_{FWHM}} \approx \frac{{\lambda_0}^2}{n\cdot\Delta\lambda_{Source}}. \tag{2.24}$$

Here, $\Delta\lambda_{FWHM}$ represents the full width at half maximum (FWHM) of the spectrum, while $\Delta\lambda_{Source}$ denotes the total spectral bandwidth of the light source. The relationship between them is approximately $\Delta\lambda_{Source} \approx 2.6\Delta\lambda_{FWHM}$ [55].

However, for swept-source systems, the emission spectrum is typically close to a top-hat shape. In this case, the coherence length and thus the axial resolution are described by [55].

$$\Delta z_{Tophat} = l_{c,Tophat} = 0.6\frac{{\lambda_0}^2}{n \cdot \Delta\lambda_{FWHM}} = 0.6\frac{{\lambda_0}^2}{n \cdot \Delta\lambda_{Source}}, \tag{2.25}$$

with $\Delta\lambda_{Source} = \Delta\lambda_{FWHM}$. This suggests that a larger spectral bandwidth results in improved axial resolution.

A common approach to measure the axial resolution of an OCT system is to use a mirror to obtain a reflection from a single point in depth. An A-scan is acquired, and the PSF of the depth profile determines the axial resolution. The narrower the PSF, the better the axial resolution.

2.2.3.2 Lateral resolution

Like other forms of optical microscopy, the lateral resolution in OCT is determined by the NA of the optical system and the wavelength of the light source. The system's ability to resolve two closely spaced lateral features is determined by the spot size of the focused light beam at the sample. As OCT systems commonly utilize light from a single-mode fiber, a beam profile that follows Gaussian optics results. Assuming the lens is fully illuminated, the NA of a collimated Gaussian beam with diameter d and an objective lens with focal length f can be approximated as:

$$NA = n\sin\theta = \frac{n \cdot d}{2f}. \tag{2.26}$$

Here, θ represents the half-angle of the maximum cone of light that the objective lens can capture. The lateral resolution can then be defined by the beam waist diameter $2\omega_0$, or by the FWHM of the Gaussian PSF. The beam waist ω_0 represents the point where the beam's intensity decreases to $1/e^2$of its maximum value. It is directly influenced by the wavelength of the light and the NA of the focusing optics:

$$\omega_0 = \frac{\lambda_0}{\pi NA}. \tag{2.27}$$

This gives us a lateral resolution of

$$\Delta x = 2\omega_0 = \frac{2\lambda_0}{\pi NA} \approx 1.27\frac{\lambda_0 f}{n \cdot d}, \tag{2.28}$$

with f being the focusing length of the sample arm optics and d the diameter of the beam [56]. In the case of defining the lateral resolution using the FWHM, ω_0 must be multiplied by a scaling factor [4]:

$$FWHM = \sqrt{2\ln 2}\,\omega_0\,. \tag{2.29}$$

The lateral resolution can then be determined by [5]:

$$\Delta x \approx \sqrt{2\ln 2}\,\omega_0 = \sqrt{2\ln 2}\frac{\lambda_0}{\pi NA} = \sqrt{2\ln 2}\frac{\lambda_0}{\pi}\frac{2f}{n \cdot d}. \tag{2.30}$$

A standard method for measuring lateral resolution involves imaging a resolution target, such as the 1951 USAF resolution test chart, which consists of well-defined patterns of decreasing feature size. The system's effective lateral resolution can be determined by analyzing the smallest resolvable elements.

2.2.3.3 Depth of focus

The depth of focus is directly related to the Rayleigh length Δz_R and describes the distance over which a focused beam remains approximately collimated before significantly diverging. The depth of focus b is then given by [6]:

$$b = 2\Delta z_R = \frac{\pi \Delta x^2}{2\lambda_0}, \tag{2.31}$$

The equation shows that since Δx is inversely proportional to the NA, an increase in NA results in a smaller Δz_R, consequently decreasing the focus depth. This relationship creates a fundamental trade-off in which higher lateral resolution allows for capturing finer structural details but results in a reduced imaging range. Therefore, when selecting optics, it is essential to consider the required imaging resolution and the desired depth of focus, as these two factors are inversely related.

2.2.4 Noise and sensitivity

Important parameters that indicate the quality of an OCT system are its sensitivity and signal-to-noise ratio (SNR). Sensitivity defines the system's ability to detect weak reflections from the sample and represents the lowest reflectivity that can still produce a detectable signal in the presence of noise. This parameter is inherent to the OCT system and is

influenced by factors such as the light source, the detector efficiency, and the optical losses within the setup.

In contrast, SNR quantifies the quality of the acquired image by comparing the intensity of the detected signal to the background noise. It is influenced by the material's backscattering properties and is given by the following equation [68]:

$$SNR = \frac{\langle {I_S}^2 \rangle}{\langle {I_N}^2 \rangle}. \tag{2.32}$$

The angle bracket $\langle \cdots \rangle$ represents the average over time, I_N the total noise of the optical detection system and I_S is the photocurrent at the detector resulting from the interference term in Equation 2.14.

Under optimal conditions, when an ideal 50:50 beam splitter and a perfectly reflecting sample, such as a mirror with 100 % reflectivity, are used, the total power reaching the detector is equal to the total power emitted by the source. In that case, I_S can be expressed as [6, 67]:

$$I_S = \frac{\eta q_e}{\hbar v_0} P, \tag{2.33}$$

with P as the optical power received by the detector, $\hbar$ being the Planck constant, v_0 is the center frequency of the light source, η is the quantum efficiency of the photodetector, and q_e is the electron charge.

However, the performance of an OCT system is inherently limited by various noise sources that introduce signal degradation. A key factor is the light interference from the sample and reference arm, which determines the strength of the detected signal relative to the background noise. In an OCT system, the principal noise components are shot noise I_{SH}, relative intensity noise I_{RIN}, and detection noise I_{DET} [67]. Since these noise sources are independent, the total noise I_N can be obtained by its sum [69]:

$$\langle {I_N}^2 \rangle = \langle {I_{RIN}}^2 \rangle + \langle {I_{DET}}^2 \rangle + \langle {I_{SH}}^2 \rangle. \tag{2.34}$$

As the signal strength depends on both the sample and reference arm intensities, increasing the reference arm power can improve sensitivity by elevating the signal above the electronic noise floor. However, this method also presents challenges, as higher reference power amplifies noise contributions from the light source, particularly relative intensity noise (RIN). RIN refers to fluctuations in the optical power of the laser over time and is generally much stronger in SS-OCT than in SD-OCT [57]. The power fluctuations in the laser source ΔP are mathematically defined relative to its average power P_{avg} [61, 70]:

$$RIN = \frac{\langle \Delta P^2 \rangle}{{P_{avg}}^2}. \tag{2.35}$$

It is expressed in units of Hz^{-1} with $\Delta P = P - P_{avg}$.

The second noise source is detection noise. It refers to the different kinds of non-optical noise that arise from the detection process and are independent of the optical signal. This includes noise sources, such as thermal (Johnson) noise and electrical noise from components like the signal digitizer or photodetector. Detection noise can be minimized by optimizing system design using low-noise components, reducing thermal effects, shielding against external interference, and implementing noise-canceling techniques.

The last source of noise is shot noise, which arises due to the discrete nature of photons and the inherent statistical variations in their arrival at a detector. It means that photons do not arrive at the detector in a perfectly uniform manner but rather follow a Poisson distribution, which is fundamentally unavoidable in any optical detection system. This type of noise is particularly important if the detected signal is weak and represents the limit for the achievable SNR.

In an ideal operating condition, shot-noise dominates all other noise sources, a state called the shot-noise limit. In this regime, the total noise power of the OCT system is primarily determined by the quantization of light and the generation of photoelectrons. When an OCT system operates at the shot-noise limit, sensitivity is no longer restricted by electronic or laser noise. Instead, it is determined only by optical power and detection efficiency. A method for effectively reducing RIN and detection noise is balanced detection. By acquiring two complementary signals and subtracting one from the other, common-mode noise is effectively canceled out in SS-OCT systems. As the reference arm power in the interferometer increases, sensitivity improves proportionally to the square root of the power. However, increasing the power does not improve sensitivity once shot-noise becomes the dominant source. This is because the shot-noise has already reached its intrinsic minimum, and additional power increases may cause photodetector saturation.

Assuming only detection noise, shot-noise, or RIN contributes to the system noise, the reference arm power must be carefully adjusted to ensure operation in the shot-noise limited regime. The relationship between sensitivity and reference arm power follows a characteristic trend, often visualized as a sensitivity curve, as shown in Figure 2.5A. The system operates in the detection noise-limited regime at low reference power levels. Sensitivity improves as the reference power increases. Beyond a certain threshold, the system enters the shot-noise limited regime. It transitions into the RIN regime if the reference power is further increased, reducing sensitivity rather than improving it. In contrast, Figure 2.5B

illustrates a scenario where the system is fundamentally constrained by detection noise or RIN, preventing it from reaching the shot-noise limited regime. In this case, even if the reference arm power is adjusted, the sensitivity remains limited by these dominant noise sources. This situation can arise from several factors, primarily due to a detector with high electronic noise or excessive fluctuations in laser intensity. As a result, the system's overall performance is suboptimal [67].

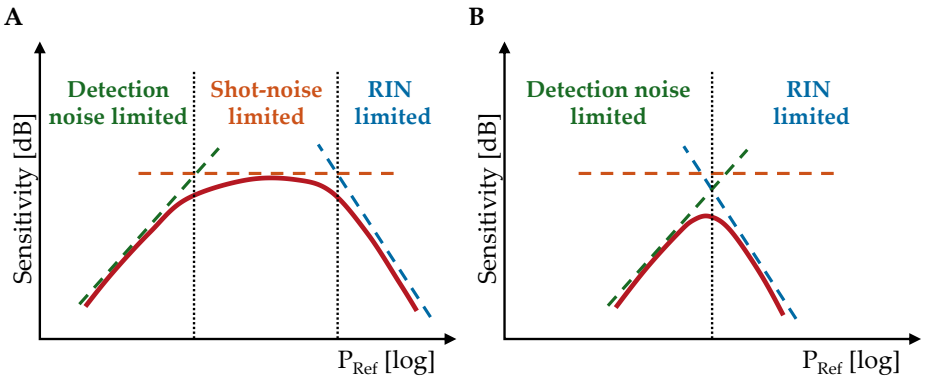

Figure 2.5 OCT sensitivity curves. The sensitivity in dB is shown as a function of the reference power (P_{Ref}) on a logarithmic scale. A: Optimal case where the system can operate in the shot-noise limited regime, depending on the reference arm power. B: Suboptimal case where detection noise or RIN prevents the system from reaching the shot-noise-limited regime, regardless of reference arm power. Adapted from [67, 69].

When the system reaches the shot noise limit, the contributions from the other noise sources become negligible. In this case, the total noise can be expressed as [6]:

$$I_N = I_{SH} = \sqrt{2q_e I_{DC} B} = \sqrt{\frac{\eta q_e}{\hbar v_0} P 2B}, \tag{2.36}$$

with B being the detection bandwidth, and I_{DC} is the DC photocurrent, which is solely attributed to the optical power from the reference arm. Substituting Equations 2.33 and 2.36 into Equation 2.32 results in the following formula:

$$SNR = \frac{\eta P}{2\hbar v_0 B}. \tag{2.37}$$

The SNR is usually expressed in logarithmic units and is:

$$SNR = 10\, log_{10}\left(\frac{\eta P}{2\hbar v_0 B}\right). \tag{2.38}$$

Here, the bandwidth B is inversely related to the integration time of a line sensor (for SD-OCT) or the duration of one sweep (for SS-OCT). The equation implies that increasing the A-scan rate can reduce the system's sensitivity [6, 67].

In general, FD-OCT systems outperform TD-OCT systems, achieving a sensitivity of around 100 dB and allowing the detection of weak signals with a reflectivity of only 10^{-10} [5, 69]. This results in a typical sensitivity advantage of 20 - 30 dB over TD-OCT systems [71]. However, FD-OCT systems experience a depth-dependent sensitivity roll-off. This effect arises from the system's finite spectral resolution. Since deeper structures produce higher-frequency interference fringes, resolving them accurately requires greater spectral resolution. As a result, signal degradation occurs with increasing depth, which limits the effective imaging range of FD-OCT systems [5].

2.3 MHz optical coherence tomography (MHz-OCT)

The development of frequency-swept light sources became particularly important for OCT applications in the 1300 nm wavelength range, where the absence of low-cost, high-performance CCD cameras limited the feasibility of spectrometer-based detection. Additionally, the benefits of balanced detection further drove interest in advancing faster and more efficient swept-source lasers [72]. However, the maximum achievable sweep rate of the swept-source lasers available in the early days was fundamentally limited by the buildup time required to generate stable laser light from the amplified spontaneous emission (ASE). To overcome this limitation, the FDML laser was developed by Huber et al. in 2006 [23]. This advancement enabled the achievement of SS-OCT systems with MHz A-scan rates, which will be referred to as MHz-OCT. The following sections will discuss a detailed description of the FDML technology and the subsequent data processing steps of the MHz-OCT system.

2.3.1 Frequency-tunable laser light sources

Tunable light sources typically comprise a wavelength-selective bandpass filter, a broadband gain medium, and a short optical resonator. The bandpass filter defines the emitted wavelength of the laser, while the gain medium provides an optical amplification over the selected spectrum. The resonator stores and facilitates multiple circulations of the light. Due to the narrow bandwidth of the optical filter, only specific longitudinal modes within its transmission window can achieve lasing.

A Fabry-Pérot filter is an example of a highly wavelength-selective filter, consisting of two parallel, partially transmissive mirrors with high reflectivity. These mirrors create an optical resonator that selectively transmits specific wavelengths based on interference effects. Only wavelengths satisfying the resonance criteria experience constructive interfer-

ence and are transmitted through the bandpass filter, while other wavelengths are significantly suppressed. For the resonance criteria to be met, the distance L between the two mirrors of the filter must be an integer multiple of λ divided by two:

$$L = \frac{m}{2} \cdot \lambda. \tag{2.39}$$

Here, m is an integer representing the order of interference. Therefore, the spacing of the mirrors and the wavelengths they transmit determine the spectral characteristics of the optical bandpass filter, specifically its central wavelength and free spectral range (FSR). The FSR defines the frequency separation between consecutive transmission peaks and is given by

$$FSR = \frac{c}{2nL}, \tag{2.40}$$

where c is the speed of light in vacuum, and n is the refractive index of the medium between the mirrors. In a ring resonator, the factor of 2 is omitted because the light completes a single round-trip instead of a double pass.

However, tuning the filter is fundamentally constrained by its mechanical properties and the continuous re-establishment of lasing modes. With each wavelength adjustment, previously existing modes lose gain and decay, necessitating the amplification of new modes from ASE. The optical field must circulate through the gain medium multiple times to sustain stimulated emission. This necessity introduces a fundamental constraint on the sweep rate, restricting early SS-OCT systems to imaging speeds in the kilohertz range.

2.3.2 Fourier domain mode locking (FDML) laser

In FDML, the optical cavity is designed so that light from a full frequency sweep propagates through the cavity and returns to the tunable Fabry-Pérot bandpass filter exactly when the optical filter is tuned to the same optical frequency. The delay line is chosen such that the round-trip time T_{RT} is an integer multiple of the filter tuning period T_{Filter}, satisfying

$$T_{RT} = n \cdot T_{Filter}, \tag{2.41}$$

where $n \in \mathbb{N}^+$ is typically equal to 1. This synchronization ensures that the light re-enters the filter at the correct frequency, enabling coherent reuse and eliminating the need to completely rebuild the laser output from ASE when the filter's transmission wavelength range is adjusted. Instead, only the losses from a single round-trip must be compensated at each wavelength [23]. A schematic drawing of the FDML laser is shown in Figure 2.6.

The filter serves as the heart of the FDML laser. It consists of a custom-designed Fabry-Pérot filter, where one of the two mirrors is attached to a piezoelectric element. The piezoelectric element expands or contracts in response to an applied voltage, enabling precise control of the mirror's position. The filter achieves efficient and stable wavelength tuning by operating at its mechanical resonance frequency, typically around 400 kHz. A DC voltage sets the filter to a specific tuning starting point or reference point. It specifically defines the central wavelength and the filter's FSR. A low-noise sinusoidal alternating voltage is applied to the piezoelectric element in addition to the DC voltage to enable dynamic tuning of the wavelength range. The alternating voltage causes the piezoelectric element to oscillate, which shifts the position of the filter's transmission window. This oscillation enables continuous wavelength adjustment, generating frequency sweeps within the desired tuning range. Nonetheless, as the mirror approaches the turning points, its speed diminishes, allowing the filter to transmit certain wavelengths for an extended period. This results in a nonlinear frequency sweep and, consequently, non-uniform spectral sampling, which must be corrected during image reconstruction (see Chapter 2.3.4).

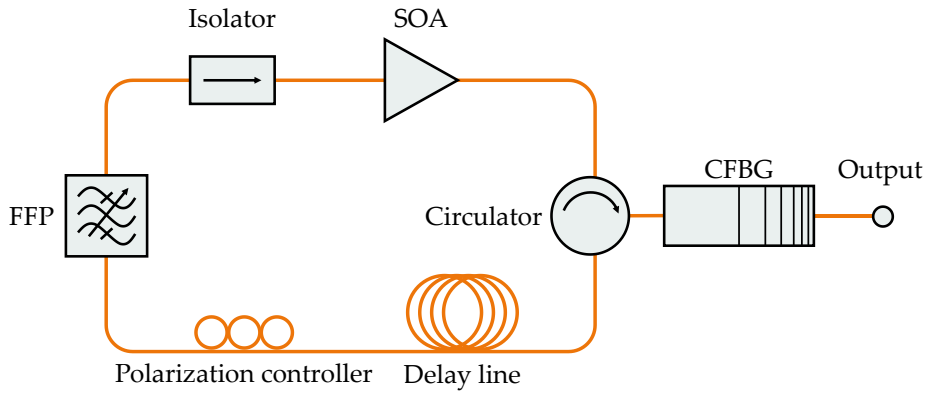

Figure 2.6 Operating principle of a Fourier domain mode locking (FDML) laser . The laser cavity consists of a semiconductor optical amplifier (SOA), an optical isolator, a tunable Fabry-Pérot filter (FFP), and an extended fiber delay line that determines the round-trip time. A circulator is used to extract the output signal. A chirped fiber Bragg grating (CFBG) is included to reduce chromatic dispersion of the laser cavity.

Optical amplification is achieved using a polarization-dependent semiconductor optical amplifier (SOA) as the gain medium, with electrical pumping provided by a laser diode driver. Since the SOA amplifies light in a specific polarization direction, fiber polarization controllers are incorporated in the resonator. These controllers adjust the polarization of light by manipulating the orientation of the fiber. This ensures that the light entering the SOA has the correct polarization state for optimal amplification, generating a stable, well-defined output spectrum. A dispersion management in the delay line compensates for

wavelength-dependent phase shifts, ensuring stable and efficient laser operation across the entire sweep range [23].

2.3.3 Optical buffering

Optical buffering is a technique that increases the speed of the FDML laser without requiring a proportional increase in the tuning frequency of the Fabry-Pérot filter. The SOA is modulated with a rectangular waveform and is only activated during a fraction $1/N$ of the total sweep time. As the waveform is synchronized with the linear region of the filter's frequency sweep, the SOA selectively amplifies only the most linear part of the filter's tuning curve. This linear section can correspond to the forward (shorter to longer wavelengths) or the backward sweep (longer to shorter wavelengths). However, the backward sweep is often favored, as it typically exhibits reduced noise levels compared to the forward sweep, despite both directions having equivalent transient power characteristics [73]. The principle of this buffering approach is illustrated in Figure 2.7. During the laser's inactive intervals within each sweep cycle, the optical signal is directed through b_S buffer stages, each introducing a precisely defined temporal delay. These delays enable several temporally shifted copies of the frequency sweep to be generated within a single filter cycle, effectively increasing the output sweep rate by a factor of $N = 2^{b_S}$, with $b_S \in \mathbb{N}^+$.

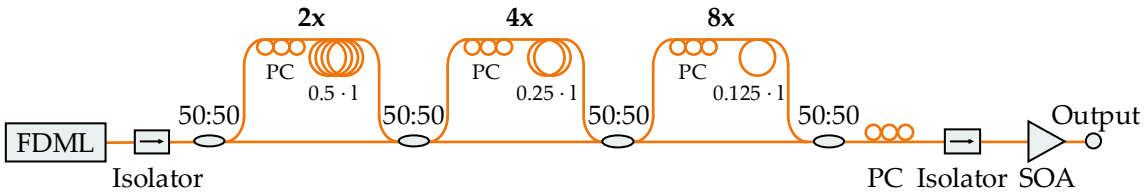

Figure 2.7 Schematic illustration of an 8x buffer stage. The output signal of the Fourier domain mode locking (FDML) laser is split and sequentially delayed using a series of fiber delay lines and 50:50 fiber couplers. Each stage introduces a defined delay so that eight time-interleaved copies of the wavelength sweep can be generated. The sweeps are recombined and directed toward the system output. PC: Polarization controller. SOA: semiconductor optical amplifier.

Each buffer stage consists of a 50:50 beam splitter, a polarization controller, and a fiber delay line. One output of the splitter is delayed by a fiber whose length l is half that of the previous stage, or half the length of the FDML resonator in the case of the first stage. The delayed and non-delayed signals are then recombined using another 50:50 splitter and passed on to the next stage. After all buffer stages, the temporally shifted copies are combined in a final 50:50 splitter and amplified using another SOA to generate the output signal. Polarization controllers within each stage align the polarization state of the light

for maximum amplification by the SOA. Optical isolators are placed after the FDML laser and the SOA to enforce unidirectional light propagation and suppress back reflections.

Although the addition of buffer stages primarily serves to increase the sweep rate, it also leads to a reduction in optical bandwidth. To compensate for this reduction, the amplitude of the sinusoidal signal driving the tunable filter can be increased, allowing the filter to sweep beyond the desired wavelength range $\Delta\lambda$. This approach helps to regain some of the lost optical bandwidth. Nonetheless, mechanical limitations on tuning speed ultimately restrict the number of buffer stages and the achievable optical bandwidth.

2.3.4 Signal processing

The electrical signal recorded by the photodiode represents raw interferometric data and must undergo extensive post-processing before image reconstruction. One of the initial steps in this process is background subtraction to reduce system-induced noise. The background signal is typically recorded with the sample arm blocked, allowing only system-related interference and detector noise to be captured. To enhance the stability and reliability of the background estimate, the signal is commonly averaged across several sweep cycles, typically comprising approximately 100 A-scans. These background measurements are usually acquired either at the start of the measurement session or directly before each acquisition. The resulting averaged background is subtracted from all raw A-scans to suppress fixed-pattern noise and improve the SNR in the subsequent image reconstruction pipeline.

In the next step, the data must be linearized. In SS-OCT, the interferometric signal is recorded as a function of time during the wavelength sweep of the laser. The depth information is encoded in the frequency spectrum of this signal. However, due to the sinusoidal operation of the FDML laser, the depth information is not evenly spaced, which can cause smearing in the resulting image. To correct this, a technique called k-clocking can be applied. It involves synchronizing the data acquisition with an external clock signal, ensuring that the sampling of depth points occurs uniformly in the wavenumber space k. However, this approach requires very high sampling rates, which can lead to temporal jitter. Therefore, several preprocessing steps are done before image reconstruction to address the non-uniform sampling.

A key advantage of FDML lasers is their high phase stability, which allows for the reliable acquisition of a recalibration signal at the beginning of each measurement session. This calibration sweep is typically obtained by capturing the interferometric pattern generated between the reference arm and a stationary mirror in the sample arm or by using a separate recalibration arm. The acquired signal is then interpolated, commonly using sinc interpolation, to increase the number of data points, providing finer temporal resolution

for more accurate resampling. To extract the phase profile, signal processing methods such as the Hilbert transform or zero-crossing detection of the interference fringes are applied. The resulting phase information is then used to resample the OCT data at uniformly spaced time points, ensuring precise depth reconstruction.

After recalibration, the next step is applying a window function, a process called apodization. This step is done to minimize spectral leakage, which arises due to the finite duration of the sampled signal. Theoretically, limiting a signal to a finite time interval is equivalent to multiplying it by a rectangular function. This corresponds to a convolution with a sinc function in the frequency domain, which causes spectral components to spread into neighboring frequencies. This spread, known as spectral leakage, can distort the frequency signal and image quality. Therefore, a window function, such as a Hann, Hamming, or Kaiser window, is applied to the signal to reduce this effect. These functions gradually reduce the signal amplitude near the boundaries, suppressing sidelobes and limiting leakage. Additionally, this step can be combined with a dispersion compensation method by applying phase adjustments.

Since the depth information is encoded in the signal's frequency spectrum, a discrete Fourier transform is performed to convert the data into the frequency domain, generating a complex signal. Zero-padding is often applied before the FFT to increase the number of frequency data points. For conventional OCT images, the magnitude of the complex signal is taken and converted to a logarithmic scale. Cut levels are subsequently set to improve contrast and optimize visualization. On the other hand, the phase component captures minute changes in optical path length, allowing for the detection of axial displacements with nanometer precision. This feature is particularly useful in applications such as elastography, Doppler OCT, and angiography, where precise measurements of tissue stiffness and fluid dynamics are essential for accurate assessment.

2.4 Speckle in OCT

Speckle is a noise-like artifact observed in coherent imaging systems, such as OCT. It arises from the random interference of light scattered by microscopic structures smaller than the system's resolution limit. This effect results from the superposition of many wavelets with random phases and path lengths, leading to constructive and destructive interference that produces a distinctive granular texture in the resulting image. A simple demonstration of this effect can be observed when a laser is aimed at a textured surface or a painted wall. The grainy, shimmering pattern that appears directly results from coherent light interfering after being scattered by uneven microscopic features.

2.4.1 Statistical properties

The first-order statistical properties of laser speckle can be understood by assuming that the amplitudes and phases of the scattered wavelets are statistically independent. Additionally, the phases of these wavelets are uniformly distributed over the interval from $-\pi$ to π, and the light is perfectly polarized. Under these conditions, the resultant speckle pattern is "fully developed" and conforms to the central limit theorem [74-76]. According to the theorem, when many independent random variables are summed, their total will tend toward a normal distribution, no matter the nature of the individual variables' distributions. This means the scattered light's total phasor $\underline{A}$ acts as a random variable, adhering to a circular complex Gaussian distribution. The probability density function $p_{I_s}(I_s)$ of the intensity $I_s = \sqrt{Re^2\{\underline{A}\} + Im^2\{\underline{A}\}}$ is negative exponential and can then be expressed as [74, 76]:

$$p_{I_s}(I_s) = \begin{cases} \frac{1}{\langle I_s \rangle} exp\left(-\frac{I_s}{\langle I_s \rangle}\right), & if\ I_s \geq 0 \\ 0, & otherwise \end{cases}, \tag{2.42}$$

where the brackets $\langle \cdots \rangle$ denote an ensemble average. The contrast of a speckle pattern can then be described as

$$C = \frac{\sigma_{I_s}}{\langle I_s \rangle}, \tag{2.43}$$

with σ_{I_s} being the standard deviation of I_s.The contrast can be reduced by averaging multiple images, given that the M speckle patterns are uncorrelated [76]:

$$C = \frac{1}{M}. \tag{2.44}$$

Speckle patterns are influenced by several factors, primarily the light source and the optical imaging system. A shorter coherence length results in faster averaging of the phase differences, thereby reducing the speckle contrast. Additionally, shorter wavelengths produce finer and more compact speckles, while longer wavelengths result in coarser patterns [76]. The NA also significantly contributes to the characteristics of the speckle pattern. A higher NA enables light to be captured from a wider angular range, resulting in finer, more detailed speckle patterns with higher contrast. The minimum resolvable feature size or speckle grain size d_S can be expressed by

$$d_S \propto \frac{\lambda}{NA}, \tag{2.45}$$

This equation utilizes diffraction-limited imaging principles to describe the optical system's resolution limit.

2.4.2 The dual nature of speckle: noise and information carrier

Although speckle may contain some structural information, it often masks fine details and reduces overall image clarity. To address this, various speckle reduction techniques have been developed, ranging from acquisition-based methods to post-processing algorithms. One common approach is spatial compounding, where multiple images are acquired under slightly shifted spatial positions. These images are subsequently combined through averaging.

While this method effectively reduces speckle noise, it comes with a trade-off. The speckle reduction often comes at the cost of spatial resolution, as fine structural details can become blurred during the averaging process. Therefore, angular compounding has been introduced, where several images are recorded from different illumination or observation angles. Since the structural features of the sample remain consistent across angles while the speckle patterns change, averaging these images reduces speckle while preserving important structural information. This effect is demonstrated in Figure 2.8, which compares non-averaged and angular-compounded OCT images of a human fingertip and fingernail. Further methods for speckle reduction are discussed by Fercher et al. [4, 74].

However, while speckle is often considered noise, it can also act as an information carrier. In OCT angiography, for instance, shifts in speckle patterns over time offer valuable insights into blood flow velocity and vessel architecture. In tissue, speckle patterns remain stable when there is no movement. But when blood flow is present, the movement of scattering particles causes these speckle patterns to shift. By analyzing these variations in speckle over time, OCT angiography can differentiate between static tissue and dynamic blood flow.

Another application is elastography, where speckle-tracking assesses tissue stiffness by analyzing the tissue's response to mechanical stress (see Chapter 3.3.3.1). When a sample is subjected to an external force, it deforms, causing a shift in the speckle patterns. By tracking these changes, the degree of tissue deformation and tissue stiffness can be quantified.

Additionally, speckle-tracking can be applied in dOCT to obtain label-free images of cellular structures. By analyzing temporal variations in speckle patterns, dOCT enables the visualization of cellular dynamics and morphology without external staining agents and with microscopic resolution. Further details on dOCT will be presented in Chapter 4.

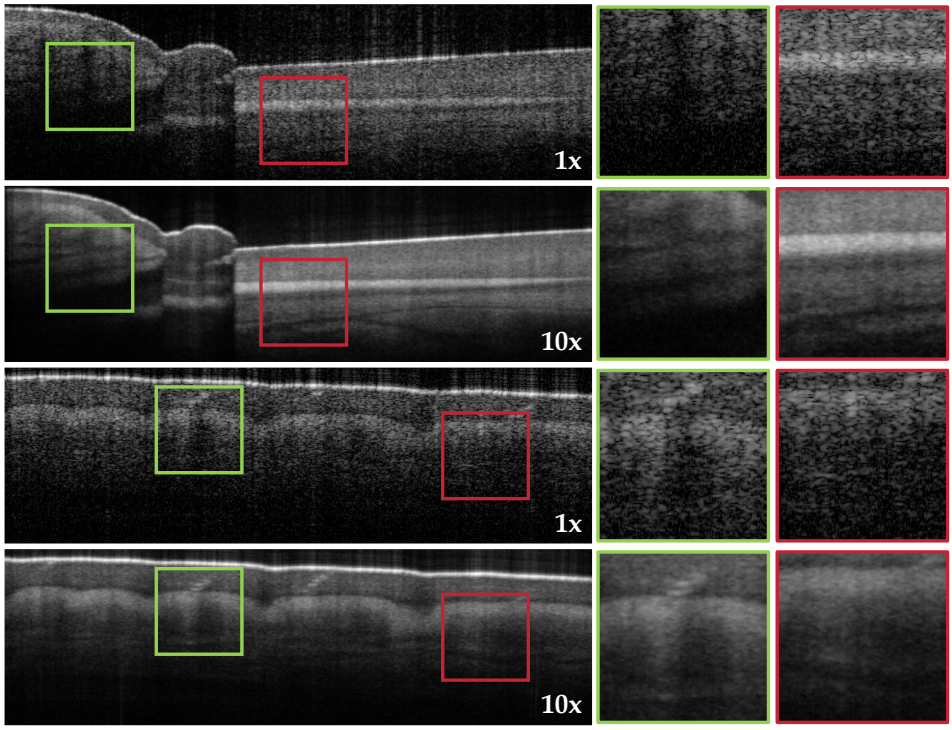

Figure 2.8 Speckle reduction through angular compounding in OCT. B-scan images of a human fingernail (top two rows) and fingertip (bottom two rows) are shown to compare non-averaged imaging (1x, first and third rows) with 10x angular compounding (second and fourth rows). Green and red boxes highlight selected areas for comparison, with magnified views displayed on the right. The compounded images demonstrate improved structural detail and a noticeable reduction in speckle noise, resulting in better visual clarity and easier interpretation of tissue features.

2.5 Phase in OCT

One optical parameter that has not yet been discussed in detail is the phase. The optical phase describes the position of a light wave within its oscillation cycle and is typically expressed as an angle between 0 and 2π. As light interacts with biological tissue, variations in tissue properties can induce changes in the optical path length, leading to phase shifts. These phase shifts provide valuable insight into the tissue's microstructure, offering a sensitivity that exceeds what intensity-based imaging techniques can achieve. Unlike speckle-tracking, phase-sensitive approaches can detect subtle changes in the order of nanometers, allowing for the identification of small depth shifts that would otherwise be missed. This phase information is essential in applications like elastography, helping to accurately measure tissue deformations, and in blood flow imaging, aiding the detection of small movements within vessels.

2.5.1 Phase extraction and unwrapping

To obtain phase information in OCT, as shown in Equation 2.22, the detected interference signal is processed by applying a Fourier transform. This results in complex data for each pixel (x, y) and at each time point t, consisting of a depth-resolved reflection profile. It is represented by the magnitude of the complex signal $A_{x,y}(t)$ along with its phase angle $\phi_{x,y}(t)$, and can be expressed as [60, 77-79]

$$I_{x,y}(t) = \mathcal{F}^{-1}\{I_{x,y}(k)\} = A_{x,y}(t)exp\left(-i\phi_{x,y}(t)\right). \tag{2.46}$$

This allows us to extract the phase information by using [8, 77]

$$\phi_{x,y}(t) = arctan\left\{\frac{Im\left(I_{x,y}(t)\right)}{Re\left(I_{x,y}(t)\right)}\right\}. \tag{2.47}$$

If the tissue is static, $\phi_{x,y}(t)$ is random but stable in time. However, if the sample undergoes displacement due to external influences, $\phi_{x,y}(t)$ can be split as follows [80]:

$$\phi_{x,y}(t) = \phi_{SR}(t) + \phi_{shift}(t) + \phi_0\,. \tag{2.48}$$

Here, $\phi_{SR}(t)$ indicates the phase between the sample and reference arm, whereas $\phi_{shift}(t)$ corresponds to the induced sample motion, and ϕ_0 to the initial phase value.

A common limitation in phase-sensitive OCT is the periodicity of the phase information, which is constrained within a 2π range. As a result, the measurable displacement between two A-scans is confined to values within the interval $-\pi$ to π, leading to phase ambiguities known as phase wraps. These ambiguities can hinder the accurate quantification of displacement and must be resolved through a phase unwrapping procedure to recover the true displacement values. The obtained unwrapped phase $\varphi_{x,y}(t)$ for each time point t and pixel (x, y) can then be expressed as [79]:

$$\varphi_{x,y}(t) = \phi_{x,y}(t) + j_{x,y}(t) \cdot 2\pi \cdot q_{x,y}(t)\,, \tag{2.49}$$

with $j_{x,y}(t)$ representing the sign of the correction value and $q_{x,y}(t)$ denoting the integer that defines the necessary multiplier of 2π.

In an ideal, noise-free scenario, phase unwrapping can be performed by identifying discontinuities in the wrapped phase signal and compensating for them by adding or subtracting appropriate integer multiples of 2π. Typically, phase jumps are detected by evaluating the phase difference between neighboring samples and determining if the magnitude of the difference exceeds a threshold of π. A phase difference surpassing this threshold indicates the occurrence of a phase wrap, necessitating the application of a correction

to ensure phase continuity. However, experimental data are inherently affected by noise, which complicates the identification of true phase discontinuities and increases the risk of unwrapping errors. Therefore, robust phase unwrapping techniques are essential for accurately reconstructing the continuous phase, particularly in applications that require precise displacement measurements.

Therefore, several advanced phase unwrapping techniques have been developed [79, 81-83]. However, despite the variety of available algorithms, no universally optimal strategy for phase unwrapping exists. Instead, selecting an appropriate method typically depends on the specific characteristics and requirements of the application.

2.5.2 Phase noise

In real-world scenarios, the phase of the signal is influenced by various noise sources, including shot noise, RIN, and detection noise, as discussed in Section 2.2.4. These noise contributions can introduce inaccuracies during phase unwrapping and affect the correctness of the functional contrast. Therefore, understanding the noise sources and implementing strategies to minimize their effects is crucial for the success of phase-sensitive OCT imaging.

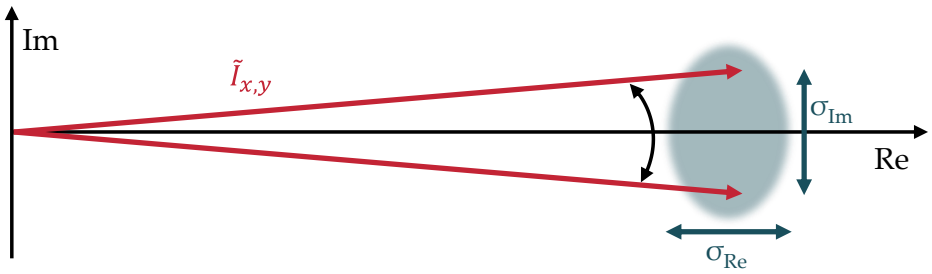

Figure 2.9 Schematic representation of phasor variability in the complex OCT signal. The phasor of the OCT signal, represented by red arrows, is influenced by random noise. The phasors vary in both angle and length in the complex space. Deviations along the horizontal direction (σ_{Re}) correspond to noise in the real component. In contrast, variations in the vertical direction (σ_{Im}) reflect fluctuations in the imaginary part of the signal. Derived from [84].

Assume the OCT signal after applying the Fourier transform is denoted as $\tilde{I}_{x,y} = Re(\tilde{I}_{x,y}) + jIm(\tilde{I}_{x,y})$, where both the real and imaginary component inherently contain statistical noise. As a result, the tip of the signal phasor does not remain fixed. Instead, it fluctuates within a region of uncertainty, whose extent is characterized by the standard deviation of the variations in the complex signal components σ_{Re} and σ_{Im}, as illustrated in Figure 2.9. In the shot noise-limited case, as described by Goodman [85], the noise vari-

ances of the real and imaginary parts of $\tilde{I}_{x,y}$ are uncorrelated and can be treated independently [84]. Under these conditions, the variances of both components are identical, such that ${\sigma_{Re}}^2 = {\sigma_{Im}}^2$. The SNR is then defined as the ratio of signal to noise power:

$$SNR = \frac{signal\ power}{noise\ power} = \frac{\left|\tilde{I}_{x,y}\right|^2}{{\sigma_{Re}}^2}. \tag{2.50}$$

Since the phase fluctuations σ_φ are primarily determined by variations in the imaginary part, the phase error can be approximated as follows:

$$sin(\sigma_\varphi) \approx \sigma_\varphi \approx \frac{\sigma_{Im}}{Re\left(\tilde{I}_{x,y}\right)} \approx \frac{1}{\sqrt{SNR}}. \tag{2.51}$$

In addition to minimizing detection-related noise sources, maintaining phase stability within the interferometer is essential. Environmental factors such as mechanical vibrations, temperature fluctuations, and air currents can introduce large phase shifts. To reduce these effects, the interferometer should be enclosed and operated under temperature-regulated conditions. Furthermore, a common-path OCT configuration can improve phase stability by having the reference and sample beams travel through the same optical path. A weak reflection is introduced from a known surface proximal to the sample to generate the reference signal, for example, using a transparent acrylic plate [86]. The front surface of the plate provides the reference reflection, while the transmitted light continues to interact with the tissue below. Because both signals travel along nearly the same optical path, environmental influences affect them equally. As a result, phase fluctuations can be corrected in post-processing by subtracting the phase signal of the reference reflection from the phase signal obtained within the tissue.

3 Optical coherence elastography for brain tumor detection

3.1 Preface

The MHz-OCE setup used in this work was already established before the start of this project. Parts of the results presented in this chapter have previously been published in a first-author paper [87]. Therefore, some of the following sections are taken verbatim from the publication with permission from © Optical Society of America, containing only minor formatting and editorial changes. Only first-author publications are listed here. Additional co-authored contributions related to this work can be found in the appendix.

- **Sazgar Burhan**, Nicolas Detrez, Katharina Rewerts, Paul Strenge, Steffen Buschschlüter, Jessica Kren, Christian Hagel, Matteo Mario Bonsanto, Ralf Brinkmann, and Robert Huber, Phase unwrapping for MHz optical coherence elastography and application to brain tumor tissue, Biomed. Opt. Express, vol. 15, no. 2, pp. 1038-1058, Feb. 2024. Optica Publishing Group.
- **Sazgar Burhan**, Nicolas Detrez, Madita Göb, Matteo Mario Bonsanto, Ralf Brinkmann, and Robert Huber, Advanced FFT-based contrast approach for MHz optical coherence elastography, in Optical Coherence Imaging Techniques and Imaging in Scattering Media V, Benjamin J. Vakoc and Maciej Wojtkowski and Yoshiaki Yasuno, Eds. SPIE, Aug.2023. pp. 1263215.
- **Sazgar Burhan**, Nicolas Detrez, Katharina Rewerts, Madita Göb, Christian Hagel, Matteo M. Bonsanto, Dirk Theisen-Kunde, Robert Huber, and Ralf Brinkmann, Characterization of brain tumor tissue by time-resolved, phase-sensitive optical coherence elastography at 3.2 MHz line rate, in Advanced Biomedical and Clinical Diagnostic and Surgical Guidance Systems XXI, Caroline Boudoux and James W. Tunnell, Eds. SPIE, Mar.2023. pp. 123680F.
- **Sazgar Burhan**, Nicolas Detrez, Katharina Rewerts, Madita Göb, Steffen Buschschlüter, Christian Hagel, Matteo M. Bonsanto, Dirk Theisen-Kunde, Robert Huber, and Ralf Brinkmann, Phase analysis strategies for MHz OCE in the large displacement regime, in Optical Coherence Tomography and Coherence Domain Optical

Methods in Biomedicine XXVII, Joseph A. Izatt and James G. Fujimoto, Eds. SPIE, 2023. pp. 123670Q.

3.2 Clinical background

The brain, one of the most complex organs in the human body, regulates vital functions and processes sensory information. It consists of billions of neurons and glial cells and weighs only 1.5 kg on average [88]. Structurally, it is divided into four main regions: the cerebrum, the cerebellum, the diencephalon, and the brain stem. These regions consist of both gray and white matter. Gray matter represents around 40 % of the brain's volume and is the outer layer, the cortex. The name and grayish-pink color arise from the dense clusters of neurons and the absence of myelin in that area. Due to the large concentration of neuron cells, the gray matter is mainly responsible for processing information, interpreting sensory inputs, and executing commands. The inner white matter is predominantly composed of myelinated axons. The myelin sheath, a fatty layer surrounding the axons, gives the characteristic color. Its main function is facilitating fast signal transmission between gray matter areas and other parts of the nervous system.

Besides, the brain is highly vulnerable to various diseases. Among the biggest threats are brain tumors. Benign tumors usually develop slowly, remain localized, and are not life-threatening. However, they can exert pressure on critical brain structures, potentially impairing their function. In contrast, malignant tumors grow rapidly, invade surrounding tissues, and often recur even after complete surgical removal.

The survival rates of people suffering from a brain tumor vary considerably depending on the tumor type, gender, and geographical region. It is estimated that every year, 3.7 men and 2.6 women per 100.000 people in the world are diagnosed with a primary malignant brain tumor, with industrialized countries tending to have an increased incidence trend rate [88]. The American Cancer Society estimates that in the United States alone, about 25.400 people, among them 14.420 men and 10.980 women, were diagnosed with malignant brain tumors in 2023. In contrast, the Robert Koch Institute reported 2020 around 7.330 malignant cases in Germany (4.080 men and 3.250 women), with five- and ten-year survival rates of 20 - 21 % and 15 - 17 %, respectively.

3.2.1 Current imaging modalities in neurosurgery

The World Health Organization (WHO) has developed a classification and grading system that assesses the histopathological characteristics of tumors for more accurate diagnosis and prognosis. Hereby, tumors are classified into grades ranging from I to IV. Lower-

grade tumors (grades I and II) tend to be less invasive and grow more slowly, while higher-grade tumors (grades III and IV) proliferate rapidly and are more aggressive. In all cases, surgical removal remains the preferred treatment approach. The goal is to remove the entire tumor tissue while preserving the surrounding healthy tissue as much as possible. However, discriminating between healthy and diseased tissue intraoperatively is a significant challenge.

In addition, so-called brain shifts present a considerable challenge during surgery. Brain shift refers to intraoperative changes in the brain's position or shape that result from cerebrospinal fluid drainage, brain tissue relaxation, tumor removal, cerebral edema, hemorrhage, or changes in intracranial pressure. These shifts can cause the brain to move or deform, making preoperative images unreliable as they may no longer reflect the brain's current state [31, 41, 42]. This makes it harder for surgeons to navigate effectively and remove the tumor while preserving healthy tissue. Therefore, surgeons are moving increasingly towards advanced intra- and preoperative imaging-guided neurosurgical systems like intraoperative magnetic resonance imaging (iMRI), intraoperative ultrasound, fluorescence-guided surgery, and neuronavigation.

First introduced in 1994, iMRI has significantly enhanced neurosurgery by providing real-time imaging during operations [31]. The real-time updates highly improve precision and support decision-making with the ability to monitor intraoperative brain shifts. While iMRI offers significant advantages, it also has several drawbacks. The systems are very expensive and have high installation, operation, and maintenance costs. In addition, they require a specially designed operating room equipped with MRI-compatible instruments and shielding.

Intraoperative ultrasound has been used since the 1980s [31]. Unlike intraoperative magnetic resonance imaging, it is more affordable and widely available. More importantly, ultrasounds are portable and easy-to-use imaging modalities that can be valuable in many neurosurgical procedures. In particular, very good visualization has repeatedly been reported for tumors such as gliomas, metastases, and meningiomas [89]. However, the effectiveness of ultrasound is largely operator-dependent, and artifacts may contribute to poor image quality in certain cases. In addition, the relatively low spatial resolution can limit the ability to distinguish fine structural details.

Fluorescence-guided surgery uses fluorescent dyes such as 5-aminolevulinic acid (5-ALA) or fluorescein sodium. These dyes accumulate in the tumor cells and glow after illumination with blue or ultraviolet light [32, 33, 90, 91]. However, it is an invasive process, and its effectiveness depends highly on the metabolic activity and vascularization of the tumor. Thus, certain tumors, such as low-grade gliomas, may not fluoresce strongly

enough to offer adequate contrast [33, 90]. This can result in difficulties detecting the tumor's full size, with a risk of false-negative outcomes if tumor parts do not fluoresce [91].

Intraoperative neuronavigation has become a standard imaging technique in neurosurgery [92, 93]. It creates a detailed three-dimensional brain map using preoperative imaging data from CT or MRI scans [41, 43, 94]. During surgery, surgical instruments are tracked in real time relative to this map, allowing the visualization of their spatial relationship to the tumor and critical brain structures, thereby enhancing surgical planning. Traditional neuronavigation systems typically rely on infrared cameras to navigate in three-dimensional space. These systems use a fixed reference frame securely attached to the skull, often through rigid fixation (pinning). Recent advances have introduced electromagnetic neuronavigation systems that eliminate the need for pinning by using a small reference sensor mounted on the skull, offering greater flexibility. In addition, improved comfort to the patient and neurosurgeon is provided as minor intraoperative head movements are allowed without compromising registration accuracy [92]. However, despite their advantages, these systems face a significant limitation as their accuracy can decline during surgery due to brain shifts.

Given these limitations, there is an increasing need for imaging systems that can integrate the benefits of existing technologies while minimizing their drawbacks. Such systems would provide real-time, high-resolution, and tissue-specific information throughout the surgical process, combining the precision of iMRI, the portability of ultrasound, the guidance of fluorescence, and the spatial awareness of intraoperative neuronavigation systems. This would allow for more accurate and efficient surgeries, with fewer complications arising from brain shifts or inadequate tumor visualization.

3.3 Optical coherence elastography (OCE)

The mechanical properties of tissues, such as elasticity or viscosity, are important tissue characterization parameters as they can undergo pathological or physiological alteration. For example, tumor tissue is generally stiffer than healthy tissues, a property commonly used in clinical practice. Therefore, during breast self-examination, the fingertips, which have a sensitivity of around 40 μm [95], can detect breast abnormalities. In addition, during neurosurgical tumor resection, surgeons often rely on palpation or mechanical scanning to identify the tumor borders. However, while this is a standard procedure, it is highly subjective and depends on the surgeon's experience. Therefore, transitioning this process to an automated detection and imaging system would improve accuracy and objectivity, assisting the operating surgeon in decision-making.

Elastography is an advanced imaging technique designed to provide insights into the mechanical properties of materials, including their elasticity and viscosity. The primary objective is to create a detailed map of local mechanical characteristics based on measured displacements. It involves applying a mechanical load to the tissue and analyzing its corresponding response. Various automated elastography techniques have been developed and tested over the years in neurosurgical applications, with intraoperative ultrasound and preoperative magnetic resonance elastography being mostly used [96-100]. However, as previously mentioned, both imaging modalities have their limitations. In addition, magnetic resonance elastography and ultrasound elastography offer a spatial resolution of approximately 1 mm and 250 μm, respectively. This makes them particularly advantageous for assessing larger tissues and deeper organs, where coarse structural changes and mechanical properties can be detected effectively. However, their relatively low spatial resolution can be a limitation, particularly for capturing fine details.

Table 3.1 Performance metrics of various elastography techniques. These performance characteristics highlight the trade-offs between imaging depth, spatial resolution, and acquisition time, which influence the suitability of each method for different biomedical applications. SNR: Signal-to-noise ratio. Reproduced from [101].

Techniques	Resolution	Imaging depth	SNR	Imaging speed	Transverse field of view
Magnetic resonance elastography	1 - 3 mm	Whole body	5 - 14 dB	2 - 20 min	Whole body
Ultrasound elastography	0.1 - 5 mm	4 - 5 cm	8 - 12 dB	4 - 30 μs	5 - 10 cm
Optical coherence elastography	15 - 100 μm	0.5 – 3 mm	10 - 25 dB	20 - 100 μs	5 – 15 mm
Brillouin microscopy	0.5 - 5 μm	0.1 - 3 mm	10 - 30 dB	2 - 5 min	0.5 - 10 mm
Atomic force microscopy	1 - 100 nm	Surface	10 - 33 dB	30 s - 30 min	0.1 - 0.5 mm

In contrast, optical coherence elastography (OCE), an imaging technique that integrates OCT with elastography, achieves a resolution of approximately 15 - 100 μm [101]. This level of precision positions OCE as a promising tool for assisting clinicians in identifying early-stage pathologies or brain tumors. Its ability to detect sub-micrometer changes in displacement allows OCE to distinguish subtle variations in tissue mechanical properties. Furthermore, the non-contact applicability of OCE makes it ideal for clinical applications where sterility and patient comfort are priorities. By offering detailed, quantitative maps of tissue mechanics, OCE has the potential to enhance tumor detection significantly and improve surgical outcomes by providing a reliable, objective tool for identifying tumor

margins. The key characteristics of different elastography techniques are outlined in Table 3.1.

3.3.1 The evolution of OCE in biomedical research

The use of OCT for elastography was first introduced and demonstrated in a pioneering study by Schmitt in 1998 [102]. In his study, samples subjected to bulk compression were imaged, and the resulting local displacement field was analyzed by correlating consecutive B-scans. Displacement maps were created, and the localized strain offered insights into the sample's mechanical properties. The term "optical coherence elastography" was first introduced in 2004 by the research group of Brett E. Bouma [103], with the initial aim of detecting atherosclerotic plaques. In 2006, Stephen Boppart's research group applied OCE to a tissue-engineered construct and, for the first time, an animal model, the *Xenopus laevis* (African frog) [104]. While these studies represented a significant step forward, the basic methodology remained the same as in Schmitt's original demonstration. Nevertheless, the results provided additional confirmation of the technique's potential.

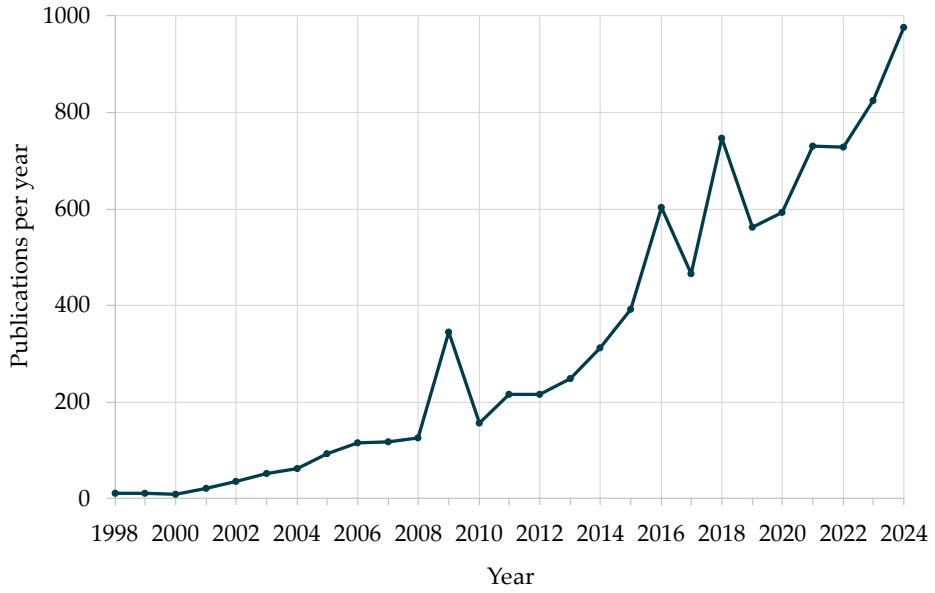

Figure 3.1 Publication trend on OCE from 1998 to 2024. This diagram illustrates the number of publications on optical coherence elastography since the fundamental work by Schmitt in 1998. The data were retrieved from Dimensions.ai (accessed January 2025).

The foundation for phase-based OCE was laid in 1997 when two research groups demonstrated that the phase information encoded in the interferometric fringe pattern enabled accurate analysis of blood flow velocity using Doppler OCT [9, 11]. However, significant advancements in phase-based OCE began around 2008, driven largely by the transition from time-domain to spectral-domain OCT systems. The primary factors behind this

were the enhanced imaging speed by several orders of magnitude, the improved sensitivity, and the phase stability that spectral-domain systems offered [48]. Wang et al. were the first ones to demonstrate phase-sensitive OCE (see Chapter 3.3.3.2) using a spectral-domain system, achieving nanometer-level sensitivity through A-scans [47] and B-scans [60] comparison. This breakthrough opened the door for developing various phase-sensitive OCE techniques [105, 106].

Figure 3.1 illustrates the publication trend on OCE over the years, based on data retrieved from Dimensions.ai. A total of 8.831 publications on the topic have been recorded to date. Notably, 8.239 papers were published since 2008, representing approximately 93.3 % of the total output. Additionally, around 1.000 publications were released in 2024 alone, highlighting the rapid growth and increasing interest in OCE research in recent years.

3.3.2 OCE tissue excitation methods

Elastography excitation methods can generally be divided into two main categories: static/quasi-static and dynamic [105, 107]. These methods can be applied either internally or externally to the tissue. Schmitt's initial demonstration utilized external static planar compression, achieved through a ring-shaped piezoelectric actuator and window on the same side as the imaging setup. This approach remained the only technique employed for OCE until 2008 [48, 102]. Since then, various excitation techniques for elastography have been developed and implemented, including contact-based and non-contact approaches. Each method has advantages and limitations, making it suitable for certain applications depending on the clinical requirements.

3.3.2.1 Static tissue excitation

Most traditional OCE techniques are categorized under the static external excitation approach. Compression can be applied either over the entire tissue surface, for example, using a glass cover [108-111], or locally with a needle or rod, known as needle-based OCE [112, 113]. Both approaches typically measure two static states, before and after the load is applied, using a steady or slowly varying force that makes time-dependent effects negligible [114]. The local axial strain, which quantifies relative deformation over a small depth range, is calculated as the spatial derivative of the axial displacement within the tissue. However, calculating Young's modulus, which quantifies tissue stiffness as the ratio of stress to strain, in a typical compression-based OCE is impossible, as the local stress applied to the tissue is unknown. The lateral resolution in compression OCE aligns with the resolution of the OCT system used. In contrast, the axial resolution depends on the

depth range used for strain calculation, which is usually 5 to 10 times larger than the axial resolution of the OCT system itself.

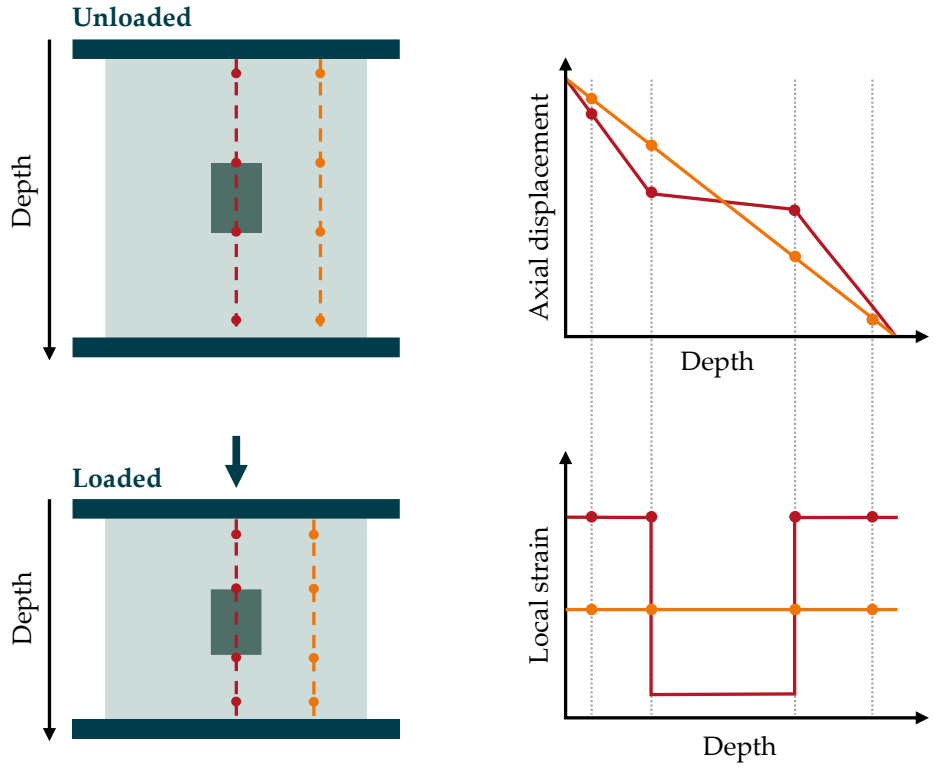

Figure 3.2 Uniaxial tissue compression with embedded inclusion. A homogeneous tissue sample with a stiff inclusion is shown in both its unloaded and compressed states. Axial displacement and strain are analyzed at two positions, one within the inclusion (red) and one in the surrounding homogeneous tissue (orange). The red plots show the influence of the inclusion, while the orange plots represent the expected uniform behavior. Modified and redrawn from [115, 116].

Figure 3.2 shows a scenario where a soft, homogeneous material contains a stiff inclusion and is subjected to an external load from above. In this case, the displacement of the material will be greater near the surface and decrease gradually in depth. This variation in displacement typically follows a linear pattern in the soft surrounding tissue. However, when the external load reaches an inclusion, the displacement will be significantly smaller within the stiffer inclusion compared to the surrounding soft material due to the higher resistance to deformation of the inclusion. In the surrounding soft tissue, where displacement varies linearly with depth, the strain will be uniform within that region. Strain is defined as the relative deformation given by the derivative of displacement with respect to depth, and for a linear displacement profile, this derivative is constant. However, at the border between the soft tissue and the stiff inclusion, the strain will change abruptly due to the difference in mechanical properties. Therefore, the strain will not be uniform

throughout the depth, as it will be affected by both the properties of the soft material and the stiff inclusion.

3.3.2.2 Dynamic tissue excitation

On the other hand, dynamic elastography methods encompass various techniques to apply time-varying forces to tissues. Unlike static elastography, which solely evaluates tissue stiffness under a constant load, dynamic elastography enables the assessment of tissue behavior under changing conditions. One approach involves applying a transient, localized pulse to generate an acoustic wave within the tissue. This can be achieved through various methods, with air puffs and laser pulses being the most employed. The resulting wave propagates through the tissue and can be measured with OCT by tracking the time-dependent displacement of tissue structures. From the wave propagation, information about the tissue's mechanical properties can be derived.

Air puff excitation is commonly used in elastography, particularly for the cornea and retina, where a controlled pulse of air is directed at the tissue [29, 87, 117-119]. This non-contact method generates mechanical waves within the tissue, allowing for the assessment of its biomechanical properties. The air puff is precise and repeatable, making it an effective tool for evaluating tissue stiffness and elasticity without causing harm or discomfort. Alternatively, pulsed lasers can be a highly precise and localized method for generating mechanical waves [120, 121]. By delivering short laser pulses, a localized and rapid increase in temperature occurs within the irradiated volume due to laser energy absorption. The sudden thermal expansion induced by the laser pulse generates ultrasonic waves (high-frequency mechanical waves) that propagate through the material. These waves are predominantly Rayleigh waves, which can be effectively used to assess the elastic properties of the tissue [121]. These transient techniques offer a key advantage by enabling direct estimation of the elastic modulus through the measurement of acoustic phase velocity with OCT. Assuming uniform density, local mechanical homogeneity, and a known Poisson's ratio, the elastic modulus is proportional to the square of the phase velocity [101].

However, the main strength of dynamic elastography lies in its ability to analyze a wide frequency range of mechanical waves propagating through the tissue [122]. Piezoelectric actuators [122-124] are particularly effective in this application, as they can generate precise and controlled mechanical waves across a broad frequency spectrum. After measuring the tissue's response to mechanical load over time, the resulting data are analyzed to compute parameters such as shear wave speed, tissue stiffness, or viscoelastic moduli. This enables the development of precise maps of tissue characteristics.

3.3.3 Mechanical contrast and displacement analysis in OCE

Speckle-tracking or phase-sensitive approaches are typically employed to analyze a sample's response to a mechanical load. The selection of an appropriate method depends on factors such as the required sensitivity, spatial resolution, and the specific characteristics of the tissue or material being examined.

3.3.3.1 Speckle-tracking

In early OCE studies, displacement was mainly measured using speckle-tracking, a technique based on digital image correlation applied to the intensity values of the OCT images. It calculates vectorial displacement through cross-correlations on the speckle patterns within predefined multi-pixel windows across successive images from identical or adjacent locations. Since a multi-pixel window must be used, this process reduces the spatial resolution of the elastogram [48]. However, interpolation techniques can be applied to improve precision, allowing displacement measurements to be determined with accuracy below the pixel size [125]. But, for accurate correlation, the speckle pattern must remain relatively stable before and during displacement, constraining the maximum allowable sample movement between consecutive frames. If the pattern changes too much, the cross-correlation fails, leading to inaccurate or noisy displacement measurements. At the same time, sufficient mechanical loading is necessary to induce noticeable speckle motion, which is crucial for accurate displacement tracking. For example, when the speckle motion between consecutive frames is smaller than a single pixel, cross-correlation methods lack the resolution necessary to track the displacement accurately.

3.3.3.2 Phase-sensitive imaging

Since the development of Fourier-domain OCT, phase-sensitive approaches have become predominant. Instead of relying solely on the structural information from the intensity signal, the phase information within the complex OCT signal is utilized. As a result, the resolution is inherently determined by the imaging wavelength. Given that OCT typically employs light sources with wavelengths around one micrometer, this method allows for detecting displacement variations at a sub-micrometer scale. However, this high displacement sensitivity can only be achieved along a single axial dimension. Once the phase information has been accurately unwrapped $\varphi_{x,y}(t)$ for each pixel (x, y) and each frame t, the displacement $\Delta d_{x,y}(t)$ can be determined as follows:

$$\Delta d_{x,y}(t) = \varphi_{x,y}(t) \cdot \frac{1}{2kn} = \varphi_{x,y}(t) \cdot \frac{\lambda_0}{4\pi n}, \tag{3.1}$$

where n is the refractive index, λ_0 the central wavelength, and $k = 2\pi/\lambda_0$ the wavenumber of the light source [60]. The displacement sensitivity σ_z, which reflects the smallest detectable axial motion, can then be derived by incorporating the phase noise expression from Equation 2.51. This leads to [84]:

$$\sigma_z = \frac{\varphi \cdot \lambda_0}{4\pi n\sqrt{SNR}}. \tag{3.2}$$

3.4 Experimental setup

3.4.1 MHz-OCT imaging system

A commercially available SS-OCT imaging system (OMES, Optores GmbH, Germany) was used for OCE measurements. This system contains a 3.2 MHz FDML laser operated with a central wavelength of 1310 nm and a bandwidth of 100 nm. The system delivered 17 mW of optical power to the sample. The scan head incorporated a pair of galvanometric scanners (dynAXIS 421, Scanlab GmbH, Germany) for precise light positioning. A scanning objective lens with an effective focal length of 54 mm, an NA of 0.037, and a working distance of 42.3 mm (LSM04, Thorlabs Inc., USA) was utilized to focus the beam onto the sample. The achieved spatial resolution was 15 µm axially and 21 µm laterally. Data acquisition was performed using a 12-bit analog-to-digital converter (ATS9373, Alazar Technologies Inc., Canada) with a sampling rate of 4 GSa/s.

Data processing was carried out on a GPU-based High-Performance Computing server, which was equipped with two AMD CPUs (AMD EPYC, Advanced Micro Devices Inc., USA) and an Nvidia graphics card (Nvidia Quadro RTX A5000, NVIDIA Corporation, USA). Measurements were conducted on a vibration-isolated optical table.

To assess the temporal phase response, 4 mm line scans were performed using unidirectional scanning with only the fast X-galvanometer scanner. During each measurement, 800 frames with 512 A-scans were acquired. This corresponds to a B-scan rate of 2.45 kHz, equivalent to a measurement duration of 0.32 s.

3.4.2 Excitation method

The brain is one of the softest tissues in the human body, with a stiffness of approximately 0.1 to 2 kPa [46, 126]. This low stiffness and fragile nature create significant challenges in

selecting an appropriate mechanical loading mechanism for elastography measurements. Due to the brain's delicate nature, excessive tension or adhesion effects can lead to irreversible damage. Therefore, the applied force must be carefully chosen to minimize the risk of tissue damage while ensuring accurate and reliable results. Given the high sensitivity of brain tissue, it is essential to use a sterile, non-contact method to prevent contamination. Furthermore, adhesion effects make compression elastography techniques unsuitable, as they risk tissue integrity and may compromise the accuracy of the measurements [46].

Given these challenges, air-jet elastography offers a promising method for detecting brain tumors. Unlike conventional air-puffs, air-jets deliver longer pulses that allow measurement of both static and dynamic tissue properties from a single excitation [127]. This non-contact approach reduces tissue risk while providing accurate measurements and allowing for a controllable force load on the tissue that can be adjusted dynamically during surgery. Therefore, the feasibility and applicability of air-jet elastography are thoroughly examined in this study. Since this method has never been demonstrated in neurosurgical applications, its potential for tumor detection in brain tissue requires thorough investigation.

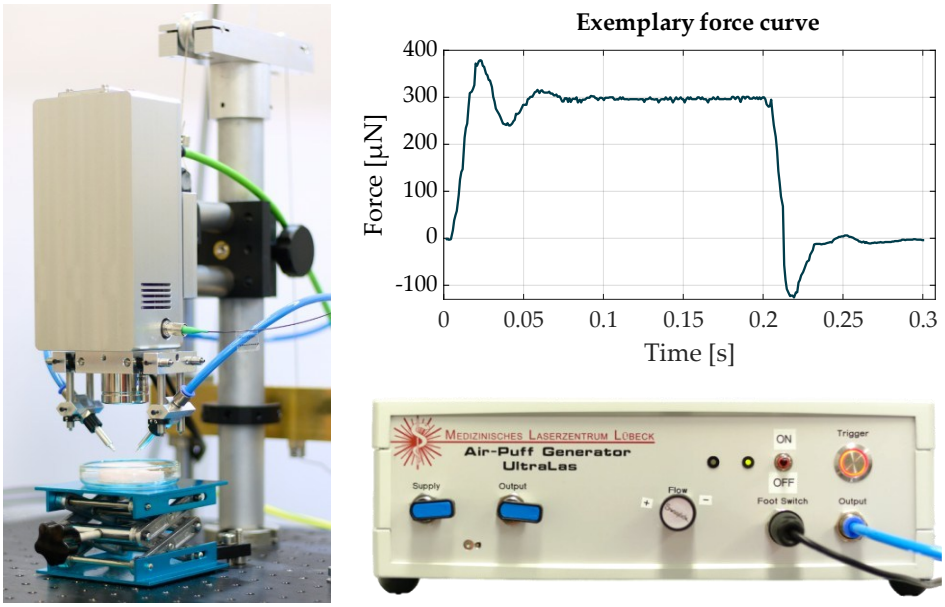

Figure 3.3 Experimental setup for tissue indentation and elastography. Left: Scan head with two 1.4 mm nozzles mounted on the objective, emitting air-jets. Right: The force curve is shown in the upper-right panel, and a front-view image of the air-jet system is shown in the lower-right panel.

For this purpose, an air-jet OCE system already available in the laboratory was used [128]. Two 1.4 mm nozzles were installed on the scan head, angled at 45° to the surface, and positioned roughly 10 mm from the sample. This setup generates a localized force on

the tissue that roughly follows a Gaussian distribution. During assembly, careful alignment ensured that the peak of the Gaussian profile was centered within the B-scans. The resulting undisturbed Gaussian force profile in air has a FWHM of 2 mm. The setup used for tissue indentation and elastography analysis is shown in Figure 3.3. The system can operate at variable flow rates, delivering forces ranging from 1 μN to 40 mN with pulse durations between 5 and 700 ms, enabling adjustment to various tissue characteristics and clinical requirements. The force needs to be incrementally raised for various samples to establish suitable force values, allowing the complete displacement curve and all relevant features to be effectively unwrapped. After finding the ideal force value, it usually stays stable across all samples of the same type.

Unless otherwise specified, each measurement was conducted using a single 200 ms air-jet pulse, with forces ranging from 30 to 85 μN based on the tissue characteristics. The resulting force curve displayed distinct features, including a rising starting edge, a plateau region, and a falling edge. The negative force observed in Figure 3.3 results from the flow sensor in the pneumatic system being placed downstream of the cut valve, which causes the air to flow backward through the sensor section. Therefore, this effect is inherent to the air-jet system and is considered a measurement artifact that does not impact the excitation of the sample.

3.4.3 Samples

A series of measurements was conducted using various samples to validate and assess the performance of the MHz-OCE system. The validation process involved several sample types. Polyvinyl alcohol (PVA) phantoms were used as synthetic tissue models for system verification. In addition, porcine *ex vivo* brain tissue was chosen to replicate the mechanical properties of healthy human brain tissue. Lastly, human *ex vivo* brain tumor tissue was used to evaluate the system's performance under conditions that approximate clinical scenarios.

3.4.3.1 PVA phantoms

As part of this study, our project partner (Söring GmbH, Germany) developed a series of PVA-based phantoms that mimic brain tissue and tumors. The mechanical properties of these phantoms were modified by subjecting them to repeated freezing and thawing cycles. These cycles caused an increase in polymer chain branching, which in turn enhanced the mechanical stiffness. The more often these cycles are done, the stiffer the phantom becomes mechanically [129]. After fabrication, the elastic modulus of each phantom was evaluated using unconfined compression.

An experienced neurosurgeon then performed manual palpation on the homogeneous phantoms to assess their haptic properties and elasticity. This process enabled the development of phantoms that accurately replicated the mechanical properties of both healthy and tumorous brain tissue. The stiffness of these phantoms ranged from 875 Pa for healthy tissue to 16.38 kPa for tumorous tissue.

Phantoms with stiff inhomogeneities were also created to simulate the transition between healthy and tumor tissue. In these phantoms, more rigid PVA inclusions were embedded within a softer PVA surrounding, mimicking the heterogeneous stiffness observed in brain tissue affected by a tumor.

3.4.3.2 *Ex vivo* porcine brain tissue

Due to ethical restrictions and the considerable challenges of obtaining healthy human brain tissue, *ex vivo* porcine brain tissue was employed as a reference model for healthy tissue. Sourced as slaughter by-products from a local butcher, the porcine tissue provided an effective substitute for assessing the system's compatibility in measuring human brain tissue. Upon excision, the tissue samples were promptly stored and transported in an ice-filled cooler to preserve their integrity and prevent degradation. The measurements were performed immediately upon arrival of the tissue samples, ensuring minimal delay between tissue excision and analysis. The aim was to preserve the mechanical properties of the tissue to enable accurate and reliable measurements that resemble the natural state of the tissue.

3.4.3.3 *Ex vivo* human brain tumor

Ex vivo studies were also conducted on human brain tumor samples. The study was reviewed and approved by the Ethics Committee at the University Hospital Schleswig-Holstein, Campus Lübeck, Germany (Approval No. AZ 19-319). All participants have given their written consent to participate in this study. After surgical removal, the samples were immediately placed into a sample container filled with Ringer's solution consisting of 8.6 g NaCl, 0.3 g KCl, and 0.33 g $CaCl_2$ per 1000 ml of distilled water to preserve tissue integrity. The samples were immediately transferred to an ice-filled cooler box for storage and transportation to ensure optimal and reproducible conditions.

3.5 Signal processing and phase correction

The one-dimensional phase unwrapping algorithm detects phase ambiguities in the signal, functioning similarly to the interpretation of a displacement-time graph. It detects

sudden changes in velocity and acceleration over time and uses an environmentally-aware predictive approach to evaluate the potential impact of corrective actions on future phase values. A detailed flowchart outlining the individual processing steps is presented in Figure 3.4. The algorithm, implemented in MATLAB R2023a, achieves a processing time of approximately 0.11 s per frame on the GPU. The full script can be found in Appendix A.1. In the following, $[\cdots]$ represents the standard rounding function, and $\lfloor \cdots \rfloor$ symbolizes the floor function.

3.5.1 Pre-processing

After extracting the phase data, a pre-processing step is applied to identify and isolate the valid sample signal from background regions. This is accomplished using MATLAB's built-in `imbinarize` function, which automatically determines the optimal threshold based on Otsu's method [130]. The method divides an image into two separate classes, foreground and background, by analyzing its histogram and balancing two criteria. It chooses a threshold that reduces the variation of pixel values within each class to maintain internal consistency. At the same time, it maximizes the difference between the classes to ensure a clear distinction. This ensures a clear separation of the relevant phase data from the background noise. By effectively segmenting the image, this method enhances processing efficiency and facilitates the post-processing steps described in section 3.5.3.

3.5.2 One-dimensional phase unwrapping algorithm

Since a MHz-OCT system is employed, analyzing the phase between successive A-scans is not advisable, as the phase shift is minimal. To increase the phase shift, the time between A-scans would need to be increased, which would reduce the imaging speed and prolong the acquisition time. Therefore, the correction process involves assessing the phase difference between two reference A-scans from consecutive B-scans. However, phase wraps are more pronounced in inter-frame phase analysis because the extended time between frames lets tissue move enough to exceed $\pm\pi$. In contrast, phase shifts between consecutive A-scans at MHz rates remain very small. This problem is further compounded by the complexity of brain tissue, which is highly elastic and inhomogeneous, especially in tumor areas. Even in healthy regions, different parts deform unevenly under the same load, causing sudden phase jumps between neighboring voxels and making phase unwrapping more challenging. Although numerous unwrapping algorithms have been proposed, many encounter difficulties correcting rapid, large inter-frame phase variations. Moreover, since a focused air pulse is used to load the sample, considerable tissue movement occurs, increasing the likelihood of significant phase jumps.

To address these challenges, the 2π ambiguities are first determined using a simple linear extrapolation $\gamma_{x,y}(t)$ at time t:

$$\gamma_{x,y}(t) = \varphi_{x,y}(t-1) + \frac{\varphi_{x,y}(t-1) - \varphi_{x,y}(t-2)}{\Delta t}. \tag{3.3}$$

Since the time difference $\Delta t = (t-1) - (t-2)$ between two successive time points is always equal to one, it can be neglected. Then the necessity of a positive or negative 2π correction is determined by evaluating the position of the extrapolation point $\gamma_{x,y}(t)$ and the wrapped phase $\phi_{x,y}(t)$:

$$j_{x,y}(t) = \begin{cases} 1, & \gamma_{x,y}(t) > \phi_{x,y}(t) \\ -1, & \gamma_{x,y}(t) < \phi_{x,y}(t) \end{cases}. \tag{3.4}$$

Afterward, the integer $q_{x,y}(t)$ that minimizes the difference between $\phi_{x,y}(t)$ and the anticipated phase value $\gamma_{x,y}(t)$ is determined (see exemplary data in Figure 3.4 under "Linear extrapolation"):

$$q_{x,y}(t) = \left[\frac{\gamma_{x,y}(t) - \phi_{x,y}(t)}{j_{x,y}(t) \cdot 2\pi}\right]. \tag{3.5}$$

Equation 2.49, $q_{x,y}(t)$ and $j_{x,y}(t)$ are used to calculate the unwrapped phase $\varphi_{x,y}(t)$. A refractive index of 1.46 was assumed for all PVA phantom measurements [131] and 1.36 for all *ex vivo* brain measurements [132]. In a subsequent evaluation step, the need for additional corrective actions is assessed. A common approach to analyze a signal is by examining its first derivative, which can reveal discontinuities or abrupt changes. If specific criteria are met, corrective actions are performed:

1. Does the temporal evolution of the phase signal Evo remains consistent after a $\pm 2\pi$ correction? This step assesses whether the correction leads to a decrease or increase of the phase and checks if it aligns with the initially determined direction $j_{x,y}(t)$:

$$Evo_{x,y}^{+2\pi}(t) = \begin{cases} -1, & \varphi_{x,y}(t-1) > \varphi_{x,y}(t) + 2\pi \\ 0, & else \end{cases}, \tag{3.6}$$

$$Evo_{x,y}^{-2\pi}(t) = \begin{cases} 1, & \varphi_{x,y}(t-1) < \varphi_{x,y}(t) - 2\pi \\ 0, & else \end{cases}, \tag{3.7}$$

$$Evo_{x,y}^{\varphi}(t) = \begin{cases} 1, & j_{x,y}(t) == Evo_{x,y}^{+2\pi}(t) \\ -1, & j_{x,y}(t) == Evo_{x,y}^{-2\pi}(t) \\ 0, & else \end{cases}. \tag{3.8}$$

2. Is there a monotonous rise or fall $Mono^{Rise/Fall}$ in the signal over the last five frames? If the sign of the last five derivatives remains consistently positive or negative, it indicates a monotonic rise or fall of the phase within this interval:

$$Mono_{x,y}^{Rise}(t) = \begin{cases} 1, & sgn\left(\dot{\varphi}_{x,y}(n)\right) == 1 \\ 0, & else \end{cases}, \tag{3.9}$$

$$Mono_{x,y}^{Fall}(t) = \begin{cases} 1, & sgn\left(\dot{\varphi}_{x,y}(n)\right) == -1 \\ 0, & else \end{cases}, \tag{3.10}$$

with $\dot{\varphi}(n) = \frac{\partial \varphi(n)}{\partial n}$ and $t-5 \leq n \leq t-1$.

3. Is the first derivative of the phase within the last two B-scans greater than π? This indicates a significant change in speed:

$$Signi_{x,y}^{Vel}(t) = \begin{cases} 1, & \left|\dot{\varphi}_{x,y}(t-1)\right| > \pi \\ 0, & else \end{cases}. \tag{3.11}$$

4. Is the first derivation or velocity Vel^{Inc} increasing? It denotes that the derivate of the signal is becoming steeper, implying an acceleration of the phase signal:

$$Vel_{x,y}^{Inc}(t) = \left|\dot{\varphi}_{x,y}(t-1)\right| > \left|\dot{\varphi}_{x,y}(t-2)\right|. \tag{3.12}$$

It is evaluated whether conditions 1, 2, and either 3 or 4 are fulfilled:

$$Dec_{x,y}(t) = \left(Evo_{x,y}^{\varphi}(t) == 1\right) \wedge Mono_{x,y}^{Fall}(t) \wedge \left(Signi_{x,y}^{Vel}(t) \vee Vel_{x,y}^{Inc}(t)\right), \tag{3.13}$$

$$Inc_{x,y}(t) = \left(Evo_{x,y}^{\varphi}(t) == -1\right) \wedge Mono_{x,y}^{Rise}(t) \wedge \left(Signi_{x,y}^{Vel}(t) \vee Vel_{x,y}^{Inc}(t)\right). \tag{3.14}$$

If the requirements are met, the sign of the first derivate $D_{x,y}^{\varphi}$ with sgn: $\mathbb{R} \rightarrow \{-1, 1\}$ is initially evaluated to detect an abrupt direction change of the signal:

$$D_{x,y}^{\varphi}(t) = \begin{cases} 1, & sgn\left(\left[\dot{\varphi}_{x,y}(t)\right]\right) \neq sgn\left(\left[\dot{\varphi}_{x,y}(t-1)\right]\right) \\ 0, & sgn\left(\left[\dot{\varphi}_{x,y}(t)\right]\right) = sgn\left(\left[\dot{\varphi}_{x,y}(t-1)\right]\right) \end{cases}. \tag{3.15}$$

An exemplary data set under “Rapid direction shift" relevant to this step is illustrated in Figure 3.4. The displacement curve exhibits a sudden positive jump, accompanied by a corresponding change in the direction of the first derivative. However, in the -2π scenario, this abrupt change is no longer apparent, confirming the appropriateness of applying a -2π correction in this specific case.

For a more comprehensive analysis, examining higher-order derivatives is beneficial, as they provide additional insights into signal behavior and enable the detection of more

complex motion patterns. Therefore, the third-order partial derivative is also evaluated to identify subtle phase ambiguities. A zero value implies that the derivative's rate of change is constant, while the opposite is valid for a non-zero value. Given the applied air-jet force and the 2.45 kHz frame rate, corresponding to a time of 0.4 ms between two B-scans, a steady force or acceleration is anticipated, except during the rising edge of the air-jet. Thus, any significant jerk in the phase signal is only likely during this period. However, the high frame rate should limit any observed jerk to a minimum. Assuming mostly constant acceleration, the displacement should exhibit minimal jerk over time:

$$Jerk_{x,y}(t) = \begin{cases} 1, & \left|\left|\dddot{\varphi}_{x,y}(t)\right|\right| \neq 0 \\ 0, & \left|\left|\dddot{\varphi}_{x,y}(t)\right|\right| = 0 \end{cases}, \tag{3.16}$$

$$q_{x,y}(t) = \begin{cases} q_{x,y}(t) - 1, & Inc_{x,y}(t) \wedge \left(D^{\varphi}_{x,y}(t) \vee Jerk_{x,y}(t)\right) \\ q_{x,y}(t) + 1, & Dec_{x,y}(t) \wedge \left(D^{\varphi}_{x,y}(t) \vee Jerk_{x,y}(t)\right) \end{cases}, \tag{3.17}$$

with $\dddot{\varphi}(t) = \frac{\partial^3 \varphi(t)}{\partial t^3}$. Equations 3.16 and 3.24 include methods to control and reduce the jerk in the phase signal. Figure 3.4 presents an exemplary dataset under "Minimize jerk" for clarity. The estimated phase exhibits a lower jerk than the $\pm 2\pi$ scenario, confirming that no further adjustments are necessary.

The impact of the estimated $q_{x,y}(t)$ value on the phase progression is then examined using an environment-aware predictive approach. Since an incorrect correction distorts the phase values of all subsequent ones, this method enables the identification and rectification of such errors. In the estimated case, a forecast is initially made for a phase value at time $t + 1$. To utilize Equation 2.49 again, it is necessary to calculate the parameters $j_{x,y}(t + 1)$ and $q_{x,y}(t + 1)$, involving a computation of $\gamma_{x,y}(t + 1)$ using the steps outlined in Equations 3.3 to 3.5. These steps are then repeated for the time $t + 2$. Various tests have shown that two predicted phase values are sufficient for reliable error detection. However, adjusting the algorithm to different needs may involve considering varying numbers of forecasted phase values, requiring suitable algorithm adaptations. Also, the effects of a $\pm 2\pi$ correction at time t are evaluated with this method. ξ^{est}indicates the predicted phase values for the estimated case. At the same time, $\xi^{+2\pi}$ and $\xi^{-2\pi}$represents the phase response after performing a $\pm 2\pi$ correction on the estimated phase value, respectively (see example data in Figure 3.4 under "Forecast future positions").

Next, it is analyzed whether the temporal evolution of the predicted phase signals $PEvo$ remains unchanged after performing a $\pm 2\pi$ correction. The results are compared with the initially determined phase direction:

$$PEvo_{x,y}^{\gamma}(t) = \gamma_{x,y}(t) - \varphi_{x,y}(t-1)\,, \tag{3.18}$$

$$PEvo_{x,y}^{+2\pi}(t) = sgn\left(\dot{\xi}_{x,y}^{+2\pi}(n)\right), \tag{3.19}$$

$$PEvo_{x,y}^{-2\pi}(t) = sgn\left(\dot{\xi}_{x,y}^{-2\pi}(n)\right), \tag{3.20}$$

$$PEvo_{x,y}^{\varphi}(t) = \begin{cases} 1, & PEvo_{x,y}^{\gamma}(t) == PEvo_{x,y}^{+2\pi}(t) \\ -1, & PEvo_{x,y}^{\gamma}(t) == PEvo_{x,y}^{-2\pi}(t) \\ 0, & else \end{cases}, \tag{3.21}$$

with $\dot{\xi}(n) = \frac{\partial \xi(n)}{\partial n}$ and $t \le n \le t+2$.

The most likely phase progression case is determined by calculating the first derivative of the predicted phase values for all potential scenarios $\dot{\xi}^{est/+2\pi/-2\pi}$. Then, the median value of all pixels within $\dot{\xi}^{est}$ is calculated. This median value is compared with $\dot{\xi}^{est/+2\pi/-2\pi}$ at each pixel (x, y), giving the absolute difference from the median $MD_{x,y}^{est/+2\pi/-2\pi}(t)$:

$$MD_{x,y}^{est/+2\pi/-2\pi}(t) = \left| \dot{\xi}_{x,y}^{est/+2\pi/-2\pi}(n) - median\left(\dot{\xi}^{est}\right) \right|, \tag{3.22}$$

with $\dot{\xi}(n) = \frac{\partial \xi(n)}{\partial n}$ and $t < n \le t+2$. If $MD_{x,y}^{est}(t)$ is greater than π, additional correction steps are required. The aim is to select a phase whose value is minimal $MinMD_{x,y}^{+2\pi/-2\pi} = \left(\left[MD_{x,y}^{+2\pi/-2\pi}(t)\right] == 0\right)$, and where the temporal evolution of the predictive phase values resembles the initially determined phase direction:

$$q_{x,y}(t) = \begin{cases} q_{x,y}(t) - 1, & \left(PEvo_{x,y}^{\varphi}(t) == 1\right) \wedge MinMD_{x,y}^{+2\pi} \wedge \neg Jerk_{x,y}(t) \\ q_{x,y}(t) + 1, & \left(PEvo_{x,y}^{\varphi}(t) == -1\right) \wedge MinMD_{x,y}^{-2\pi} \wedge \neg Jerk_{x,y}(t) \end{cases}. \tag{3.23}$$

Furthermore, as previously described, an additional step is necessary to minimize the jerk in the phase signal (see Equation 3.16). Therefore, an error check based on the MD values is conducted:

$$q_{x,y}(t) = \begin{cases} q_{x,y}(t) - 1, & \left(\left[MD_{x,y}^{+2\pi}(t)\right] < \left[MD_{x,y}^{-2\pi}(t)\right]\right) \wedge Jerk_{x,y}(t) \\ q_{x,y}(t) + 1, & \left(\left[MD_{x,y}^{-2\pi}(t)\right] < \left[MD_{x,y}^{+2\pi}(t)\right]\right) \wedge Jerk_{x,y}(t) \end{cases}. \tag{3.24}$$

The signal is unwrapped by applying this process to each frame, allowing the true phase to be determined over time.

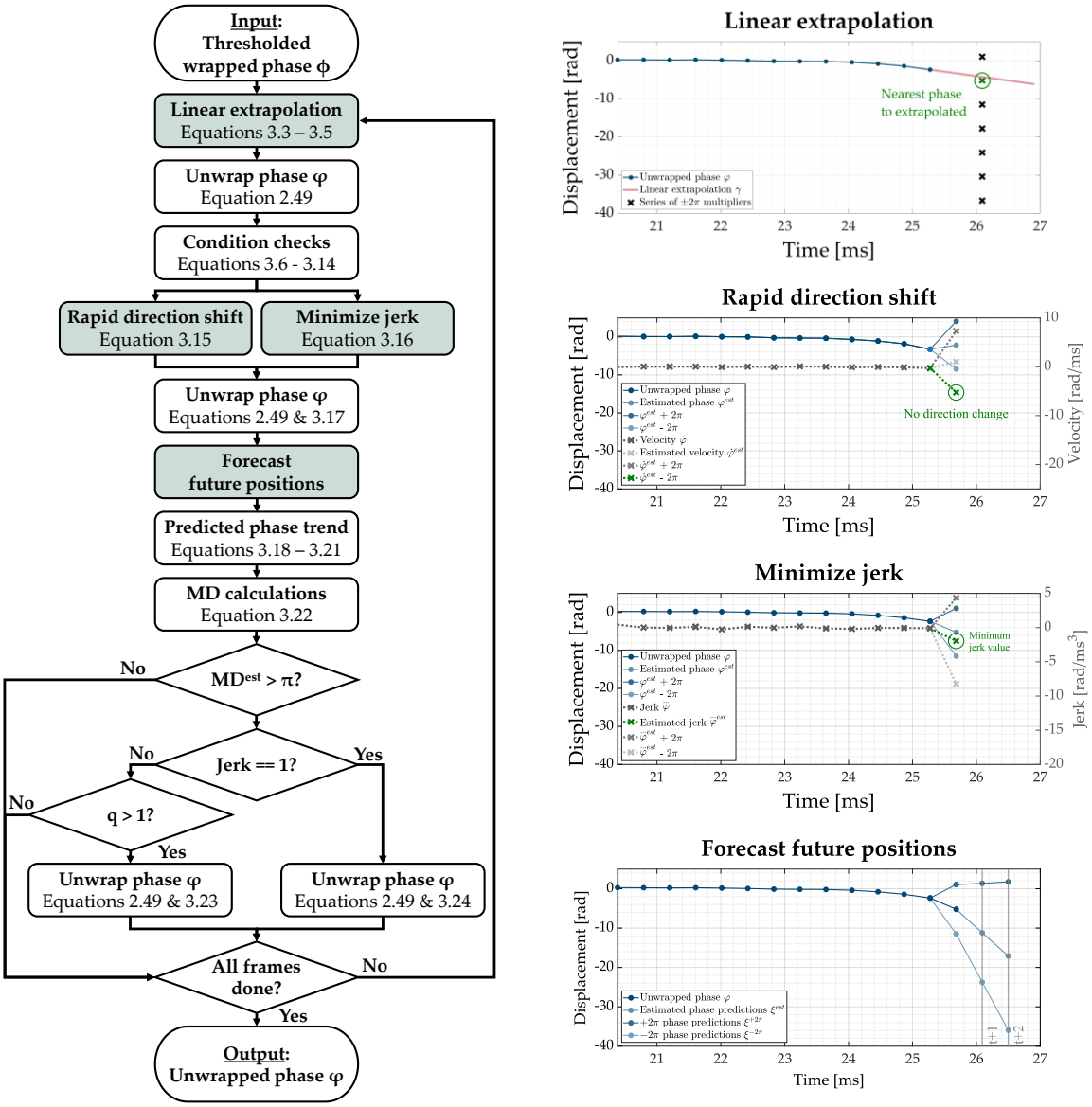

Figure 3.4 Flowchart of the phase unwrapping algorithm. The plots on the right illustrate examples corresponding to the steps highlighted in green. Adapted from [87].

3.5.3 Outlier detection using a local median filter

Since the phase data is highly sensitive, and accurate results for the entire sample are essential for subsequent tissue analysis and assessment, a post-processing step is necessary to eliminate any remaining random aberrations. Therefore, a local median filter detects and corrects single outliers. The post-processing procedure starts by calculating the phase difference between each pixel and its immediate vertical neighbor in the last frame of the acquired OCT dataset. This step helps to identify significant deviations that may indicate noise or other phase irregularities. If the phase difference between two adjacent pixels exceeds a threshold of π, it is considered an outlier. Once identified, these outliers are corrected using a 5x5 sliding median window, where the median value of the surrounding

pixels is used to replace the outlier. The significant advantage of this approach is that, unlike global smoothing techniques, only local outliers are corrected without losing structural information by smoothing the entire image.

3.6 Experimental setup validation

3.6.1 Phase stability analysis

To investigate the phase noise ϕ_{noise} of the experimental 3.2 MHz-OCT setup, a measurement was performed on a stationary PVA phantom without applying any mechanical load. Subsequently, the phase data were unwrapped using the standard MATLAB unwrap function (The MathWorks, Natick, Massachusetts, USA). The results are presented in Figure 3.5. The left part of Figure 3.5 shows the phase progression of different pixel positions within the central A-scan, spaced 40 pixels apart in depth. The blue curve corresponds to the lowest depth, while the green curve represents the highest depth. The right part of Figure 3.5 illustrates the phase difference, denoted as $\Delta\phi_{noise}$, between the first and all subsequent depths in time. It simulates the situation where a reference reflection is used to unwrap the phase information.

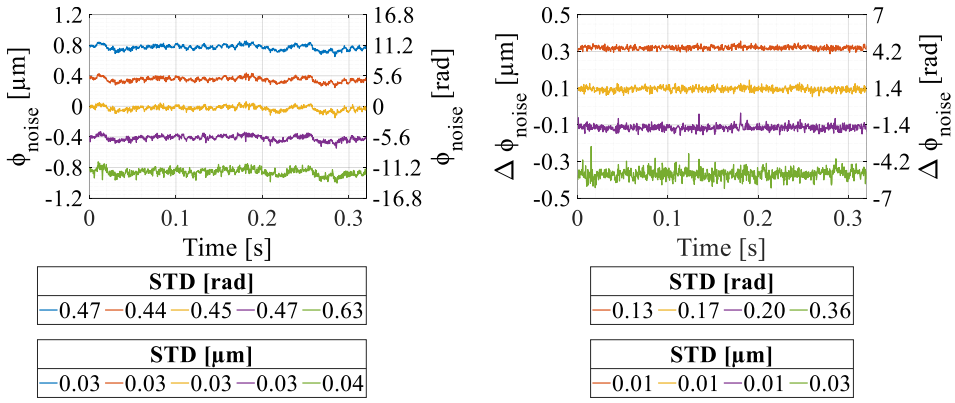

Figure 3.5 Analysis of the phase stability of the MHz-OCT setup. One measurement was taken on a PVA phantom without applying any mechanical load. The left part shows the phase progression of different pixel positions within the central A-scan, spaced 40 pixels apart. The blue curve corresponds to the lowest depth, while the green curve represents the highest depth. The phase difference between the first depth and all subsequent ones is shown on the right side. For better visualization, artificial offsets were set. The standard deviation (STD) is shown in rad and µm. Adapted from [87].

The known phase change caused by the reflection can be used as a reference or calibration value to unwrap the signal, as already demonstrated by other groups [86]. The phase noise remains similar at the first three depths but increases with the depth of the examined

phase signal. This trend can also be observed for $\Delta\phi_{noise}$. This is because the signal intensity decreases with increasing sample depth, leading to a reduced SNR and thus higher phase noise. Nevertheless, the standard deviation remains at a comparatively low value of 10 to 30 nm, which is sufficient to resolve mechanically relevant displacements in the tissue.

It should be noted that the phase noise of the entire system is considered. Thus, all influencing factors, such as environmental movements, trigger jitter, electronic noise, and clocking instability, are included. Many additional factors influence the real phase instability, resulting in a phase noise value higher than the mathematically calculated ideal value. However, a high phase stability of the system is an essential requirement for obtaining displacement maps, regardless of the correction algorithm applied. The results indicate that the MHz-OCT setup has a remarkably low $\Delta\phi_{noise}$ value, indicating no global timing jitter, which is usually a problem with SS-OCT systems.

3.6.2 Detection of structural inhomogeneities

Various measurements were performed on an inhomogeneous PVA phantom to investigate whether different structures within the tissue can be detected. For this, the surrounding matrix with a Young's modulus of 820 Pa, the PVA inclusion with an elastic modulus of 2.26 kPa, and the transition between the two were measured with a peak force of 33 µN. Figure 3.6 shows the *en face* sample projections, the 20-times average B-scans taken from the 3D volume, and the displacement maps. Red areas on the maps show lower displacement, while blue areas indicate higher displacement. The line scans were conducted along the orange line.

The displacement maps show a striking contrast. The surrounding matrix exhibits a larger displacement, represented by the blue color, while the PVA inclusion displays a comparatively smaller indentation, indicated by a yellow-greenish color in the displacement map. A similar color representation is observed when the transition from the surrounding matrix to the inclusion is measured. Therefore, the pseudo-colored displacement maps identify the different PVA structures. Since the results display the sample displacement obtained directly from the phase information, the force profile of the excitation source can be observed in the surrounding PVA matrix. This means that the measured displacements reflect both the local mechanical properties and the spatial distribution of the applied force. To obtain a pure representation of the tissue mechanics, the force profile has to be corrected. However, the presented OCE imaging method and phase unwrapping algorithm enable effective visualization and identification of different mechanical properties of the PVA phantom.

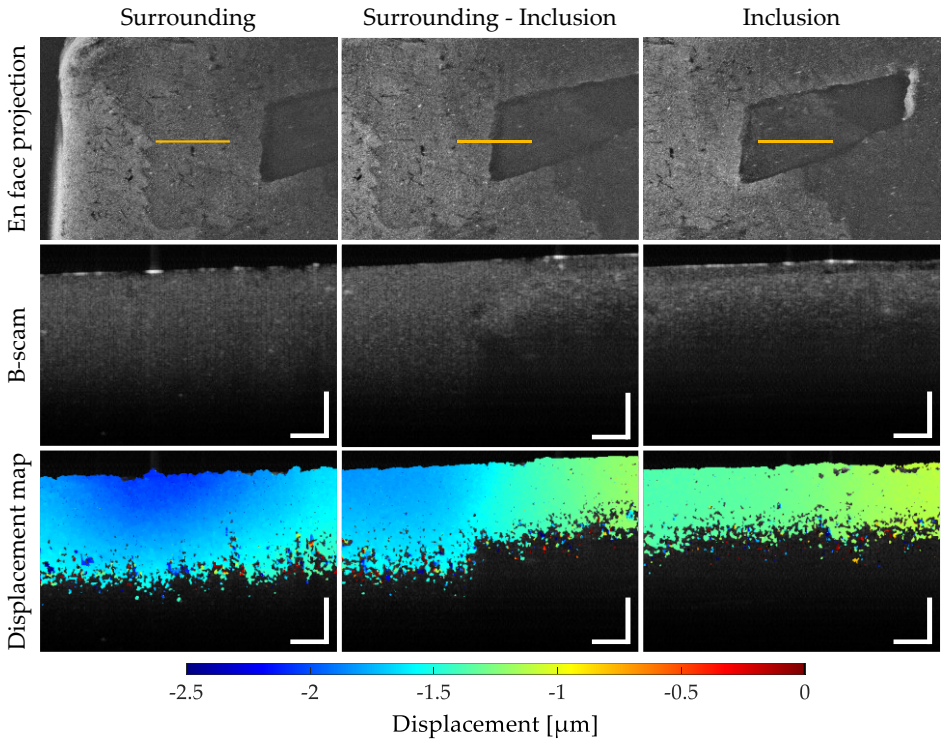

Figure 3.6 Evaluation of irregularity detection using inhomogeneous PVA phantoms. A composite image of the *en face* projections, the 20 times averaged B-scans of the scan position taken from the 3D volume, and the corresponding displacement maps are shown. Measurements were performed on the surrounding PVA matrix, the PVA inclusion, and the transition region between these two structures. The line scans were acquired along the orange line. Each scale bar corresponds to a length of 500 µm. Adapted from [87].

Similar measurements were also conducted on an *ex vivo* brain tumor sample using an air-jet excitation with an estimated peak force of approximately 30 µN. The experiments focused on both gray matter and the transition between gray and white matter. Given that different brain regions are known to exhibit distinct biomechanical properties [46], the aim was to evaluate whether mechanical differences in biological tissue can also be detected with the current setup. Figure 3.7 shows the corresponding results. It includes a photograph of the sample, the corresponding displacement maps, and 20 times averaged B-scans from a previously acquired volume at the same position for speckle reduction.

A clear difference in mechanical response was observed between gray and white matter in the displacement map. The gray matter showed noticeably larger displacements than the white matter. However, when imaging only the gray matter, the displacement map did not appear uniform. This is likely due to the uncorrected force distribution of the air-jet, which resulted in a visible Gaussian-shaped profile in the central region. This effect is especially pronounced here because the tissue is soft and mostly homogeneous.

These findings extend the results from phantom experiments to biological tissue, demonstrating that MHz-OCE can reliably detect local mechanical differences in *ex vivo* brain samples. Despite minor artifacts caused by the uncorrected air-jet excitation profile,

the imaging approach enabled consistent mapping. These artifacts could potentially be corrected through numerical compensation, provided the force distribution of the excitation is accurately characterized.

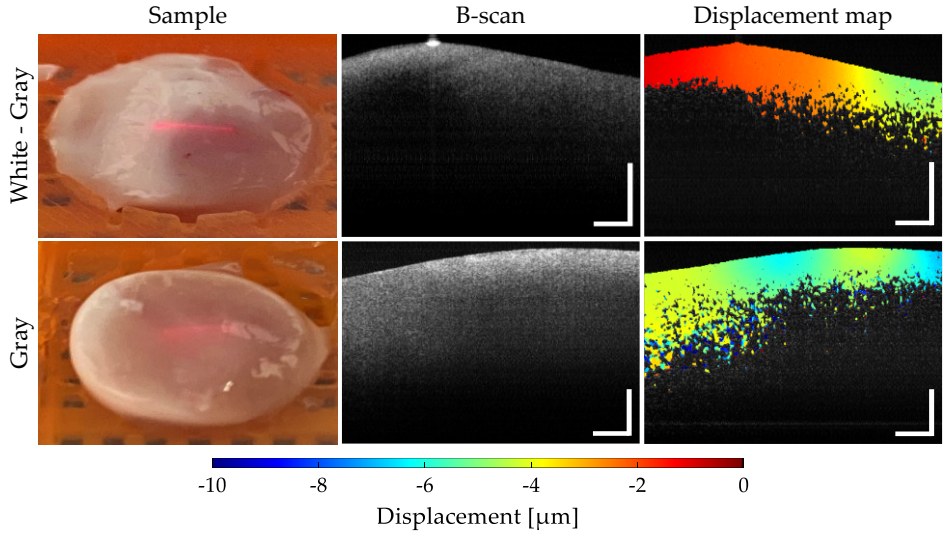

Figure 3.7 Detection of structural irregularities in *ex vivo* porcine brain tissue. The two rows show different brain regions. The top row shows the transition between gray and white matter, while the bottom row shows a brain region consisting mainly of gray matter. A photo of the sample, the 20 times averaged B-scans taken from a previously acquired 3D volume at the same scan positions, and the corresponding displacement maps are shown. The scale bar corresponds to 500 µm.

3.6.3 Reproducibility and consistency evaluation

After confirming the ability to visualize different structures within a tissue, the next step was to investigate the capability to obtain reproducible results. For this purpose, four measurements were performed in direct succession on an inhomogeneous PVA phantom and on an *ex vivo* WHO grade II meningioma brain tumor sample with an applied peak force between 30 and 32 µN. The applied force values for each measurement are provided in Figure 3.8.

The first column illustrates the measurement results obtained with the PVA phantom. Following the methodology used in the previous chapter, the transition between the surrounding matrix and the PVA inclusion was measured and plotted. Referring to Figure 3.8, a clear distinction is evident based on the color representation. Three additional measurements were taken at the same location to demonstrate the algorithm's reproducibility. In addition, four measurements were performed at two distinct positions of the *ex vivo* brain tumor sample. Again, a clear differentiation within the heterogeneous tissue can be observed. The difference between the first and subsequent measurements was determined to quantify reproducibility. The mean difference and the standard error of the

mean were then calculated. The determined variations were as follows: 249 ± 87 nm for the phantom, 132 ± 12 nm for meningioma brain tumor position 1, and 268 ± 7 nm for meningioma brain tumor position 2.

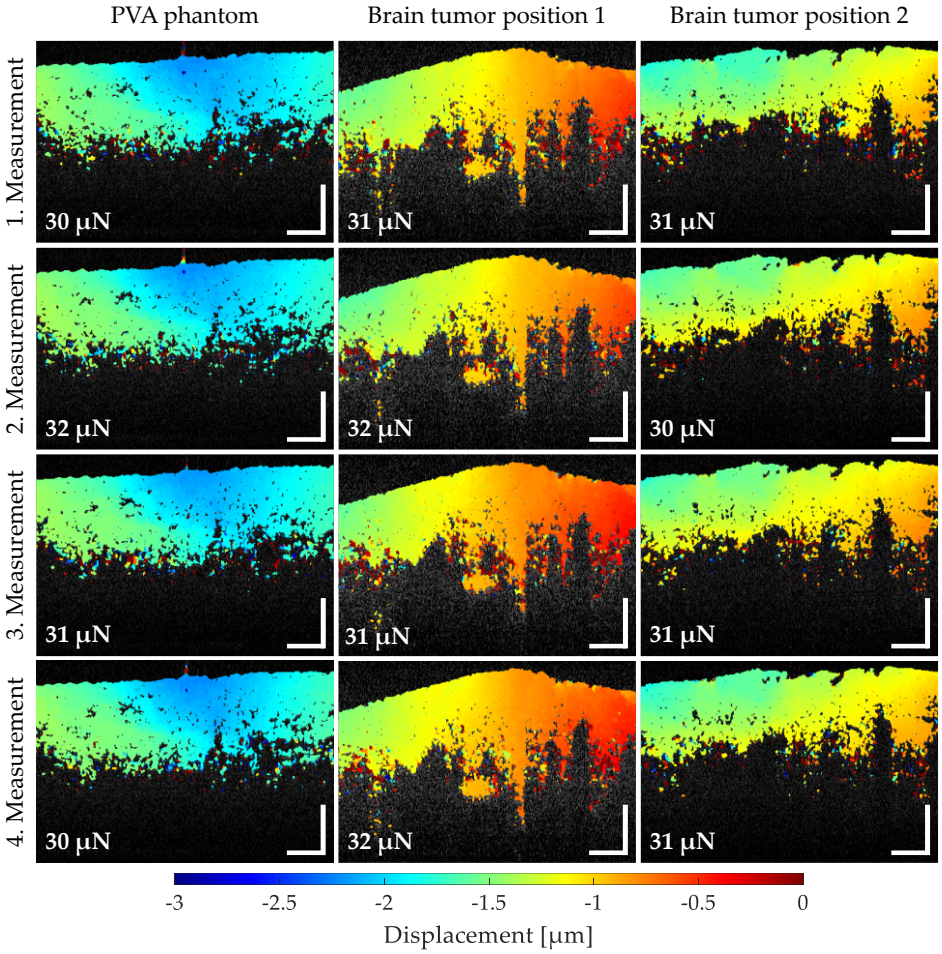

Figure 3.8 OCE reproducibility measurements on phantom and brain tumor samples. Measurements were performed on a PVA phantom (first column) and an *ex vivo* WHO grade II meningioma brain tumor sample (second and third columns). The brain tumor sample was examined at two different positions. Four measurements were taken at each position in immediate succession. The corresponding displacement maps at the time of maximum load are shown. The applied force is indicated for each measurement. Each scale bar is equal to 500 µm. Adapted from [87].

Therefore, the repeated measurements show remarkably consistent results, indicating high reproducibility. It should be noted that slight variations may occur due to the successive measurements, as repeated measurements can cause minor deviations and changes. However, the results indicate that the algorithm can accurately identify and visually present displacement differences across several iterations.

3.6.4 Impact of elastic moduli and forces on sample displacement

For validations, measurements were also conducted on homogeneous PVA phantoms with varying elastic moduli ranging from 875 Pa to 16.38 kPa and a mechanical load between 31 and 33 µN. The applied force values for each measurement are given in Figure 3.9, together with the corresponding displacement maps and the unaveraged B-scan.

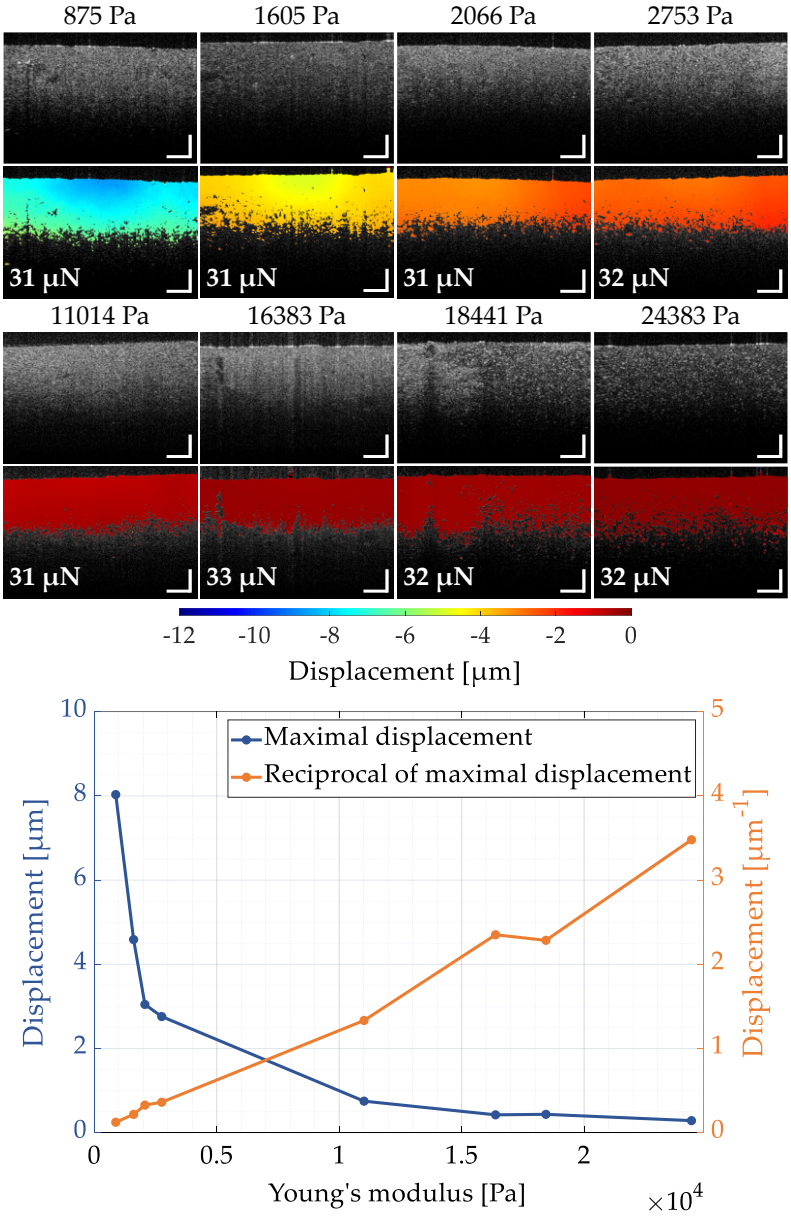

Figure 3.9 Sample displacement examination using homogeneous PVA phantoms. The effect of applying a constant force (31 - 33 µN) to eight PVA phantoms with elastic moduli from 875 Pa to 24.38 kPa is shown. For each measurement, the applied force, displacement maps, and the unaveraged B-scan are displayed. The diagram presents the median displacement of the central A-scan at maximum load, with sample displacement in blue and its reciprocal in orange. The scale bar indicates 500 µm. Modified from [87].

It is evident from the figure that the determined displacement decreases with increasing elastic moduli. Furthermore, unlike the inhomogeneous datasets in subsection 3.6.2, the maps exhibit a nearly homogeneous sample displacement over the entire scanning range. However, again, the force profile of the air-jet is noticeably visible, especially for the softer phantoms.

In addition, the median displacement of the different phantoms was evaluated for the central A-scan and at maximum load to enable the data comparison without needing a force profile correction. The force $F = k \cdot x$ can be determined by the spring constant k and the displacement x. Assuming a constant force F, it can be derived that $k = 1/x$. The plot shows the maximum displacement in blue and its reciprocal in orange as a function of the Young's modulus of the PVA samples.

The blue curve shows an exponential decrease in displacement as the stiffness of the phantom increases. The observed linear trend of the reciprocal emphasizes that we operate within the linear range of the stress-strain curve, highlighting the significance of using phase-sensitive OCT. Accordingly, apart from the requirement for a sufficiently high sample-dependent force, there is also the need for the lowest possible force, particularly in the case of highly viscoelastic and nonlinear brain tissue.

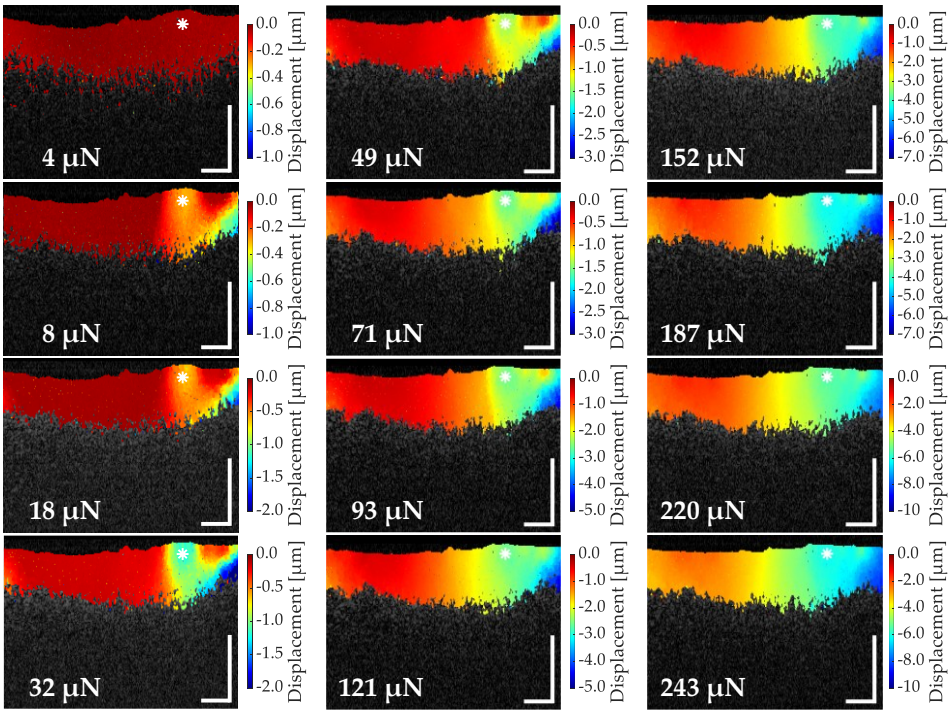

Figure 3.10 Displacement maps of a WHO grade I meningioma under increasing load. The displacement maps illustrate the maximum indentation per pixel obtained at different forces between 4 and 243 µN. The scale bars are equal to 500 µm. Adapted from [87].

At a specific pixel position, indicated by a white star in the maps, Figure 3.11A illustrates the phase progression over the entire acquisition time. The graph shows that the

maximum indentation of the sample increases with a higher load, which corresponds very well with the theory of a material with linear stiffness. For a more detailed analysis, the displacement at the time of maximum indentation was plotted against the applied force, illustrated in Figure 3.11B in gray.

The results obtained reveal a noticeable non-linear trend curve. A linear fit (shown in red) was added to the graph for better clarification. It is worth noting that the curve shows a decreasing trend for forces above approximately 187 µN. The sample displacement curve should be distinguishable from the noise floor to determine mechanical parameters precisely. In Figure 3.11A, these features can be seen at a force of 71 µN and above. Figure 3.11B shows that the linear regime persists up to an indentation of 3.61 µm for that specific sample type during the maximum load from the air-jet.

Since the required force depends strongly on the sample, this emphasizes the necessity of using appropriate, sufficiently high sample-dependent forces and a suitable phase correction algorithm. As reproducible results are obtained, the observed contrast can be reliably determined.

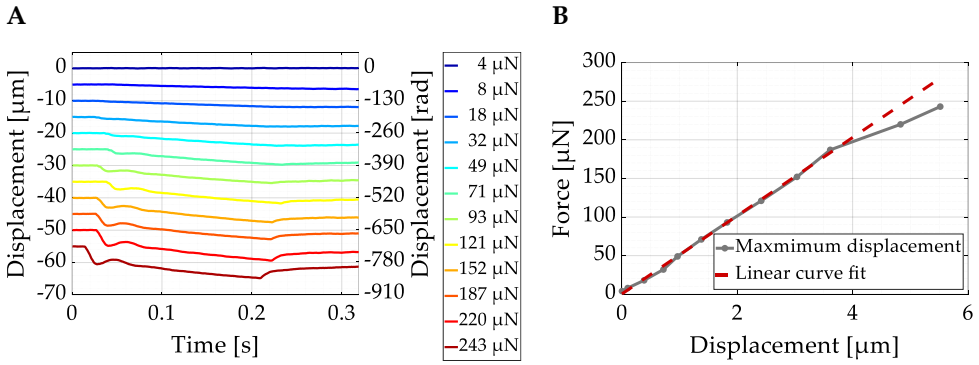

Figure 3.11 Force-dependent phase progression and displacement analysis. A: Phase progression over the entire acquisition time at a specific pixel position marked by a white star in the displacement maps in Figure 3.10. Each color represents a different mechanical load. Artificial offsets were added for better visualization. B: Corresponding displacement-force at the time of maximum load (gray) and linear curve fit (red). The force applied is specified for every measurement. Adapted from [87].

3.7 Linking tissue morphology and mechanical properties

3.7.1 Sample preparation and histological correlation

3D-printed molds containing two cylindrical elevations with a diameter of 12 mm were used to ensure a uniform shape of the tumor samples and to allow accurate correlation with histologic evaluations. These molds were placed in biopsy embedding cassettes (Sanowa Laborprodukte GmbH, Germany) and filled with liquid agar. After the agar had cooled, the molds were removed. The tumor samples were cut into 12 mm segments with

a punch and placed in these wells for future correlation of the OCE data and the histological sections. After imaging, the left half of the acquired line scan was labeled with green histological dye (WAK HM G 1/60, WAK Chemie Medical GmbH, Germany).

Subsequently, the samples were embedded in paraffin and stained with hematoxylin & eosin (H&E). Ten sections were taken along the marked line at 200 µm distances to ensure a histological image of the acquired line scan and to enable histopathological evaluation. The slides were then digitized (VENTANA iScan HT, Roche Holding AG, Switzerland), registered, and correlated with the acquired OCT images. A thorough explanation of the registration technique is available in the work published by Strenge et al. [133]. Since the green histological dye is only visible on the left side of the sample surface, the orientation of the histological image could be determined and retrospectively correlated with the sample position during acquisition. The histological evaluation was performed by experienced pathologists.

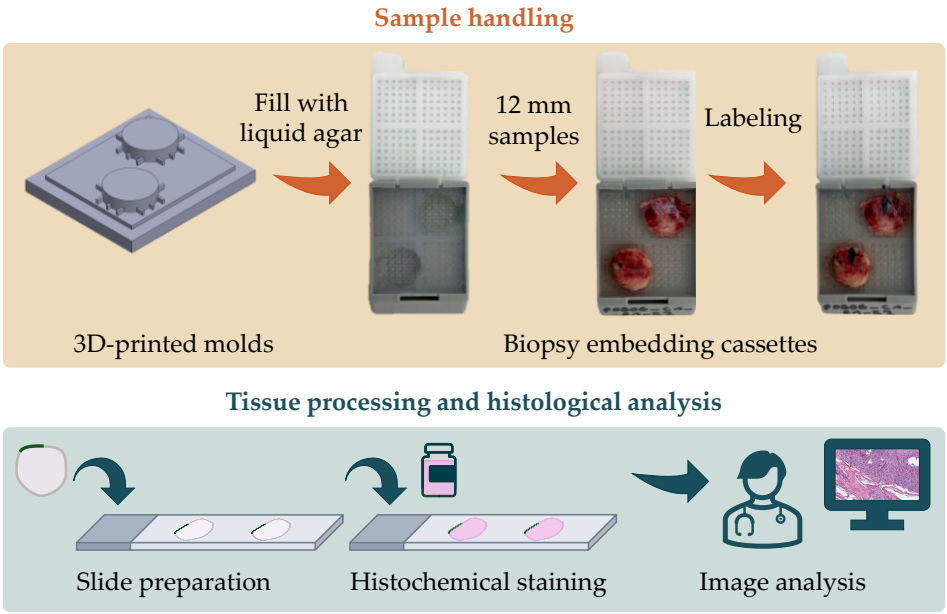

Figure 3.12 Tissue processing pipeline for correlated imaging and histology. The upper panel depicts the sample handling process, where tumor tissue is shaped using 3D-printed molds, embedded in agar within biopsy cassettes, and labeled to maintain orientation. The lower panel illustrates the post-imaging workflow, which includes slide preparation, histochemical staining, and digital histological analysis to achieve spatial correlation with the OCT data.

3.7.2 Stiffness mapping in *ex vivo* brain: meningioma and healthy sample

An *ex vivo* WHO grade I meningioma brain tumor sample was subjected to histological analysis under a mechanical load of 87 µN to correlate findings from mechanical imaging with histological features. A photograph and an *en face* projection of the sample are shown in Figure 3.13A and B, respectively. Line scans were conducted along the orange line. The

resulting 20 times averaged intensity image, extracted from the 3D volume, is displayed in Figure 3.13C. The respective H&E-stained histological image and stiffness map of the scan area are given in Figure 3.13D and Figure 3.13E.

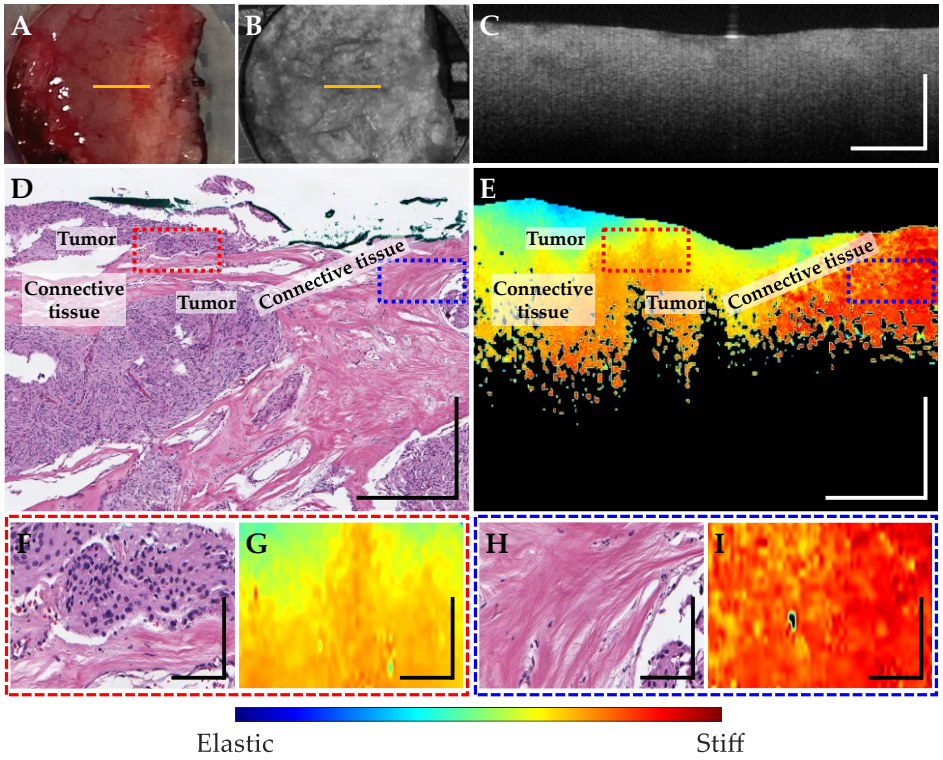

Figure 3.13 Correlation of histology and displacement of a meningioma brain tumor. Photo (A) and *en face* projection (B) of the sample. Line scans were obtained along the orange line. C: 20 times averaged OCT B-scan taken from the 3D volume. Corresponding histological section (D) and registered stiffness map (E). F - I: Enlarged views of (D) and (E) at the red and blue outlined rectangle. In all images, the scale bars represent 500 µm, except in magnified views, where they denote 100 µm. Adapted from [87].

For initial tests, the stiffness $k_{x,y}(t)$ was determined by dividing the sample displacement at the time of maximum indentation $\Delta d_{x,y}(t)$ by the corresponding force of the air-jet $F_{x,y}(t)$:

$$k_{x,y}(t) = F_{x,y}(t)/\Delta d_{x,y}(t). \tag{3.25}$$

The sample displacement obtained directly from the phase information was used without applying any additional correction steps. After normalization, adaptive histogram equalization was applied to the stiffness data to enhance the visual distinction between different structural components in the map. Consequently, the values presented are considered pseudo-values. Again, a rainbow color spectrum was used to improve the visual representation of the stiffness variations, where red signifies high stiffness and blue indicates low stiffness. As mentioned in the previous chapter, a nonlinear image transformation

was applied to the stiffness map to ensure precise overlay with the accompanying histological image.

In the H&E-stained image, dense and irregular connective tissue surrounds the tumor predominantly on its right side. They can be identified by their light pink staining, elongated structures, and low nucleus density. The connective tissue consists of collagen fibers and other proteins that support and stabilize the surrounding tissue. These characteristics give the tissue a higher stiffness and, as a result, greater resistance to deformation. The adjacent tissue is the tumor, distinguished by its darker staining and high nucleus density. It should be noted that the paraffin embedding of the tissue samples resulted in visible fissures and may have caused small sections to be missing from the surface.

The stiffness map identifies the connective tissue, which has a significantly higher stiffness than the tumor tissue in the upper left region. Furthermore, the map follows the diagonal orientation of the connective tissue. Figure 3.13F/G and H/I provide a magnified view of the two regions indicated by a red and a blue rectangle. The red-outlined region shows the boundary between the connective and tumor tissue. This boundary is also visible in the stiffness map, where the connective tissue appears stiffer in the lower, reddish region. Simultaneously, the tumor seems more elastic in the upper, bluish area. The enlarged region highlighted in blue marks another boundary between different tissue types. In this case, the entire region appears red and stiff since the tumor tissue is surrounded by connective tissue. Thus, the results show that the phase contrast generated by the algorithm can precisely and reliably detect structural variations within the tissue.

In addition, a healthy human *ex vivo* brain sample was analyzed under a mechanical stress of 70 μN. The tissue originated from a region of healthy brain that was unintentionally removed along with the tumor during surgery, as the tumor was located directly beneath it. This small part of the brain tissue remained connected to the resected tumor sample and was then cut out and imaged. Histological analysis confirmed the presence of a healthy brain structure, characterized by low cellular density and the absence of histopathological features indicative of tumor involvement.

The OCE imaging outcomes are shown in Figure 3.14. A photo of the excised tissue is displayed in (A), alongside the corresponding *en face* projection in (B), with the orange line indicating the approximate position of the OCT line scans. Panel (C) shows a 20-times averaged B-scan from the 3D OCT volume, while panel (D) presents the corresponding H&E-stained histological section. The stiffness map is shown in (E), where color coding from blue to red indicates increasing tissue stiffness, similar to the previous figure. Due to a tear near the surface of the sample caused during the sectioning process, it was not possible to automatically register the mechanical data with the corresponding histological section in this case. As a result, manual alignment was performed. However, this is not

critical in this specific case, as the histological section exhibits consistent structural features throughout the sample. The only visible issue is that the surfaces no longer align perfectly, and the scale bars may differ slightly due to imprecise image resizing.

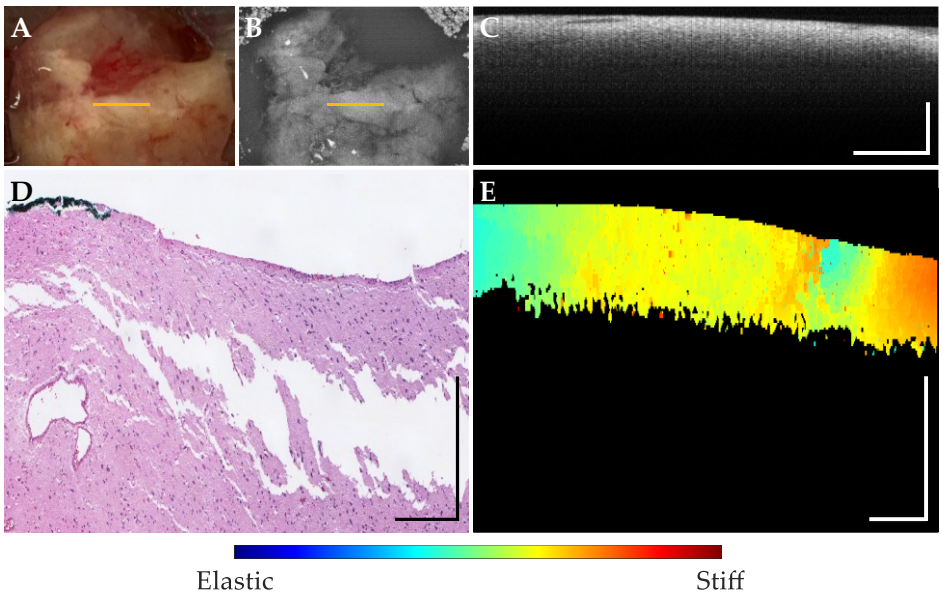

Figure 3.14 Histological and stiffness mapping of healthy human brain tissue. Photo (A) and *en face* projection (B) of the sample. Line scans were obtained along the orange line. C: 20 times averaged OCT B-scan taken from the 3D volume. Corresponding histological section (D) and stiffness map (E). In all images, the scale bars represent 500 μm.

The stiffness map reveals that the sample is largely homogeneous, with only slightly stiffer regions visible near the center and along the right edge. These localized variations are likely caused by imperfect compensation of the air-jet force profile. This effect is particularly pronounced when the sample is soft and homogeneous, as is the case here. Similar observations were made in both the phantom and the porcine brain sample, as shown in the previous chapters.

A comparison between tumor and healthy brain tissue shows a clear difference in their mechanical properties. In the *ex vivo* meningioma sample, the average displacement was 1.26 μm with a standard deviation of 0.48 μm, indicating relatively low and consistent deformation. In contrast, the healthy brain sample showed a significantly higher average displacement of 9.34 μm, with a standard deviation of 0.99 μm. This amounts to more than a sevenfold increase in deformation, consistent with the softer and more homogeneous healthy brain tissue.

3.8 Alternative contrast method using Fourier analysis

3.8.1 Limitations of phase-sensitive OCE contrast approaches

Phase-sensitive OCE offers high sensitivity to tissue displacements, enabling the detection of subtle mechanical features. However, it faces several challenges that limit its accuracy and applicability. As previously discussed, a key issue is the need for phase unwrapping to reconstruct continuous displacement signals. This unwrapping process is computationally intensive and error-prone, and undetected phase jumps during this step can lead to significant distortions in the data. These errors compromise the accuracy of mechanical property estimation and can introduce inaccuracies in the final analysis. The necessity of complex procedures such as phase reconstruction increases computational overhead, resulting in slower processing speeds. This can hinder the ability to perform dynamic or real-time tissue monitoring, which is valuable for diagnostic and intraoperative applications. Furthermore, the lack of standardized protocols and guidelines for data processing presents a significant challenge. This lack of standardization complicates the comparison of findings between different laboratories or studies. Given these challenges, there is a clear need for a method that addresses these limitations while preserving the high sensitivity and specificity derived from the phase information. It should not have computationally intensive steps, should enable real-time tissue monitoring, and be adaptable to different OCT systems and research settings.

3.8.2 Complex signal-based data processing and visualization

To avoid the problems associated with analyzing phase data alone, the complete complex OCT signal, including both amplitude and phase components, was also examined as part of this work. Processing the complete signal rather than relying solely on intensity or phase data enables richer contrast and improved sensitivity. Importantly, this approach eliminates the need for computationally intensive phase unwrapping.

The raw OCT data is first processed according to the steps described in Chapter 2.3.4. Next, the intensity (magnitude) component is removed from the complex signal to isolate the phase-related information. This improves the ability to detect subtle biomechanical changes that would otherwise be masked by intensity fluctuations or speckle noise.

A Hanning window is then applied to reduce spectral leakage, resulting in a clearer, more stable frequency spectrum for analysis. Motion-related variations are then analyzed by using a FFT along the temporal axis of the complex signal. Only the positive frequency components are kept for analysis. At each depth point, the absolute values of the transformed signal are calculated, and frequency bands of interest are selected. These bands

are color-coded in RGB values, with low-frequency components from 0 to 3.6 Hz in blue, intermediate frequencies from 3.6 to 12 Hz in green, and high-frequency components from 12 to 29.9 Hz in red. At the end, an adaptive histogram equalization is applied to improve contrast, with a local median filter used to suppress residual noise and remove outliers. An overview of the data processing workflow is provided in Figure 3.15, and the corresponding implementation code can be found in Appendix A.2.

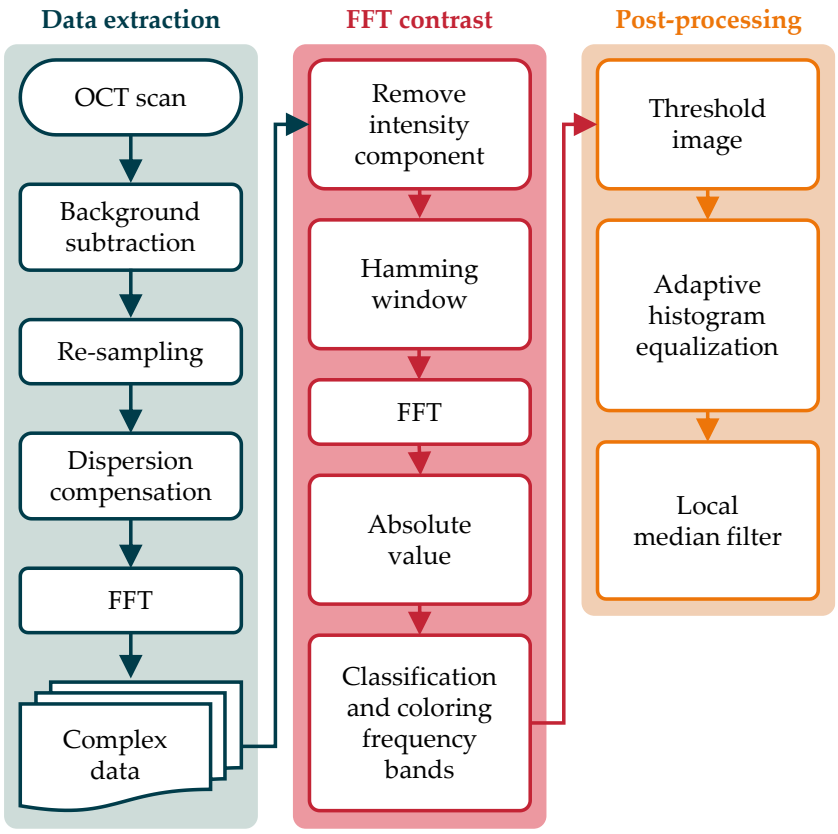

Figure 3.15 Data processing workflow using complex Fourier analysis. The figure shows the overall processing flowchart divided into three main stages: data extraction, FFT contrast, and post-processing.

3.8.3 Comparison with conventional phase-sensitive OCE

Three WHO grade I meningioma brain tumor samples were examined to evaluate the Fourier-based analysis outcomes. Each sample was mechanically loaded with a force of approximately 70 µN. For reference, a ten-times averaged B-scan is provided for each dataset. In addition to the Fourier-based method, the phase information was unwrapped using the algorithm developed in this thesis to allow direct comparison. Displacement maps are visualized using pseudo-coloring, where low displacements are shown in blue, high displacements in red, and intermediate values follow a rainbow gradient. Adaptive histogram equalization was applied to enhance contrast, and all displacement values were normalized to a range between 0 and 1. The results are presented in Figure 3.16.

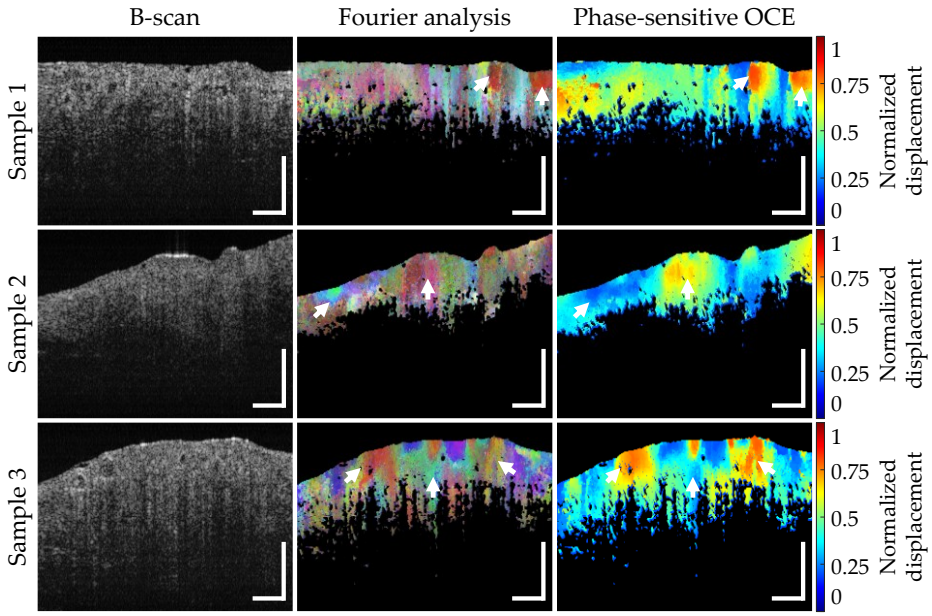

Figure 3.16 Comparison of displacement- and Fourier-based visualization approaches. From left to right, the panels display. The ten-times averaged B-scans, the frequency-based visualization generated from the complex OCT signal, and the normalized displacement map obtained from the unwrapped phase information. White arrows highlight key regions discussed in the text. Low-frequency components between 0 and 3.6 Hz are represented in blue, intermediate frequencies from 3.6 to 12 Hz in green, and high-frequency components from 12 to 29.9 Hz in red. Each scale bar corresponds to a length of 500 µm

It is important to emphasize that the comparison should focus on the spatial variations within the tissue rather than the specific colors used. While the RGB image represents frequency components integrated over the full scan duration, the displacement map depicts tissue deformation at a particular point in time using pseudo-color coding. In the following, all relevant regions described are highlighted by white arrows in Figure 3.16 to facilitate direct comparison.

Across the three samples analyzed, consistent spatial patterns can be observed between the displacement-based and Fourier-based methods. In the first sample, both imaging approaches reveal structurally similar regions within the tissue. For example, two prominent red areas are visible on the right side of the sample. These regions indicate a pronounced tissue response. In the second sample, similar agreement can be observed. The images highlight a prominent area of increased tissue motion located centrally, evident in both visualizations. Additionally, a bluish region on the left side, indicating reduced motion, is consistently present in both methods. The third sample presents a distinct bluish structure centrally located within the tissue, again consistently visible in both processing approaches. This area likely corresponds to a region of low displacement or frequency content. Surrounding this feature, red-colored regions appear on both sides, indicating localized areas of increased mechanical response to the applied load.

These observations validate that the proposed Fourier-based method captures tissue motion characteristics and agrees strongly with conventional displacement-based mapping.

3.9 Discussion

A fundamental challenge in neuro-oncology is accurately distinguishing between pathology and healthy brain tissue during surgery. This task is complicated by the tendency of tumors to infiltrate adjacent regions, obscuring tissue boundaries and making precise identification difficult. To overcome this, there is a critical need for real-time, intraoperative 3D visualizations that enable precise localization and enhance surgical outcomes. Traditional grayscale imaging, however, can be difficult to interpret quickly and accurately in the demanding operating room environment. Therefore, easy-to-interpret, high-contrast visualizations highlighting essential tissue differences are required to support efficient decision-making.

In this context, tissue elasticity has emerged as a promising biomarker, offering a strong contrast between healthy and pathological tissue based on their distinct mechanical properties. Several key requirements must be met to translate this biomarker into a practical intraoperative tool. The imaging technique must provide high spatial resolution, real-time feedback, three-dimensional visualization, and be minimally invasive.

OCE addresses these requirements by combining high-resolution structural imaging from OCT with the ability to measure tissue mechanical properties at the micrometer scale. However, intraoperative imaging presents inherent challenges due to motion artifacts arising from environmental factors in the surgical setting and physiological movements of the patient. Therefore, OCT systems operating at MHz-range A-scan rates are essential to address these issues and achieve stable visualization of elasticity contrasts. Although OCE has demonstrated significant potential for characterizing various types of tissues, it has not yet been applied to brain tissue specifically. Consequently, its intraoperative application in neuro-oncology remains an open area of research.

Adapting OCE for brain tissue introduces unique challenges, particularly the need for an appropriate mechanical excitation method that is both non-contact and gentle enough to preserve delicate neural structures. This study addresses this challenge by employing a focused air-jet to deliver precisely controlled mechanical stimulation minimally invasively.

3.9.1 Phase wrapping challenges in brain tissue measurements

A critical step in translating raw displacement measurements into accurate elasticity maps involves robustly resolving phase ambiguities. To address this challenge, a phase-processing pipeline was developed as part of this thesis. The proposed algorithm was validated using various experimental models, including PVA phantoms, porcine brain tissue, and *ex vivo* human brain tissue. It enables precise evaluation and analysis of sample displacements with high spatial resolution and pixel-level accuracy throughout the acquisition time. Depending on the excitation force and stiffness of the sample, accurate analysis of multiple 2π displacements is achievable. In the measurements presented in this study, the maximum phase shift between two B-scans was always 4π, corresponding to a displacement of 0.96 μm, assuming a refractive index of 1.36 for brain tissue [132]. Histological findings verified the presented results.

However, for effective jerk analysis, it is crucial to have a sufficient sampling rate to maintain a quasi-constant force, as slower sampling rates can impair the performance of the jerk analysis. Therefore, although this remains largely unstudied, the algorithm may need adaptation for other, slower systems. Nevertheless, based on initial findings, our system could also unwrap the phase information by utilizing every third dataset, thereby reducing the processing time by a factor of three. Moreover, to optimize processing speed, the detection interval can be limited to a specific segment within the air pulse, for example, during the strong edge. However, comprehensive testing using multiple datasets would be required, and suitable algorithm adjustments should be implemented if needed. Additionally, since the algorithm has not been extensively tested with excitation methods other than the air-jet approach, additional adjustments may be required to guarantee optimal performance with various excitation techniques.

Furthermore, more than two predicted phase values can be considered during the unwrapping process to enhance accuracy, depending on the specific requirements. However, extending the algorithm to include more predictions would increase processing times and may necessitate further algorithmic adjustments. Yet, no substantial benefit from incorporating additional predictive values beyond two was observed during algorithm development. If residual phase wraps persist after the initial evaluation, the unwrapping algorithm can be iteratively reapplied to previously processed datasets to detect and correct remaining errors.

One significant challenge encountered during algorithm development involved the predictive values used for phase unwrapping, as the raw phase data can be highly noisy at specific time points during acquisition. Then, the predictive phase values become unreliable, leading to excessive or insufficient 2π corrections. Initial tests showed that a more

robust method may involve calculating a representative value from a small surrounding region of data points, rather than relying on single predictive values. Such an adaptation could enhance robustness against noisy data and improve the reliability of the phase unwrapping process. This approach showed mixed results. While it enhanced unwrapping performance in some samples, it was less effective in others. This inconsistency may be attributed to regions exhibiting sharp transitions between soft and hard tissue, where spatial averaging can obscure mechanical boundaries or introduce erroneous phase corrections. Therefore, further investigation is needed to evaluate the general effectiveness.

Overall, the developed phase-unwrapping algorithm enabled clear differentiation of mechanical responses across the tested samples. Distinct displacement patterns were observed between several PVA phantoms, *ex vivo* brain tumor tissue, and healthy brain tissue samples. Healthy brain tissue generally exhibited larger displacements, indicating softer mechanical properties, whereas tumor regions showed reduced displacements, reflecting increased stiffness. Differences were also observed between white and gray matter within healthy tissue, consistent with their distinct mechanical characteristics. These findings suggest that the algorithm can support the identification of pathological regions and provide insight into tissue-specific mechanical behavior.

3.9.2 Fourier-based analysis as an alternative to phase unwrapping

In parallel, an alternative Fourier-based contrast method was assessed, which utilizes the complex OCT signal to extract elasticity-related information. This approach eliminates the need for phase unwrapping and provides a complementary strategy for contrast generation. The method was validated on *ex vivo* human brain tissue, demonstrating the ability to highlight mechanical contrast effectively. The results were compared to those obtained with the traditional phase-based approach. They showed qualitative agreement, supporting the potential of the Fourier-based method as a viable alternative for certain imaging scenarios.

However, because the Fourier-based method evaluates the full frequency content over the entire scan duration, the resulting contrast maps can appear overly colorful and visually complex. While these images contain rich information, they may be difficult for clinicians to interpret efficiently. One possible way to address this limitation is by restricting the analysis to specific time segments of the air-jet excitation, such as the strong rising edge or the plateau region. Focusing on these regions, where tissue response is most pronounced or stable, may enhance the interpretability of the resulting images.

Furthermore, additional testing across a range of mechanical excitation techniques is necessary to fully assess the robustness and applicability of the Fourier-based contrast method. The current validation was limited to air-jet stimulation with specific temporal

characteristics. Other excitation methods, such as piezoelectric actuators or contact-based mechanical loading, produce different signal dynamics that could affect the performance and interpretability of the Fourier-based analysis. Systematic evaluation using diverse excitation strategies will be necessary to determine whether the method is highly adaptable or requires further optimization.

Another limitation of the Fourier-based approach is that it inherently provides information in the frequency domain, and the precise quantitative relationship between the resulting contrast and absolute mechanical parameters remains to be fully established. The contrast arises from tissue motion in response to the mechanical excitation: regions that move differently due to variations in stiffness, damping, or geometry produce distinct frequency signatures in the complex OCT signal. Consequently, the Fourier-based analysis can identify regions with different mechanical responses, and initial comparisons to phase-based displacement measurements indicate a correlation. However, mechanical analysis, particularly for calculating properties such as strain or stiffness, often requires displacement data in the time domain. One possible solution involves converting the frequency-domain information back into time-domain displacement estimates through inverse transformations or by correlating specific frequency components with known mechanical responses. Alternatively, the Fourier-based contrast could be used primarily as a qualitative tool to guide the selection of regions of interest for more detailed phase-based analyses. Further development and validation are required to determine the most effective strategy for integrating this method into a comprehensive mechanical analysis workflow.

Nonetheless, the Fourier-based method provides significant practical benefits. The computational requirements are relatively low, as the technique primarily involves fast Fourier transform calculations, enabling rapid processing that can be implemented in real-time. This speed makes the method particularly attractive for intraoperative applications. Furthermore, because the technique does not depend on resolving small phase changes over time, it may not require the same high temporal sampling density. This opens the possibility of applying the method to volumetric scans, which may require the development of advanced scanning protocols that potentially enable faster imaging.

3.10 Conclusion

In this work, a novel framework for intraoperative brain tissue assessment using MHz-OCE was developed and systematically evaluated. A custom phase-processing pipeline was implemented to generate elasticity maps from raw displacement data. The algorithm was optimized for a MHz SS-OCT system using non-contact air-jet excitation and was validated on multiple experimental models, including *ex vivo* human brain tissue.

Predictive unwrapping strategies and localized correction techniques were introduced, yielding promising results. In parallel, a complementary Fourier-based contrast method was explored to extract elasticity-related information directly from the complex OCT signal. Although this method does not provide displacement values over time, it offers fast processing capabilities and may enable more flexible or volumetric scanning protocols. Qualitative comparisons with the traditional phase-based approach demonstrated good agreement. While both methods showed promise for improving intraoperative decision-making in neuro-oncology, further validation across different excitation modalities and continued algorithmic development will be necessary for clinical translation.

4 Dynamic MHz-OCT for label-free cell visualization of kidney tissue

4.1 Preface

Functional contrast was extracted using a MATLAB script developed by the research group before this project. It was applied to datasets acquired using an already established volumetric scanning strategy. The script was used without major modifications. The home-built MHz-OCT setup with the 4f optical system was also already available in the lab. Due to Madita Göb's parental leave, the results presented in Chapter 4.4 were produced jointly with her.

The three-axis linear robot used for large-area scanning was developed as part of a bachelor's thesis supervised by the author during this PhD project. However, all other image data processing steps mentioned in this thesis, as well as the robot's control software, were developed and implemented by the author. Parts of this work have been published in a peer-reviewed co-first-author journal article [134] and are reused with modifications with permission from © Springer Nature. Only first-author publications are listed here. Additional co-authored contributions related to this work can be found in the appendix.

- **Sazgar Burhan**, Madita Göb, Mario Pieper, Tjalfe Laedtke, Thorge Grahl, Michael Münter, Hinnerk Schulz-Hildebrandt, Gereon Huettmann, and Robert Huber, Label-free volumetric imaging of porcine kidney tissue over extended areas using dynamic MHz-OCT, Scientific Reports, vol. 15, no. 1, pp. 32426, Sep. 2025.
- **Sazgar Burhan**, Madita Göb, Mario Pieper, Tjalfe Laedtke, Thorge Grahl, Michael Münter, Hinnerk Schulz-Hildebrandt, Gereon Hüttmann, Peter König, and Robert Huber, Large-area dynamic contrast MHz optical coherence tomography for label-free imaging of porcine tissue, in Optical Coherence Tomography and Coherence Domain Optical Methods in Biomedicine XXIX, Rainer A. Leitgeb and Yoshiaki Yasuno, Eds. SPIE, Mar.2025. pp. 1330502.

- **Sazgar Burhan**, Madita Göb, Gereon Hüttmann, and Robert Huber, Non-Equidistant Temporal Scanning in Dynamic MHz-OCT for Higher Speed, in European Conferences on Biomedical Optics 2025, Optica Publishing Group, 2025. pp. S4B.3.

4.2 Clinical background

This section introduces the clinical background and motivation for using dynamic MHz-OCT in kidney imaging. It outlines relevant anatomical features, current limitations in assessing organ viability, and the potential of dynamic contrast methods to address existing diagnostic gaps.

4.2.1 Anatomy of the kidney

The kidneys are two reddish-brown, bean-shaped organs on both sides in the retroperitoneal space. Each kidney weighs approximately 200 g and measures around 12 cm in length [135]. Although the kidneys account for only a small fraction of the body's mass, they receive approximately 20 % of the cardiac output, corresponding to about one liter of blood per minute [136]. Their primary role is to continuously filter the blood, remove metabolic by-products, and regulate the composition of body fluids.

It consists of three main regions. The renal cortex forms the outer part of the kidney. A fibrous capsule and a layer of perirenal fat surround it. Inside this region are the glomeruli, compact networks of capillaries enclosed by Bowman's capsules. Together, they form the renal corpuscles, the kidney's initial stage of blood filtration. Here, blood plasma is filtered so that water and small solutes enter the functional unit, while larger molecules and blood cells remain in the circulation. The resulting primary urine then moves through the proximal and distal tubules. Substances essential to the body, such as water, electrolytes, and glucose, are reabsorbed into the bloodstream. In contrast, waste products and excess ions remain in the tubular fluid and are ultimately excreted in the urine.

The anatomy of the kidney is shown in Figure 4.1. The renal medulla is the inner region of the kidney, located beneath the cortex, and plays a central role in urine concentration. It is organized into multiple renal pyramids, which contain loops of Henle, collecting ducts, and capillary networks arranged in parallel and extend from the outer medulla toward the center of the kidney. Urine formed in these structures flows toward the pyramid's tip, entering small collecting chambers called minor calyces. These calyces converge into major calyces, which then drain into the renal pelvis before the urine is transported through the ureter to the bladder.

The innermost renal pelvis acts as the primary collection area for urine. It gathers fluid directly from the major calyces and channels it into the ureter. The renal pelvis plays a crucial role in ensuring the smooth flow of urine from the kidney into the lower urinary tract, where it is temporarily stored before excretion. Its funnel shape supports efficient drainage, helping to prevent pressure buildup within the renal system.

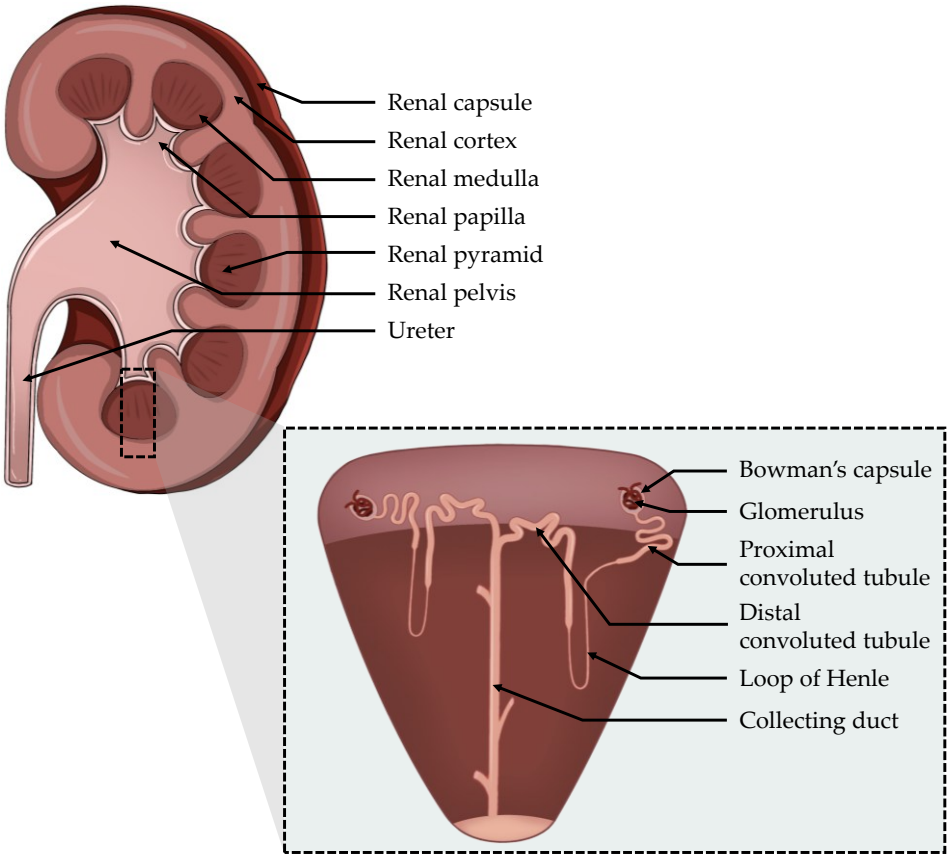

Figure 4.1 Anatomy of the kidney. Major anatomical regions of the kidney, including the cortex and medulla, are shown. An enlarged view illustrates the general layout of a kidney. Own illustration of the kidney cross-section, inspired by Servier Medical Art.

4.2.2 Clinical motivation for functional kidney imaging

Kidney transplantation is widely regarded as the most effective treatment for end-stage renal disease, offering better long-term survival and quality of life compared to dialysis. However, the continued imbalance between organ supply and demand has led transplant programs to accept a wider range of donor kidneys. As a result, kidneys from expanded criteria donors (ECD) are being used more frequently [52]. Typically, these donors are over 60 or have clinical risk factors like diabetes, high blood pressure, or pre-existing impaired kidney function. Despite the higher likelihood of complications, ECD kidneys remain a preferable alternative to long-term dialysis, especially for older patients.

With higher age, the kidneys' structure and function undergo gradual changes, many of which occur at the microscopic level. A key age-related process is nephrosclerosis, marked by the progressive hardening and scarring of kidney tissue, particularly within the glomeruli. From around the age of 30, it is estimated that the kidneys lose approximately 6000 to 6500 nephrons each year, largely due to this scarring [52]. As the vessel walls thicken and the extracellular matrix builds up, the filtration capacity of the kidney declines. These microscopic alterations underscore the necessity for precise and timely evaluation of organ viability before transplantation to reduce post-operative complications.

Therefore, numerous complementary strategies have been introduced to support clinical decision-making during organ assessment. These include visual inspection of the kidney during surgery, donor risk scoring systems, histological analysis, perfusion-based evaluation, and various imaging techniques, each offering different types of information with varying degrees of accuracy and practicality [53].

Visual inspection is often performed during surgery to assess the external appearance of donor kidneys for signs of damage such as fibrosis, surface irregularities, or scarring [53, 137]. While this method is straightforward and can be completed quickly, it is inherently subjective and depends heavily on the surgical team's experience. Additionally, it does not provide information about microscopic alterations that may affect graft viability and long-term function.

Risk assessment models, such as the Kidney Donor Risk Index and the Kidney Donor Profile Index, are commonly used to support graft evaluation [53]. These tools incorporate donor parameters, including age, serum creatinine, diabetes status, and cause of death [138]. However, these scoring systems are not intended to determine donor suitability independently. Instead, they should be part of a comprehensive evaluation considering additional clinical and diagnostic information.

Histological analysis is often conducted using pre-transplant biopsies to obtain more detailed insight into structural damage. Although regarded as the gold standard, biopsy-based evaluation has several challenges. These include variability in sampling techniques, delays in tissue processing, differences in preparation techniques, and inconsistencies in interpretation between pathologists. Moreover, studies report conflicting results regarding the predictive value of biopsy findings for long-term graft outcomes [53, 139, 140]. Therefore, biopsy results should be considered in conjunction with other clinical and diagnostic findings.

As an alternative or complement to tissue sampling, perfusion-based evaluation has become increasingly established, particularly with hypothermic machine perfusion (HMP) [141-143]. HMP is a preservation technique in which a cold perfusion solution is

continuously circulated through the donor kidney to reduce metabolic activity and slow tissue degradation during storage. This process helps maintain organ viability by reducing metabolic activity and enables real-time monitoring of functional parameters that may reflect the quality of the graft. Among these, renal resistance and flow rate are the most monitored parameters, serving as indicators of graft quality and perfusion efficiency [53, 141]. Several studies have reported that trends in renal resistance during HMP, such as persistently high values or a lack of the expected decline over time, may be associated with a higher risk of delayed graft function and reduced long-term graft survival, particularly in kidneys from ECDs [143, 144]. However, despite these findings, other studies have reported no clear or consistent relationship between perfusion parameters and transplant success [53, 141].

In addition to these methods, imaging techniques are often used to evaluate anatomical and vascular features, especially in living donor transplantation. Doppler ultrasound and computed tomography angiography provide detailed anatomical information that supports accurate detection of vascular variations and estimation of kidney volume. Infrared thermography, hyperspectral imaging, near-infrared fluorescence angiography, MRI, and positron emission tomography have also shown promise for assessing graft perfusion. However, while some of these techniques can be applied intraoperatively, others are restricted to pre- or post-transplant settings due to technical and logistical limitations [53].

Despite ongoing advancements, no current method provides a comprehensive solution for the rapid, high-resolution, and label-free assessment of kidney viability during transplantation. Each technique addresses part of the challenge, yet none combine microscopic detail, wide-field coverage, and real-time feedback in a single, non-invasive approach suitable for intraoperative use. What remains missing is a modality that can bridge this diagnostic gap and provide objective insights into tissue integrity without damaging the organ or requiring invasive procedures.

4.2.3 Dynamic OCT as a potential tool for viability assessment

While conventional OCT has proven to be highly effective for structural kidney imaging at micrometer resolution [145-148], it remains mostly limited to static tissue images and offers little ability to distinguish different tissue structures. Dynamic optical coherence tomography (dOCT) addresses this limitation by incorporating the analysis of time-dependent signal variations within the imaging process. By repeatedly acquiring data at a fixed location and evaluating signal fluctuations over time, dOCT provides motion-based contrast that reveals functional characteristics not visible in conventional structural images.

By providing additional functional insight, it may enhance intraoperative evaluation and support more informed decision-making during kidney transplantation. In this context, OCT offers several important advantages. It provides real-time imaging at micrometer resolution, operates label-free and non-invasively. Furthermore, the ability to visualize microstructural and dynamic features *in situ* and *in vivo* may help identify subtle signs of viability concerns that are not detectable through conventional methods.

Oldenburg et al. pioneered this approach by demonstrating that temporal variations in OCT signal intensity could serve as a meaningful contrast mechanism. In their 2012 study, they applied standard deviation mapping to visualize dynamic features in a mouse trachea model [49]. This concept was further advanced in 2015 using OCT fluctuation spectroscopy, enabling the detection of microscale activity within organoids. These early works laid the foundation for the broader field of dOCT [50].

Since then, dOCT has expanded through a wide range of implementation strategies and contrast mechanisms. Building on early variance-based approaches [49, 50, 149, 150], subsequent developments introduced more advanced methods such as logarithmic intensity variance [151] and temporal frequency analysis using Fourier-based techniques [152, 153]. These contrast methods have been applied across different OCT systems, including spectral-domain [49, 50, 152, 153], swept-source [151], and full-field configurations [149, 150], each offering specific advantages in terms of acquisition speed, spatial resolution, and temporal stability.

To facilitate the interpretation of the dOCT data, various color-coding schemes have been employed to visualize the functional contrast. Among the most widely used approaches is RGB color coding [51, 153], where different temporal frequency components or motion speeds are mapped to the red, green, and blue channels. Another common approach is the hue-saturation-value (HSV) method [150]. In this scheme, hue encodes the dominant frequency at each pixel, meaning different colors represent different fluctuation rates. Saturation reflects the spectral bandwidth of the signal or the strength of that frequency, while value (brightness) reflects the overall signal amplitude.

4.3 Experimental setup and data processing

This section provides an overview of the MHz-dOCT imaging approach, including the system setup, data acquisition and processing workflows, and the procedures used for sample preparation and histological validation.

4.3.1 MHz-dOCT system

The dOCT setup is based on a home-built, all-fiber-based FDML laser with an 8x buffering stage, achieving an effective A-scan rate of 3.2 MHz. The central wavelength was set to 1310 nm and the spectral bandwidth to 110 nm to achieve a theoretical axial resolution of 9.4 µm and an imaging range of 5 mm in air. With a sample power of 38.5 mW, the system achieves a sensitivity of around 101 dB. The interference signal is detected using a 1.6 GHz balanced photodetector (PDB480C-AC, Thorlabs Inc., USA). Digitization was performed using a 4 GS/s analog-to-digital converter (ATS9373, Alazar Technologies Inc., Canada) with a 12-bit sampling resolution, corresponding to approximately 1200 sampling points per A-scan. Synchronization is managed through a PXIe multifunction input/output module (PXIe-6363, National Instruments Corporation, USA), which controls the XY galvanometric scanners, the three-axis linear robot, and generates hardware triggers.

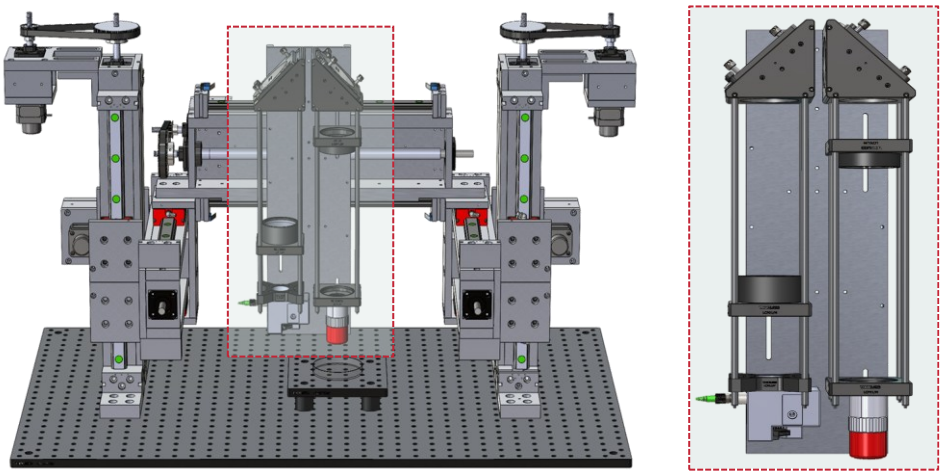

Figure 4.2 Home-built motorized three-axis linear robot with scanning unit. The left panel displays the complete robotic stage, comprising an XYZ configuration with one X-axis for transverse motion, two Y-axes for precise lateral movement, and two vertical Z-axes for height adjustment and mechanical stabilization. The right panel provides a detailed view of the scanning unit.

For dOCT imaging, a home-built scanning unit was used. It comprises a small scan block equipped with two galvanometric scanners (dynAXIS 421, Scanlab GmbH, Germany) and a fiber collimator (F260APC-C, Thorlabs Inc., USA). Higher lateral resolution was achieved compared to standard MHz-OCT configurations, using two interchangeable microscope objectives with different NAs (M Plan Apo NIR 10X and 20X, Mitutoyo, Japan). To fully utilize the resolving power of these objectives, two different 4f optical relay systems were used to expand the scanning beam diameter to match the objectives' back apertures. The 10X objective provided a lateral resolution of 3.48 µm and a FOV of 1410 x 1460 µm², while the 20X objective achieved 2.76 µm lateral resolution with a

1040 x 1060 µm² FOV. A more detailed description of the scanning unit can be found in the corresponding publication [134].

The entire scan head was mounted on a home-built motorized three-axis linear robot, allowing for precise positioning over large sample areas. More details about the design and operation of the three-axis linear robot can be found in Chapter 4.5. An image of the scanning system is shown in Figure 4.2. All measurements were taken on an actively isolated optical table to minimize motion artifacts.

4.3.2 Data acquisition workflow

An inter-volume scanning protocol, already established within the research group, was used to improve imaging efficiency and reduce overall acquisition time. The volumetric dataset was divided into 40 subvolumes, with 2048 x 50 x 600 A-scans. Each subvolume was scanned unidirectionally and acquired 50 times to ensure sufficient temporal sampling. The system operated at a frame rate of 612 Hz, resulting in a subvolume acquisition rate of 12.2 Hz and an approximate total scan time of 3.3 s. To capture a larger FOV, multiple volumes were recorded in an overlapping mosaic arrangement using the motorized three-axis linear robot (see Chapter 4.5.4).

After data acquisition, all OCT datasets were processed using a LabVIEW-based processing software. Due to scanner limitations and the system running at 3.2 MHz, the data was oversampled approximately five times. Therefore, to reduce data size and simplify processing, the A-scans were averaged twice. The resulting datasets were resized and cropped along the Z-axis to show only the relevant imaging depth. Standard intensity images were exported on a logarithmic scale, with ten colocalized B-scans averaged to improve image quality. The same dataset was also exported in linear values for functional contrast calculation.

4.3.3 Functional contrast computation

The dOCT processing workflow comprises several sequential steps, implemented entirely in MATLAB (R2023a, The MathWorks, Inc., USA). An overview of the signal processing steps is illustrated in Figure 4.5, and a detailed description of the processing steps can be found in the corresponding publication [51]. The resulting frequency spectrum is divided into three predefined bands. For each band, the signal amplitude is integrated and assigned to one of the three RGB color channels. Blue for low-frequency fluctuations (0 - 0.5 Hz), green for mid-range frequencies (0.5 - 3 Hz), and red for higher-frequency

components (3 - 6 Hz). Unless otherwise specified in the subsequent sections, these frequency intervals are used consistently throughout this work. To keep consistent spatial dimensions, the volumes were resized along the Y-axis.

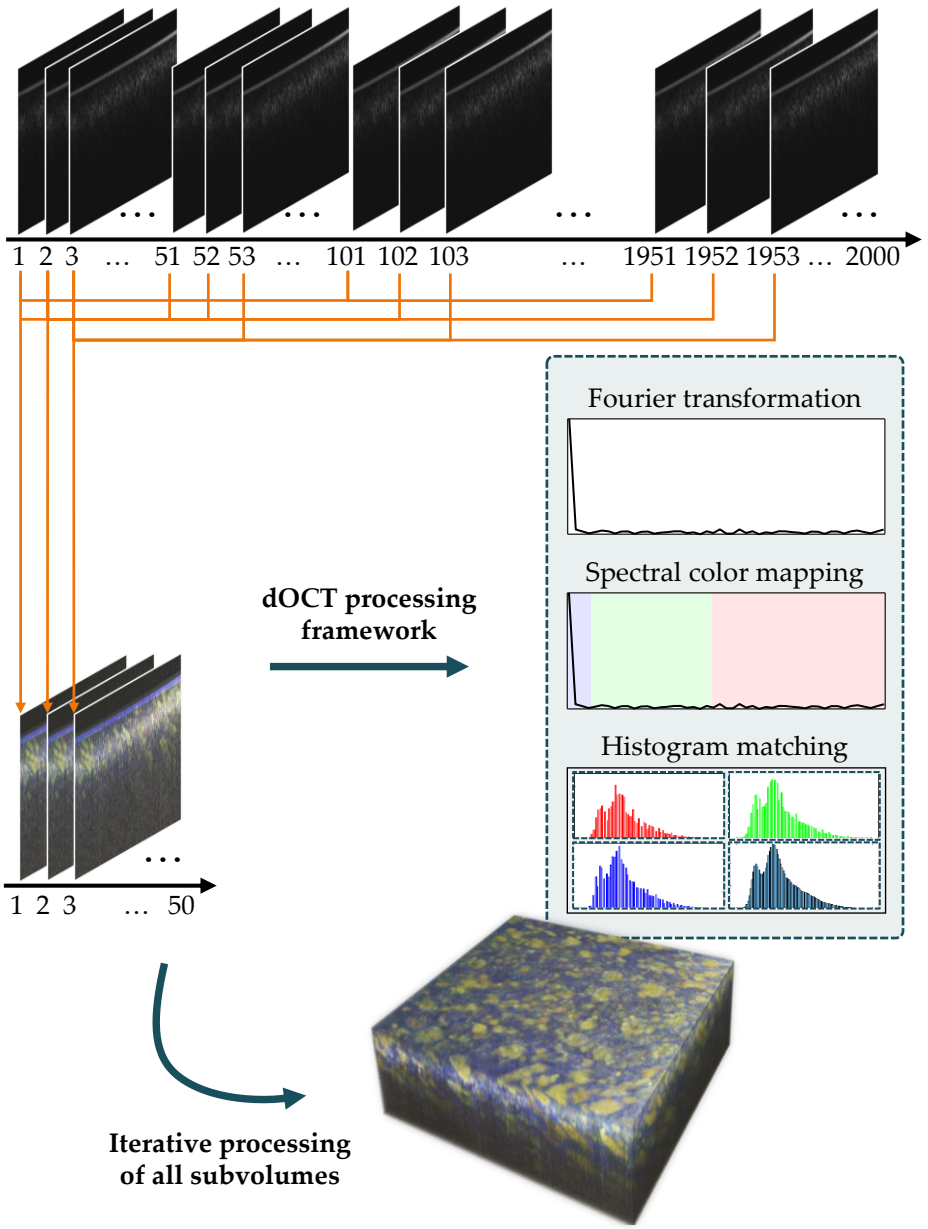

Figure 4.3 Signal processing pipeline for dOCT imaging. The steps involved in calculating and visualizing the dynamic contrast are illustrated. The lower right corner shows a representative three-dimensional dOCT volume of a porcine kidney.

To minimize motion-related artifacts between repeated acquisitions, image registration is performed using MATLAB's `imregcorr` function within the already available processing script. This approach worked reliably when a single dataset was processed at a time, but performance was limited when several subvolumes were loaded and processed sequentially. Loading all subvolumes at once was not feasible due to the large size of the

unprocessed OCT data. Therefore, after calculating the functional contrast, the resulting subvolumes showed positional shifts along the Z-axis. These shifts led to discrepancies in relative heights and created challenges for subsequent volume stitching. To address this, an additional post-processing script was written in MATLAB and applied to all subvolumes.

The first acquired subvolume was defined as the reference, and all subsequent subvolumes were aligned to it. For each subvolume, the intensity profile along the Z-axis was extracted from the blue channel. Since a glass plate was placed on the sample during imaging, it produced a stable, low-frequency signal that appeared most clearly in the blue channel and served as a reliable reference for surface registration. For each frame, the median intensity across all lateral pixels was computed to generate a depth-intensity profile for alignment. These profiles were normalized and smoothed using a Gaussian filter to minimize noise. A local region around the most prominent peak was then analyzed to refine the alignment, with the peak position determined with sub-pixel accuracy through polynomial fitting. The height difference between the reference and moving subvolumes was calculated and used as a Z-axis shift to ensure consistent depth alignment across all channels and subvolumes.

4.3.4 Sample preparation and histological validation

Dynamic MHz-OCT imaging was performed on *ex vivo* porcine kidney tissue to evaluate system performance and contrast generation. Fresh porcine kidneys, categorized as slaughter by-products, were sourced from a local butcher. Immediately after excision, the organs were stored and transported in an ice-filled cooler to maintain tissue integrity. For imaging, kidney samples were sectioned into 12 mm segments using a biopsy punch and placed in standard biopsy embedding cassettes (Sanowa Laborprodukte GmbH, Germany). After imaging, the tissue samples were fixed in 4 % buffered paraformaldehyde at 6 °C. The fixed samples were subsequently embedded in paraffin, sectioned into 5 μm slices using a microtome, stained with H&E, and digitized using an automated slide scanner (PANNORAMIC MIDI II, 3DHISTECH Ltd., Hungary). An experienced medical doctor and biologist performed the histological evaluation.

In the imaging experiments, two distinct regions of the kidney were examined. A sample from the renal cortex was excised from the organ surface and positioned with the cortex facing upward to replicate *in vivo* imaging conditions. To investigate the renal medulla, an additional tissue segment was resected from the inner part of the kidney.

4.4 Evaluation of functional imaging applicability

To evaluate the applicability of functional imaging in kidney tissue, targeted measurements using MHz-dOCT were performed. These experiments focus on the influence of resolution and the ability to visualize anatomical structures in different regions of the kidney. The following sections present the corresponding results.

4.4.1 Functional imaging performance at varying resolutions

To assess the influence of lateral resolution on the visualization of functional structures, imaging was performed using both microscope objectives. The results obtained with the lower magnification are presented in Figure 4.4A - E, and those from the higher magnification are shown in Figure 4.4F - J. Representative *en face* dOCT images were extracted at a depth of 59 µm for the 10X configuration and 143 µm for the 20X objective, as shown in Figure 4.4B and G. For comparison, conventional OCT intensity images processed without functional contrast are presented in Figure 4.4A and F. Dashed lines in the *en face* views indicate the locations of the corresponding cross-sectional scans, shown in Figure 4.4D and I for the intensity images and in Figure 4.4E and J for the dOCT images. Enlarged views of selected image regions are displayed in Figure 4.4C and H. A histological section of the same kidney sample is included in Figure 4.4K.

It should be noted that although the OCT measurements and histological analysis were performed on the same sample and targeted approximately the same region, exact colocalization was not achieved. This also applies to the comparison with the 10X and 20X objectives. The discrepancy resulted from differences in tissue processing, sectioning, and imaging procedures, as well as the mechanical adjustments required when switching between the two resolution configurations.

The 10X objective offers a wider FOV of approximately 1.4 x 1.4 mm² and a longer Rayleigh range, which enhances visibility over a greater axial extent in the cross-sectional images. This is evident in Figure 4.4E, where layered structures remain visible across a broader depth range compared to Figure 4.4J. However, this advantage comes at the cost of reduced lateral resolution. In contrast, the 20X objective offers higher lateral resolution within a smaller FOV of approximately 1 x 1 mm², enabling clearer visualization of subcellular features in the *en face* view. This setup, however, has a narrower depth of focus, which restricts structural visibility away from the focal plane. Additionally, it exhibits vignetting artifacts in the lower image corners due to suboptimal light coupling into the objective.

Cellular structures that remain unrecognizable in the static OCT intensity images become visible in the dOCT images. This contrast is particularly noticeable in the B-scans, where intensity images reveal little to no discernible cellular detail. In contrast, the corresponding dOCT B-scans display these features with high clarity, allowing for detailed and precise analysis. Similarly, although the *en face* intensity images may suggest the presence of cellular structures, they lack the definition and detail provided by the *en face* dOCT images, which offer a more comprehensive and accurate representation.

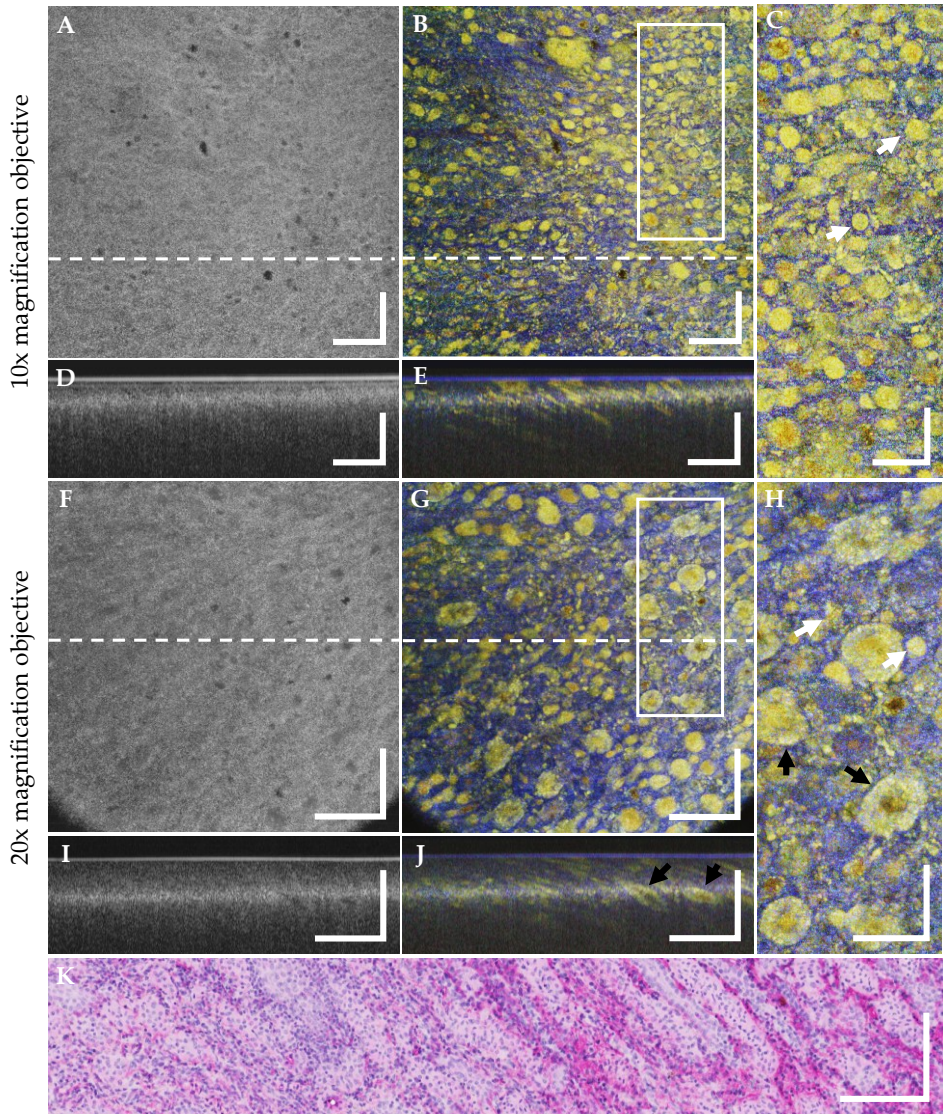

Figure 4.4 Visualization of renal microstructures at different objective magnifications. Imaging was performed with 10X (A–E) and 20X (F–J) objectives to assess structural and functional features of the inner renal medulla. OCT *en face* intensity images are shown in (A) and (F), with corresponding dOCT representations in (B) and (G). White boxes highlight magnified regions shown in (C) and (H). Cross-sectional B-scan intensity views are presented in (D) and (I), and B-scans along the dashed lines in (B) and (G) appear in (E) and (J). White arrows indicate Henle's loops, black arrows indicate collecting ducts. The H&E-stained section is shown in (K). Scale bars represent 200 μm, except for (C), (H), and (K), where they indicate 100 μm. Adapted from [134].

With both the 10X and 20X objectives, round and elongated structures are visible, with diameters as small as a few micrometers. Comparable features are also present in the corresponding histological section shown in Figure 4.4K. In the magnified *en face* views in Figure 4.4C and H, selected structures are indicated by white arrows. These features correspond in size to Henle's loops, which typically range from 20 to 50 μm. Additionally, even smaller elements, potentially representing additional cellular components, can be observed. At 20X magnification, the internal architecture of larger collecting ducts becomes visible, as marked by black arrows in Figure 4.4H and J. These ducts exhibit a light-green outer region and an orange interior. The light-green area corresponds to the compact cellular wall of the duct, characterized by medium signal frequencies. In contrast, the orange interior reflects higher-frequency signals, which are likely associated with fluid motion within the duct. In the B-scan views, the elongated shape of the ducts is recognizable. Especially outside the focal plane, dOCT provides enhanced contrast, allowing for the identification of structures that remain difficult to detect using standard intensity OCT.

4.4.2 Assessment of anatomical detail in the outer renal cortex

Following the imaging of the inner renal medulla, additional measurements were performed in the outer renal cortex to assess the method's ability to resolve small anatomical details near the tissue surface. Corresponding histological data were used to support and interpret the dOCT observations. Figure 4.5A displays the volumetric dOCT dataset acquired using 20X magnification, while Figure 4.5B presents an *en face* cross-section extracted at a depth of 122 μm. A magnified view of a selected region is shown in Figure 4.5C. The positions of the orthogonal cross-sectional B-scans are indicated by white dotted lines and shown in Figure 4.5F and E. The matching histological section of the same tissue region is provided in Figure 4.5D.

Distinct anatomical structures are visible in the dOCT data, with renal corpuscles appearing particularly prominent, as indicated by white arrows. The imaging clearly distinguishes the glomerulus from the surrounding Bowman's capsule. The glomerulus appears bluish and is associated with a low-frequency signal, likely due to limited motion within its cellular matrix. In contrast, Bowman's space, the fluid-filled region surrounding the glomerulus, appears yellow, indicating a higher scattering signal that reflects its low cellular density. These optical differences allow for clear differentiation of the two components. While the filtration units can be detected in B-scan views, accurate localization and morphological evaluation benefit from full volumetric reconstruction. In contrast, the tubular network is best visualized in the *en face* view.

The convoluted tubules, visible in yellow tones and marked by black arrows, could also be resolved. Although the tissue was imaged several hours after excision, residual molecular motion remains detectable. A higher-frequency signal appears in the center of the tubules, while the surrounding areas display lower-frequency contrast and appear green.

Histological analysis confirms the presence of both convoluted tubules and corpuscles, with measured dimensions falling within the reported range of 100 to 250 µm [154]. However, the scale bars shown in the dOCT images and the histological sections are not directly comparable. This difference results from tissue shrinkage during histological processing, which led to a size reduction by a factor of 1.5 to 2. Adjusting the scale bar to account for this variation is challenging, as the shrinkage is not uniformly distributed across the sample.

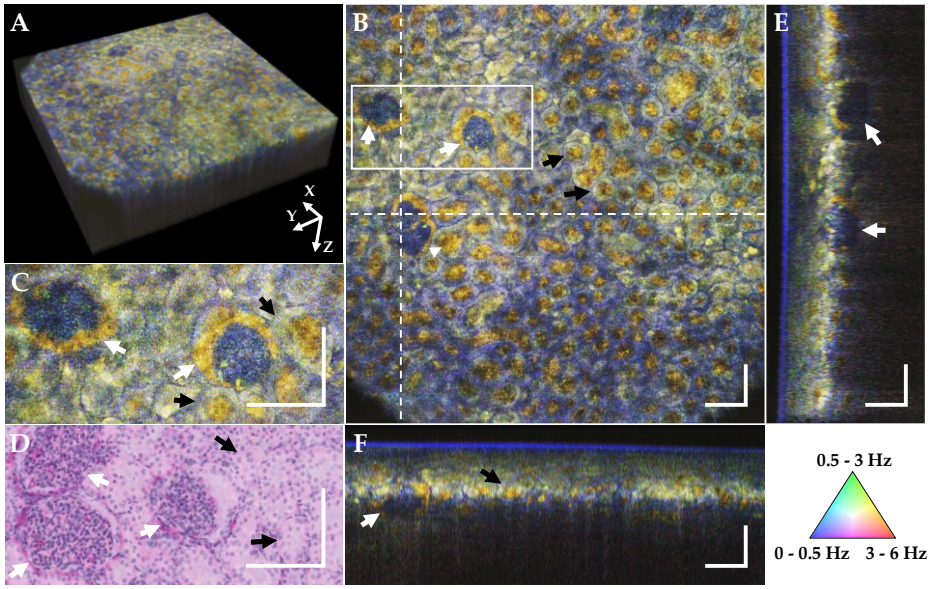

Figure 4.5 Dynamic OCT imaging of the outer renal cortex. A: Three-dimensional dOCT volume acquired using a 20X magnification objective. Slight vignetting appears in the corners, likely due to imperfect light coupling into the high-NA objective. B: *En face* cross-sectional view extracted at a depth of 122 µm. Dashed lines indicate the positions of the orthogonal slices shown in (E) and (F). C: Enlarged view of the white rectangular region in (B). D: Corresponding H&E-stained histological section. The discrepancy in the scale bars is attributable to sample shrinkage during histological processing. E and F: Orthogonal dOCT B-scans in the YZ and XZ planes, respectively. White arrows indicate renal corpuscles, and black arrows highlight selected convoluted tubules. Each scale bar corresponds to 100 µm.

4.5 Large-area dOCT imaging

4.5.1 Development of the three-axis linear robot

For large-area functional imaging, a home-built three-axis linear robot was developed to enable precise and automated positioning of the OCT scan head. The system offers a translational travel range of approximately 19 x 19 x 19 cm along the Cartesian axes. It comprises three independently controllable linear axes, with two Y-axes and two Z-axes arranged in parallel to support and stabilize the central X-axis. Although the robot does not provide angular degrees of freedom, its precise linear motion combined with a stationary sample position makes it well-suited for dynamic imaging. In particular, the system's mechanical stability minimizes motion artifacts and ensures consistent imaging conditions across large scan volumes. Figure 4.6 provides a visual representation of the axis layout, highlighting the spatial configuration and mechanical integration of the individual components.

The robot utilizes two-phase stepper motors (QSH4218-51-10-049-10K, Analog Devices Inc., USA) with a step angle of 1.8°, resulting in 200 full steps per revolution. Each motor is equipped with a high-resolution optical encoder capable of 10.000 lines or 40.000 counts per revolution. The encoders generate pulse signals whenever motor movement is detected, allowing for the accurate monitoring of position, angular displacement, and rotational direction.

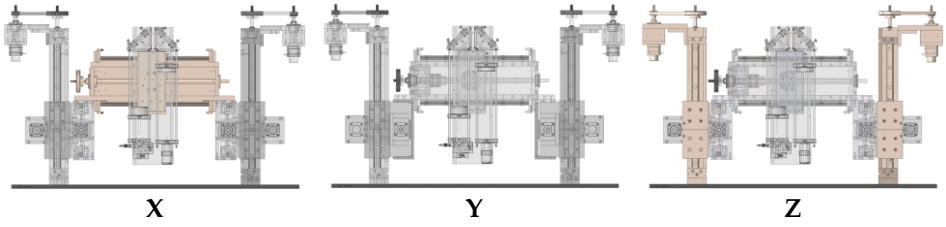

Figure 4.6 Visualization of the linear robot with highlighted axis. Front views of the robotic scanning system are presented with color overlays used to distinguish individual linear axes. From left to right, the X-axis, Y-axis, and Z-axis assemblies are highlighted.

The five stepper motors are controlled via two TMCM-3110-TMCL driver boards (Analog Devices Inc., USA), which support microstepping with a resolution of up to 256 microsteps per full step, resulting in a theoretical minimum step size of 0.007°. Each board operates at a maximum coil current of up to 2.8 A and a DC supply voltage of 48 V. It integrates a TMC429 motion controller, which manages trajectory generation and multi-axis coordination, and three TMC262 driver ICs, which provide intelligent current control and error diagnostics for individual motor channels. A total of 16 input/output terminals

are available, including dedicated connections for motors, encoder inputs, reference switches, general-purpose digital signals, and step/direction control. The extensive interface facilitates synchronization with the OCT imaging system, ensuring that motor movements are precisely synchronized with image acquisition events.

All axes are constructed from CNC-milled aluminum profiles and are equipped with linear guide rails. To ensure mechanical stability and precision along the vertical direction, each Z-axis is equipped with a 390 mm linear guide rail (EGR25R, HIWIN GmbH, Germany) and two carriages (QEH25CAZ0H, HIWIN GmbH, Germany). This dual-carriage configuration helps prevent tilting or misalignment of mounted components while also increasing load capacity, stiffness, and resistance to bending forces. In comparison, the X- and Y-axes use 340 mm guide rails of the same type, each assembled with a single preloaded carriage (QEH25CAZAH, HIWIN GmbH, Germany). These carriages incorporate oversized steel balls that generate a built-in internal preload, increasing contact with the guide rail to eliminate backlash and enhance overall rigidity.

Table 4.1 Gear configurations and resulting travel times for each axis. The table presents the gear ratios and resulting motion characteristics for each linear axis under a microstepping configuration of 256 microsteps per full step. The variation in gear configurations directly affects both motion resolution and the total time required to complete the full 19 cm travel range.

Axis	Microsteps	Motor gear (teeth number)	Driven gear (teeth number)	Steps per mm	Travel time (full axis)
X	256	25	72	29491	22 s
Y	256	34	52	15661	25 s
Z	256	25	72	29491	22 s

Each linear axis is driven by a precision ball screw assembly consisting of a ball screw spindle (KGS-R-1605-RH-T5, NEFF Gewindetriebe GmbH, Germany) and a matching ball nut (KGF-D-1605-RH-EE, NEFF Gewindetriebe GmbH, Germany). The spindles have a lead of 5 mm and a diameter of 16 mm, with a maximum lead deviation of 23 µm over a travel length of 300 mm. The ends of the spindles were custom-machined. To eliminate backlash between the ball screw nut and the spindle, the ball screw nuts were preloaded during assembly by the manufacturer. Motion is transferred via a timing belt system, which comprises two gears and a 9 mm wide timing belt (Mädler GmbH, Germany) with a 3 mm pitch and a high-torque drive (HTD) tooth profile. The gears have a bore diameter of 8 mm and feature a custom keyway modification for secure coupling to the shaft.

A fixed-floating bearing arrangement was implemented to ensure proper axial and radial support of the spindle. The fixed bearing (FK12-C5, HIWIN GmbH, Germany) serves as the primary axial reference and is designed to absorb both radial and axial forces. While

a single bearing can be sufficient under moderate loads, the use of an additional bearing is generally recommended for higher mechanical stress. For this reason, the system also includes a floating bearing (FF12-C5, HIWIN GmbH, Germany), which supports only radial loads and is capable of compensating for axial displacement or thermal expansion of the spindle shaft. This configuration helps prevent mechanical stress caused by assembly tolerances or temperature-related expansions.

To reduce the risk of damaging the objective lens during vertical motion and ensure user safety, several protective measures were incorporated into the design of the linear robot. Given its mechanical power and range of motion, the system poses a potential hazard in the event of technical failure or human error. One of the primary risks involves the potential for body parts to become trapped between the moving stage and the base plate. To mitigate this, a mechanical depth stop in the form of a threaded rod was installed at the rear end of the Y-axis. Its height can be adjusted quickly and easily using a clamping lever (66577810, Mädler GmbH, Germany). To ensure safe operation at the electronic level, an emergency stop switch is installed near the robot to interrupt the system's power supply in the event of an emergency. Electronic components that are not permanently integrated with the linear robot are enclosed to prevent accidental contact with live circuits. Additionally, cable routing has been designed to remain clear of all moving components, thereby reducing the risk of mechanical wear, entanglement, or interference with moving components.

All measurements and performance evaluations in this thesis were conducted using a microstepping resolution of 256 steps per full step to achieve the highest possible positioning accuracy. With the selected gear ratios and a microstepping resolution of 256 microsteps per full step, axis travel times between 24 and 47 s were achieved for the full travel range of 19 cm, as summarized in Table 4.1.

The number of steps required per millimeter of travel was calculated based on the microstepping resolution ($microsteps$), the number of full steps per motor revolution ($steps/rev$), and the mechanical transmission via gears. The ratio of teeth between the driven gear (T_{driven}) and the motor gear (T_{motor}), together with the lead of the ball screw ($lead$), determines how motor rotation translates into linear displacement. This relationship can be expressed as:

$$\frac{steps}{mm} = \frac{microsteps \cdot steps/rev \cdot T_{driven}}{lead \cdot T_{motor}}. \tag{4.1}$$

4.5.2 Control software implementation and operation

A LabVIEW-based control software (National Instruments, USA) was developed, building upon an earlier version created by the author during her master's thesis. While the initial implementation supported control of a single motor board, the new version was restructured to operate two independent motor driver boards. Particular attention was given to the integration and synchronization of the additional axes introduced with the current system design. While the previous version of the software controlled only a single XYZ-axis, the updated version was redesigned to support synchronized control of two parallel Y-axes and Z-axes. This necessitated the implementation of coordinated motion routines to ensure that the paired motors operate in a synchronized and mechanically aligned manner. Using an improved readout and command structure, alignment deviations between the corresponding motors were reliably detected and corrected in real-time.

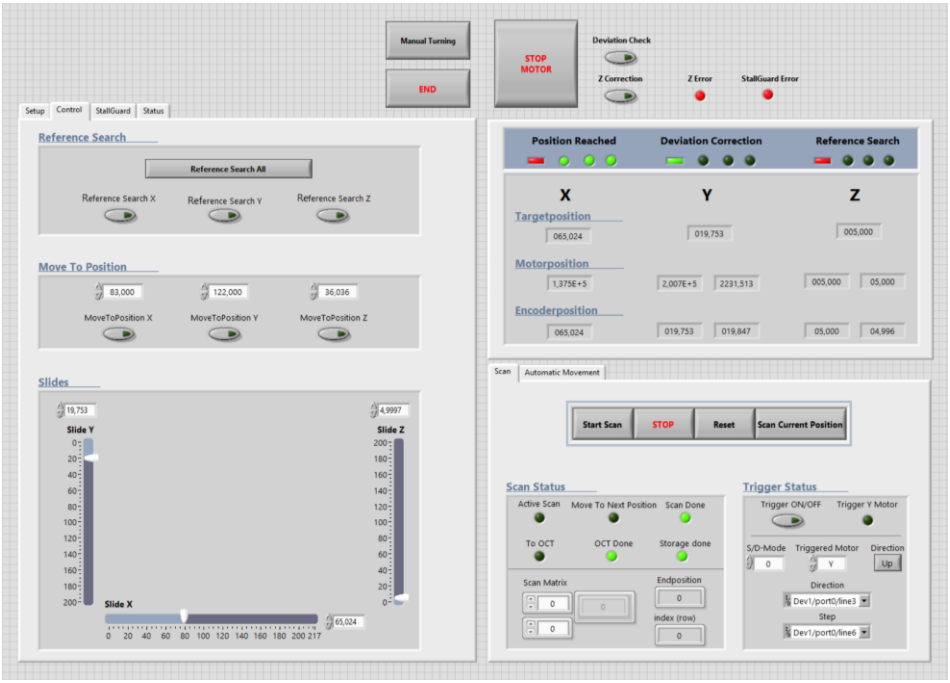

Figure 4.7 Graphical user interface for controlling the three-axis linear robot. The LabVIEW-based graphical user interface provides comprehensive control over the three-axis linear robot. It includes functions for reference searching, manual positioning, and automated scan execution. Real-time feedback on motor and encoder positions is displayed for all three axes, along with scan status, trigger settings, and synchronization indicators.

The software utilizes Virtual Instrument Software Architecture (VISA) interfaces to communicate with the motor driver boards, which are connected to the PC via a USB port. Through an intuitive graphical user interface (GUI), operators can configure various stepper motor settings and read positional data. Additionally, the GUI offers comprehensive

functionality, enabling users to initiate reference searches for individual or all axes simultaneously, enter exact target positions numerically, or manually adjust each axis position using graphical sliders. A screenshot of the GUI is given in Figure 4.7.

To ensure accurate and reliable motion execution, the system continuously monitors motor performance by comparing commanded target positions with the real-time encoder feedback. Any positional deviations are automatically detected, and correction mechanisms are activated if necessary. Status indicators within the GUI inform the user of ongoing corrections and potential mismatches.

Real-time feedback is continuously displayed through visual indicators, informing users when the target positions have been reached and whether any deviation corrections or reference searches are active. Numeric readouts of target, motor, and encoder positions further facilitate system monitoring.

Scanning operations are managed through dedicated control elements within the GUI, allowing for initiation, termination, and reset of scans. Complex scan patterns can be created using a separate LabVIEW software developed by the author as part of her master's thesis. Synchronization between the three-axis linear robot and the OCT imaging software is achieved through several notifier functions, enabling coordinated motion and data acquisition. The system operates in an automated, stepwise manner. The robot moves to a predefined scanning position, triggers image acquisition, and only proceeds to the next position after the current scan is completed. Status signals are provided throughout the process to monitor scan activity and ensure correct coordination between motion and data acquisition. Additionally, integrated trigger management options provide flexible synchronization with external devices via the step/direction interface, enabling precise control through configurable triggering modes if needed.

4.5.3 Quantitative evaluation of positioning accuracy

To evaluate the positioning accuracy and stability of the three-axis linear robot, a UI1490LE industrial camera (IDS Imaging, Germany) was employed. The camera is equipped with a 10-megapixel CMOS sensor, featuring a resolution of 3840 x 2748 pixels and a pixel size of 1.67 μm. As the light source, a 1060 nm booster optical amplifier (BOA) was used, selected to match the camera's sensitivity range.

A collimator lens with a focal length of 70 mm was used to focus the laser onto the camera sensor. To avoid sensor saturation at higher laser currents while maintaining a measurable Gaussian intensity distribution on the detector, a 1:99 optical coupler was inserted before the collimator, with only 1 % of the light directed toward the sensor. This configuration enabled the stable operation of the BOA at 40 mA. Since the laser emits a Gaussian-shaped intensity profile, its position can be determined with high accuracy by

fitting a two-dimensional Gaussian function to the recorded intensity distribution. To reduce the impact of ambient vibrations and ensure measurement stability, all tests were conducted on a vibration-isolated optical table.

4.5.3.1 Validation of the camera-based assessment method

Compared to conventional mechanical dial indicators, optical evaluation using a camera offers several advantages. Mechanical gauges typically measure displacement at a single point along one axis and require direct contact with the moving part, which can introduce mechanical loading, backlash, or alignment errors. In contrast, the camera-based approach enables contact-free, two-dimensional position measurements with sub-pixel accuracy. Therefore, the method is well-suited for automated evaluation workflows, allowing for objective and repeatable measurements.

To verify the precision and stability of the camera-based measurement setup, a repeatability test was conducted with the linear robot held in a stationary position. Over 20 minutes, 100 consecutive measurements were acquired. The recorded positional fluctuations were minimal, with standard deviations of approximately 0.04 µm in the X-direction and 0.03 µm in the Y-direction. The maximum deviations never exceed 0.2 µm. A follow-up measurement performed one hour later yielded comparable results, although a positional shift of around 0.5 µm in the X-direction and 0.4 µm in the Y-direction was observed. This variability may be attributed to minor thermal drifts, mechanical relaxation effects, and electronic noise within the motor control or camera readout system.

Comparative experiments using a mechanical dial indicator with a resolution of 1 µm and a measurement range of 12.7 mm confirmed the reliability of the camera-based method. Approximately 70 % of all measuring points showed the same results using both measurement methods. The maximum observed deviation between the two approaches was 0.4 µm. The camera-based measurement method demonstrated superior performance compared to the mechanical dial indicator, which operated near its resolution limit. It delivered more stable and precise results that closely matched the commanded step sizes.

This higher accuracy and repeatability, along with its non-contact nature, justified its use for the continued evaluation of the robotic system's positioning accuracy and stability. However, it also requires careful calibration and consistent alignment between the laser, camera, and linear robot. Misalignment or improper focusing can introduce systematic errors, and the relatively limited FOV restricts the usable measurement range. Nevertheless, when properly configured, the camera-based method provides a reliable and precise

approach for evaluating positioning accuracy and repeatability. Therefore, all measurements used to evaluate the robot's positioning performance were obtained using the camera-based method unless stated otherwise.

4.5.3.2 Positioning accuracy

To evaluate the positioning accuracy of the linear robot, a series of step commands ranging from 1 μm to 1000 μm were assessed on the X- and Y-directions. The results, summarized in Table 4.2, provide detailed metrics on average step size, mean error, standard deviation, and maximum deviation for each nominal step.

At large step sizes (500 μm and 1000 μm), the robot exhibits high absolute positioning accuracy. The mean error remains below ±1.5 μm, corresponding to a relative error of less than 0.3 %. For example, at 1000 μm, the mean error is 1.46 μm in X and 0.28 μm in Y. At 500 μm, the values are 0.24 μm in X and -0.90 μm in Y.

Table 4.2 Measured positioning accuracy of the three-axis linear robot. This table summarizes the positioning performance of the self-developed three-axis linear robot for commanded step sizes ranging from 1 μm to 100 μm. For each step size, the average executed step, the mean error relative to the commanded value, the standard deviation, and the maximum deviation are reported separately for the X- and Y-directions.

Nominal step size	Direction	Avg. step size [μm]	Mean error [μm]	Std. dev. [μm]	Max. deviation [μm]
1 μm	X	0.90	-0.10	0.20	0.35
	Y	0.26	-0.74	0.07	0.84
5 μm	X	4.86	-0.14	0.38	0.64
	Y	4.53	-0.47	0.28	0.81
10 μm	X	9.83	-0.18	0.36	1.31
	Y	9.41	-0.59	0.57	1.63
20 μm	X	19.93	-0.07	0.45	0.98
	Y	19.53	-0.47	0.83	2.54
50 μm	X	49.86	-0.14	0.56	1.17
	Y	49.43	-0.57	0.81	2.57
100 μm	X	99.90	-0.10	0.72	1.58
	Y	99.34	-0.66	0.68	2.69
500 μm	X	500.24	0.24	0.10	2.46
	Y	499.11	-0.90	1.40	3.24
1000 μm	X	1001.46	1.46	0.84	5.22
	Y	1000.28	0.28	0.82	3.84

As the commanded step size decreases below 100 μm, both absolute and relative errors increase. At 10 μm, the mean error in X is -0.18 μm (1.8 %) and in Y -0.59 μm (5.9 %). At

the smallest tested step size of 1 µm, the X-direction still achieves an average step of 0.90 µm (-0.10 µm mean error). In contrast, the Y-direction shows a clear deviation from the nominal value, reaching only 0.26 µm on average, which corresponds to a 73.7 % reduction relative to the intended step size.

Across all tested step sizes, the X-axis consistently outperforms the Y-axis in terms of both accuracy and repeatability. The mean error in the X-direction ranges from 1.46 µm at a nominal step size of 1000 µm to -0.10 µm at 1 µm. In contrast, the Y-direction shows greater variability with predominantly negative errors, ranging from 0.28 µm to -0.74 µm over the same step size range. The standard deviation of the executed steps is also lower in the X-direction under most conditions. While a single motor drives the X-axis, the Y-axis relies on two motors running in parallel. Imperfect synchronization between these two motors may have contributed to the observed inaccuracies and variability, particularly at smaller step sizes.

Overall, the system provides reliable and repeatable step performance for nominal step sizes of 10 µm and above, particularly in the X-direction. For step sizes below 10 µm, performance in the Y-direction degrades significantly. At 1 µm, the average displacement in Y reaches only 0.26 µm, indicating a reduction of approximately 74 % relative to the commanded step size. In contrast, the X-direction remains usable down to 1 µm with a relative error of around 10 %.

4.5.3.3 Backlash characterization

Backlash refers to small amounts of unintended motion that occur when a mechanical system reverses direction. This effect is usually caused by minor gaps between transmission components, such as the threads of the lead screw and the matching ball screw nut used to convert rotational motion into linear motion. To quantify this effect using the three-axis linear robot, a bidirectional scanning protocol was employed. A snake-like scan pattern was used, in which the robot performed continuous movements along one axis while incrementally advancing along the perpendicular axis. This scanning procedure was carried out in both directions, with step sizes of 50 µm. The results are shown in Figure 4.8.

The analysis revealed measurable backlash in both movement directions. In the X-direction, the intended step size of 50 µm resulted in an average displacement of 47.77 µm, indicating a deviation of 2.23 µm. In the Y-direction, the average displacement was 48.17 µm, corresponding to a deviation of 1.83 µm.

In most MHz-dOCT imaging scenarios, such levels of mechanical play are unlikely to pose a significant problem, as the current lateral resolution of the system is limited to approximately 3 µm. Additionally, large-area imaging is typically performed with some

overlap between adjacent volumes, which further reduces the impact of small positioning errors. Further reduction of backlash could be achieved by improving the mechanical fit of the coupling components.

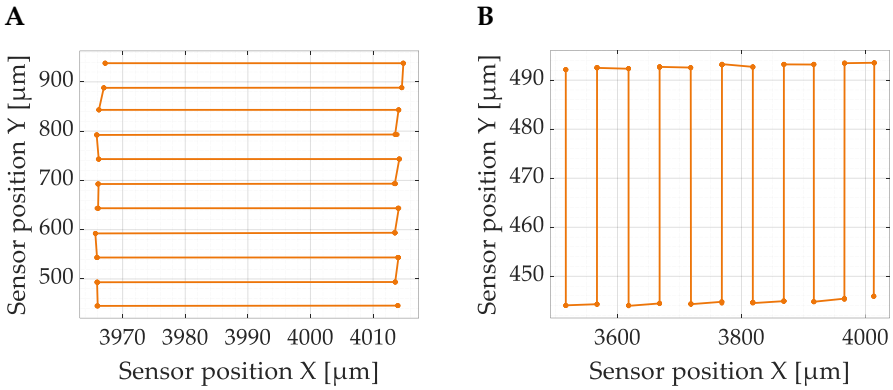

Figure 4.8 Snake-like scan paths used for backlash evaluation in X- and Y-directions. (A): The scan path used to assess backlash along the X-axis by executing repeated horizontal movements at incremented Y-positions. (B): The corresponding procedure for evaluating backlash along the Y-axis involves vertical displacements at fixed X-positions. In both cases, the stepwise motion follows a snake-like pattern, allowing detection of direction-dependent deviations that occur when the movement direction changes.

4.5.3.4 Revisitation error analysis

To evaluate revisitation error, which refers to the spatial deviation observed when a robotic imaging system attempts to return to a previously visited position, a series of OCT scans was performed from the same predefined location using the three-axis linear robot. For this experiment, only the scan block was used, consisting of the two galvanometric scanners and the fiber collimator. Before each scan, the robot was moved 50 mm away from the target position in all spatial directions and then returned to the original location. The scans were conducted using a simple 50 mm spherical scan lens with a FOV of 4.5 x 4.5 mm².

A 1951 USAF resolution target (R1DS1P, Thorlabs Inc., USA) was used as the sample because its high-contrast, well-defined grid structures effectively help in detecting even small positional deviations. This procedure was repeated three times. The resulting *en face* projections were assigned the colors red, green, and blue and then combined using the open-source software Fiji. In the absence of revisitation error, the overlay of repeated scans would result in a uniform grayscale image. Any visible color fringing reveals misalignments between scans and provides a qualitative indication of revisitation inaccuracy.

The results of the revisitation experiment are illustrated in Figure 4.9. The left column shows the three individual *en face* projections, each assigned to one of the red, green, and blue color channels. The right panel displays the resulting composite overlay. A magnified

region highlights group 2, element 4 of the 1951 USAF resolution target. The composite image reveals subtle color shifts along the vertical edges of the test pattern. A slight purple tint appears on the left edge, while a greenish hue is visible on the right. The color fringing pattern further suggests that the first and second scans, as well as the second and third scans, are laterally offset along the horizontal. The offset is approximately 3 pixels, corresponding to 14 µm, whereas the first and third scans appear well aligned. In contrast, the horizontal edges show no noticeable fringing, suggesting consistent alignment in the vertical direction.

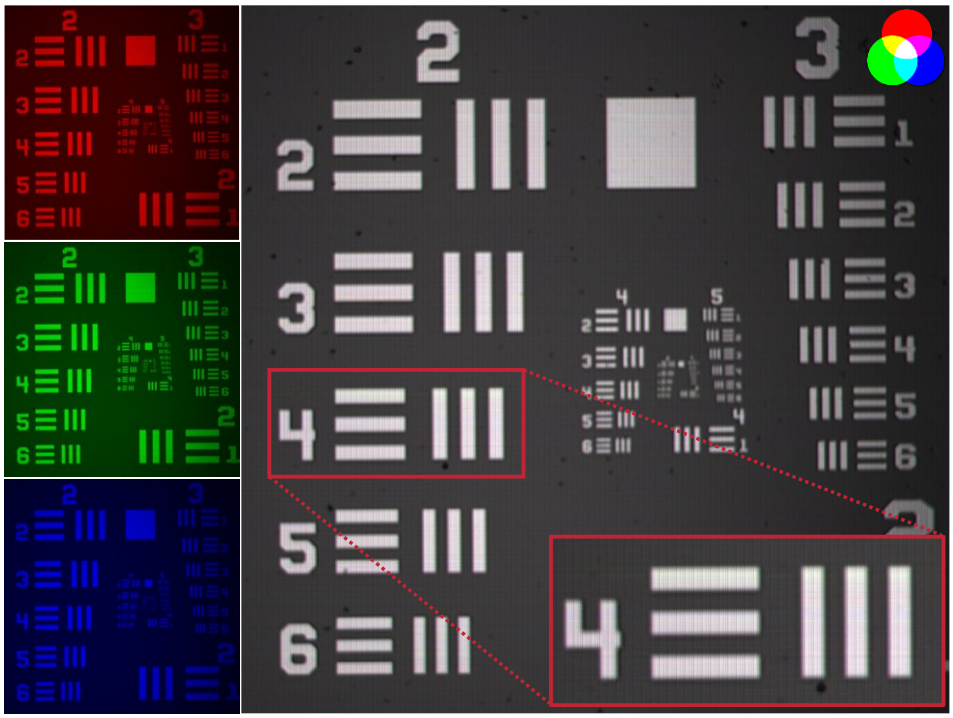

Figure 4.9 RGB overlay of repeated OCT scans on a 1951 USAF test target. A 1951 USAF resolution target was scanned three times from the same predefined position to assess positioning accuracy. Before each scan, the three-axis linear robot was moved 50 mm away from the predefined target position in all directions and then returned to that position for acquisition. The resulting images were color-coded (red, green, blue) and overlaid using Fiji to visualize alignment deviations.

These observations indicate that revisitation deviations occurred primarily along the X-direction, whereas the Y-direction remained stable. Therefore, smaller step sizes in the X-axis may be required, which would necessitate adjusting the gear ratio. Furthermore, as this measurement was performed only once, potential inaccuracies during the acquisition cannot be excluded. However, the absence of visible misalignment in the Y-axis also suggests that the use of two stepper motors for parallel Y-axis movement did not introduce measurable positioning errors in the image. No definitive conclusions can be drawn regarding the Z-direction based on this image, as deviations along this axis would primarily

result in a change in focus rather than a visible shift or color fringe in the overlay. However, visual inspection of the three individual images revealed no noticeable loss of sharpness, suggesting that no significant defocus occurred during any of the repeated scans.

These observations show that while minor horizontal misalignments may occur between repeated scans, the overall positional consistency of the robotic system is sufficiently high to support reliable dOCT imaging. Moreover, the observed precision is fully adequate for large-area dOCT imaging, where scan regions are intentionally acquired with overlap to enable image stitching.

4.5.4 Image registration and volume stitching

To enable volumetric imaging over an extended FOV, multiple adjacent scans were acquired and subsequently merged into a single, composite dataset. For this, the scan head was sequentially positioned at four distinct locations, as indicated in Figure 4.10. Red arrows illustrate the order and direction of movement. Using the 10X microscope objective, each scan captured a lateral FOV of 1.4 x 1.4 mm², with an approximately 15 % overlap between adjacent volumes to ensure seamless stitching. Figure 4.11 displays the dOCT result of an *ex vivo* porcine kidney sample extracted from the renal pyramids within the inner medullary region. A stitched cross-sectional *en face* image at 40 µm depth is shown alongside the stitched three-dimensional scan. The resulting composite dataset has a total FOV of around 2.6 x 2.6 mm² and is densely sampled with 4096 x 4096 x 600 voxels.

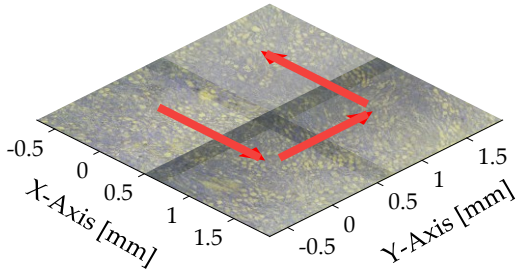

Figure 4.10 Movement path of the linear robot. Four sequentially acquired subvolumes were merged into a composite dataset covering a large area of the renal medulla. Red arrows indicate the scan order and direction of movement between individual acquisitions.

To combine the volumes into a single, large-area representation, a multi-step registration and blending process was used. First, the volumes were registered using the open-source software Elastix [155], accessed via the Python interface itk-elastix. This interface allows Elastix to be embedded directly within the Insight Toolkit (ITK) [156], a widely used open-source framework for medical image processing. Instead of running Elastix as a standalone command-line tool, the interface enables registration tasks to be performed directly within a Python environment using ITK data structures. The algorithm

minimizes a cost function that quantifies alignment quality by iteratively optimizing the transformation parameters. Mutual information is used as the similarity metric to determine the spatial correspondence between the volumes. The resulting transformations were then applied, and each volume was mapped to a common coordinate system. The registration was carried out on the four dOCT volumes.

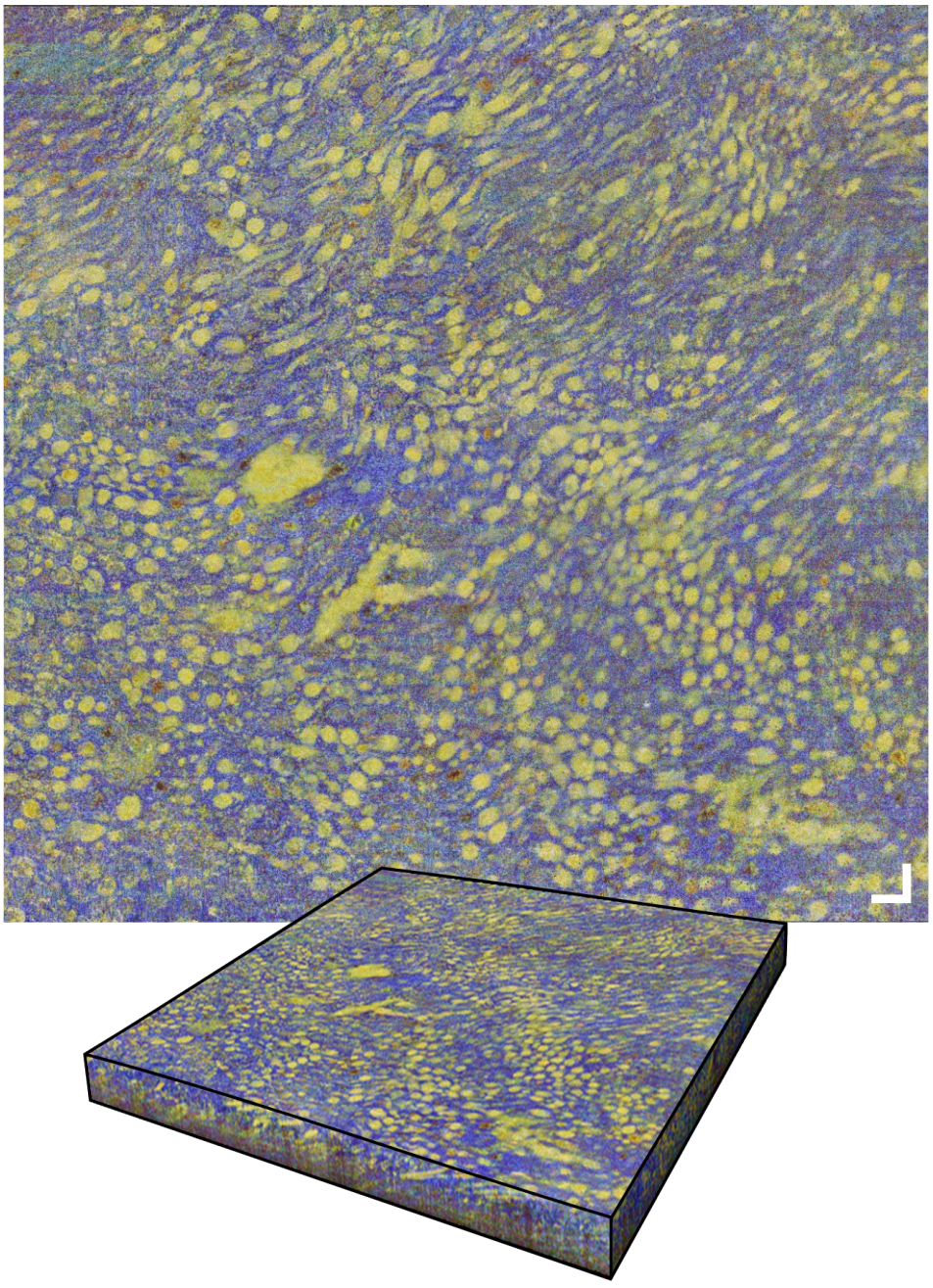

Figure 4.11 Large-area dOCT imaging of the inner medullary region. The top panel shows the dOCT *en face* image at a depth of 40 μm. Yellow-green elongated and rounded structures stand out against a blue background, corresponding to Henle's loops and collecting ducts. The bottom panel shows the 3D stitched dOCT volume. The scale bar represents 100 μm.

After registration, the following processing steps were carried out in MATLAB. Histogram matching was performed using a reference column taken from the *en face* image within the focal region of the first volume. Column-wise histogram matching across all color channels ensured consistent color distribution among the four stitched volumes. These volumes were then blended using arithmetic averaging to minimize intensity discontinuities in overlapping areas. To enhance visual consistency, hard edges were detected and smoothed.

Then, any color casts caused by the histogram adjustments were corrected by equalizing the average intensity across the three color channels of the entire RGB volume. This global normalization step aligns the red, green, and blue channels to the same mean intensity, ensuring a neutral color balance throughout the dataset. The method is conceptually similar to white balance, but it is applied uniformly to the full volume rather than relying on a specific reference region. The final volume was sharpened and cropped. An intensity attenuation was applied along the depth axis to suppress signal artifacts in the noise-dominated areas that can result from the histogram matching process.

The stitched volume allowed for large-scale visualization of distinct morphological features in the renal medulla. Elongated and rounded yellow-green structures appeared clearly against a primarily blue background. Their shape and spatial distribution match the expected cross-sectional view of Henle's loops and collecting ducts. By examining sequential image slices at different depths, the spatial arrangement of the renal pyramids and the progression of the tubular structures could be analyzed in detail. However, accurately distinguishing between ducts and loops remains challenging, as both exhibit similar scattering characteristics and primarily differ in diameter.

4.6 Non-equidistant temporal scanning

Dynamic OCT relies on acquiring repeated B-scans at the same spatial location to capture temporal fluctuations that reveal tissue activity. In the current scanning protocol, each subvolume is sampled using 50 repeated frames, which took 82 ms. A complete volume consists of 40 such subvolumes, resulting in a total acquisition time of around 2.7 min. Reducing the number of repeated frames to, for example, 20 would shorten this to 1.1 min, offering significant time savings of around 60 %.

However, reducing the number of frames often leads to a substantial loss of dynamic contrast. Although previous studies have shown that even five frames can be sufficient to detect motion [157], this typically results in a pronounced decrease of the dynamic signal. The challenge, therefore, is to find a way to reduce the number of repetitions without severely compromising the quality of the dynamic signal. Functional signals in biological

tissue can span a broad range of temporal frequencies, which depend strongly on the sample type and physiological processes involved. Equidistant sampling, with repeated line scans acquired at uniform time intervals, may not align well with these frequency components. For high-frequency fluctuations, very short sampling intervals are required, whereas low-frequency processes benefit from much longer acquisition times. Using a fixed, equidistant strategy can therefore result in redundant images that add little functional contrast, while at the same time prolonging the overall acquisition.

Non-equidistant temporal scanning provides a potential solution. By distributing frame acquisition times in a non-uniform manner, it becomes possible to target only relevant temporal frequency ranges. This approach could improve sensitivity to relevant dynamic processes while maintaining a low total number of frames. As a result, dynamic contrast can be preserved or potentially even increased despite a reduction in the number of frames.

To validate this approach, it is necessary to systematically investigate whether non-equidistant sampling can preserve dynamic contrast when the number of frames is reduced. A direct comparison with conventional equidistant sampling is essential to evaluate potential improvements in contrast-to-noise ratio (CNR) and dynamic signal. The analysis should examine how different temporal distributions influence the detectability of relevant dynamic features and whether non-equidistant strategies provide a measurable advantage in capturing functional signals.

4.6.1 Contrast-to-noise ratio (CNR)

To assess the effect of different temporal sampling strategies, the CNR was used as a quantitative metric to evaluate how well dynamic regions could be distinguished from background areas in the processed image data.

Rather than relying on Fourier-based analysis, temporal standard deviation was computed directly over selected frames to quantify dynamic activity. A key advantage of this method is that it does not rely on equidistant sampling and can be applied flexibly to time points that are unevenly spaced. Standard deviation is computationally efficient and directly interpretable, allowing consistent comparison across different sampling methods without the need for additional spectral decomposition. Furthermore, since no RGB color coding was applied, the results accurately reflect the actual temporal contrast, without introducing the visual biases often associated with frequency-based representations. This allows for a more direct and unbiased evaluation of the dynamic signal, as the results are based solely on measured intensity fluctuations.

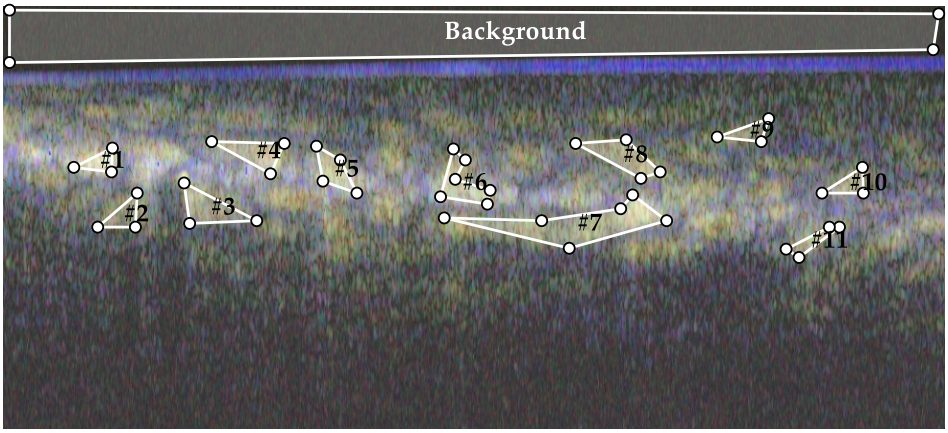

Figure 4.12 Manually annotated background and signal regions. The dynamic image was computed from the OCT time series of 500 frames to visualize dynamic activities in the *ex vivo* kidney cortex sample. One large background region was selected to represent areas with minimal dynamic activity. In contrast, multiple numbered regions of interest were manually defined to capture areas exhibiting dynamic contrast. All regions were interactively marked using polygon tools to enable precise masking. Color channels: Blue >0.5 Hz, green 0.5 - 3 Hz, red 3 - 6 Hz.

To enable region-based signal analysis, specific areas within the dOCT image were manually annotated, as shown in Figure 4.12. To evaluate the impact of different temporal sampling strategies, the dynamic signal was analyzed from an *ex vivo* porcine kidney cortex sample. For annotation purposes only, the dOCT image was calculated using our standard algorithm. A large background region was selected to represent areas without significant dynamic activity, serving as a reference for noise. In addition, multiple regions of interest were manually drawn to capture areas exhibiting dynamic contrast. Each region was interactively marked by the user using polygonal selection tools, allowing flexible and precise masking.

Before analysis, image registration was performed to correct for minor translational shifts between frames using MATLAB's `imregcorr` function. For each region, the mean and standard deviation of the pixel values were then computed. The CNR was calculated using the following equation:

$$CNR = \frac{\overline{m_s} - \overline{m_b}}{\sigma_b}. \tag{4.2}$$

Here, $\overline{m_s}$ and $\overline{m_b}$ denote the mean values in the signal and background regions, respectively. The term σ_b represents the standard deviation of the background noise. Higher CNR values indicate a greater degree of contrast between dynamic and static regions. This metric was used to compare and provide an overview of the performance between the equidistant and non-equidistant sampling strategies.

4.6.2 Comparative analysis of non-equidistant frame selection methods

Using the 20X objective, a total of 11000 frames were acquired as line scans and at a frame rate of 610 Hz, corresponding to a scan duration of about 18 s. To investigate the impact of different temporal sampling strategies, subsets of this dataset were retrospectively analyzed. Specifically, four acquisition configurations were defined by selecting 2000, 5000, 8000, or 11000 consecutive line scans from the full acquisition, thereby simulating shorter or longer scan durations. Within each configuration, a reduced number of frames, ranging from 5 to 50, was selected per volume using various non-equidistant sampling methods. For each case, the temporal standard deviation was calculated across the selected frames, and the resulting image contrast was quantitatively assessed using the CNR. For comparison, an equivalent equidistant sampling was computed for each condition.

Seven non-equidistant sampling methods, including logarithmic, balanced, chirp-based, and different adaptive strategies, were compared to conventional equidistant sampling across multiple total frame numbers and sampling densities. The MATLAB function is provided in Appendix A.3.

To illustrate their distinct temporal spacing, representative examples of each sampling strategy were generated for a total of 2000 frames and are shown in Figure 4.13 to Figure 4.15. This preliminary evaluation was performed to obtain an initial understanding of how the different strategies produce results and to identify potential advantages or limitations before conducting a more detailed analysis focused on the frequency ranges relevant for the sample.

Logarithmic (Log): Frames are distributed according to a logarithmic scale, resulting in dense sampling of high-frequency or fast dynamics.

Balanced: The balanced method selects frame indices according to the Fibonacci sequence. To avoid overrepresenting the smallest Fibonacci numbers, the sequence is transformed using a logarithmic function and then rescaled to the full frame range, resulting in a more even and balanced distribution across the acquisition window. This provides a non-uniform spacing that offers broad temporal coverage, with an emphasis on slower dynamics, while still capturing faster fluctuations.

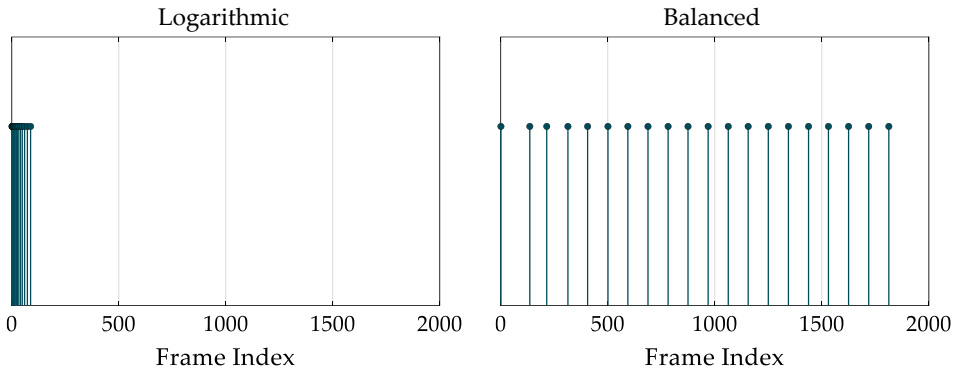

Figure 4.13 Comparison of logarithmic and balanced temporal sampling. This exemplary plot shows a total of 20 selected frames from 2000 input frames. In the logarithmic approach, the sampling is concentrated at early time points, whereas the balanced approach distributes the selected frames across the entire acquisition range.

Linear and quadratic chirp: The two chirp-based strategies progressively reduce the spacing between sampled frames over time, thereby emphasizing slower, low-frequency dynamics by allocating more samples to later time points. In the linear-chirp scheme, the gaps between selected frames narrow gradually. In the quadratic chirp strategy, the intervals between the frames decrease more rapidly over time.

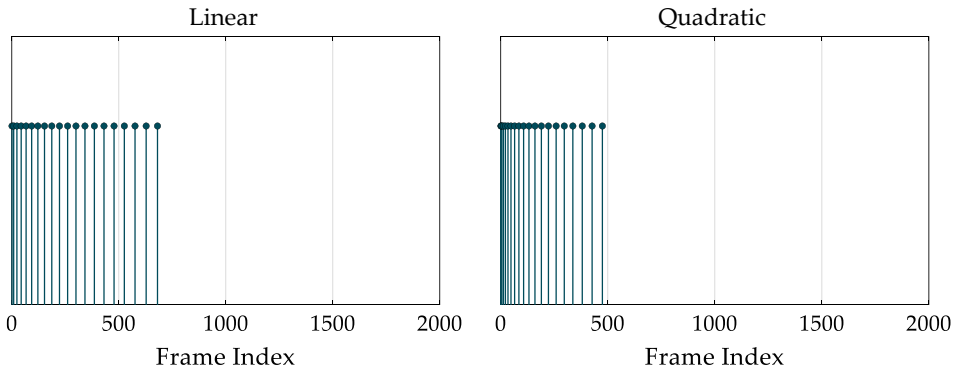

Figure 4.14 Illustration of linear and quadratic chirp sampling. The plot illustrates the selection of 20 frames out of a total of 2000 input frames. In both sampling schemes, the selected frames are concentrated toward the beginning of the acquisition. However, the quadratic chirp (right) emphasizes early time points more strongly than the linear chirp (left).

Adaptive: In one configuration, most frames are allocated to the first ≈ 30 % of the total scan time, providing high temporal resolution for rapid, high-frequency dynamics that appear early and decay quickly. Another variant focuses sampling around the central third of the acquisition window, effectively targeting intermediate frequencies. A third approach allocates most frames toward the end of the scan, thereby enhancing sensitivity to slow, low-frequency processes.

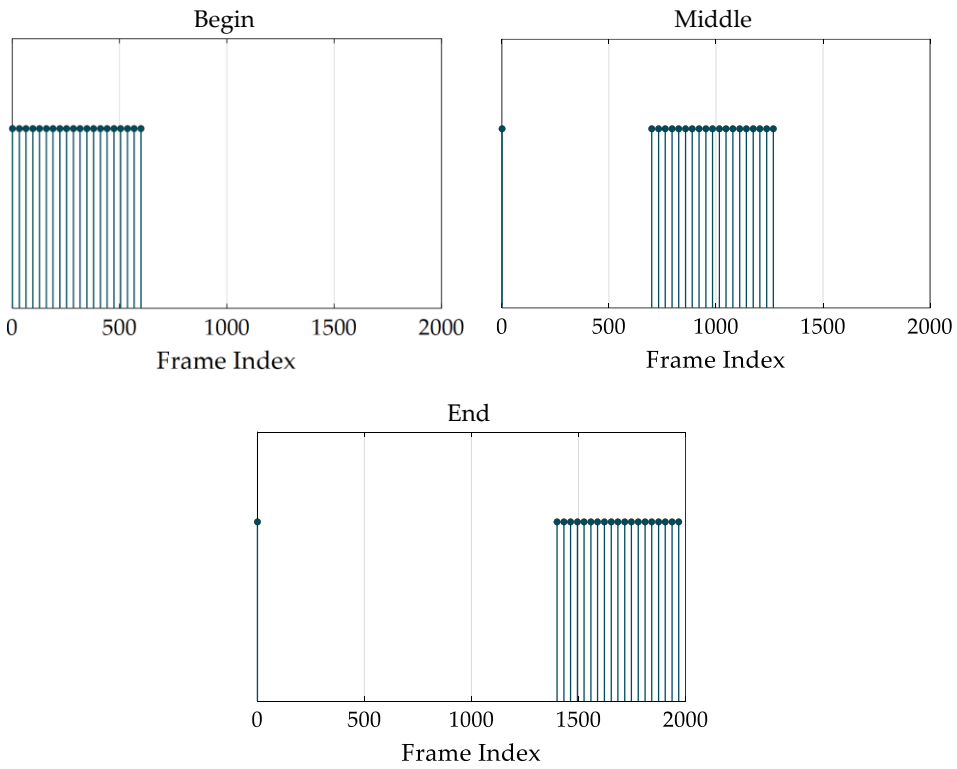

Figure 4.15 Adaptive temporal sampling strategies. The plot shows 20 selected frames from 2000 input frames using three configurations, each concentrating sampling in a specific third of the acquisition to target fast (top left), intermediate (top right), or slow (bottom) temporal dynamics.

4.6.2.1 CNR analysis of equidistant and non-equidistant sampling

Figure 4.16 summarizes the CNR performance of various temporal sampling strategies across four different scan durations. For each configuration, the CNR is plotted as a function of the number of selected frames. The individual sampling methods are color-coded and are listed in the legend. The equidistant reference is shown as a dashed black line.

Across all acquisition lengths, a clear trend is evident. As the number of selected frames increases, the CNR improves accordingly. Furthermore, longer acquisitions consistently result in higher absolute CNR values for the same number of selected frames, indicating that longer temporal sampling provides a more accurate determination of dynamic activity. However, equidistant sampling almost always results in the highest CNR values across all conditions.

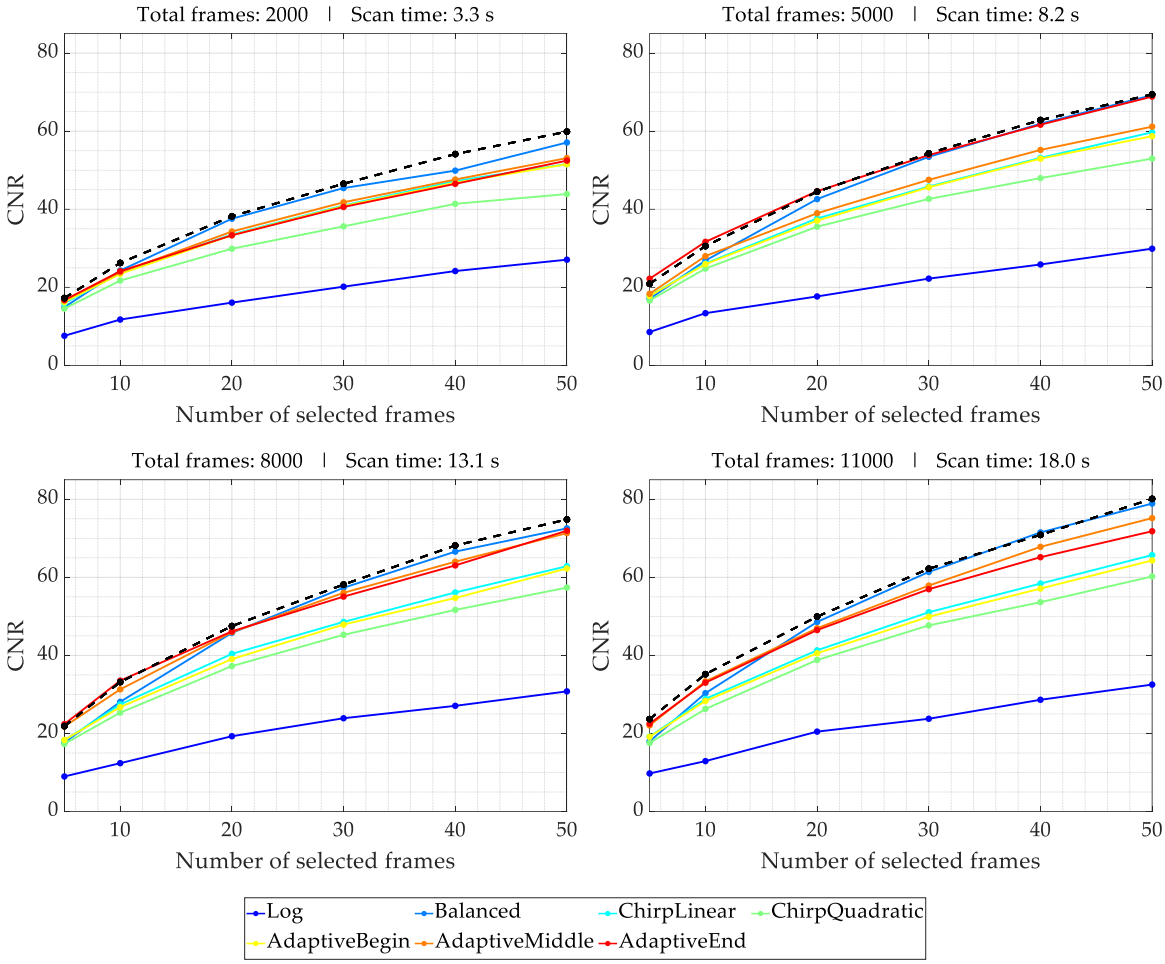

Figure 4.16 Effect of scan duration and sampling strategy on CNR performance. Contrast-to-noise ratio (CNR) is shown as a function of the number of selected frames for four different total frame counts: 2000, 5000, 8000, and 11000 frames, corresponding to scan durations of 3.3 to 18.0 s. Each subplot presents the results for one acquisition length and includes eight non-equidistant sampling strategies: logarithmic, balanced, chirp linear, chirp quadratic, and three adaptive approaches. These are compared to an equidistant reference shown as a dashed black line. With increasing scan duration, all sampling strategies exhibit higher CNR values. The balanced method performs almost comparably to equidistant sampling, whereas logarithmic sampling consistently has the lowest contrast.

When comparing sampling strategies, the balanced method consistently yields CNR values that closely match the equidistant reference, especially at higher total frame counts. This favorable performance is achieved using logarithmically scaled Fibonacci numbers, which results in a well-spread selection of frames across the entire acquisition range. The distribution avoids excessive clustering at either the beginning or end of the scan, allowing both rapid fluctuations and slower dynamic processes to be captured effectively, even with a small number of selected frames. The AdaptiveEnd and AdaptiveMiddle strategies also demonstrate comparatively strong performance across most conditions. In contrast, logarithmic sampling exhibits the lowest performance across all conditions, likely due to

its concentration of frames at early time points and insufficient representation of slower dynamics.

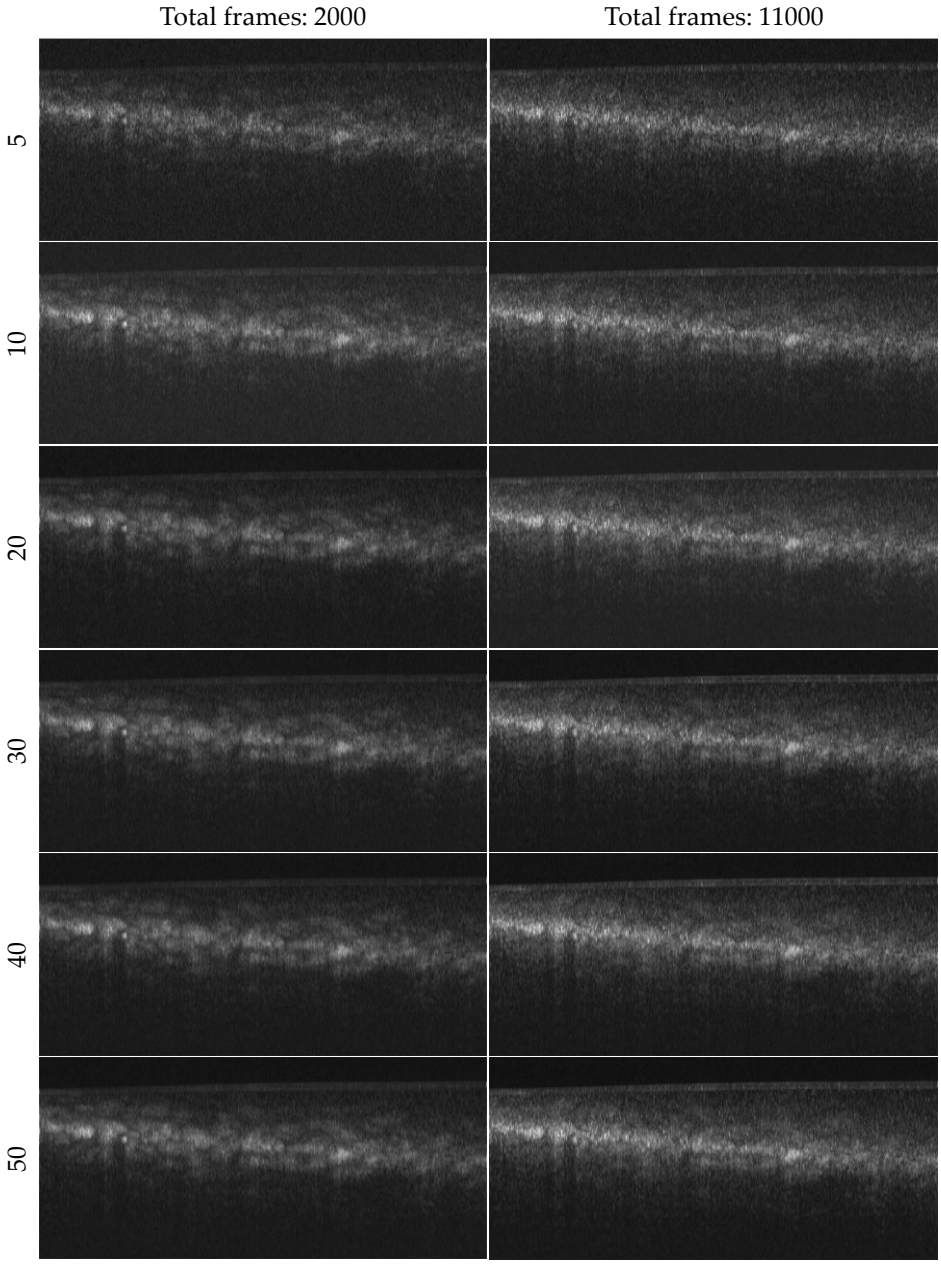

Figure 4.17 Equidistant standard deviation images at increasing sampling densities. Temporal standard deviation images from equidistantly sampled frames are shown at varying sampling densities. Each panel displays a B-scan based on a different number of selected frames from the same OCT acquisition. Bright regions indicate higher temporal fluctuations and dynamic tissue activity.

In addition to the quantitative CNR analysis, the equidistant temporal standard deviation images were also visually assessed across all acquisition lengths. Figure 4.17 shows the results for the shortest and longest scan durations (T = 2000 and T = 11000) for all eval-

uated sampling densities. A consistent observation was that longer scan durations typically result in increasing CNR values in the quantitative analysis. However, these images appeared noisier with longer scan durations, and in some regions where dynamic signals were expected, no clear activity was visible. This reduced visibility is likely caused by increased sample movement, which becomes more pronounced with longer acquisition times, and the image registration applied may not have compensated sufficiently for the movements.

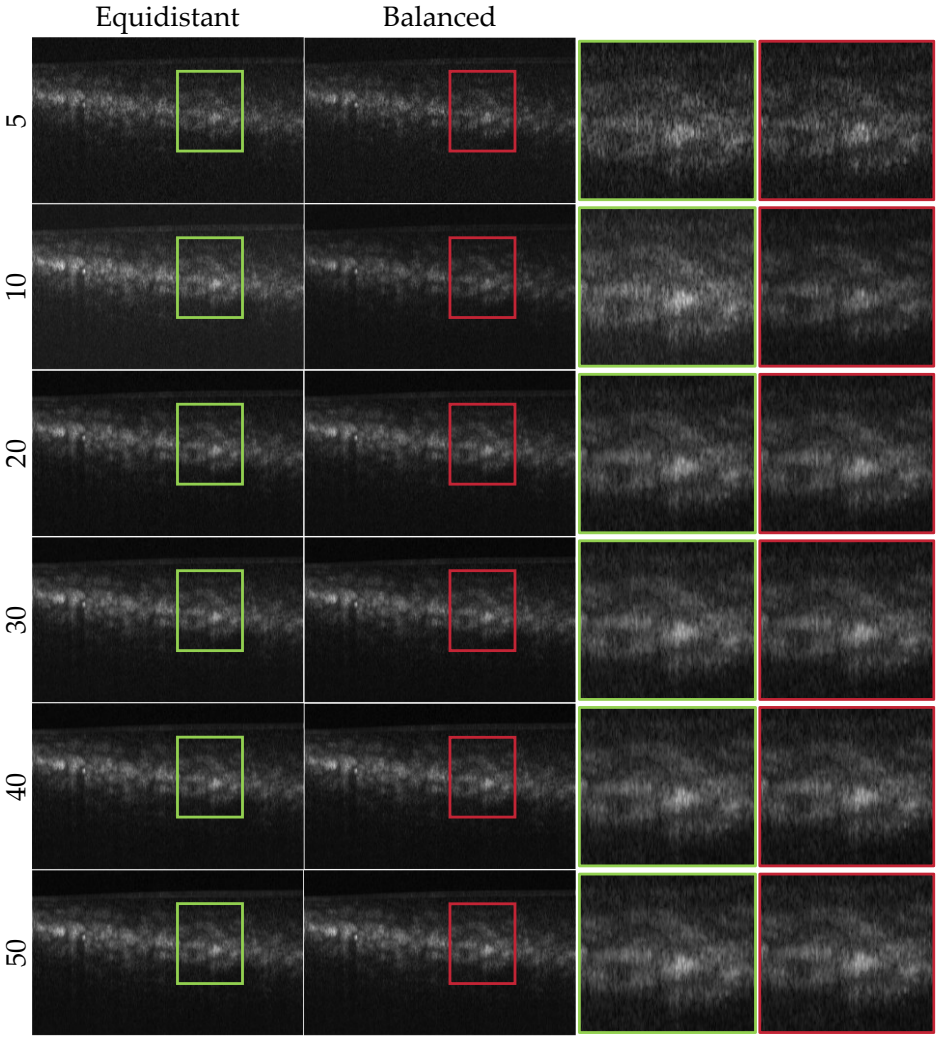

Figure 4.18 Comparison of equidistant and balanced sampling at 2000 frames. Temporal standard deviation images for equidistant (green) and balanced (red) sampling are shown across increasing sampling densities from a 2000 frame acquisition. Each row represents a different number of selected frames, with zoomed-in regions on the right. At low frame counts (up to 20), the balanced method shows clearer structure and stronger contrast. From 30 frames onward, differences become minimal. Overall, non-equidistant sampling yields less noisy images.

Therefore, balanced and equidistant sampling strategies were closely evaluated using a total of 2000 frames. The balanced method was selected due to its consistently strong

performance. Figure 4.18 shows the resulting temporal standard deviation images for both methods at increasing sampling densities. Up to 20 selected frames, the balanced method visibly highlights dynamic regions more clearly than equidistant sampling. From 30 frames onward, no substantial visual difference is observed between the two methods. Although the equidistant approach yields higher CNR values, the resulting standard deviation images appear noticeably noisier compared to those obtained with non-equidistant sampling.

A similar trend was observed for the shorter acquisition with a total of 11000 frames, as shown in Appendix Figure B.1. In this case as well, the balanced sampling strategy provided visibly stronger dynamic contrast in the region of interest at lower sampling densities, particularly up to 20 selected frames. From 30 frames onward, the visual differences between balanced and equidistant sampling diminished, and both methods produced comparable results. This observation aligns with the CNR analysis, which also showed nearly identical values for the balanced and equidistant sampling at and above 30 selected frames.

4.6.3 Analysis of dominant temporal frequency components

While the comparison of temporal standard deviation images provided valuable insights into how different sampling strategies influence the standard deviation images, this analysis does not reveal which specific temporal frequencies contribute most to the observed signal. To better understand the temporal structure of these fluctuations and identify the frequency components most relevant to dynamic contrast generation, a principal component analysis (PCA) was applied to the temporal frequency spectra of the same dataset, aiming to reveal key frequency patterns within the image data.

4.6.3.1 Principal component analysis of the frequency spectrum

Principal component analysis is a mathematical technique used to reduce the complexity of large datasets by identifying patterns that account for the most variation. It does so by transforming the data into a new coordinate system. The new axes, known as principal components, are ordered according to the amount of variance they capture. The first principal component represents the direction of maximum variance in the dataset. The second captures the second-highest variance orthogonal to the first, and so on. This transformation enables a more compact and interpretable representation of the most relevant features present in the signal.

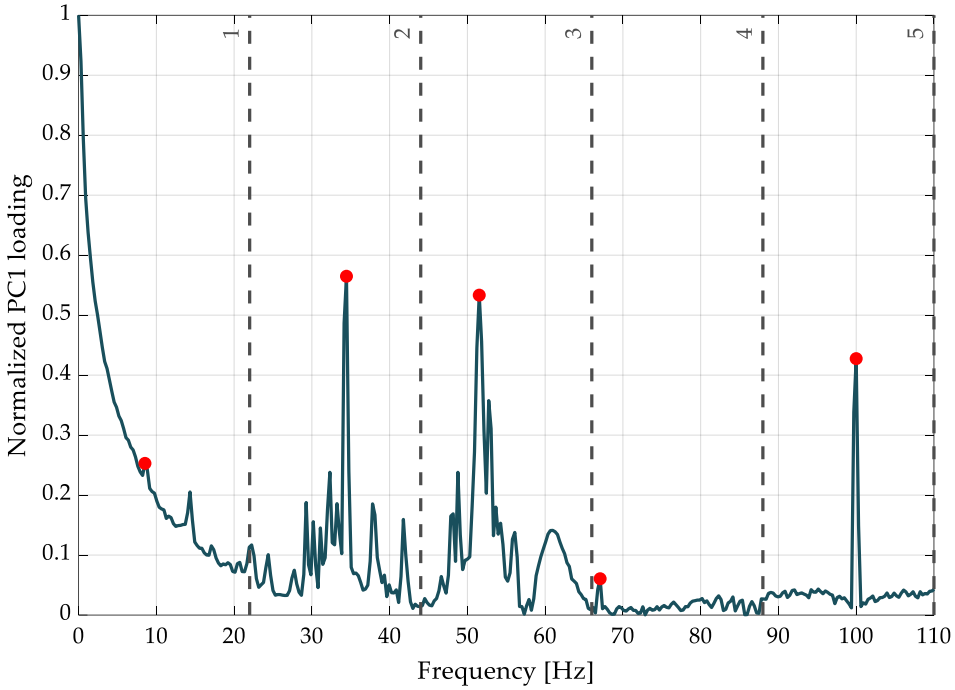

Figure 4.19 Peak detection in PCA-derived frequency spectrum using adaptive bands. The PCA-derived frequency spectrum is divided exemplarily into five bands to ensure broad and balanced coverage across the temporal frequency range. Within each band, the highest peak is marked in red. This visualization represents the first principal component (PC1) obtained from the entire 3D dataset.

The analysis was performed using MATLAB's built-in `pca` function. The two-dimensional linear images acquired over time were first reshaped into a two-dimensional matrix, where each row represents a single pixel from the image, and each column corresponds to a specific time point. A temporal Fourier transform was then applied to each row to obtain the frequency spectrum at each pixel location. This matrix was then used as input for the PCA algorithm. Among the resulting outputs, the most relevant for this analysis is the coefficient matrix, which contains the principal component vectors. Each column represents one principal component, while each row corresponds to a specific time point in the original image sequence. The values in each column indicate the contribution of each frequency to the corresponding principal component, revealing dominant temporal patterns across all pixels. Due to spectral leakage and the observation that the dominant peaks primarily appeared at lower frequencies, the analysis was limited to a frequency range up to 110 Hz.

To ensure broad temporal coverage, the PCA-derived frequency spectrum was divided into various bands. This approach avoids bias toward only low- or high-frequency peaks. It provides broad temporal coverage, which, as shown in the measurements in Section 4.6.2.1, is necessary to achieve the best results. Within each band, the highest spectral peak was identified and selected. These peak frequencies were then converted into peri-

odic frame indices, and the most frequently recurring frames across all bands were determined for use in subsequent non-equidistant sampling. Based on the desired number of total selected frames, the most frequently recurring frame indices were selected. Figure 4.19 shows an example of the peak detection process applied to the PCA-derived frequency spectrum using a five-band division. The highest peak in each band is marked in red. In this example, a noticeable peak was detected near 100 Hz, which is likely due to electronic noise. However, as there was no other distinct peak in this specific band, the 100 Hz peak was selected to ensure that the band was considered in the analysis.

4.6.3.2 PCA-based CNR analysis across various selected bands

To evaluate the influence of the band division on the contrast performance, the PCA-derived temporal spectrum was segmented into varying numbers of bands, ranging from 5 to 50. Within each band, the location of the maximum peak was identified, and the corresponding peak frequencies were then converted into periodic frame indices. For each resulting selection, the standard deviation image was computed, and the CNR was subsequently calculated. The reconstructions were then compared to the equidistant reference, which is shown as a black dashed line. Figure 4.20 illustrates the CNR values obtained across all band numbers.

A clear trend emerges across all six subplots, each corresponding to a different total number of selected frames. As expected, the overall CNR values are lower when fewer frames are selected. In addition, when only five frequency bands are used, the CNR is consistently the lowest. As the number of bands increases, the CNR improves notably, especially in the range from 5 to 15 bands. Beyond 20 bands, the CNR tends to stabilize, with only minor changes observed when the band count is further increased up to 50. In almost all cases, the CNR values obtained using the PCA-guided, non-equidistant frame selection are comparable to or slightly higher than those of the equidistant reference. These findings suggest that dividing the PCA-derived spectrum into around 20 to 30 bands provides sufficiently broad temporal coverage to capture relevant dynamics.

To further evaluate the impact of band selection on visual image quality, standard deviation images were computed for each case. Figure 4.21 presents these results, where each row corresponds to a different total number of selected frames. The image on the left always shows the outcome using only five bands, while the image on the right displays the result for the band count that achieved the highest CNR for that specific total number of selected frames.

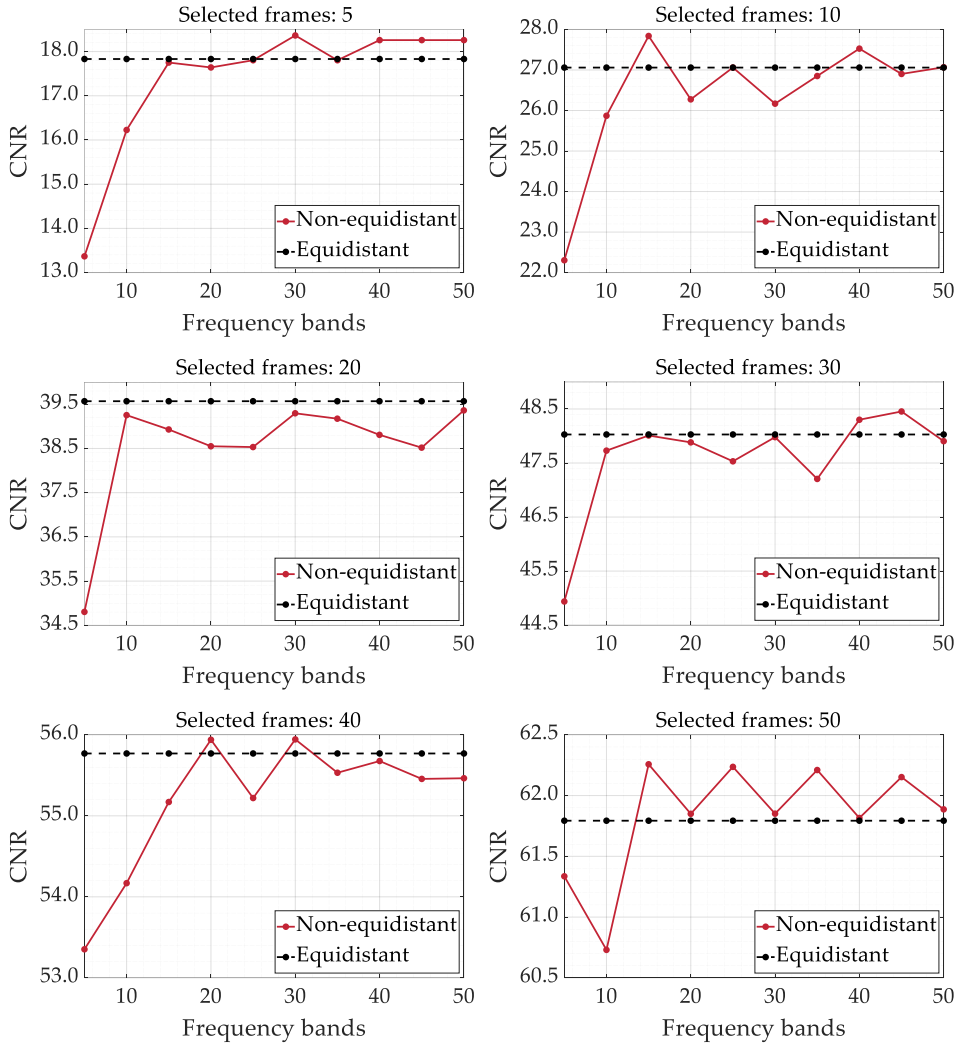

Figure 4.20 CNR performance of PCA-based frame selection. Each panel shows the contrast-to-noise ratio (CNR) using PCA-guided frame selection and band-wise frequency peak detection. For each selection, a standard deviation image was computed before calculating the CNR. The number of frequency bands varied from 5 to 50, and the resulting CNR values (red) are compared against the corresponding equidistant reference (black dashed line). The results are shown for different total numbers of selected frames.

In general, the images obtained with non-equidistant sampling appear less noisy than those acquired with equidistant frame selection. This visual improvement is particularly evident when only a small number of frames are used, where the dynamic regions become more clearly defined and background noise is effectively suppressed. Notably, the band numbers that yield the highest CNR also tend to produce stronger contrast, combining reduced noise with enhanced dynamic signal intensity. However, as the total number of selected frames increases, the visual differences between the two sampling strategies become less pronounced. Notably, the contrast improvements achieved with the non-equidistant approach make it particularly advantageous for reducing acquisition time and data storage requirements without sacrificing image quality.

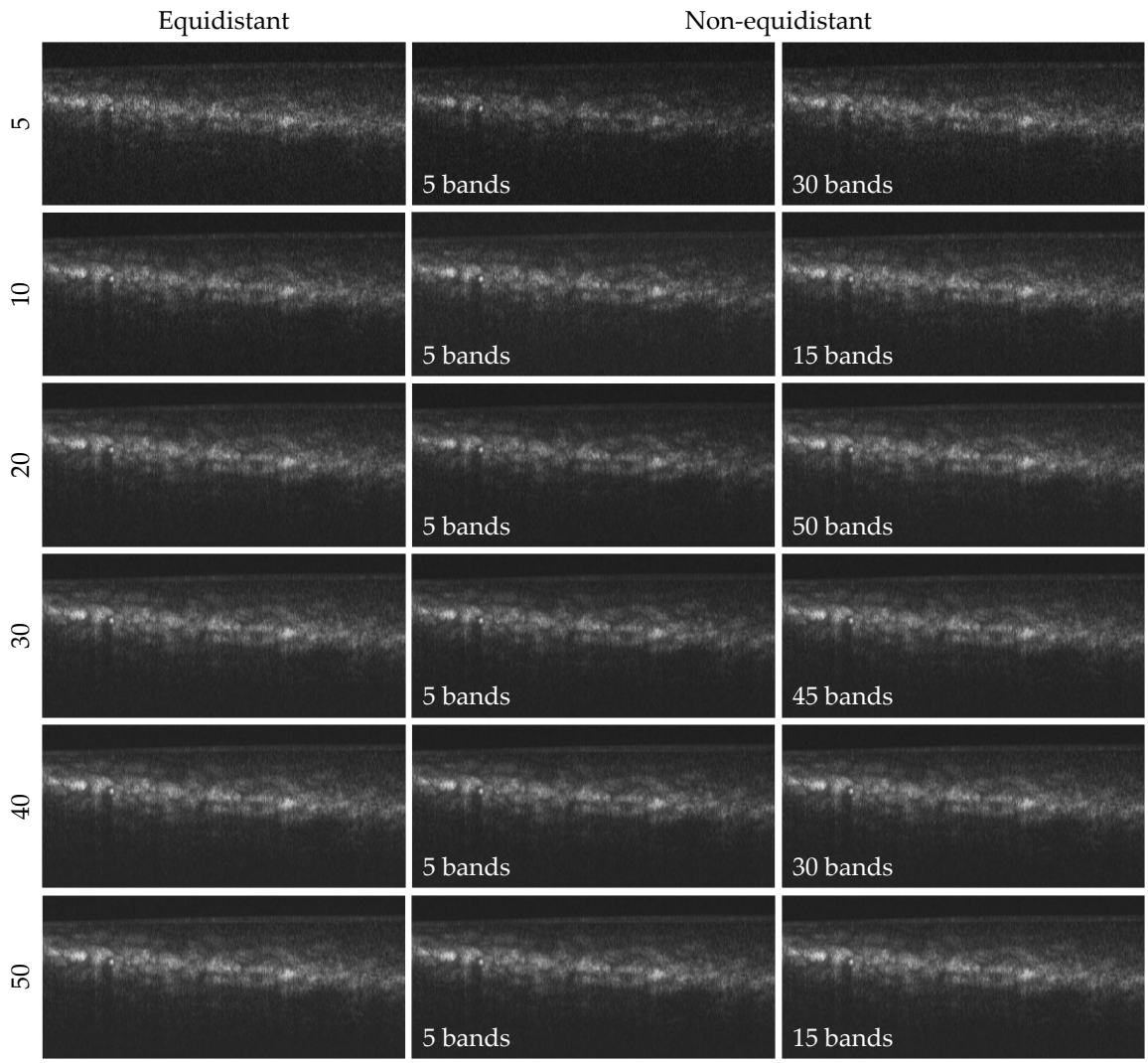

Figure 4.21 Effect of frequency band count on dynamic image contrast. The figure presents standard deviation images computed using PCA-guided, non-equidistant frame selection based on varying numbers of frequency bands. Each row compares two results for the same total number of selected frames. The left image shows the outcome using only five frequency bands, while the right image displays the standard deviation image obtained with the number of bands that achieved the highest CNR for that case.

4.7 Discussion

Accurately assessing tissue viability remains a key challenge in kidney transplantation. In this context, dOCT has become a promising imaging technique capable of detecting subtle temporal variations in scattering tissue, thereby providing functional information in addition to traditional structural imaging. To reliably observe these functional processes, high temporal sampling rates are necessary. Therefore, a 3.2 MHz-OCT system was used in this work to enable the acquisition of densely sampled 3D volumes within a clinically feasible timeframe. However, several technical challenges need to be addressed before clinical adoption. These include achieving adequate spatial resolution over large areas,

reducing the extensive data, and developing sampling methods that improve imaging efficiency without sacrificing contrast quality. This thesis focuses on these issues by evaluating the imaging performance of MHz-dOCT in *ex vivo* porcine kidney tissue, developing a three-axis linear robot for extended-area acquisition, and exploring non-equidistant temporal sampling strategies.

4.7.1 Imaging performance in renal tissue

One focus of this work was to evaluate whether MHz-dOCT provides sufficient spatial and temporal resolution to resolve fine anatomical structures and dynamic tissue properties that could be relevant for kidney assessment. The imaging experiments demonstrated that the system is capable of visualizing functional microscopic processes within the tissue. In the renal medulla, structures such as collecting ducts could be identified, while in the renal cortex, more complex features, including components of the renal corpuscles, were successfully resolved.

Therefore, the axial resolution of approximately 16 µm and lateral resolutions of 3.48 µm with the 10X objective and 2.76 µm with the 20X objective were found to be sufficient for renal tissue imaging. The 10X objective provided a larger FOV and greater depth of focus. In contrast, the 20X objective revealed finer structural details within the focal plane. Volumetric dynamic imaging further enabled a spatially accurate representation of anatomical structures such as renal tubules, which were often difficult to delineate in the cross-sectional images. Therefore, only volumetric functional visualization of the tissue enables accurate assessment of kidney morphology, function, and overall viability in a clinical setting. However, given the optical penetration depth of only 1 - 2 mm, the method is currently limited to superficial imaging of the renal cortex. Accessing deeper medullary regions *in vivo* would require the development of needle-based probes [158].

In comparison to earlier OCT approaches in kidney transplant imaging [145-148], the incorporation of dynamic contrast in this work significantly improves the visualization of characteristic anatomical structures. The renal corpuscles, including the glomeruli, Bowman's space, and capsule, were well-resolved, which may offer valuable insight into pathological changes such as glomerulosclerosis. Comparable to the work by Wierwille et al., who employed Doppler OCT to measure glomerular perfusion *in vivo* [159], the presented method also holds potential for assessing functional parameters in pre-transplant kidney tissue. The *ex vivo* data suggests that MHz-dOCT may detect structural alterations in glomeruli that occur post-excision. Moreover, the imaging approach could support quantitative analysis methods [146, 148]. Parameters such as tubular diameter could provide diagnostic information relevant to identifying tubular necrosis and may serve as imaging biomarkers for assessing organ viability. MHz-dOCT not only provided

a comprehensive three-dimensional visualization of the tubular system but also resolved fine details within individual renal tubules.

Nonetheless, differentiating specific tubular structures in the renal cortex, such as proximal and distal convoluted tubules, remains difficult due to their similar morphology and scattering properties. Improved image resolution may be necessary to achieve clearer separation of these structures. Both healthy and diseased kidney tissue should be imaged to determine whether relevant pathological changes can be reliably detected. Here, a systematic comparison of the dOCT results with corresponding histological sections of the same location would be essential to evaluate the accuracy and clinical relevance of the method. In addition, comparisons with established viability parameters are required to evaluate whether dOCT can provide meaningful information for kidney transplantation. Furthermore, it is not yet clear whether the achieved resolution and contrast are equally effective across other tissue types. Broader validation across various biological samples is needed to assess the generalizability of the system.

4.7.2 Large-area dynamic imaging

A major limitation of the current dOCT systems is the restricted FOV of individual dynamic volumes. Since exchanging scan lenses is not feasible due to the requirement for high lateral resolution, repositioning the scan head is necessary to image larger tissue areas. To address this, a self-built motorized three-axis linear robot with micrometer-level precision was utilized, enabling scanning over areas of 2.6 x 2.6 mm^2 and allowing for flexible extension to larger regions.

A camera-based measurement technique was developed and validated for assessing the performance of the linear robot. The positioning performance of the three-axis linear robot was evaluated across a wide range of set step sizes from 1 µm to 1000 µm. The system demonstrated high accuracy and repeatability, particularly in the X-direction, with mean step errors remaining below ±1.5 µm for larger displacements, corresponding to less than 0.3 % of the commanded step size. For steps smaller than 10 µm, the Y-direction showed increasing deviations, likely due to minor synchronization errors between its dual-motor setup. In contrast, the X-direction maintained reliable behavior even at the smallest tested step size of 1 µm, with only minor deviations. Overall, the robot proved suitable for dOCT imaging. Additional measurements to assess mechanical backlash revealed small, direction-dependent errors, with a maximum deviation of 2.23 µm in the X-direction and 1.83 µm in the Y-direction. These values remain below the lateral resolution of the imaging system and are therefore unlikely to impact imaging performance,

especially since a defined overlap between adjacent scan regions is used for volumetric stitching purposes.

Despite the successful acquisition of large-area datasets through robotic scanning and stitching, residual artifacts remain in the final stitched volume. These artifacts are primarily caused by slight misalignments between adjacent tiles, which may be addressed through more advanced registration algorithms and improved stitching strategies. At present, the registration and stitching procedures are implemented in separate programming environments, which complicates the workflow and can introduce inconsistencies. Unifying these processes within a single, user-friendly software would enhance processing efficiency and accelerate data handling. Particularly in *in vivo* scenarios, identifying and implementing an optimal registration approach remains a challenging task.

Additionally, the large data size of the individual volumes poses a significant challenge for storage, processing, and real-time analysis. Each raw volume, composed of repeated subvolumes, results in a total data size of approximately 480 GB. To manage this, new scanning and processing strategies are required that allow for the acquisition of a broad frequency range while minimizing both acquisition time and data volume. Although not utilized in the current experiments, the robot is fully synchronized with the OCT imaging software, allowing automated coordination between scanning and acquisition. This enables the implementation of more advanced scanning strategies in future applications.

4.7.3 Non-equidistant temporal scanning

One scanning strategy tested in this context was the non-equidistant temporal sampling approach. The aim was to preserve or enhance dynamic contrast while reducing the number of acquired frames by selecting time points that are most relevant for capturing the characteristic temporal behavior of the tissue. This approach seeks to improve imaging efficiency without compromising the quality of the resulting images. Therefore, using *ex vivo* porcine kidney tissue, several non-uniform sampling schemes were compared to conventional equidistant sampling across varying frame counts and scan durations.

The results demonstrate that non-equidistant sampling provides measurable advantages when only a limited number of frames are used. Particularly when fewer than 20 frames are selected, approaches such as the balanced and adaptive strategies showed improved visual contrast compared to equidistant sampling. This suggests that appropriate temporal spacing can preserve dynamic signal strength even when the number of frames is significantly reduced. However, the differences in performance became less pronounced as the number of selected frames increased. Beyond approximately 30 frames, both the CNR and the visual contrast become comparable between the non-equidistant

and equidistant methods. Nonetheless, this is of limited concern because the primary objective is to obtain high-contrast dynamic images using as few frames as possible, which is the case where non-equidistant sampling demonstrates the most benefits.

To identify the frequency components most relevant to the dynamic behavior of the imaged tissue, PCA was applied to the temporal frequency spectrum of the linear OCT data. This method revealed dominant fluctuation patterns within the dataset, which were then used to select frame indices that best represent the underlying temporal dynamics. In this context, the PCA-derived frequency spectrum was divided into several bands, and the most prominent frequency peak within each band was chosen. This strategy resulted in improved dynamic contrast, particularly when using 20 to 30 selected bands. At low sampling densities, the resulting images showed again clearer separation of dynamic regions and reduced background noise compared to conventional equidistant sampling. Although the measured CNR values were often similar or slightly higher, the visual appearance of the images was consistently more informative. This indicates that CNR alone does not always reflect perceived image quality and should therefore not be used as the sole parameter for evaluating dynamic contrast.

Despite the promising results demonstrated in this study, several questions remain unanswered. The optimal sampling strategy has not yet been established, especially given the variability in dynamic behavior across different tissue types. Further research is needed to identify which temporal distributions are best suited for specific tissues. Additionally, the mechanisms underlying the performance differences between sampling strategies are not fully understood and require further detailed analysis.

The current study was limited to grayscale standard deviation images, which offer a simplified representation of dynamic activity but do not capture the more intuitive, color-coded visualizations commonly used in dOCT. It remains unclear how the observed advantages of non-equidistant sampling translate to such visualization methods. Conventional RGB dynamic contrast relies on frequency decomposition methods that assume equidistant temporal sampling. Therefore, applying such techniques to non-uniformly spaced data would require alternative processing approaches, such as a non-uniform Fourier transform or specific algorithms developed to handle irregular temporal spacing. Additionally, all results presented here were based on retrospective selection from fully acquired datasets. This limits the ability to assess practical feasibility, as none of the optimized sampling strategies have been tested during actual imaging procedures.

4.8 Conclusion

This chapter provided a detailed investigation of MHz-OCT for functional tissue imaging using *ex vivo* porcine kidney samples. The MHz-dOCT system enabled functional imaging of the tissue, resolving key anatomical features such as collecting ducts and renal corpuscles with micrometer-scale resolution. Volumetric dynamic imaging proved essential for accurately representing the spatial structure of renal structures. To enable large-area volumetric imaging, a three-axis linear robot was developed and validated, showing high positioning accuracy across various scan ranges. Using this system, multiple overlapping volumes were acquired, registered, and subsequently stitched together into a continuous dataset. To achieve faster and more efficient acquisition, non-equidistant temporal sampling strategies were evaluated and compared to traditional equidistant sampling across various frame counts and scan durations. Additionally, PCA was performed to identify the dominant temporal fluctuation patterns within the dataset, enabling targeted frame selection based on the most relevant frequency components. Non-equidistant temporal sampling preserved or even enhanced dynamic contrast at lower frame counts, especially below 20 frames, leading to images that appeared visually clearer and less noisy than those acquired with equidistant sampling. While these findings demonstrate the potential of dynamic MHz-OCT for efficient functional imaging, several challenges remain. These include real-time implementation, adaptation to different tissue types with varying dynamic behaviors, and implementation of optimized scanning protocols.

5 Outlook

This thesis explored functional imaging techniques for MHz-OCT systems, with a focus on applications in brain tumor detection and on kidney assessment for potential transplant applications. By highlighting the role of mechanical and dynamic tissue properties, the work demonstrates the value of extending OCT with functional capabilities to gain deeper insight into tissue structure and behavior. The following sections outline future directions for improving elastography and dOCT, highlighting the steps necessary to advance these technologies toward clinical translation and real-time surgical guidance.

5.1 Future directions in OCE

Future work in OCE should focus on adapting the system for clinical application. Key areas include integrating the scan head into a robotic arm, utilizing faster resonant scanners to expand the imaging range, and developing motion correction techniques suitable for *in vivo* conditions. Additionally, the potential of alternative contrast mechanisms, including speckle-tracking and AI-based approaches, should be evaluated for their applicability in surgical conditions. Finally, systematic correlation with histopathological findings is necessary to validate the mechanical parameters derived from the OCE setup.

Image registration and motion correction: A critical step toward clinical application is the development of a reliable numerical motion correction strategy suitable for *in vivo* settings, where physiological motion and environmental disturbances can significantly affect measurement accuracy. While phase-based methods provide high precision, they are particularly sensitive to noise and motion, which poses a major challenge in the operating room's dynamic and less-controlled environment. Consequently, it is essential to pre-register phase datasets to accurately identify the unwrapped phase. Regarding this, several registration techniques were evaluated, including cross-correlation of entire volumetric datasets, localized subvolumes registration, and volume registration using the open-source software `elastix` [155]. These preliminary evaluations suggest that the fast imaging rates provided by MHz-OCT make three-dimensional registration and motion correction feasible. However, the implementation is demanding and will require further

research to address technical challenges and ensure robustness in clinical settings. A key difficulty is distinguishing between tissue motion caused by the air-jet excitation, which carries meaningful mechanical information, from bulk motion that must be corrected to ensure accurate elasticity measurements.

Alternative contrast mechanisms for volumetric, real-time imaging: In this context, speckle-tracking offers a promising alternative due to its robustness under varying imaging conditions and its suitability for processing volumetric datasets, which are increasingly important for comprehensive intraoperative assessment. Although it generally provides lower precision than phase-based methods, its ease of implementation and reduced sensitivity to motion artifacts make it a practical tool for generating mechanical contrast in real-time during surgery. A hybrid approach may offer significant advantages, where speckle-tracking is first used for rapid, full-volume screening to identify regions of interest, followed by targeted, high-precision phase-based analysis for detailed mechanical characterization if needed. This strategy integrates the benefits of rapid, full-volume screening with speckle-tracking and the detailed accuracy of phase-based analysis, enabling both efficient assessment and precise mechanical characterization.

In addition to speckle-tracking, a Fourier-based contrast approach has been investigated as a further alternative. This method directly analyzes the frequency content of the complex OCT signal, bypassing the need for explicit phase unwrapping. It offers fast processing and may be well suited for volumetric or intraoperative applications where speed is critical. However, its clinical applicability should be further evaluated, focusing on improving its interpretability and establishing a reliable link between the frequency-domain signal and measurable mechanical properties such as displacement or stiffness.

Robotic arm integration: Within the scope of the overall project, the OCT scan head will be integrated into a robotic arm (KUKA LBR med 14 R820, KUKA AG, Germany). In neurosurgery, access to the target area is often constrained by a small craniotomy, which makes positioning the imaging device particularly difficult. Additionally, surgeons may be required to operate at uncomfortable angles, which increases operator fatigue and the risk of hand tremors, potentially compromising precise positioning. The robotic arm system helps address these ergonomic limitations by enabling stable and flexible imaging from various orientations. For safety reasons, the surgeon will manually guide the scan head rather than operate it autonomously, allowing for controlled adjustment and minimizing the risk of unintended contact with brain tissue. However, further investigations are required to ensure reliable elastography measurements, as the system has not yet been tested in a clinical setting.

Expanding scan range with resonant scanners: In the current configuration, 792 frames consisting of 512 A-scans were acquired at a B-scan rate of 2.45 kHz, resulting in a total acquisition time of 0.32 s. The system employs a galvanometric scanner configured for line scanning and optimized for phase-based OCT, which enables the acquisition of displacement maps. However, this configuration inherently restricts the lateral scan range and spatial coverage. Initial tests indicated that every third B-scan can be used to reduce acquisition time. Nevertheless, obtaining reliable phase information necessitates high temporal sampling, making fast scanning essential. As a result, the current setup restricts the ability to perform broader scans or to image even small volumetric regions efficiently. To overcome these limitations, the use of resonant scanners should be explored. Operating at significantly higher frequencies, resonant scanners offer the potential to extend the lateral scan range and enable faster image acquisition, thereby allowing more comprehensive tissue assessment. Nonetheless, this requires additional development effort in the data acquisition system, as precise synchronization between the OCT laser and the resonant scanner is technically challenging.

AI-based unwrapping approach: Instead of relying only on rule-based algorithms, artificial intelligence (AI) models, such as neural networks, can learn to recognize and correct phase jumps based on training data. In this project, initial tests of an AI-based phase unwrapping approach were carried out using phase maps generated by the proposed unwrapping algorithm as reference data. These maps provided reliable ground-truth information to train the model. However, initial tests showed that the AI model incorrectly unwrapped the phase in background regions, resulting in unrealistic displacement curves. This highlights the need for careful training and validation, particularly in areas with low signal quality. Nevertheless, AI-based unwrapping remains a promising strategy that could improve robustness and speed, especially for real-time applications. Further development is required to improve reliability across varying noise levels and tissue types, including targeted training on background regions, better filtering of non-tissue areas, and refinement of model architectures to handle diverse signal conditions more effectively.

Mechanical characterization and histopathological correlation: Within this project, 16 human brain tumor samples were imaged using the proposed OCE framework. Across these samples, 119 distinct imaging positions were recorded to capture a wide range of tissue characteristics and anatomical variability. Each measurement included an air-jet excitation with a force of approximately 80 μN for phase-sensitive OCE, while a stronger force of around 360 μN was applied for speckle-tracking analysis. Detailed clinical information, including tumor type and WHO grade, is available for each sample. The last 10 samples were additionally processed for histological analysis to enable direct comparison with the elastography findings. This has resulted in a large and diverse dataset with

considerable potential for further investigation. However, a systematic histological evaluation of all samples is still pending. In particular, the mechanical parameters derived from the OCE data must be correlated with the histological features in close collaboration with pathologists to ensure accurate interpretation and clinical relevance. This analysis could provide a foundation for training machine learning models.

5.2 Future directions in dynamic OCT

Dynamic OCT is an emerging modality with significant potential to enhance the functional assessment of biological tissues. While the results presented in this thesis demonstrate the feasibility of MHz-dOCT for imaging kidney tissue, several challenges and areas for further development remain. Future work should address current limitations in data volume, processing speed, interpretability, and system integration to make the method applicable in clinical settings. The following sections highlight important directions for future research.

System validation across diverse tissue types: To establish the robustness and clinical applicability of MHz-dOCT, further evaluation across a wide range of tissue types is essential. While the current work demonstrates the system's potential in renal imaging, other organs have different structural and optical properties that may affect the generation and visualization of the dynamic contrast. While sufficient for renal structures, the current axial resolution may be inadequate for resolving finer microstructures in other organs. This raises the need for tissue-specific optimization of the imaging setup. Systematic testing on various samples will be critical to assess the system's generalizability and verify whether improvements in resolution or contrast mechanisms are required. Correlating dOCT findings with histopathological results will further support the validation.

Integration into live imaging software: Another future goal is integrating the dOCT processing pipeline into the LURO imaging software. This would enable live, low-latency 4D-OCT imaging, allowing dynamic contrast to be visualized directly during the acquisition process. Currently, two home-built post-processing software programs, based on LabVIEW and MATLAB, must be used before any dynamic contrast results can be displayed. As a result, it is currently difficult to determine whether dynamic contrast has been successfully captured during the experiment. Incorporating dynamic processing into LURO would overcome this limitation by providing immediate visual feedback. Since the core processing step for generating dynamic contrast relies primarily on FFTs, the computational load is relatively low, making real-time implementation technically feasible. This functionality could be embedded directly into the existing C++-based LURO software for optimal performance.

Alternatively, a separate processing module could be implemented in a widely used language such as Python, which is generally easier to read and maintain. While this modular approach offers development flexibility by allowing researchers to implement, modify, and test processing routines independently from the main imaging software, it also introduces several important considerations. Developing the processing pipeline in a separate language can simplify algorithm development due to its readable syntax and extensive library support. This would enable faster prototyping, easier debugging, and quicker integration of new processing features. However, it requires efficient data transfer between the imaging software and the external processing module, typically through shared memory or streaming interfaces. This additional complexity may lead to increased latency and reduced performance, especially when low-latency feedback is essential. As a result, while the modular approach can accelerate development and experimentation, its suitability for real-time or clinical applications must be carefully evaluated to ensure that responsiveness and processing speed meet the requirements.

Data size reduction for improved workflow efficiency: Minimizing the data volume is another important step in optimizing the system for clinical use. Current volumetric scans, which include numerous repeated subvolumes for dynamic contrast analysis, produce large datasets that can exceed several hundred gigabytes per measurement. This creates bottlenecks in storage, data transfer, and offline processing, limiting experimental flexibility and clinical feasibility. One strategy to address this is to reduce redundancy in the scanning protocol. This includes avoiding excessive spatial and temporal sampling, such as acquiring more repeated volumes or A-scans than are necessary to extract reliable dynamic contrast. This strategy was evaluated in this thesis using a non-equidistant sampling approach, where only selected volumes were processed to reduce data size and computation time. While initial results were promising, further evaluation is needed to determine the robustness of this approach across various tissue types and imaging conditions. Lowering the amount of data will accelerate analysis workflows and support integration with real-time visualizations.

Automated frequency mapping for RGB contrast: Another promising future direction is the automation of RGB color coding. In the current approach, the frequency ranges mapped to the red, green, and blue channels are often manually selected based on visual assessment, which can introduce subjectivity and inconsistency between datasets. Automating this process would enable the system to identify the most relevant frequency components directly from the data and assign them to color channels in a standardized and reproducible way. Such an approach could involve using signal analysis techniques or machine learning algorithms to detect dominant frequency bands. AI-based frequency selection methods are currently being evaluated within the institute by a different research

group using a SD-OCT system [157]. However, the applicability of this approach for MHz-dOCT has yet to be evaluated. Therefore, further investigation is necessary to determine whether existing models are sufficient or whether alternative frequency selection strategies need to be developed, particularly for live, low-latency applications. Automating this step would improve consistency and objectivity, supporting real-time use by eliminating the need for manual adjustments during or after acquisition.

5.3 Concluding remarks

This thesis has demonstrated the potential of MHz-OCT for functional imaging by integrating high-speed acquisition with contrast mechanisms sensitive to tissue dynamics and mechanical properties. New processing strategies and imaging protocols were developed to extend OCT beyond structural analysis, supporting its future use in applications such as viability assessment and image-guided diagnostics. While further work is needed to address challenges in data management, real-time implementation, and clinical translation, the results presented here provide a solid foundation for the continued advancement of MHz-OCT for functional tissue analysis.

A Code

A.1 Phase unwrapping algorithm

```
function [unwrapped_stack_raw, unwrapped_stack] = unwrap_phase(phase_data,mask,postp)

% ------------------------------------------------------------------------ %
%                                                                          %
% FUNCTION "unwrap_phase": 1D phase unwrapping alogrithm. It uses a        %
% environment-aware predictive method to examine the impact of the         %
% estimated phase value on the phase progression.                          %
%                                                                          %
% phase_data        Raw phase information                                  %
% mask              Image thresholding                                     %
% postp             Post processor where a local median filter is          %
%                   applied to the data, if postp == 1 (default == 0).     %
%                                                                          %
% Sazgar Burhan - December 19, 2023                                        %
% Institute of Biomedical Optics, University of Luebeck                    %
%                                                                          %
% ------------------------------------------------------------------------ %

tic
disp('Unwrapping Stack')

% CPU to GPU.
phase_data = gpuArray(phase_data);

% Handle default cases.
if (~exist('mask','var') | size(mask) == 0) & (~exist('postp','var') | size(postp) == 0)
    mask = 1;
elseif (~exist('mask','var') | size(mask) == 0) & postp == 1
    error('Not enough input argument. Mask is required for post-processing.');
elseif mask == 0
    mask = 1;
end

% Threshold phase data.
phase_data = phase_data.*mask;

% Calculation of the phase shift between subsequent B-scans,
% thus it is checked whether phase wraps occur.
phase_data =  permute(phase_data, [3 1 2]);

% Initialization.
unwrapped_stack_raw = gpuArray(zeros(size(phase_data)));
unwrapped_stack_raw(1:5,:,:) = phase_data(1:5,:,:);

% 1D phase unwrapping to obtain the phase progression over time.
for t = 6:size(phase_data,1)-2

    % Initialization.
    j = zeros(1,size(phase_data,2), size(phase_data,3));
    EvoPlus = zeros(1,size(phase_data,2), size(phase_data,3));
```

```
    EvoMinus = zeros(1,size(phase_data,2), size(phase_data,3));
    EvoPhase = zeros(1,size(phase_data,2), size(phase_data,3));
    JerkCorr = zeros(1,size(phase_data,2), size(phase_data,3));
    MDest = zeros(1,size(phase_data,2), size(phase_data,3));

    % LINEAR EXTRAPOLATION
    % Simple linear extrapolation.
    EPol = interp1(unwrapped_stack_raw(t-2:t-1,:,:), 3,'linear', 'extrap');

    % Determining whether a positive or negative correction needs to be
    % made by considering the position of the extrapolation point.
    j(EPol > phase_data(t,:,:)) = 1;
    j(EPol < phase_data(t,:,:)) = -1;

    % Determination of the phase value that is closest to the
    % extrapolation point. q is an integer matrix specifing the desired
    % multiplier of 2π.
    q = round((EPol - phase_data(t,:,:)) ./ (j.*2*pi));
    unwrapped_stack_raw(t,:,:) =  phase_data(t,:,:) + j.*2*pi.*q;

    % CONDITION CHECKS
    % This process assesses the need for supplementary analysis and
    % corrective measures.

    % 1. Does the temporal evolution of the phase signal change if a
    % ±2π correction is made? It examines whether this correction leads
    % to a decrease/increase of the phase and if it matches with j:
    EvoPlus(unwrapped_stack_raw(t-1,:,:) > (phase_data(t,:,:) + sign(j).*2*pi.*(q+1))) =
-1;
    EvoMinus(unwrapped_stack_raw(t-1,:,:) < (phase_data(t,:,:) + sign(j).*2*pi.*(q-1))) =
1;

    EvoPhase(j == EvoPlus) = 1;
    EvoPhase(j == EvoMinus) = -1;

    % 2. Is there a monotonous rise or fall over the past five frames?
    % If the last five derivatives are all positive/negative, it
    % indicates a continuous rise/fall of the phase within this interval.
    MonoRise = all(sign(diff(unwrapped_stack_raw(t-5:t-1,:,:))) == 1);
    MonoFall = all(sign(diff(unwrapped_stack_raw(t-5:t-1,:,:))) == -1);

    % 3. Is the first derivate between the the last two frames greater
    % than π? This indicates that the rate of change of the function or
    % velocity within this interval is significant.
    SignifVel = abs(diff(unwrapped_stack_raw(t-2:t-1,:,:))) > pi;

    % 4. Is the first derivate or velocity increasing between the last two
    % frames? This indicates that the function is becoming steeper,
    % implying an acceleration of the phase signal.
    VelInc = abs(diff(unwrapped_stack_raw(t-2:t-1,:,:),1)) > abs(diff(un-
wrapped_stack_raw(t-3:t-2,:,:),1));

    % Set conditions.
    Dec = (EvoPhase == 1) & MonoFall & (SignifVel | VelInc);
    Inc = (EvoPhase == -1) & MonoRise & (SignifVel | VelInc);

    % ABRUPT DIRECTION CHANGE ANALYSIS
    % Check if sign of the first derivate changes within the current and
    % last frame with sign: R → [-1,1]. If there's a change in sign from
    % positive to negative (or vice versa), it indicates an abrupt
    % direction change of the signal.
    D = all(sign(round(diff(unwrapped_stack_raw(t-2:t,:,:)))) ~= 0);
    D = D & sign(round(diff(unwrapped_stack_raw(t-1:t,:,:)))) ~= sign(round(diff(un
wrapped_stack_raw(t-2:t-1,:,:))));

    % MINIMIZE JERK
    % Assuming a mostly constant acceleration value between two frames,
    % the displacement should experience minimal jerk over time.
    Jerk = floor(abs(diff(unwrapped_stack_raw(t-3:t,:,:),3))) ~= 0;
```

```
    % Note: The jerk is examined more closely in the next steps
    % (see JERK ANALYSIS below). Therefore, the variable JerkCorr
    % was introduced.
    JerkCorr(Jerk & ~D) = 1;

    % UNWRAP PHASE
    q(Inc & (D | Jerk)) = q(Inc & (D | Jerk)) - 1;
    q(Dec & (D | Jerk)) = q(Dec & (D | Jerk)) + 1;

    unwrapped_stack_raw(t,:,:) = phase_data(t,:,:) + j.*2*pi.*q;

    % FORECAST FUTURE POSITIONS
    % An environment-aware predictive approach is used to examine the
    % impact of the estimated phase value on the phase progression of the
    % next two frames. Since it is known that a wrong correction distorts
    % the phases of all following ones, errors can be identified and
    % rectified with this method.

    % Forecasting of the next two phase values for the estimated case.
    PredPhaseEst = futurePositions(unwrapped_stack_raw,phase_data,0,t,3);
    % Forecasting of the next two phase values, if a +2π correction
    % is made.
    PredPhasePlus = futurePositions(unwrapped_stack_raw,phase_data,2*pi,t,3);
    % Forecasting of the next two phase values, if a -2π correction
    % is made.
    PredPhaseMinus = futurePositions(unwrapped_stack_raw,phase_data,-2*pi,t,3);

    % ANALYSIS OF PREDICTED PHASE EVOLUTION
    % Determine progression direction within the next three frames.
    PEvoEPol = sign(EPol - unwrapped_stack_raw(t-1,:,:));
    PEvoPlus = sign(diff(PredPhasePlus));
    PEvoMinus = sign(diff(PredPhaseMinus));

    % ABSOLUTE DIFFERENCE FROM THE MEDIAN
    % Here, in the final step, the most probable phase progression case
    % is determined based on the predictive results. For this purpose,
    % the absolute difference from the median (MD) is calculated:

    % Calculate the MD values for both ±2π correction options.
    EstPhase = PredPhaseEst(2:3,:,:);
    MDplus = round(abs(diff(PredPhasePlus(2:3,:,:)) - median(diff(EstPhase(:)),'omit
nan')));
    MDminus = round(abs(diff(PredPhaseMinus(2:3,:,:)) - median(diff(EstPhase(:)),'omit
nan')));

    % If the MDest value is greater than π, a correction should be made.
    MDest(abs(diff(EstPhase) - median(diff(EstPhase(:)),'omitnan')) > pi) = 1;

    % MINIMIZE MD / PREDICTIVE PHASE VALUES ANALYSIS
    % The aim is to select a phase whose MD value is minimal, and where
    % the temporal evolution of the predictive phase values resembles
    % the initally determined phase direction.

    % Requirements:
    % 1. MDest > π.
    % 2. Integer q must be higher than 1.
    % 3. ~JerkCorr: Error which were caused due to the jerk analysis
    % are corrected seperately (see JERK ANALYSIS).
    ReqMAD = MDest & ~JerkCorr & q > 1;

    % Set conditions.
    PosCond = all(PEvoEPol == PEvoPlus) & MDplus == 0;
    NegCond = all(PEvoEPol == PEvoMinus) & MDminus == 0;

    % Apply q factor.
    q(ReqMAD & PosCond) = q(ReqMAD & PosCond) - 1;
    q(ReqMAD & NegCond) = q(ReqMAD & NegCond) + 1;
```

```
    % JERK ANALYSIS
    % Here, ±2pi jumps that were incorrectly determined in the previous
    % steps "MINIMIZE JERK" are corrected.
    ReqAcc = MDest & JerkCorr;

    % Apply q factor.
    q(ReqAcc & MDplus < MDminus) = q(ReqAcc & MDplus < MDminus) - 1;
    q(ReqAcc & MDminus < MDplus) = q(ReqAcc & MDminus < MDplus) + 1;

    % UNWRAPPED PHASE
    unwrapped_stack_raw(t,:,:) =  phase_data(t,:,:) + j.*2*pi.*q;

end

% Skip the last two remaining frames. Otherwise at some last pixels they
% will be wrapped phase errors.
unwrapped_stack_raw = unwrapped_stack_raw(1:t-2,:,:);

% Set background to zero.
unwrapped_stack_raw(isnan(unwrapped_stack_raw)) = 0;

% All phase values should start at zero.
unwrapped_stack_raw = unwrapped_stack_raw - unwrapped_stack_raw(1,:,:);

% GPU to CPU
unwrapped_stack_raw = gather(permute(unwrapped_stack_raw, [2 3 1]));

% Measured time required to run function
disp('Stack Unwrapped')
disp(['Phase Unwrapping Time: ',num2str(toc),' s'])

% POST-PROCESSOR:
% Default case.
if ~exist('postp','var') | size(postp) == 0 , postp = 0; end

if postp == 1
    tic
    disp('Post-Processing Stack')

    unwrapped_stack = postprocessor(unwrapped_stack_raw,mask);

    disp('Stack Post-Proccessed')
    disp(['Post-Processing Time: ',num2str(toc),' s'])

else
    disp('Stack not post-processed')
    unwrapped_stack = nan;
end

end


function [output] = futurePositions(input,phase_data,corr,z,FutNbr)

% ------------------------------------------------------------------------ %
%                                                                          %
% FUNCTION "futurePositions":                                              %
% Calculation of future phase positions.                                   %
%                                                                          %
% input             Unwrapped stack                                        %
% phase_data        Raw wrapped phase data                                 %
% corr              Analyze the effect of a ±2π correction at frame z.     %
% z                 Current frame number                                   %
% FutNbr            Number of phase values that should be predicted.       %
%                   Note that if FutNbr = 1 no future position will        %
%                   be aquired, only that of the current frame z.          %
%                                                                          %
% Sazgar Burhan - October 19, 2023                                         %
% Institute of Biomedical Optics, University of Luebeck                    %
```

```
%                                                                       %
% ------------------------------------------------------------------- %

output = zeros(FutNbr, size(input,2), size(input,3));

if FutNbr == 0
    msg = 'Calculation not possible for zero future positions.';
    error(msg)

else

    if corr == 0
        output(1,:,:) = input(z,:,:);
    end

    if corr ~= 0
        output(1,:,:) = input(z,:,:)  + corr;
    end

    if FutNbr > 1
        for idx = 2:FutNbr
            % Simple linear interpolation
            input(z-1+(idx-1),:,:) = output(idx-1,:,:);
            EPol = interp1(input(z-1+(idx-2):z+(idx-2),:,:), 3,'linear', 'extrap');

            % Determine if a positive or negative correction has to be made.
            j = zeros(1, size(input,2), size(input,3));
            j(EPol < phase_data(z+(idx-1),:,:)) = -1;
            j(EPol > phase_data(z+(idx-1),:,:))= 1;

            % Determination of the phase value that is closest to the
            % extrapolation point. q is an integer matrix specifing
            % the desired multiplier of 2π.
            q = round((EPol-phase_data(z+(idx-1),:,:))./(2*pi.*sign(j)));

            % Future phase positions.
            output(idx,:,:) = phase_data(z+(idx-1),:,:) + j.*2*pi.*q;
        end
    end
end
end


function unwrapped_stack = postprocessor(unwrapped_stack,mask)

% ------------------------------------------------------------------- %
%                                                                     %
% FUNCTION "postprocessor":                                           %
% Applies a local median filter to remove outliers.                   %
%                                                                     %
% unwrapped_stack   Unwrapped stack                                   %
% mask              Image thresholding                                %
%                                                                     %
% Sazgar Burhan - October 19, 2023                                    %
% Institute of Biomedical Optics, University of Luebeck               %
%                                                                     %
% ------------------------------------------------------------------- %

% Pad.
mask = padarray(mask, [2 2],0);
unwrapped_stack = padarray(unwrapped_stack, [2 2],0);

% If the phase in the last frame differs to much from its vertically
% adjacent neighbor, it will be corrected.
dPhase = diff(unwrapped_stack(:,:,end),1,1);

for y = 1:size (unwrapped_stack,2)
    for x = 1:size (unwrapped_stack,1)
        if mask(x,y) == 1 && abs(dPhase(x,y)) > pi
```

```
            % 5x5 window.
            MedMask = unwrapped_stack(x-2:x+2,y-2:y+2,:);

            % Ignore zero background values.
            MedMask(MedMask == 0) = nan;

            % 5x5 local median.
            unwrapped_stack(x,y,:) = median(median(MedMask,'omitnan'),'omitnan');

            % Recalculate the phase difference.
            dPhase(x:end,y) = diff(unwrapped_stack(x:end,y,end),1,1);

        end
    end
end

% Unpad
unwrapped_stack = unwrapped_stack(5:end,5:end,:);

end
```

A.2 Fourier analysis algorithm

```
% ------------------------------------------------------------------------ %
%                                                                          %
% This script provides an alternative approach to Optical Coherence       %
% Elastography (OCE) by processing complex OCT data to visualize tissue   %
% dynamics. The output is a color-coded image that highlights tissue       %
% motion at various frequencies, which is useful for visualizing           %
% biomechanical properties of tissues.                                     %
%                                                                          %
% Sazgar Burhan, May 05, 2025                                              %
% Institute of Biomedical Optics, University of Luebeck                    %
%                                                                          %
% ------------------------------------------------------------------------ %

% Step 1: Calculate complex data
Stack.calcComplexData();

% Step 2: Remove intensity background information
CData = Stack.cpx.Z(1:396,:,:) ./ Stack.cpx.Magnitude(1:396,:,:);

% Step 3: Apply Hanning window
L = length(CData); % Signal length
Window3D = bsxfun(@times, bsxfun(@times, hamming(1,'symmetric'), hamming(1,"symmet-
ric").'), permute(hamming(L,'symmetric'), [3 2 1]));
CDataWin = CData .* Window3D;

% Step 4: Fourier transform calculation
nFFT = 2^nextpow2(L); % Transform length
FFTAmpNoInt = abs(fft(CDataWin, nFFT, 3)); % FFT calculation

% Step 5: Adaptive histogram equalization and frequency ranges
clear RGBImage_adap;

% Red - fast frequencies
% Green - medium frequencies
% Blue - slow frequencies

% Set divider for datasets with varying lengths
x = round(3 * size(FFTAmpNoInt, 3) / 2 / 512);
y = round(10 * size(FFTAmpNoInt, 3) / 2 / 512);
z = round(25 * size(FFTAmpNoInt, 3) / 2 / 512);
```

```
% Display frequency ranges
HzFactor = 2450 / size(FFTAmpNoInt, 3) / 2;
disp('Frequency Ranges:')
disp(['[1.0000 - ', num2str(x * HzFactor), ' Hz]']);
disp(['[', num2str(x * HzFactor), ' - ', num2str(y * HzFactor), ' Hz]']);
disp(['[', num2str(y * HzFactor), ' - ', num2str(z * HzFactor), ' Hz]']);

% Frequency band calculation and RGB color coding
B = sum(FFTAmpNoInt(4:end,:,1:x), 3) .* AMPbin(1:393,:);
G = sum(FFTAmpNoInt(4:end,:,x:y), 3) .* AMPbin(1:393,:);
R = sum(FFTAmpNoInt(4:end,:,y:z), 3) .* AMPbin(1:393,:);

RGBImage = zeros(size(R, 1), size(R, 2), 3);
RGBImage(:,:,1) = R;
RGBImage(:,:,2) = G;
RGBImage(:,:,3) = B;

RGBImage = uint8(rescale(RGBImage, 0, 255));

% Step 6: Apply Adaptive Histogram Equalization
RGBImage_adap(:,:,1) = adapthisteq(RGBImage(:,:,1), 'NumTiles', [8 8], 'ClipLimit', 0.1,
'NBins', 1024, 'Distribution', 'uniform');
RGBImage_adap(:,:,2) = adapthisteq(RGBImage(:,:,2), 'NumTiles', [8 8], 'ClipLimit', 0.1,
'NBins', 1024, 'Distribution', 'uniform');
RGBImage_adap(:,:,3) = adapthisteq(RGBImage(:,:,3), 'NumTiles', [8 8], 'ClipLimit', 0.1,
'NBins', 1024, 'Distribution', 'uniform');

% Apply local median filter
RGBImage_adap = LocalMedian(RGBImage_adap, AMPbin, 0);

% Step 7: Display Results
figure('Units', 'normalized', 'Position', [0.25 0.25 0.4 0.535], 'visible', 'on');
imagesc(RGBImage_adap);
axis off;
set(gcf, 'Color', 'w');

% Local median function
function data = LocalMedian(data,mask,thresh)

% ------------------------------------------------------------------------ %
%                                                                          %
% FUNCTION "LocalMedian":                                                  %
% Applies a local median filter to remove outliers                         %
%                                                                          %
% data   Image with noise and outliers                                     %
% mask   Global image threshold                                            %
%                                                                          %
% Sazgar Burhan, March 23, 2023                                            %
% Institute of Biomedical Optics, University of Luebeck                    %
%                                                                          %
%                                                                          %
% ------------------------------------------------------------------------ %

% Pad.
mask = padarray(mask, [2 2],0);
data = padarray(data, [2 2],0);

% If the phase differs to much from its vertically adjacent neighbor,
% it will be corrected.
dPhase = diff(data(:,:,1),1,1);

for y = 1:size (data,2)
    for x = 1:size (data,1)
        if mask(x,y) == 1 && abs(dPhase(x,y)) > thresh

            % 5x5 window.
            MedMask = data(x-2:x+2,y-2:y+2,:);

            % 5x5 local median.
```

```
            data(x,y,:) = median(median(MedMask,'omitnan'),'omitnan');

            % Recalculate the phase difference.
            dPhase(x:end,y) = diff(data(x:end,y,end),1,1);

        end
    end
end

% Unpad
data = circshift(data,2,1);
data = data(5:end,5:end-2,:);

end
```

A.3 Non-equidistant sampling strategies

```
function selectedFrames = applySamplingStrategy(method, totalFrames, numSamples,
varargin)
%   applySamplingStrategy selects frame indices using common non-equidistant
%   temporal sampling schemes.
%
%   selectedFrames = applySamplingStrategy (method, totalFrames, numSamples)
%   returns a 1×numSamples vector containing the frame numbers (1-based) to
%   acquire out of a total of TOTALFRAMES.
%
%   INPUT ARGUMENTS
%   ---------------
%   method       Character array or string specifying the sampling method.
%                Accepted values (case-insensitive):
%                   'log'             - logarithmic spacing (dense early)
%                   'balanced'        - balanced sequence scaling
%                   'chirplinear'     - linear-power chirp (mild late bias)
%                   'chirpquadratic'  - quadratic-power chirp (strong late bias)
%                   'adaptivebegin'   - frames in first 30 % of timeline
%                   'adaptivemiddle'  - frames in middle 30 %
%                   'adaptiveend'     - frames in last 30 %
%
%   totalFrames  Total number of frames available in the raw acquisition.
%   numSamples   Desired number of frames to keep.
%
%   OPTIONAL ARGUMENTS (NAME-VALUE PAIRS)
%   -------------------------------------
%   'alpha'      Alpha parameter for the exponential method (default = 4).
%
%   OUTPUT ARGUMENTS
%   ----------------
%   selectedFrames  1×numSamples vector with sorted, unique frame indices.
%
%   NOTES
%   -----
%   * Frame 1 is guaranteed to be included in the output.
%   * When a method initially yields fewer or more than NUMSAMPLES indices,
%     the function adds or removes frames to meet the exact target count
%     while preserving the overall temporal weighting.
%

methodLower = lower(method);

switch methodLower
    %---------------------------------------------------------------------
    % 1) Logarithmic spacing - dense sampling of early, fast dynamics
    %---------------------------------------------------------------------
    case 'log'
        rawFrames = round(logspace(0, log10(totalFrames), numSamples*2));
```

```
        selectedFrames = unique(rawFrames);

    %--------------------------------------------------------------------
    % 2) Balanced spacing - smooth non-uniform coverage, slow-dynamic bias
    %--------------------------------------------------------------------
    case 'balanced'
        fibSeq = [1 2];
        while fibSeq(end) < totalFrames*10
            fibSeq(end+1) = fibSeq(end) + fibSeq(end-1);
        end
        scaledFib = round(rescale(log(fibSeq), 1, totalFrames));
        selectedFrames = unique([1, scaledFib]);

    %--------------------------------------------------------------------
    % 3) Linear-chirp spacing - mild late bias (power = 1.5)
    %--------------------------------------------------------------------
    case 'chirplinear'
        rawFrames = round((linspace(0,1,numSamples*2).^1.5) * (totalFrames-1)) + 1;
        selectedFrames = unique([1, rawFrames]);

    %--------------------------------------------------------------------
    % 4) Quadratic-chirp spacing - pronounced late bias (power = 2)
    %--------------------------------------------------------------------
    case 'chirpquadratic'
        rawFrames = round((linspace(0,1,numSamples*2).^2) * (totalFrames-1)) + 1;
        selectedFrames = unique([1, rawFrames]);

    %--------------------------------------------------------------------
    % 5) Adaptive Begin - first 30 % of timeline (fast dynamics)
    %--------------------------------------------------------------------
    case 'adaptivebegin'
        selectedFrames = round(linspace(1, round(0.3*totalFrames), numSamples));
        selectedFrames = unique([1, selectedFrames]);

    %--------------------------------------------------------------------
    % 6) Adaptive Middle - middle 30 % (intermediate dynamics)
    %--------------------------------------------------------------------
    case 'adaptivemiddle'
        startIdx = round(0.35*totalFrames);
        endIdx   = round(0.65*totalFrames);
        selectedFrames = round(linspace(startIdx, endIdx, numSamples));
        selectedFrames = unique([1, selectedFrames]);

    %--------------------------------------------------------------------
    % 7) Adaptive End - last 30 % (slow dynamics)
    %--------------------------------------------------------------------
    case 'adaptiveend'
        startIdx = round(0.7*totalFrames);
        selectedFrames = round(linspace(startIdx, totalFrames, numSamples));
        selectedFrames = unique([1, selectedFrames]);

    otherwise
        error('applySamplingStrategy_thesis:UnknownMethod', ...
            'Unknown sampling method "%s".', method);
end

% --------------------------------------------------------------------
% Post-processing: enforce sample count and frame-1 inclusion
% --------------------------------------------------------------------
selectedFrames = unique(selectedFrames);

% Ensure frame 1 is included
if ~ismember(1, selectedFrames)
    selectedFrames = unique([1, selectedFrames]);
end

% Trim or extend to exact NUMSAMPLES frames
if numel(selectedFrames) > numSamples
    selectedFrames = selectedFrames(1:numSamples);
```

```
elseif numel(selectedFrames) < numSamples
    extras = setdiff(1:totalFrames, selectedFrames);
    needed = numSamples - numel(selectedFrames);
    selectedFrames = unique(sort([selectedFrames, datasample(extras, needed, 'Replace',
false)]));
end
end

% ========================================================================
function val = getArg(args, name, default)
%GETARG  Retrieve a name-value pair or return default.
idx = find(strcmpi(args, name), 1, 'first');
if ~isempty(idx) && idx + 1 <= numel(args)
    val = args{idx + 1};
else
    val = default;
end
end
% ========================================================================
```

B Supplement material

B.1 Comparison of equidistant and balanced sampling

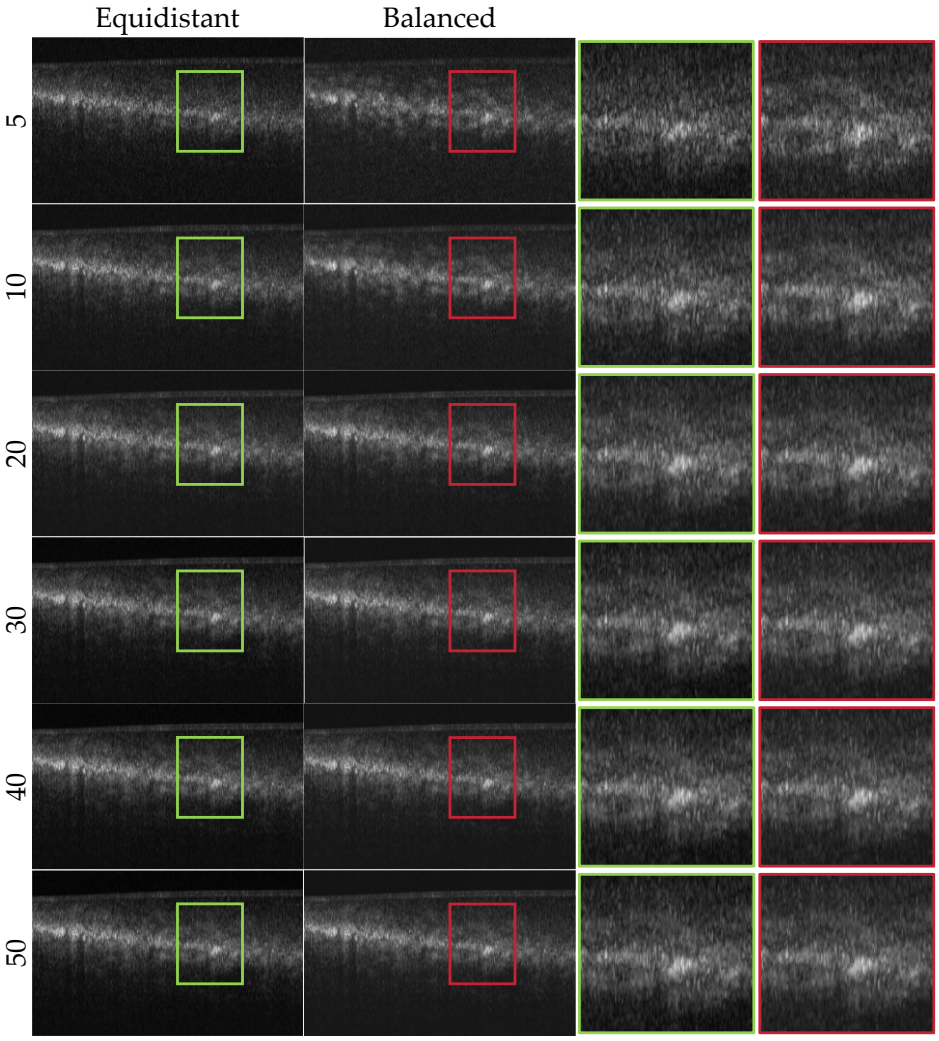

Figure B.1 Comparison of equidistant and balanced sampling at 11000 frames. Temporal standard deviation images are shown for equidistant (left column, green boxes) and balanced (right column, red boxes) sampling strategies, evaluated using a total of 11000 frames and increasing numbers of selected frames. Each row corresponds to a different sampling density. At lower sampling densities, the balanced method reveals finer dynamic detail compared to equidistant sampling. At higher frame counts, the visual difference between the two methods diminishes, which corresponds with the CNR analysis.

Bibliography

1. D. Huang, E. A. Swanson, C. P. Lin, J. S. Schuman, W. G. Stinson, W. Chang, M. R. Hee, T. Flotte, K. Gregory, C. A. Puliafito, and J. G. Fujimoto, "Optical Coherence Tomography," Science **254**, 1178-1181 (1991).
2. J. G. Fujimoto, C. Pitris, S. A. Boppart, and M. E. Brezinski, "Optical coherence tomography: an emerging technology for biomedical imaging and optical biopsy," Neoplasia (New York, N.Y.) **2**, 9-25 (2000).
3. W. Drexler, M. Liu, A. Kumar, T. Kamali, A. Unterhuber, and R. Leitgeb, "Optical coherence tomography today: speed, contrast, and multimodality," Journal of biomedical optics **19**, 071412 (2014).
4. A. Fercher, W. Drexler, C. Hitzenberger, and T. Lasser, "Optical Coherence Tomography—Principles and Applications," Rep. Prog. Phys **66**(2003).
5. S. Aumann, S. Donner, J. Fischer, and F. Müller, "Optical Coherence Tomography (OCT): Principle and Technical Realization," in *High Resolution Imaging in Microscopy and Ophthalmology: New Frontiers in Biomedical Optics*, J. F. Bille, ed. (Springer International Publishing, Cham, 2019), pp. 59-85.
6. H. Molly Subhash and R. Wang, "Optical Coherence Tomography: Technical Aspects," Biomedical Optical Imaging Technologies, Biological and Medical Physics, Biomedical Engineering. ISBN 978-3-642-28390-1. Springer-Verlag Berlin Heidelberg, 2013, p. 163, 163 (2013).
7. M. R. Hee, D. Huang, E. A. Swanson, and J. G. Fujimoto, "Polarization-sensitive low-coherence reflectometer for birefringence characterization and ranging," J. Opt. Soc. Am. B **9**, 903-908 (1992).
8. J. F. de Boer, C. K. Hitzenberger, and Y. Yasuno, "Polarization sensitive optical coherence tomography - a review [Invited]," Biomed. Opt. Express **8**, 1838-1873 (2017).
9. Z. Chen, T. E. Milner, S. Srinivas, X. Wang, A. Malekafzali, M. J. C. van Gemert, and J. S. Nelson, "Noninvasive imaging of in vivo blood flow velocity using optical Doppler tomography," Optics letters **22**, 1119-1121 (1997).
10. Y. Zhao, Z. Chen, C. Saxer, S. Xiang, J. F. de Boer, and J. S. Nelson, "Phase-resolved optical coherence tomography and optical Doppler tomography for imaging blood flow in human skin with fast scanning speed and high velocity sensitivity," Optics letters **25**, 114-116 (2000).
11. J. Izatt, M. Kulkarni, S. Yazdanfar, J. Barton, and A. Welch, "In vivo bidirectional color Doppler flow imaging of picoliter blood volumes using optical coherence tomography," Optics letters **22**, 1439-1441 (1997).
12. R. A. Leitgeb, L. Schmetterer, W. Drexler, A. F. Fercher, R. J. Zawadzki, and T. Bajraszewski, "Real-time assessment of retinal blood flow with ultrafast acquisition by color Doppler Fourier domain optical coherence tomography," Opt. Express **11**, 3116-3121 (2003).
13. B. R. White, M. C. Pierce, N. Nassif, B. Cense, B. H. Park, G. J. Tearney, B. E. Bouma, T. C. Chen, and J. F. de Boer, "In vivo dynamic human retinal blood flow imaging

using ultra-high-speed spectral domain optical Doppler tomography," Opt. Express **11**, 3490-3497 (2003).
14. B. J. Vakoc, S. H. Yun, J. F. d. Boer, G. J. Tearney, and B. E. Bouma, "Phase-resolved optical frequency domain imaging," Opt. Express **13**, 5483-5493 (2005).
15. B. J. Vakoc, R. M. Lanning, J. A. Tyrrell, T. P. Padera, L. A. Bartlett, T. Stylianopoulos, L. L. Munn, G. J. Tearney, D. Fukumura, R. K. Jain, and B. E. Bouma, "Three-dimensional microscopy of the tumor microenvironment in vivo using optical frequency domain imaging," Nature Medicine **15**, 1219-1223 (2009).
16. R. K. Wang, S. L. Jacques, Z. Ma, S. Hurst, S. R. Hanson, and A. Gruber, "Three dimensional optical angiography," Opt. Express **15**, 4083-4097 (2007).
17. Y. K. Tao, A. M. Davis, and J. A. Izatt, "Single-pass volumetric bidirectional blood flow imaging spectral domain optical coherence tomography using a modified Hilbert transform," Opt. Express **16**, 12350-12361 (2008).
18. L. An, J. Qin, and R. K. Wang, "Ultrahigh sensitive optical microangiography for in vivo imaging of microcirculations within human skin tissue beds," Opt. Express **18**, 8220-8228 (2010).
19. J. K. Barton and S. Stromski, "Flow measurement without phase information in optical coherence tomography images," Opt. Express **13**, 5234-5239 (2005).
20. A. Mariampillai, B. A. Standish, E. H. Moriyama, M. Khurana, N. R. Munce, M. K. K. Leung, J. Jiang, A. Cable, B. C. Wilson, I. A. Vitkin, and V. X. D. Yang, "Speckle variance detection of microvasculature using swept-source optical coherence tomography," Optics letters **33**, 1530-1532 (2008).
21. C. Blatter, B. Grajciar, T. Schmoll, R. Leitgeb, T. Klein, W. Wieser, R. André, and R. Huber, "Ultrahigh-speed non-invasive widefield angiography," Journal of biomedical optics **17**, 070505 (2012).
22. Z. Liu and D. X. Hammer, "Wide-field choriocapillaris mapping with 3.4 MHz adaptive optics-optical coherence tomography angiography," Biomed. Opt. Express **16**, 3255-3269 (2025).
23. R. Huber, M. Wojtkowski, and J. G. Fujimoto, "Fourier Domain Mode Locking (FDML): A new laser operating regime and applications for optical coherence tomography," Opt Express **14**, 3225-3237 (2006).
24. W. Wieser, T. Klein, D. C. Adler, F. Trépanier, C. M. Eigenwillig, S. Karpf, J. M. Schmitt, and R. Huber, "Extended coherence length megahertz FDML and its application for anterior segment imaging," Biomed. Opt. Express **3**, 2647-2657 (2012).
25. M. Azimipour, J. V. Migacz, R. J. Zawadzki, J. S. Werner, and R. S. Jonnal, "Functional retinal imaging using adaptive optics swept-source OCT at 1.6 MHz," Optica **6**, 300-303 (2019).
26. J. V. Migacz, I. Gorczynska, M. Azimipour, R. Jonnal, R. J. Zawadzki, and J. S. Werner, "Megahertz-rate optical coherence tomography angiography improves the contrast of the choriocapillaris and choroid in human retinal imaging," Biomed. Opt. Express **10**, 50-65 (2019).
27. Z. Zhi, W. Qin, J. Wang, W. Wei, and R. K. Wang, "4D optical coherence tomography-based micro-angiography achieved by 1.6-MHz FDML swept source," Optics letters **40**, 1779-1782 (2015).
28. S. Wang, M. Singh, A. L. Lopez, C. Wu, R. Raghunathan, A. Schill, J. Li, K. V. Larin, and I. V. Larina, "Direct four-dimensional structural and functional imaging of

cardiovascular dynamics in mouse embryos with 1.5 MHz optical coherence tomography," Optics letters **40**, 4791-4794 (2015).

29. M. Singh, C. Wu, C. H. Liu, J. Li, A. Schill, A. Nair, and K. V. Larin, "Phase-sensitive optical coherence elastography at 1.5 million A-Lines per second," Optics letters **40**, 2588-2591 (2015).
30. S. Song, W. Wei, B.-Y. Hsieh, I. Pelivanov, T. T. Shen, M. O'Donnell, and R. K. Wang, "Strategies to improve phase-stability of ultrafast swept source optical coherence tomography for single shot imaging of transient mechanical waves at 16 kHz frame rate," Applied Physics Letters **108**(2016).
31. S. Bayer, A. Maier, M. Ostermeier, and R. Fahrig, "Intraoperative Imaging Modalities and Compensation for Brain Shift in Tumor Resection Surgery," International journal of biomedical imaging **2017**, 6028645 (2017).
32. W. Stummer, U. Pichlmeier, T. Meinel, O. D. Wiestler, F. Zanella, and H. J. Reulen, "Fluorescence-guided surgery with 5-aminolevulinic acid for resection of malignant glioma: a randomised controlled multicentre phase III trial," The Lancet. Oncology **7**, 392-401 (2006).
33. S. Y. Ji, J. W. Kim, and C. K. Park, "Experience Profiling of Fluorescence-Guided Surgery I: Gliomas," Brain tumor research and treatment **7**, 98-104 (2019).
34. M. Lacroix, D. Abi-Said, D. R. Fourney, Z. L. Gokaslan, W. Shi, F. DeMonte, F. F. Lang, I. E. McCutcheon, S. J. Hassenbusch, E. Holland, K. Hess, C. Michael, D. Miller, and R. Sawaya, "A multivariate analysis of 416 patients with glioblastoma multiforme: prognosis, extent of resection, and survival," Journal of neurosurgery **95**, 190-198 (2001).
35. G. E. Keles, B. Anderson, and M. S. Berger, "The effect of extent of resection on time to tumor progression and survival in patients with glioblastoma multiforme of the cerebral hemisphere," Surgical Neurology **52**, 371-379 (1999).
36. G. E. Keles, K. R. Lamborn, and M. S. Berger, "Low-grade hemispheric gliomas in adults: a critical review of extent of resection as a factor influencing outcome," Journal of neurosurgery **95**, 735-745 (2001).
37. P. Schödel, K. M. Schebesch, A. Brawanski, and M. A. Proescholdt, "Surgical resection of brain metastases-impact on neurological outcome," International journal of molecular sciences **14**, 8708-8718 (2013).
38. S. Hu, H. Kang, Y. Baek, G. El Fakhri, A. Kuang, and H. S. Choi, "Real-Time Imaging of Brain Tumor for Image-Guided Surgery," Advanced healthcare materials **7**, e1800066 (2018).
39. D. C. A. Bastos, P. Juvekar, Y. Tie, N. Jowkar, S. Pieper, W. M. Wells, W. L. Bi, A. Golby, S. Frisken, and T. Kapur, "Challenges and Opportunities of Intraoperative 3D Ultrasound With Neuronavigation in Relation to Intraoperative MRI," Front Oncol **11**, 656519 (2021).
40. M. Regmi, Y. Li, Y. Wang, W. Liu, Y. Dai, S. Liu, K. Ma, L. Pan, J. Gan, H. Liu, X. Zheng, J. Yang, J. Wu, and C. Yang, "Intraoperative fluorescence redefining neurosurgical precision," International Journal of Surgery **111**, 998-1013 (2025).
41. A. Raheja, V. Tandon, A. Suri, P. Sarat Chandra, S. S. Kale, A. Garg, R. M. Pandey, M. Kalaivani, A. K. Mahapatra, and B. S. Sharma, "Initial experience of using high field strength intraoperative MRI for neurosurgical procedures," Journal of Clinical Neuroscience **22**, 1326-1331 (2015).

42. M. Ferrant, A. Nabavi, B. t. Macq, P. M. Black, F. A. Jolesz, R. Kikinis, and S. K. Warfield, "Serial registration of intraoperative MR images of the brain," Medical Image Analysis **6**, 337-359 (2002).
43. W. A. Hall and C. L. Truwit, "Intraoperative MR-guided neurosurgery," Journal of Magnetic Resonance Imaging **27**, 368-375 (2008).
44. O. M. Carrasco-Zevallos, C. Viehland, B. Keller, M. Draelos, A. N. Kuo, C. A. Toth, and J. A. Izatt, "Review of intraoperative optical coherence tomography: technology and applications [Invited]," Biomed Opt Express **8**, 1607-1637 (2017).
45. O. Bin-Alamer, H. Abou-Al-Shaar, Z. C. Gersey, S. Huq, J. A. Kallos, D. J. McCarthy, J. R. Head, E. Andrews, X. Zhang, and C. G. Hadjipanayis, "Intraoperative Imaging and Optical Visualization Techniques for Brain Tumor Resection: A Narrative Review," Cancers **15**(2023).
46. S. Budday, T. C. Ovaert, G. A. Holzapfel, P. Steinmann, and E. Kuhl, "Fifty Shades of Brain: A Review on the Mechanical Testing and Modeling of Brain Tissue," Archives of Computational Methods in Engineering **27**, 1187-1230 (2020).
47. R. Wang, Z. Ma, and S. Kirkpatrick, "Tissue Doppler optical coherence elastography for real time strain rate and strain mapping of soft tissue," Applied Physics Letters **89**, 144103-144103 (2006).
48. K. V. Larin and D. D. Sampson, "Optical coherence elastography - OCT at work in tissue biomechanics [Invited]," Biomed Opt Express **8**, 1172-1202 (2017).
49. A. L. Oldenburg, R. K. Chhetri, D. B. Hill, and B. Button, "Monitoring airway mucus flow and ciliary activity with optical coherence tomography," Biomed. Opt. Express **3**, 1978-1992 (2012).
50. A. L. Oldenburg, X. Yu, T. Gilliss, O. Alabi, R. M. Taylor, and M. A. Troester, "Inverse-power-law behavior of cellular motility reveals stromal-epithelial cell interactions in 3D co-culture by OCT fluctuation spectroscopy," Optica **2**, 877-885 (2015).
51. M. Münter, M. vom Endt, M. Pieper, M. Casper, M. Ahrens, T. Kohlfaerber, R. Rahmanzadeh, P. König, G. Hüttmann, and H. Schulz-Hildebrandt, "Dynamic contrast in scanning microscopic OCT," Optics letters **45**, 4766-4769 (2020).
52. H. Argani, "Expanded Criteria Donors," Experimental and clinical transplantation : official journal of the Middle East Society for Organ Transplantation **20**, 13-19 (2022).
53. N. Warmuzińska, K. Łuczykowski, and B. Bojko, "A Review of Current and Emerging Trends in Donor Graft-Quality Assessment Techniques," Journal of clinical medicine **11**(2022).
54. A. Dubois, *Handbook of full-field optical coherence microscopy : technology and applications* (Pan Stanford Publishing Pte, Ltd., Singapore, 2016).
55. J. P. Fingler, "Motion Contrast Using Optical Coherence Tomography," Dissertation, California Institute of Technology 2007).
56. J. A. Izatt and M. A. Choma, "Theory of Optical Coherence Tomography," in *Optical Coherence Tomography: Technology and Applications*, W. Drexler and J. G. Fujimoto, eds. (Springer Berlin Heidelberg, Berlin, Heidelberg, 2008), pp. 47-72.
57. B. Braaf, "Angiography and Polarimetry of the Posterior Eye with Functional Optical Coherence Tomography," PhD-Thesis - Research and graduation internal 2015).

58. J. Walther and E. Koch, "14. Optische Kohärenztomographie," in *Band 7 Medizinische Bildgebung*, D. Olaf and M. B. Thorsten, eds. (De Gruyter, Berlin, Boston, 2014), pp. 471-504.
59. A. F. Fercher, C. K. Hitzenberger, G. Kamp, and S. Y. El-Zaiat, "Measurement of intraocular distances by backscattering spectral interferometry," Optics Communications **117**, 43-48 (1995).
60. R. K. Wang, S. J. Kirkpatrick, and M. T. Hinds, "Phase-sensitive optical coherence elastography for mapping tissue microstrains in real time," Applied Physics Letters **90**, 164105 (2007).
61. W. Wieser, "Optische Kohärenztomographie mit Millionen Tiefenschnitten pro Sekunde und hoher Bildqualität," Dissertation, LMU München (2016).
62. O. P. Kocaoglu, T. L. Turner, Z. Liu, and D. T. Miller, "Adaptive optics optical coherence tomography at 1 MHz," Biomed. Opt. Express **5**, 4186-4200 (2014).
63. M. Wojtkowski, R. Leitgeb, A. Kowalczyk, T. Bajraszewski, and A. F. Fercher, "In vivo human retinal imaging by Fourier domain optical coherence tomography," Journal of biomedical optics **7**, 457-463 (2002).
64. J. Fujimoto and E. Swanson, "The Development, Commercialization, and Impact of Optical Coherence Tomography," Investigative ophthalmology & visual science **57**, Oct1-oct13 (2016).
65. W. Wieser, B. R. Biedermann, T. Klein, C. M. Eigenwillig, and R. Huber, "Multi-Megahertz OCT: High quality 3D imaging at 20 million A-scans and 4.5 GVoxels per second," Opt. Express **18**, 14685-14704 (2010).
66. T. Klein and R. Huber, "High-speed OCT light sources and systems [Invited]," Biomed. Opt. Express **8**, 828-859 (2017).
67. Y. Yasuno, *Optical coherence tomography -- principles, implementation, and applications in ophthalmology* (2022).
68. S. H. Yun, G. J. Tearney, J. F. de Boer, N. Iftimia, and B. E. Bouma, "High-speed optical frequency-domain imaging," Opt. Express **11**, 2953-2963 (2003).
69. R. Leitgeb, C. K. Hitzenberger, and A. F. Fercher, "Performance of fourier domain vs. time domain optical coherence tomography," Opt. Express **11**, 889-894 (2003).
70. S. Schneider, "Optical coherence tomography for characterization of nanocomposite materials," Ph.D. thesis Karlsruher Institut für Technologie (KIT), 2020).
71. M. A. Choma, M. V. Sarunic, C. Yang, and J. A. Izatt, "Sensitivity advantage of swept source and Fourier domain optical coherence tomography," Opt. Express **11**, 2183-2189 (2003).
72. R. Huber, M. Wojtkowski, K. Taira, J. G. Fujimoto, and K. Hsu, "Amplified, frequency swept lasers for frequency domain reflectometry and OCT imaging: design and scaling principles," Opt. Express **13**, 3513-3528 (2005).
73. R. Huber, D. C. Adler, and J. G. Fujimoto, "Buffered Fourier domain mode locking: unidirectional swept laser sources for optical coherence tomography imaging at 370,000 lines/s," Optics letters **31**, 2975-2977 (2006).
74. A. F. Fercher, "Inverse Scattering, Dispersion, and Speckle in Optical Coherence Tomography," in *Optical Coherence Tomography: Technology and Applications*, W. Drexler and J. G. Fujimoto, eds. (Springer Berlin Heidelberg, Berlin, Heidelberg, 2008), pp. 119-146.

75. N. George, C. R. Christensen, J. S. Bennett, and B. D. Guenther, "Speckle noise in displays," J. Opt. Soc. Am. **66**, 1282-1290 (1976).
76. J. Goodman, *Speckle Phenomena in Optics: Theory and Applications* (2007).
77. R. Wang and A. Nuttall, "Phase-sensitive optical coherence tomography imaging of the tissue motion within the organ of Corti at a subnanometer scale: a preliminary study," Journal of biomedical optics **15**, 056005 (2010).
78. C. Sun, B. Standish, and V. Yang, "Optical coherence elastography: current status and future applications," Journal of biomedical optics **16**, 043001 (2011).
79. E. Pijewska, I. Gorczynska, and M. Szkulmowski, "Computationally effective 2D and 3D fast phase unwrapping algorithms and their applications to Doppler optical coherence tomography," Biomed. Opt. Express **10**, 1365-1382 (2019).
80. G. Liu, Y. Jia, A. D. Pechauer, R. Chandwani, and D. Huang, "Split-spectrum phase-gradient optical coherence tomography angiography," Biomed. Opt. Express **7**, 2943-2954 (2016).
81. R. M. Goldstein, H. A. Zebker, and C. L. Werner, "Satellite radar interferometry: Two-dimensional phase unwrapping," Radio Science **23**, 713-720 (1988).
82. K. Itoh, "Analysis of the phase unwrapping algorithm," Appl. Opt. **21**, 2470-2470 (1982).
83. M. A. Schofield and Y. Zhu, "Fast phase unwrapping algorithm for interferometric applications," Optics letters **28**, 1194-1196 (2003).
84. R. A. Leitgeb and M. Wojtkowski, "Complex and Coherence-Noise Free Fourier Domain Optical Coherence Tomography," in *Optical Coherence Tomography: Technology and Applications*, W. Drexler and J. G. Fujimoto, eds. (Springer International Publishing, Cham, 2015), pp. 195-224.
85. J. W. Goodman, *Statistical Optics*, 1st ed. (Wiley, New York, 1995).
86. G. Lan, M. Singh, K. V. Larin, and M. D. Twa, "Common-path phase-sensitive optical coherence tomography provides enhanced phase stability and detection sensitivity for dynamic elastography," Biomed. Opt. Express **8**, 5253-5266 (2017).
87. S. Burhan, N. Detrez, K. Rewerts, P. Strenge, S. Buschschlüter, J. Kren, C. Hagel, M. M. Bonsanto, R. Brinkmann, and R. Huber, "Phase unwrapping for MHz optical coherence elastography and application to brain tumor tissue," Biomed. Opt. Express **15**, 1038-1058 (2024).
88. M. L. Bondy, M. E. Scheurer, B. Malmer, J. S. Barnholtz-Sloan, F. G. Davis, D. Il'yasova, C. Kruchko, B. J. McCarthy, P. Rajaraman, J. A. Schwartzbaum, S. Sadetzki, B. Schlehofer, T. Tihan, J. L. Wiemels, M. Wrensch, and P. A. Buffler, "Brain tumor epidemiology: consensus from the Brain Tumor Epidemiology Consortium," Cancer **113**, 1953-1968 (2008).
89. A. Šteňo, J. Buvala, V. Babková, A. Kiss, D. Toma, and A. Lysak, "Current Limitations of Intraoperative Ultrasound in Brain Tumor Surgery," Front Oncol **11**, 659048 (2021).
90. B. Kiesel, J. Freund, D. Reichert, L. Wadiura, M. T. Erkkilae, A. Woehrer, S. Hervey-Jumper, M. S. Berger, and G. Widhalm, "5-ALA in Suspected Low-Grade Gliomas: Current Role, Limitations, and New Approaches," Frontiers in Oncology **11**(2021).
91. R. Díez Valle, S. Tejada Solis, M. A. Idoate Gastearena, R. García de Eulate, P. Domínguez Echávarri, and J. Aristu Mendiroz, "Surgery guided by 5-aminolevulinic fluorescence in glioblastoma: volumetric analysis of extent of

resection in single-center experience," Journal of Neuro-Oncology **102**, 105-113 (2011).
92. E. Harwick, I. Singhal, B. Conway, W. Mueller, R. Treffy, and M. O. Krucoff, "Pinless Electromagnetic Neuronavigation During Awake Craniotomies: Technical Pearls, Pitfalls, and Nuances," World Neurosurgery **175**, e159-e166 (2023).
93. D. Orringer, A. Golby, and F. Jolesz, "Neuronavigation in the surgical management of brain tumors: Current and future trends," Expert review of medical devices **9**, 491-500 (2012).
94. N. Foroglou, A. Zamani, and P. Black, "Intra-operative MRI (iop-MR) for brain tumour surgery," British Journal of Neurosurgery **23**, 14-22 (2009).
95. J. W. Morley, A. W. Goodwin, and I. Darian-Smith, "Tactile discrimination of gratings," Experimental Brain Research **49**, 291-299 (1983).
96. G. M. Della Pepa, G. Menna, V. Stifano, A. M. Pezzullo, A. M. Auricchio, A. Rapisarda, V. M. Caccavella, G. La Rocca, G. Sabatino, E. Marchese, and A. Olivi, "Predicting meningioma consistency and brain-meningioma interface with intraoperative strain ultrasound elastography: a novel application to guide surgical strategy," Neurosurgical focus **50**, E15 (2021).
97. R. M. S. Sigrist, J. Liau, A. E. Kaffas, M. C. Chammas, and J. K. Willmann, "Ultrasound Elastography: Review of Techniques and Clinical Applications," Theranostics **7**, 1303-1329 (2017).
98. Y. K. Mariappan, K. J. Glaser, and R. L. Ehman, "Magnetic resonance elastography: a review," Clinical anatomy (New York, N.Y.) **23**, 497-511 (2010).
99. M. Simon, J. Guo, S. Papazoglou, H. Scholand-Engler, C. Erdmann, U. Melchert, M. Bonsanto, J. Braun, D. Petersen, I. Sack, and J. Wuerfel, "Non-invasive characterization of intracranial tumors by magnetic resonance elastography," New Journal of Physics **15**, 085024 (2013).
100. J. Guo, S. Hirsch, A. Fehlner, S. Papazoglou, M. Scheel, J. Braun, and I. Sack, "Towards an Elastographic Atlas of Brain Anatomy," PLOS ONE **8**, e71807 (2013).
101. B. F. Kennedy, P. Wijesinghe, and D. D. Sampson, "The emergence of optical elastography in biomedicine," Nature Photonics **11**, 215-221 (2017).
102. J. M. Schmitt, "OCT elastography: imaging microscopic deformation and strain of tissue," Opt. Express **3**, 199-211 (1998).
103. R. C. Chan, A. H. Chau, W. C. Karl, S. Nadkarni, A. S. Khalil, N. Iftimia, M. Shishkov, G. J. Tearney, M. R. Kaazempur-Mofrad, and B. E. Bouma, "OCT-based arterial elastography: robust estimation exploiting tissue biomechanics," Opt. Express **12**, 4558-4572 (2004).
104. H.-J. Ko, W. Tan, R. Stack, and S. Boppart, "Optical Coherence Elastography of Engineered and Developing Tissue," Tissue engineering **12**, 63-73 (2006).
105. X. Liang, V. Crecea, and S. A. Boppart, "Dynamic optical coherence elastography: A review," Journal of Innovative Optical Health Sciences **03**, 221-233 (2010).
106. M. Singh, F. Zvietcovich, and K. V. Larin, "Introduction to optical coherence elastography: tutorial," J. Opt. Soc. Am. A **39**, 418-430 (2022).
107. B. F. Kennedy, K. M. Kennedy, and D. D. Sampson, "A Review of Optical Coherence Elastography: Fundamentals, Techniques and Prospects," IEEE Journal of Selected Topics in Quantum Electronics **20**, 272-288 (2014).

108. Q. Fang, L. Frewer, R. Zilkens, B. Krajancich, A. Curatolo, L. Chin, K. Y. Foo, D. D. Lakhiani, R. W. Sanderson, P. Wijesinghe, J. D. Anstie, B. F. Dessauvagie, B. Latham, C. M. Saunders, and B. F. Kennedy, "Handheld volumetric manual compression-based quantitative microelastography," J Biophotonics **13**, e201960196 (2020).
109. K. M. Kennedy, L. Chin, R. A. McLaughlin, B. Latham, C. M. Saunders, D. D. Sampson, and B. F. Kennedy, "Quantitative micro-elastography: imaging of tissue elasticity using compression optical coherence elastography," Scientific reports **5**, 15538 (2015).
110. Z. Quince, D. Alonso-Caneiro, S. A. Read, and M. J. Collins, "Static compression optical coherence elastography to measure the mechanical properties of soft contact lenses," Biomed Opt Express **12**, 1821-1833 (2021).
111. W. M. Allen, P. Wijesinghe, B. F. Dessauvagie, B. Latham, C. M. Saunders, and B. F. Kennedy, "Optical palpation for the visualization of tumor in human breast tissue," Journal of Biophotonics **12**, e201800180 (2019).
112. K. Kennedy, R. McLaughlin, B. Kennedy, A. Tien, B. Latham, C. Saunders, and D. Sampson, "Needle optical coherence elastography for the measurement of microscale mechanical contrast deep within human breast tissues," Journal of biomedical optics **18**, 121510 (2013).
113. K. M. Kennedy, B. F. Kennedy, R. A. McLaughlin, and D. D. Sampson, "Needle optical coherence elastography for tissue boundary detection," Optics letters **37**, 2310-2312 (2012).
114. K. J. Parker, M. M. Doyley, and D. J. Rubens, "Imaging the elastic properties of tissue: the 20 year perspective," Physics in medicine and biology **56**, R1-r29 (2011).
115. F. G. Malheiro, "Towards clinical optical elastography: high-speed 3D imaging using volumetric phase detection," (Universidade de Lisboa, 2014).
116. *Optical Coherence Elastography: Imaging Tissue Mechanics on the Micro-Scale* (AIP Publishing LLC).
117. D. Alonso-Caneiro, K. Karnowski, B. J. Kaluzny, A. Kowalczyk, and M. Wojtkowski, "Assessment of corneal dynamics with high-speed swept source Optical Coherence Tomography combined with an air puff system," Opt. Express **19**, 14188-14199 (2011).
118. S. Wang and K. V. Larin, "Noncontact depth-resolved micro-scale optical coherence elastography of the cornea," Biomed Opt Express **5**, 3807-3821 (2014).
119. S. Song, N. M. Le, Z. Huang, T. Shen, and R. K. Wang, "Quantitative shear-wave optical coherence elastography with a programmable phased array ultrasound as the wave source," Optics letters **40**, 5007-5010 (2015).
120. C.-H. Liu, D. Nevozhay, A. Schill, M. Singh, S. Das, A. Nair, Z. Han, S. Aglyamov, K. V. Larin, and K. V. Sokolov, "Nanobomb optical coherence elastography," Optics letters **43**, 2006-2009 (2018).
121. C. Li, Z. Huang, and R. K. Wang, "Elastic properties of soft tissue-mimicking phantoms assessed by combined use of laser ultrasonics and low coherence interferometry," Opt. Express **19**, 10153-10163 (2011).
122. X. Feng, G.-Y. Li, and S.-H. Yun, "Ultra-wideband optical coherence elastography from acoustic to ultrasonic frequencies," Nature Communications **14**, 4949 (2023).

123. X. Feng, G.-Y. Li, A. Ramier, A. M. Eltony, and S.-H. Yun, "In vivo stiffness measurement of epidermis, dermis, and hypodermis using broadband Rayleigh-wave optical coherence elastography," Acta Biomaterialia **146**, 295-305 (2022).
124. S. G. Adie, X. Liang, B. F. Kennedy, R. John, D. D. Sampson, and S. A. Boppart, "Spectroscopic optical coherence elastography," Opt. Express **18**, 25519-25534 (2010).
125. C. Sun, B. Standish, B. Vuong, X.-Y. Wen, and V. X. Yang, "Digital image correlation–based optical coherence elastography," Journal of biomedical optics **18**, 121515 (2013).
126. P. Sáez, C. Borau, N. Antonovaite, and K. Franze, "Brain tissue mechanics is governed by microscale relations of the tissue constituents," Biomaterials **301**, 122273 (2023).
127. N. Detrez, S. Burhan, K. Rewerts, J. Kren, C. Hagel, M. M. Bonsanto, D. Theisen-Kunde, R. Huber, and R. Brinkmann, *Air-Jet based optical coherence elastography: processing and mechanical interpretation of brain tumor data*, SPIE BiOS (SPIE, 2023), Vol. 12381.
128. N. Detrez, S. Burhan, K. Rewerts, J. Kren, S. Buschschlüter, D. Theisen-Kunde, M. M. Bonsanto, R. Huber, and R. Brinkmann, "Flow-Controlled Air-Jet for In Vivo Quasi Steady-State and Dynamic Elastography With MHz Optical Coherence Tomography," IEEE Transactions on Biomedical Engineering **72**, 1008-1020 (2025).
129. C. U. Devi, R. M. Vasu, and A. K. Sood, "Design, fabrication, and characterization of a tissue-equivalent phantom for optical elastography," Journal of biomedical optics **10**, 44020 (2005).
130. N. Otsu, "A Threshold Selection Method from Gray-Level Histograms," IEEE Transactions on Systems, Man, and Cybernetics **9**, 62-66 (1979).
131. M. N. Polyanskiy, "Refractive index database", retrieved 05-02, 2023, https://refractiveindex.info.
132. J. Sun, S. J. Lee, L. Wu, M. Sarntinoranont, and H. Xie, "Refractive index measurement of acute rat brain tissue slices using optical coherence tomography," Opt. Express **20**, 1084-1095 (2012).
133. P. Strenge, B. Lange, C. Grill, W. Draxinger, V. Danicke, D. Theisen-Kunde, C. Hagel, S. Spahr-Hess, M. M. Bonsanto, R. Huber, H. Handels, and R. Brinkmann, "Registration of histological brain images onto optical coherence tomography images based on shape information," Physics in Medicine & Biology **67**, 135007 (2022).
134. S. Burhan, M. Göb, M. Pieper, T. Laedtke, T. Grahl, M. Münter, H. Schulz-Hildebrandt, G. Hüttmann, P. König, and R. Huber, "Label-free volumetric imaging of porcine kidney tissue over extended areas using dynamic MHz-OCT," Scientific reports **15**, 32426 (2025).
135. H. Knipe, T. Walizai, and J. Southi, "Kidneys" (May 24, 2025), retrieved https://radiopaedia.org/articles/kidneys.
136. R. Dalal, Z. S. Bruss, and J. S. Sehdev, "Physiology, Renal Blood Flow and Filtration," in *StatPearls* (StatPearls Publishing Copyright © 2025, StatPearls Publishing LLC., 2025).
137. A. J. Dare, G. J. Pettigrew, and K. Saeb-Parsy, "Preoperative Assessment of the Deceased-Donor Kidney: From Macroscopic Appearance to Molecular Biomarkers," Transplantation **97**, 797-807 (2014).

138. P. S. Rao, D. E. Schaubel, M. K. Guidinger, K. A. Andreoni, R. A. Wolfe, R. M. Merion, F. K. Port, and R. S. Sung, "A Comprehensive Risk Quantification Score for Deceased Donor Kidneys: The Kidney Donor Risk Index," Transplantation **88**, 231-236 (2009).
139. Y. T. Yap, Q. Y. Ho, T. Kee, C. Y. Ng, and C. Y. Chionh, "Impact of pre-transplant biopsy on 5-year outcomes of expanded criteria donor kidney transplantation," Nephrology **26**, 70-77 (2021).
140. C. Traynor, S. A., O. C. E., E. A., O. K. P., d. F. D. G., D. A. M., C. P. J., and C. M. and O'Seaghdha, "Pre-transplant histology does not improve prediction of 5-year kidney allograft outcomes above and beyond clinical parameters," Renal Failure **39**, 671-677 (2017).
141. A. Peris, G. E. Fulceri, C. Lazzeri, M. Bonizzoli, V. Li Marzi, S. Serni, L. Cirami, and M. L. Migliaccio, "Delayed graft function and perfusion parameters of kidneys from uncontrolled donors after circulatory death," Perfusion **36**, 299-304 (2021).
142. P. Peng, Z. Ding, Y. He, J. Zhang, X. Wang, and Z. Yang, "Hypothermic Machine Perfusion Versus Static Cold Storage in Deceased Donor Kidney Transplantation: A Systematic Review and Meta-Analysis of Randomized Controlled Trials," Artificial organs **43**, 478-489 (2019).
143. M. Bissolati, P. G. Gazzetta, R. Caldara, G. Guarneri, O. Adamenko, F. Giannone, M. Mazza, G. Maggi, D. Tomanin, R. Rosati, A. Secchi, and C. Socci, "Renal Resistance Trend During Hypothermic Machine Perfusion Is More Predictive of Postoperative Outcome Than Biopsy Score: Preliminary Experience in 35 Consecutive Kidney Transplantations," Artificial organs **42**, 714-722 (2018).
144. S. K. Patel, O. G. Pankewycz, N. D. Nader, M. Zachariah, R. Kohli, and M. R. Laftavi, "Prognostic Utility of Hypothermic Machine Perfusion in Deceased Donor Renal Transplantation," Transplantation Proceedings **44**, 2207-2212 (2012).
145. P. M. Andrews, Y. Chen, M. L. Onozato, S.-W. Huang, D. C. Adler, R. A. Huber, J. Jiang, S. E. Barry, A. E. Cable, and J. G. Fujimoto, "High-resolution optical coherence tomography imaging of the living kidney," Laboratory Investigation **88**, 441-449 (2008).
146. B. Konkel, C. Lavin, T. T. Wu, E. Anderson, A. Iwamoto, H. Rashid, B. Gaitian, J. Boone, M. Cooper, P. Abrams, A. Gilbert, Q. Tang, M. Levi, J. G. Fujimoto, P. Andrews, and Y. Chen, "Fully automated analysis of OCT imaging of human kidneys for prediction of post-transplant function," Biomed. Opt. Express **10**, 1794-1821 (2019).
147. X. Ma, M. Moradi, X. Ma, Q. Tang, M. Levi, Y. Chen, and H. K. Zhang, "Large area kidney imaging for pre-transplant evaluation using real-time robotic optical coherence tomography," Communications Engineering **3**, 122 (2024).
148. Q. Li, M. L. Onozato, P. M. Andrews, C.-W. Chen, A. Paek, R. Naphas, S. Yuan, J. Jiang, A. Cable, and Y. Chen, "Automated quantification of microstructural dimensions of the human kidney using optical coherence tomography (OCT)," Opt. Express **17**, 16000-16016 (2009).
149. C. Apelian, F. Harms, O. Thouvenin, and A. C. Boccara, "Dynamic full field optical coherence tomography: subcellular metabolic contrast revealed in tissues by interferometric signals temporal analysis," Biomed. Opt. Express **7**, 1511-1524 (2016).

150. J. Scholler, K. Groux, O. Goureau, J.-A. Sahel, M. Fink, S. Reichman, C. Boccara, and K. Grieve, "Dynamic full-field optical coherence tomography: 3D live-imaging of retinal organoids," Light: Science & Applications **9**, 140 (2020).
151. I. Abd El-Sadek, A. Miyazawa, L. Tzu-Wei Shen, S. Makita, S. Fukuda, T. Yamashita, Y. Oka, P. Mukherjee, S. Matsusaka, T. Oshika, H. Kano, and Y. Yasuno, "Optical coherence tomography-based tissue dynamics imaging for longitudinal and drug response evaluation of tumor spheroids," Biomed. Opt. Express **11**, 6231-6248 (2020).
152. T. Kohlfaerber, M. Pieper, M. Münter, C. Holzhausen, M. Ahrens, C. Idel, K.-L. Bruchhage, A. Leichtle, P. König, G. Hüttmann, and H. Schulz-Hildebrandt, "Dynamic microscopic optical coherence tomography to visualize the morphological and functional micro-anatomy of the airways," Biomed. Opt. Express **13**, 3211-3223 (2022).
153. M. Münter, M. Pieper, T. Kohlfaerber, E. Bodenstorfer, M. Ahrens, C. Winter, R. Huber, P. König, G. Hüttmann, and H. Schulz-Hildebrandt, "Microscopic optical coherence tomography (mOCT) at 600 kHz for 4D volumetric imaging and dynamic contrast," Biomed. Opt. Express **12**, 6024-6039 (2021).
154. T. Samuel, W. E. Hoy, R. Douglas-Denton, M. D. Hughson, and J. F. Bertram, "Applicability of the glomerular size distribution coefficient in assessing human glomerular volume: the Weibel and Gomez method revisited," Journal of anatomy **210**, 578-582 (2007).
155. S. Klein, M. Staring, K. Murphy, M. A. Viergever, and J. P. W. Pluim, "elastix: A Toolbox for Intensity-Based Medical Image Registration," IEEE Transactions on Medical Imaging **29**, 196-205 (2010).
156. L. Ibanez, W. Schroeder, L. Ng, J. Cates, J. Kim, J. Jomier, S. Aylward, T. Sundaram, J. Jin, C. Imielinska, M. Foskey, and M. Malaterre, *The ITK Software Guide* (2003).
157. N. Heldt, C. Holzhausen, M. Ahrens, M. Pieper, P. König, and G. Hüttmann, "Improved image quality in dynamic OCT imaging by reduced imaging time and machine learning based data evaluation," SPIE BiOS **PC12830**(2024).
158. H. Schulz-Hildebrandt, M. Wang-Evers, N. Meyer-Schell, D. Karasik, M. Casper, T. Eixmann, F. Hilge, R. Birngruber, D. Manstein, and G. Hüttmann, "Optical coherence tomography needle probe for real-time visualization of temperature-induced phase changes within subcutaneous fatty tissue," Journal of biomedical optics **30**, 035002 (2025).
159. J. Wierwille, P. M. Andrews, M. L. Onozato, J. Jiang, A. Cable, and Y. Chen, "In vivo, label-free, three-dimensional quantitative imaging of kidney microcirculation using Doppler optical coherence tomography," Laboratory Investigation **91**, 1596-1604 (2011).

Academic contributions

Journal articles as first author

- **Sazgar Burhan**, Berenice Schulte, Madita Göb, Awanish Pratap Singh, Bayan Mustafa, Simon Lotz, Wolfgang Draxinger, Philipp Lamminger, Yasmeine Saker, Tim Eixmann, Martin Ahrens, Marvin Heimke, Tillmann Heinze, Thilo Wedel, Maik Rahlves, Mark Ellrichmann, and Robert Huber, Dual-resolution megahertz optical coherence tomography prototype rectoscope for enhanced visualization of colorectal microstructures, Journal of Biomedical Optics, vol. 31, no. 4, pp. 046002, 2026. SPIE.
- **Sazgar Burhan**, Madita Göb, Mario Pieper, Tjalfe Laedtke, Thorge Grahl, Michael Münter, Hinnerk Schulz-Hildebrandt, Gereon Huettmann, and Robert Huber, Label-free volumetric imaging of porcine kidney tissue over extended areas using dynamic MHz-OCT, Scientific Reports, vol. 15, no. 1, pp. 32426, Sep. 2025.
- **Sazgar Burhan**, Nicolas Detrez, Katharina Rewerts, Paul Strenge, Steffen Buschschlüter, Jessica Kren, Christian Hagel, Matteo Mario Bonsanto, Ralf Brinkmann, and Robert Huber, Phase unwrapping for MHz optical coherence elastography and application to brain tumor tissue, Biomed. Opt. Express, vol. 15, no. 2, pp. 1038-1058, Feb. 2024. Optica Publishing Group. **[Top downloads Biomedical Optics Express February and March 2024]**

Peer-reviewed conference papers and talks as first author

- **Sazgar Burhan**, Madita Göb, Gereon Hüttmann, and Robert Huber, Non-Equidistant Temporal Scanning in Dynamic MHz-OCT for Higher Speed, in European Conferences on Biomedical Optics 2025, Optica Publishing Group, 2025. pp. S4B.3.
- **Sazgar Burhan**, Berenice Schulte, Madita Göb, Awanish Pratap Singh, Bayan Mustafa, Simon Lotz, Wolfgang Draxinger, Philipp Lamminger, Yasmeine Saker, Tim Eixmann, Martin Ahrens, Marvin Heimke, Tillmann Heinze, Thilo Wedel, Maik Rahlves, Mark Ellrichmann, and Robert Huber, Switchable lateral resolution real-time MHz-OCT rectoscopy for enhanced colorectal disease diagnosis, in Optical Coherence Tomography and Coherence Domain Optical Methods in Biomedicine XXIX, Rainer A. Leitgeb and Yoshiaki Yasuno, Eds. SPIE, Mar.2025. pp. 1330512. **[Best poster award]**
- **Sazgar Burhan**, Madita Göb, Mario Pieper, Tjalfe Laedtke, Thorge Grahl, Michael Münter, Hinnerk Schulz-Hildebrandt, Gereon Hüttmann, Peter König, and Robert

Huber, Large-area dynamic contrast MHz optical coherence tomography for label-free imaging of porcine tissue, in Optical Coherence Tomography and Coherence Domain Optical Methods in Biomedicine XXIX, Rainer A. Leitgeb and Yoshiaki Yasuno, Eds. SPIE, Mar.2025. pp. 1330502. **[Best paper award finalist]**

- **Sazgar Burhan**, Nicolas Detrez, Madita Göb, Matteo Mario Bonsanto, Ralf Brinkmann, and Robert Huber, Advanced FFT-based contrast approach for MHz optical coherence elastography, in Optical Coherence Imaging Techniques and Imaging in Scattering Media V, Benjamin J. Vakoc and Maciej Wojtkowski and Yoshiaki Yasuno, Eds. SPIE, Aug.2023. pp. 1263215.
- **Sazgar Burhan**, Nicolas Detrez, Katharina Rewerts, Madita Göb, Christian Hagel, Matteo M. Bonsanto, Dirk Theisen-Kunde, Robert Huber, and Ralf Brinkmann, Characterization of brain tumor tissue by time-resolved, phase-sensitive optical coherence elastography at 3.2 MHz line rate, in Advanced Biomedical and Clinical Diagnostic and Surgical Guidance Systems XXI, Caroline Boudoux and James W. Tunnell, Eds. SPIE, Mar.2023. pp. 123680F.
- **Sazgar Burhan**, Nicolas Detrez, Katharina Rewerts, Madita Göb, Steffen Buschschlüter, Christian Hagel, Matteo M. Bonsanto, Dirk Theisen-Kunde, Robert Huber, and Ralf Brinkmann, Phase analysis strategies for MHz OCE in the large displacement regime, in Optical Coherence Tomography and Coherence Domain Optical Methods in Biomedicine XXVII, Joseph A. Izatt and James G. Fujimoto, Eds. SPIE, 2023. pp. 123670Q.

Other journal contributions

- Tjalfe Laedtke, **Sazgar Burhan**, Simon Lotz, Madita Göb, Robert Huber, Angular compounding for speckle reduction in robotically assisted optical coherence tomography, under review in Journal of Biomedical Optics.
- Nicolas Detrez, **Sazgar Burhan**, Steffen Buschschlüter, Dirk Theisen-Kunde, Matteo Mario Bonsanto, Robert Huber, and Ralf Brinkmann, Processing pipeline for large optical coherence elastography datasets with quasi-static air-jet excitation: application to human brain tumor tissue, Biomed. Opt. Express, vol. 17, no. 3, pp. 1335-1358, Mar. 2026. Optica Publishing Group.
- Nicolas Detrez, **Sazgar Burhan**, Katarina Rewerts, Jessica Kren, Steffen Buschschlüter, Dirk Theisen-Kunde, Matteo Mario Bonsanto, Robert Huber, and Ralf Brinkmann, Flow-Controlled Air-Jet for In Vivo Quasi Steady-State and Dynamic Elastography With MHz Optical Coherence Tomography, IEEE Transactions on Biomedical Engineering, vol. 72, no. 3, pp. 1008-1020, Mar. 2025.

- Jessica Kren, Patrick Kuppler, Steffen Buschschlüter, Nicolas Detrez, **Sazgar Burhan**, Robert Huber, Ralf Brinkmann, and Matteo Mario Bonsanto, Mechanical characteristics of glioblastoma and peritumoral tumor-free human brain tissue, Acta Neurochirurgica, vol. 166, no. 1, pp. 102, Feb. 2024.

Other peer-reviewed proceeding contributions

- Nicolas Detrez, **Sazgar Burhan**, Jakob Matschke, Dirk Theisen-Kunde, Matteo Mario Bonsanto, Robert Huber, Ralf Brinkmann, Mechanical Property Mapping of Brain Tumor Tissue via Air-Jet based Optical Coherence Elastography, in International Symposium on Brain Mechanics 2025, CRC 1540 "Exploring Brain Mechanics", pp. P07.
- Madita Göb, **Sazgar Burhan**, Gereon Hütttmann, and Robert Huber, In vivo Megahertz Dynamic Optical Coherence Tomography of Human Skin, in European Conferences on Biomedical Optics 2025, Optica Publishing Group, 2025. pp. Tu3C.4.
- Tjalfe Laedtke, **Sazgar Burhan**, Simon Lotz, Madita Göb, and Robert Huber, Speckle Reduction Through Angular Compounding in Robotically Assisted MHz-OCT, in European Conferences on Biomedical Optics 2025, Optica Publishing Group, 2025. pp. W1D.4.
- Awanish Pratap Singh, Madita Göb, **Sazgar Burhan**, Nikolay Tesmer, Wolfgang Draxinger, Simon Lotz, Berenice Schulte, Mark Ellrichmann, Robert Huber, and Maik Rahlves, Multi-MHz-OCT Endoscopic Imaging with an Automated Pullback Mechanism, in European Conferences on Biomedical Optics 2025, Optica Publishing Group, 2025. pp. M1C.1.
- Nicolas Detrez, Dirk Theisen-Kunde, Wolfgang Draxinger, Thies Höcher, Veit Danike, **Sazgar Burhan**, Jessica Kren, Matteo Mario Bonsanto, Robert Huber, Ralf Brinkmann, Co-robot supported air-jet based optical coherence elastography towards in-situ brain tumor tissue delineation, in European Conferences on Biomedical Optics 2025, Optica Publishing Group, 2025. pp. M3A.36.
- Nicolas Detrez, **Sazgar Burhan**, Jakob Matschke, Matteo Mario Bonsanto, Robert Huber, Ralf Brinkmann, Air-Jet based Optical Coherence Elastography for brain tumor tissue delineation and fundamental research in tissue mechanics, 76. Jahrestagung der Deutschen Gesellschaft für Neurochirurgie (DGNC).
- Berenice Schulte, **Sazgar Burhan**, Awanish Pratap Singh, Wolfgang Draxinger, Simon Lotz, Marvin Heimke, Tillmann Heinze, Thilo Wedel, Maik Rahlves, Robert Huber, and Mark Ellrichmann, Hochauflösende Rektoskopie mittels dual-mode MHz optischer Kohärenztomographie - ein Schritt zur real time 3D Endoskopie, Z Gastroenterol, vol. 62, no. 09, pp. KV 355, Sep. 2024. Georg Thieme Verlag KG.

- Tjalfe Laedtke, **Sazgar Burhan**, Simon Lotz, Robert Huber. Robotically-enabled angular compounding for speckle reduction in optical coherence tomography. 13th Student Conference on Medical Engineering Science, Infinite Science Publishing, Lübeck University Press and Academic Printing. Mar 2024. **[Best oral presentation in Track A (Medical Electronics, Biomedical Engineering, Biomedical Optics)]**
- Madita Göb, Simon Lotz, Linh Ha-Wissel, **Sazgar Burhan**, Sven Böttger, Floris Ernst, Jennifer Hundt, and Robert Huber, Advances in large area robotically assisted OCT (LARA-OCT): towards drive-by continuous motion imaging, in Optical Coherence Imaging Techniques and Imaging in Scattering Media V, Benjamin J. Vakoc and Maciej Wojtkowski and Yoshiaki Yasuno, Eds. SPIE, Aug.2023. pp. 126321N.
- Madita Göb, Simon Lotz, Linh Ha-Wissel, **Sazgar Burhan**, Sven Böttger, Floris Ernst, Jennifer Hundt, and Robert Huber, Large area robotically assisted optical coherence tomography (LARA-OCT) for skin imaging with MHz-OCT surface tracking, in Optical Coherence Tomography and Coherence Domain Optical Methods in Biomedicine XXVII, Joseph A. Izatt and James G. Fujimoto, Eds. SPIE, Mar.2023. pp. 123670C.
- Nicolas Detrez, **Sazgar Burhan**, Paul Strenge, Jessica Kren, Christian Hagel, Matteo Mario Bonsanto, Dirk Theisen-Kunde, Robert Huber, and Ralf Brinkmann, Air-jet based optical coherence elastography of brain tumor tissue: stiffness evaluation by structural histological analysis, in Emerging Technologies for Cell and Tissue Characterization II, Seemantini K. Nadkarni and Giuliano Scarcelli, Eds. SPIE, 2023. pp. 126290M.
- Nicolas Detrez, **Sazgar Burhan**, Katharina Rewerts, Jessica Kren, Christian Hagel, Matteo Mario Bonsanto, Dirk Theisen-Kunde, Robert Huber, and Ralf Brinkmann, Air-Jet based optical coherence elastography: processing and mechanical interpretation of brain tumor data, in Optical Elastography and Tissue Biomechanics X, Kirill V. Larin and Giuliano Scarcelli and Frédérique Vanholsbeeck, Eds. SPIE, 2023. pp. 1238105.
- Madita Göb, **Sazgar Burhan**, Simon Lotz, and Robert Huber, Towards ultra-large area vascular contrast skin imaging using multi-MHz-OCT, in Optical Coherence Tomography and Coherence Domain Optical Methods in Biomedicine XXVI, Joseph A. Izatt and James G. Fujimoto, Eds. SPIE, Mar.2022. pp. 27 -- 31.

Teaching

SoSe 2022 **Physics laboratory course for medical students**
„Geometrische Optik / Auge + Spektralphotometer / Labordiagnostik“

WS 2022/23 **Physics laboratory course for engineering students**
„Geometrische Optik + Wellenoptik“

SoSe 2023 **Physics laboratory course for medical students**
„Geometrische Optik / Auge + Spektralphotometer / Labordiagnostik“

WS 2023/24 **Physics laboratory course for engineering students**
„Geometrische Optik + Wellenoptik“

Thesis supervision

2022 **Bachelor's thesis by Thorge Grahl**
“Entwicklung eines ultra-stabilen 3-Achs Linearroboters für großflächige, phasenbasierte funktionale optische Kohärenztomographie”

2024 **Master's thesis by Bayan Mustafa (During M. Göb's absence 11/2023 - 02/2024)**
“Optical multiplex beam delivery system for dual-resolution endoscopic OCT”

2024 **Master's internship by Tjalfe Laedtke**
“Robotergestütztes Angular Compounding zur Speckle-Reduktion in der optischen Kohärenztomographie”

2025 **Master's thesis by Tjalfe Laedtke**
“Speckle-Reduktion durch Winkelkomposition in der robotergestützten MHz-OCT”

Assistance in grant proposal writing

2023 **Deutsche Krebshilfe “Operativ-chirurgisch orientierte Forschungsvorhaben“**
UKSH Lübeck, Universität zu Lübeck, Medizinisches Laserzentrum Lübeck GmbH
"Intraoperative functional Neuro-OCT combined with optical tumor localization"
36 months, 638.780 €

2024 **Deutsche Forschungsgemeinschaft (DFG)**
UKSH Lübeck, Universität zu Lübeck
"Real-time MHz-OCT zur Planung, Überwachung und Funktionskontrolle während Bypass Operationen am schlagenden Herzen ohne Herz-Lungen-Maschine (OPCAB)"
36 months, 638.417 €

Acknowledgements

Diese Arbeit entstand nicht nur durch eigene Anstrengung, sondern auch durch die Unterstützung vieler Menschen, die mir mit Rat, Motivation und Vertrauen zur Seite standen. Ich danke Ihnen allen von Herzen.

Dabei möchte ich mich an erster Stelle bei meinem Doktorvater Robert Huber bedanken, bei dem ich in den vergangenen Jahren sowohl fachlich als auch persönlich viel lernen konnte. Für Fragen war seine Tür immer offen, und er hat mir stets mit klaren und hilfreichen Ratschlägen zur Seite gestanden. Besonders dankbar bin ich ihm auch dafür, dass er mir die Möglichkeit gegeben hat, unsere Ergebnisse mehrfach auf internationalen Konferenzen vorzustellen und dabei wertvolle Kontakte zu knüpfen.

Außerdem möchte ich mich bei Ralf Brinkmann bedanken, der mir in der Anfangszeit durch die finanzielle Unterstützung den Einstieg in die Promotion ermöglicht hat. Für sein Vertrauen, seine beständige Unterstützung und das stets angenehme und kollegiale Miteinander bin ich ihm sehr dankbar.

Des Weiteren möchte ich mich bei der gesamten Arbeitsgruppe bedanken, darunter Marie Klufts, Asim Bashir, Madita Göb, Simon Lotz, Philipp Lamminger und Wolfgang Draxinger. Die Zusammenarbeit war stets angenehm, kollegial und geprägt von gegenseitiger Unterstützung. Ich hätte mir keine bessere Gruppe vorstellen können. Ich möchte mich auch bei allen Studierenden bedanken, mit denen ich in dieser Zeit zusammenarbeiten durfte. Besonders danke ich die von mir betreuten Studenten Thorge Grahl und Tjalfe Laedtke, deren Engagement und Beiträge diese Arbeit inhaltlich bereichert und vorangebracht haben.

Ebenso möchte ich mich bei allen Kolleginnen und Kollegen im UltraLas-Projekt bedanken. Mein besonderer Dank gilt dabei den klinischen Partnern Matteo Mario Bonsanto, Jessica Kren und Christian Hagel für die gute Zusammenarbeit. Ich danke außerdem der Firma Söring für die gute Kooperation, insbesondere Steffen Buschschlüter, der uns mehrere Phantome zur Verfügung gestellt hat. Auch den Mitarbeitenden des MLLs danke ich herzlich, darunter Dirk Theisen-Kunde, Susanna Cuturic, Paul Strenge und Nicolas Detrez. Besonders hervorheben möchte ich die enge und erfolgreiche Zusammenarbeit mit Nick.

Darüber hinaus möchte ich mich bei Mario Pieper und Peter König bedanken. Ihr fachliches Wissen hat mir sehr dabei geholfen, die dOCT-Ergebnisse besser zu verstehen. Für diese Unterstützung bin ich beiden sehr dankbar.

Ein herzlicher Dank geht auch an alle Mitarbeitenden und Studierenden am BMO und am MLL. Die freundliche und hilfsbereite Atmosphäre hat das tägliche Arbeiten sehr angenehm gemacht. Bei Fragen zu fachlichen oder organisatorischen Themen haben sich alle stets Zeit genommen. Das habe ich besonders geschätzt. Mein besonderer Dank gilt Bianka Pohlmann, die mit ihrer strukturierten und verlässlichen Art immer den Überblick behielt und bei organisatorischen Anliegen jederzeit eine passende Antwort hatte. Ihre Unterstützung hat vieles deutlich einfacher gemacht.

Zu guter Letzt danke ich meiner ganzen Familie für ihre Unterstützung, Geduld und ihren Rückhalt während der gesamten Promotionszeit. Ohne ihren Zuspruch und das Vertrauen in meinen Weg wäre vieles deutlich schwerer gewesen. Gerade in den stillen, schweren Stunden war es meine Familie, die wie ein fester Anker wirkte.

Editorial tools

Online tools, such as Grammarly, DeepL, and ChatGPT, were utilized to enhance language editing and clarity.